Prog. Theor. Exp. Phys. **2012**, 04D001 (110 pages)
DOI: 10.1093/ptep/pts072

Physics achievements from the Belle experiment

Jolanta Brodzicka[1], Thomas Browder[2], Paoti Chang[3], Simon Eidelman[4], Bostjan Golob[5,6], Kiyoshi Hayasaka[7], Hisaki Hayashii[8], Toru Iijima[7], Kenji Inami[7], Kay Kinoshita[9], Youngjoon Kwon[10], Kenkichi Miyabayashi[8], Gagan Mohanty[11], Mikihiko Nakao[12], Hideyuki Nakazawa[13], Stephen Olsen[14], Yoshihide Sakai[12], Christoph Schwanda[15], Alan Schwartz[9], Karim Trabelsi[12,*], Sadaharu Uehara[12], Shoji Uno[12], Yasushi Watanabe[16], and Anze Zupanc[17] for the Belle Collaboration

[1] *H. Niewodniczanski Institute of Nuclear Physics, Krakow*
[2] *University of Hawaii, Honolulu, Hawaii 96822*
[3] *Department of Physics, National Taiwan University, Taipei*
[4] *Budker Institute of Nuclear Physics SB RAS and Novosibirsk State University, Novosibirsk 630090*
[5] *Faculty of Mathematics and Physics, University of Ljubljana, Ljubljana*
[6] *Jozef Stefan Institute, Ljubljana*
[7] *Kobayashi–Maskawa Institute, Nagoya University, Nagoya*
[8] *Nara Women's University, Nara*
[9] *University of Cincinnati, Cincinnati, Ohio 45221*
[10] *Yonsei University, Seoul*
[11] *Tata Institute of Fundamental Research, Mumbai*
[12] *High Energy Accelerator Research Organization (KEK), Tsukuba*
[13] *National Central University, Chung-li*
[14] *Seoul National University, Seoul*
[15] *Institute of High Energy Physics, Vienna*
[16] *Kanagawa University, Yokohama*
[17] *Institut für Experimentelle Kernphysik, Karlsruher Institut für Technologie, Karlsruhe*
[*] E-mail: karim.trabelsi@kek.jp

Received November 4, 2012; Accepted November 8, 2012; Published December 29, 2012

The Belle experiment, running at the KEKB e^+e^- asymmetric energy collider during the first decade of the century, achieved its original objective of precisely measuring differences between particles and antiparticles in the B system. After collecting $1000\,\mathrm{fb}^{-1}$ of data at various Υ resonances, Belle also obtained the many other physics results described in this article.

1. Introduction

In the sections that follow, we describe the physics accomplishments of the Belle experiment, which ran at the KEKB [1] e^+e^- asymmetric energy collider in Tsukuba, Japan between 1999 and 2010. KEKB broke all records for integrated and instantaneous luminosity for a high energy accelerator. As a result Belle was able to integrate over $1000\,\mathrm{fb}^{-1}$ or one inverse attobarn of data.

Belle was designed and optimized for the observation of CP violation in the B meson system. In 2001, Belle (along with BaBar, a competing and similar experiment located in Stanford, California) was indeed able to observe large CP asymmetries in B decays, which were expected and consistent with the theoretical proposal of Kobayashi and Maskawa. This experimental result was explicitly recognized in the 2008 Physics Nobel Prize citation.

Nevertheless, the Belle spectrometer was a general purpose device with reasonable solid coverage as well as high quality vertexing with silicon strip detectors, charged particle tracking with a central drift chamber, and excellent electromagnetic calorimetry, as well as muon and K_L detection. These detector capabilities allowed Belle to not only cover most of the important topics in B physics (in addition to the CP violation measurements) but also to make important discoveries in charm physics, tau lepton physics, hadron spectroscopy, and two-photon physics.

Most of the Belle luminosity was recorded on or near the $\Upsilon(4S)$ resonance, which is the optimal center of mass (CM) energy for the production of $B\bar{B}$ pairs used in B physics analysis. However, KEKB has some flexibility in energy and Belle also recorded a series of *unique data sets* at the $\Upsilon(1S)$, $\Upsilon(2S)$, and $\Upsilon(5S)$ resonances. The latter data set is of special interest in hadron spectroscopy as a large number of new and some exotic states were found in analyses of this sample.

2. The Belle detector and its data samples

2.1. Overview

The Belle detector is located at the interaction region of an asymmetric energy e^+e^- collider, called KEKB [1]. Belle is optimized to measure time-dependent CP violation in B-meson decay. Therefore, the detector has good vertex resolution and good particle identification capabilities for leptons and hadrons. The detector material is minimized to reduce multiple scattering for charged particles and to maintain high efficiency and good resolution for low energy photons. The acceptance is asymmetric (covering the polar angle region from 17° to 150°) to match the boost from the asymmetric 8 on 3.5 GeV energy collisions. Belle is a general purpose 4π detector, which can accommodate various physics programs, including studies of τ pairs, two-photon physics, and $q\bar{q}$ continuum processes.

Figure 1 shows the Belle detector configuration. The detector is built around a 1.5 Tesla superconducting solenoid and iron structure. The beam crossing angle is ± 11 mrad. B-meson decay vertices are measured by a double-sided silicon vertex detector (SVD) situated around a cylindrical beryllium beam pipe. There are two inner detector configurations: SVD1 (three layers before the summer of 2003) and SVD2 (four layers). Charged particle tracking is provided by a central drift chamber (CDC). Particle identification is provided by dE/dx measurements in the CDC, aerogel Cerenkov counters (ACC), and time-of-flight counters (TOF) situated radially outside of the CDC. Electromagnetic showers are detected by an array of CsI(Tl) crystals (ECL) located inside the solenoid coil. Muons and K_L mesons are identified by arrays of resistive plate counters (KLM) interspersed in the iron yoke. An array of bismuth germanate oxide (BGO) crystals called the extreme forward calorimeter (EFC) is located on the surface of the cryostats of the compensation solenoid magnets in the forward and backward directions. The EFC is used as an active shield against beam background and also measures the online luminosity. Each subdetector is briefly described in the following subsections; more detailed information is available in Ref. [2].

2.2. The beam pipe

The Belle detector beam pipe [3] is connected to the KEKB accelerator beam pipe. The pipe is a double-wall beryllium structure with liquid paraffin cooling to remove the heat generated by the beams. The inner diameter is only 30 mm (40 mm) for the SVD2 (SVD1) inner detector configuration to optimize vertex resolution. A 10 μm-thick layer of gold is sputtered inside the beryllium wall to prevent synchrotron radiation photons from entering the detector.

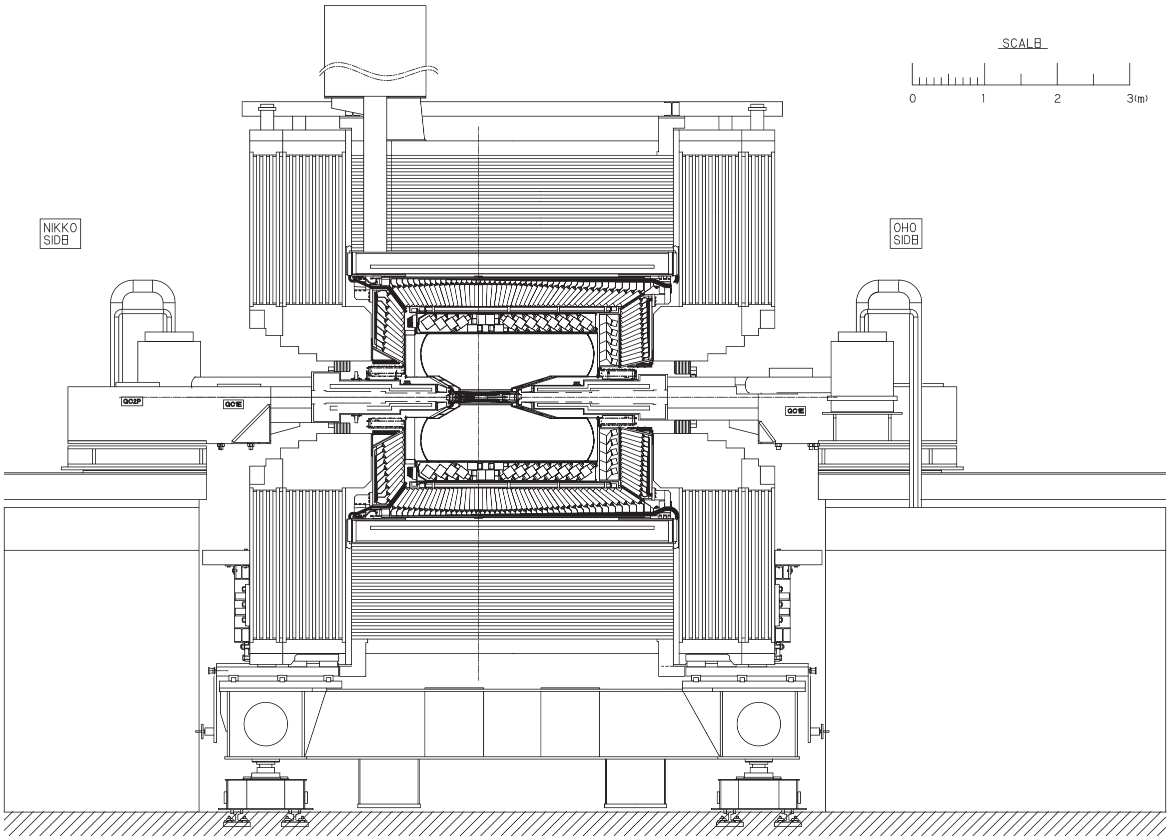

Fig. 1. Side view of the Belle detector.

2.3. *The SVD detector*

The SVD consists of four layers in a barrel-only design (SVD2 [4,5]). Each layer is independently constructed and consists of ladders. Each ladder consists of double-sided silicon strip detectors (DSSDs) reinforced by support ribs. The design uses two types of DSSDs. For the second version, the DSSDs of the 4th layer are shorter and wider than those of the other layers. The readout chain for the DSSDs is based on a VA1 (Viking architecture) integrated circuit. The back-end electronics is a system of flash analog-to-digital converters (FADCs) and field programmable gate arrays (FPGAs), which perform online common-mode noise subtraction, data sparsification, and data formatting.

Before the summer of 2003, there were three DSSD layers with slightly less angular coverage (SVD1). In addition, the beam pipe diameter was larger (40 mm versus 30 mm for the final data taking configuration).

2.4. *The CDC detector*

The structure of the CDC is asymmetric in the z direction in order to optimize the angular coverage. The longest wires are 2400 mm long. The inner radius extends to 80 mm without any walls in order to obtain good tracking efficiency for low momentum tracks with minimal intervening material. The outer radius is 880 mm. The forward and backward smaller-r regions have conical shapes in order to clear the accelerator components while maximizing the acceptance. A low-Z gas, a He–C_2H_6(50/50) gas mixture, is used in order to minimize multiple scattering. The chamber has 50 cylindrical layers, each containing between three and six axial or small-angle stereo layers, and three cathode strip layers. The CDC has a total of 8400 drift cells. We chose three layers for the two innermost stereo super-layers and four layers for the three outer stereo super-layers in order to provide a highly efficient and fast z-trigger, which is combined with the information from the cathode strips.

During the summer of 2003, the cathode part of the CDC was replaced by a compact small cell type drift chamber in order to make enough space for the SVD2 vertex detector. The cell sizes are only 5 mm in both the radial and azimuthal directions to accommodate two layers (128 cells per layer) in a limited space. The maximum drift time is rather small ($\sim$100 nsec); this feature can provide the first trigger signal for the SVD2 readout latch.

2.5. The ACC subsystem

The ACC consists of 960 counter modules segmented into 60 cells in the ϕ direction for the barrel part and 228 modules arranged in 5 concentric layers for the forward end-cap part of the detector. All the counters are arranged in a semi-projective geometry, pointing to the interaction point (IP). In order to obtain good pion/kaon separation to cover the entire kinematical range of two-body B decays, the refractive indices of the aerogel blocks vary between 1.01 and 1.03, depending on their polar angle region. Five aerogel tiles are stacked in a thin (0.2 mm thick) aluminum box of approximate dimensions $12 \times 12 \times 12\,\mathrm{cm}^3$. In order to detect Cerenkov light effectively, one or two fine mesh-type photomultiplier tubes (FM-PMTs), which are operated in a 1.5 T magnetic field, are attached directly to the aerogel on the sides of the box. We use Hamamatsu Photonics PMTs of three different diameters: 3, 2.5, and 2 inches, depending on the refractive index of the aerogel block, in order to obtain a uniform response for relativistic particles.

2.6. The TOF subsystem

The TOF system consists of 128 TOF counters and 64 thin trigger scintillation counters (TSC). Two trapezoidal shaped TOF counters and one TSC counter, with a 1.5 cm intervening radial gap, form a single module. In total, 64 TOF/TSC modules located at a radius of 1.2 m from the IP cover a polar angle range from 34° to 120°. The thicknesses of the scintillators (BC408, Bicron) are 4 cm and 0.5 cm for the TOF and TSC counters, respectively. The fine mesh PMTs operating inside the 1.5 T magnetic field, with a 2-inch diameter and 24 stages, were attached to both ends of the TOF counter with an air gap of 0.1 mm. For the TSCs, the tubes were glued to the light guides at the backward ends of the counters.

2.7. The ECL detector subsystem

A highly segmented array of CsI(Tl) crystals with silicon photodiode readout were selected for the ECL [6–8]. Each crystal has a tower-like shape and is arranged so that it nearly points to the IP. The calorimeter covers the full Belle angular region. A small gap between the barrel and end-cap crystals provides a pathway for the cables and room for supporting members of the inner detectors. The entire system contains 8736 counters. The size of each crystal is typically 55 mm $\times$ 55 mm (front face) and 65 mm $\times$ 65 mm (rear face). The 30 cm length (16 radiation lengths) is chosen to avoid deterioration of the energy resolution for high energy gammas due to fluctuations in the shower leakage out the rear of the counter. Each counter is read out by an independent pair of silicon PIN photodiodes and charge sensitive preamplifiers attached at the end of the crystal.

2.8. The KLM detector

The KLM consists of alternating layers of charged particle detectors and 4.7 cm-thick iron plates, which are the magnetic flux return in the barrel and endcap regions [9,10]. There are 15 detector layers and 14 iron layers in the octagonal barrel region and 14 detector layers in each of the forward and backward end-caps. The iron plates provide a total of 3.9 interaction lengths of material for a particle traveling normal to the detector planes. The detection of charged particles is provided by glass-electrode resistive plate counters (RPCs). The resistive plate counters have two parallel plate electrodes of 2.4 mm-thick commercially available float glass. The bulk resistivity of the glass is 10^{12}–$10^{13}\,\Omega\,\mathrm{cm}$ at room temperature. To distribute the high voltage on the glass, the outer surface was coated with carbon ink, which achieves a surface resistivity of 10^6–$10^7\,\Omega/\mathrm{square}$. The discharge signal can then be obtained from external pickup strips. The readout of 38K pickup strips is accomplished with the use of custom-made VME-based discriminator/time multiplexing boards.

2.9. Trigger and data acquisition

The Belle trigger system consists of a Level-1 hardware trigger and a Level-3 software trigger [11–13]. The latter is implemented in the online computer farm. The Level-1 trigger system consists of a subdetector trigger system and a central trigger system called global decision logic (GDL). The subdetector trigger systems are based on two categories: track triggers and energy triggers. The CDC and TOF are used to yield trigger signals for charged particles. The ECL trigger system [14] provides triggers based on total energy deposit and cluster counting of crystal hits. These two categories have sufficient redundancy. The KLM trigger gives additional information on muons. The EFC triggers are used for tagging two-photon events as well as Bhabha events.

The Belle data acquisition system used one type of multi-hit TDC modules for all subsystems except for the SVD. The signal pulse height is recorded as timing information using a charge to time conversion chip (Q-to-T chip). Precise timing information in the TOF is recorded by commercial TDC modules with special time expansion modules. The TDC modules did not have a pipe-line readout scheme. Therefore, the readout deadtime is large (around 30 μsec). There were several electronics upgrades in order to reduce deadtime carried out during the latter parts of the experiment. The TDC modules were gradually replaced with pipe-lined TDCs (2.8 μsec) for most of the subdetectors in the 2007–2009 running period [15]. It was carefully checked that these electronics upgrades did not affect the data quality.

Belle turned off the detector high voltage during beam injection, as do other experiments. The KEKB injection time was slightly longer than at PEP-II (the collider hosting the BaBar experiment) and the average efficiency was lower. In order to reduce such losses, a continuous injection scheme [1] was implemented in January 2004. The detector high voltage was kept on and the trigger signals were vetoed for a 3.5 msec interval just after each beam injection. This scheme leads to 3.5% deadtime only in the case of a 10 Hz injection rate. After adopting continuous injection, the KEKB machine became more stable and the peak luminosity improved due to the leveling of the beam currents.

2.10. Detector performance

The charged track reconstruction mainly uses the CDC. Good momentum resolution is obtained by combining CDC tracks together with SVD hit information, especially for low momentum tracks, thanks to the limited amount of intervening material. The following expression gives the momentum

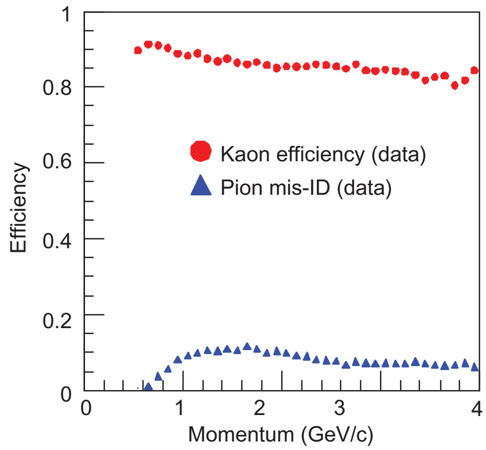

Fig. 2. Kaon identification efficiency and fake rate as a function of momentum.

resolution for a charged track as a function of its transverse momentum:

$$\sigma_{p_t}/p_t = 0.0019\ p_t[\mathrm{GeV}/c] \oplus 0.0030/\beta \tag{2.1}$$

The typical mass resolution of D^0 mesons is 5 MeV in hadronic events. The z-vertex resolution is 61 μm in the $J/\psi \to \mu^+\mu^-$ mode. A similar resolution is also obtained in the $r - \phi$ plane. The energy resolution of the ECL is 1.7% for Bhabha events. A π^0 mass resolution of 4.8 MeV is obtained for low momentum photons in hadronic events.

Pion/kaon/proton separation is obtained by combining ACC, TOF, and CDC dE/dx information. The kaon efficiency and the fake rate are shown in Fig. 2. The typical electron identification efficiency is 90% with a small fake rate (0.3%). Muons are also identified with 90% efficiency (2% fake rate) for charged tracks with momenta larger than 0.8 GeV (Fig. 3). More detailed information is available in Refs. [16–19].

2.11. Luminosity

Belle started data taking on 1 June 1999. After that, data runs were taken for 6–9 months every year until the final shutdown on 30 June 2010. The total integrated luminosity reached 1040 fb^{-1}, as shown in Fig. 4. Belle took most of its data at the energy of the $\Upsilon(4S)$ resonance in order to study B-meson decay. Off-resonance data were collected 60 MeV below the resonance peak energy for 10% of the running time about every two months in order to determine the non-$B\bar{B}$ background. The first non-$\Upsilon(4S)$ data were taken at the energy of the $\Upsilon(5S)$ resonance for just three days in 2005. In the same year, $\Upsilon(3S)$ resonance data were taken to search for invisible decay modes of the $\Upsilon(1S)$ resonance. The last $\Upsilon(4S)$ resonance data were taken in June 2008. During the last two years of operation, $\Upsilon(1S)$, $\Upsilon(2S)$, and $\Upsilon(5S)$ resonance data samples were taken as well as energy scans between the $\Upsilon(4S)$ and $\Upsilon(6S)$ resonances. The integrated luminosity collected by Belle for each CM energy is listed in Table 1 and is calculated using barrel Bhabha events after removing bad runs, which could not be used in physics analysis due to serious detector problems. The systematic error in the luminosity measurement is about 1.4%; the statistical error is usually small compared with the systematic error. Integrated luminosities for $\Upsilon(4S)$ data are shown separately for the SVD1 and SVD2 data sets, which were taken with different inner detector hardware configurations as described in the previous subsection. Other resonance and scan data were taken in the SVD2 configuration.

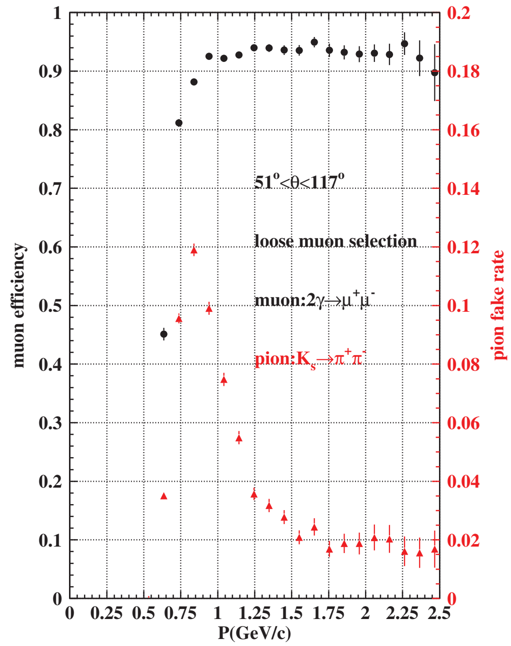

Fig. 3. Muon identification efficiency and fake rate as a function of momentum.

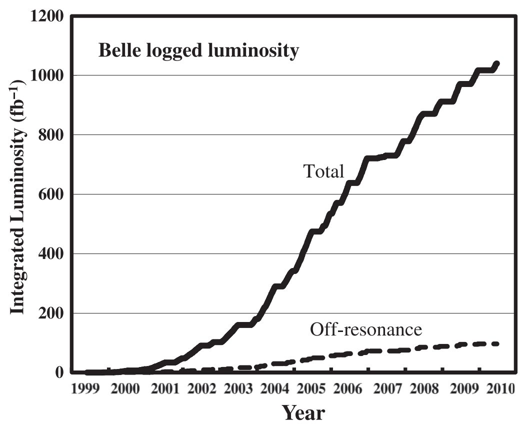

Fig. 4. Integrated luminosity taken by Belle.

Table 1. Summary of the luminosity integrated by Belle, broken down by CM energy.

Resonance	On-peak luminosity (fb^{-1})	Off-peak luminosity (fb^{-1})	Number of resonances
$\Upsilon(1S)$	5.7	1.8	102×10^6
$\Upsilon(2S)$	24.9	1.7	158×10^6
$\Upsilon(3S)$	2.9	0.25	11×10^6
$\Upsilon(4S)$ SVD1	140.0	15.6	152×10^6 $B\bar{B}$
$\Upsilon(4S)$ SVD2	571.0	73.8	620×10^6 $B\bar{B}$
$\Upsilon(5S)$	121.4	1.7	7.1×10^6 $B_s\bar{B}_s$
Scan		27.6	

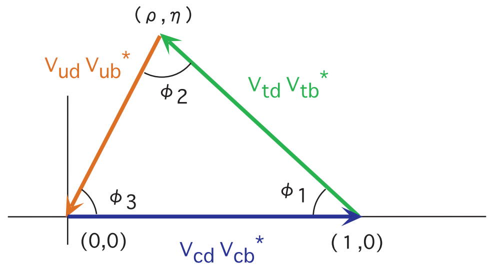

Fig. 5. The unitarity triangle relevant to B decays. The CP violation parameters are defined as the angles ϕ_1, ϕ_2, and ϕ_3.

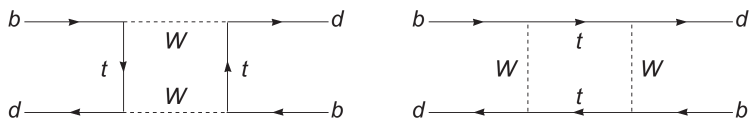

Fig. 6. Box diagrams that contribute to B^0–$\overline{B}^0$ mixing.

3. CKM angle measurements

3.1. The Kobayashi–Maskawa model and unitarity triangle

The phenomenon of CP violation was one of the major unresolved issues in elementary particle physics after its discovery in 1964 in neutral kaon decay [20]. In 1973, M. Kobayashi and T. Maskawa proposed a model in which a quark-mixing matrix among six quark flavors includes a single irreducible complex phase that causes CP violation [21]. Conventionally the quark-mixing matrix is written as [22]:

$$\begin{pmatrix} V_{ud} & V_{us} & V_{ub} \\ V_{cd} & V_{cs} & V_{cb} \\ V_{td} & V_{ts} & V_{tb} \end{pmatrix} = \begin{pmatrix} 1-\lambda^2/2 & \lambda & A\lambda^3(\rho - i\eta) \\ -\lambda & 1-\lambda^2/2 & A\lambda^2 \\ A\lambda^3(1-\rho-i\eta) & -A\lambda^2 & 1 \end{pmatrix} + o(\lambda^4), \tag{3.1}$$

where the nontrivial complex phases are assigned to V_{ub} and V_{td}. Due to the unitarity of this matrix, the following relation is expected to hold, in particular for the terms involving the b-quark:

$$V_{td}V_{tb}^* + V_{cd}V_{cb}^* + V_{ud}V_{ub}^* = 0. \tag{3.2}$$

This expression can be visualized as a closed triangle in the complex plane as shown in Fig. 5. Here the phase of V_{td} plays a fundamental role and induces time-dependent CP asymmetries via interference with amplitudes containing V_{cb} and V_{ub}. Measurements of the relevant time-dependent CP violation parameters are used to determine the CP-violating angles, ϕ_1 and ϕ_2[1], that are described in Sects. 3.4 and 3.5. In contrast, the angle ϕ_3 is determined by the direct CP asymmetries in $B \to DK^{(*)}$ decays and is discussed in Sect. 3.6.

[1] Another naming convention, $\beta(=\phi_1)$, $\alpha(=\phi_2)$, and $\gamma(=\phi_3)$, is also used in the literature.

3.2. *CP violation and B^0–$\overline{B}^0$ mixing*

Neutral B mesons, B^0 and $\overline{B}^0$, can transform or mix into their antiparticles through box diagrams as shown in Fig. 6. The frequency of the mixing transition (oscillation) is $\Delta m_d = (0.507 \pm 0.004)\ \mathrm{ps}^{-1}$ [23], while the lifetime (τ_{B^0}) is 1.519 ± 0.007 ps [23].

A.I. Sanda, A.R. Carter, and I.I. Bigi showed that a sizable CP violation can appear in B-meson decays if B^0–$\overline{B}^0$ mixing is large [24–26]. In neutral B decays to the CP eigenstate (f_{CP}), both B^0 and $\overline{B}^0$ can decay to the same final state. Because of B^0–$\overline{B}^0$ mixing, the decay proceeds through two paths; one from direct decay, $B^0 \to f_{CP}$, and the other through B^0–$\overline{B}^0$ mixing, $B^0 \to \overline{B}^0 \to f_{CP}$. These two amplitudes have a phase difference of $\phi_{\mathrm{mix}} - 2\phi_D$ where ϕ_{mix} is the weak phase of B^0–$\overline{B}^0$ mixing, $\arg(V_{td}V_{tb}^*/V_{td}^*V_{tb})$, and ϕ_D is the weak phase of the $B^0 \to f_{CP}$ decay. In the Wolfenstein representation, $\phi_{\mathrm{mix}} = 2\phi_1$ and the phase difference is given as $2(\phi_1 - \phi_D)$. The interference term for the two amplitudes has opposite signs for B^0 and $\overline{B}^0$ decays and leads to CP violation effects proportional to $\sin 2(\phi_1 - \phi_D)$.

3.3. *Experimental approach at a B-factory*

At a B-factory, pairs of neutral B mesons in a coherent state with $C = -1$ are produced by $\Upsilon(4S) \to B^0\overline{B}^0$ decays In a decay in which one B meson decays to f_{CP} and the other B meson decays to a flavor specific final state, f_{tag}, the decay rate is given as

$$\mathcal{P}(\Delta t, q; \mathcal{S}, \mathcal{A}) = \frac{e^{-|\Delta t|/\tau_{B^0}}}{4\tau_{B^0}}\left\{1 + q \cdot \left[\mathcal{S}\sin(\Delta m_d \Delta t) + \mathcal{A}\cos(\Delta m_d \Delta t)\right]\right\}. \tag{3.3}$$

Here $\Delta t = t_{CP} - t_{\mathrm{tag}}$ is the difference between the proper decay times of f_{CP} and f_{tag}, $q = \pm 1$ is the flavor of f_{tag} ($+1$ for $B^0 \to f_{\mathrm{tag}}$). The quantities $\mathcal{S}$ and $\mathcal{A}$ are CP violation parameters that are dependent on the decay mode. The parameter $\mathcal{S}$ describes mixing-induced CP violation and is given by $\mathcal{S} = -\eta_{CP}\sin 2(\phi_1 - \phi_D)$, where η_{CP} is the CP eigenvalue of f_{CP}. The other parameter, $\mathcal{A}$, corresponds to direct CP violation (i.e. no CP violation in the $B^0 \leftrightarrow \overline{B}^0$ transition rates). It should be noted that, depending on the weak phase of the decay, CP violation measurements give information on the various angles of the unitarity triangle. The asymmetry in the rate of B^0 and $\overline{B}^0$ decays is given by

$$A(\Delta t) \equiv \frac{\mathcal{P}(\Delta t, +1; \mathcal{S}, \mathcal{A}) - \mathcal{P}(\Delta t, -1; \mathcal{S}, \mathcal{A})}{\mathcal{P}(\Delta t, +1; \mathcal{S}, \mathcal{A}) + \mathcal{P}(\Delta t, -1; \mathcal{S}, \mathcal{A})} = \mathcal{S}\sin\Delta m_d \Delta t + \mathcal{A}\cos\Delta m_d \Delta t. \tag{3.4}$$

An experimental measurement of time-dependent CP violation at a B-factory includes the following steps:

1. Reconstruct one B decaying to f_{CP}.
2. Determine q using all available information on the $B \to f_{\mathrm{tag}}$ decay.
3. Reconstruct vertices for f_{CP} and f_{tag} and determine Δt from the distance between the two B vertices.
4. Obtain $\mathcal{S}$ and $\mathcal{A}$ by fitting the Δt distribution of reconstructed signal candidates.

Each step is described in more detail below.

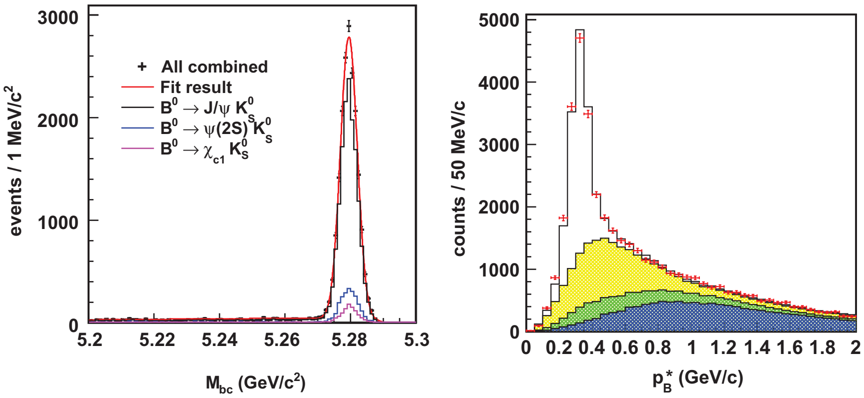

Fig. 7. M_{bc} distribution within the ΔE signal region for $B^0 \to J/\psi K^0_S$ (black), $\psi(2S)K^0_S$ (blue), and $\chi_{c1}K^0_S$ (magenta); the superimposed curve (red) shows the fit result for all modes combined (left) and the p^*_B distribution for $B^0 \to J/\psi K^0_L$ candidates with the results of the fit separately shown as signal (open histogram), background with a real J/ψ and a real K^0_L (yellow), background with a real J/ψ but without a real K^0_L (green), and background without a real J/ψ (blue) (right).

3.4. *Measurement of ϕ_1*

At the quark level neutral B meson decays into $(c\bar{c})K^0$ are induced by a $b \to c\bar{c}s$ transition. Since both leading and sub-leading order diagrams of this process contain neither V_{ub} nor V_{td}, there is no complex phase in the decay amplitude. Thus ϕ_D is zero and the mixing-induced CP violation parameter $\mathcal{S}$ is directly related to one of the CP-violating angles, ϕ_1. In the SM,

$$\mathcal{S} = -\eta_{CP} \cdot \sin 2\phi_1 \quad \text{and} \quad \mathcal{A} \approx 0 \tag{3.5}$$

are expected.

3.4.1. $B^0 \to (c\bar{c})K^0$ reconstruction. We reconstruct $J/\psi K^0_S$, $J/\psi K^0_L$, $\psi(2S)K^0_S$, and $\chi_{c1}K^0_S$ as the f_{CP} in neutral B meson decays to $(c\bar{c})K^0$. J/ψ mesons are reconstructed via their decay into oppositely charged lepton pairs (e^+e^- or $\mu^+\mu^-$) while $\psi(2S)$ mesons are reconstructed by lepton pairs as well as $J/\psi\pi^+\pi^-$ final states. We reconstruct χ_{c1} mesons in the $J/\psi\gamma$ mode and K^0_S mesons in the $\pi^+\pi^-$ final state.

For $B^0 \to J/\psi K^0_S$, $\psi(2S)K^0_S$, and $\chi_{c1}K^0_S$ candidates, the B signal is identified using two kinematic variables calculated in the $\Upsilon(4S)$ CM: the energy difference $\Delta E \equiv E^*_B - E^*_{\mathrm{beam}}$ and the beam-energy constrained mass $M_{\mathrm{bc}} \equiv \sqrt{(E^*_{\mathrm{beam}})^2 - (p^*_B)^2}$, where E^*_{beam} is the beam energy in the CM of the $\Upsilon(4S)$ resonance, and E^*_B and p^*_B are the CM energy and momentum of the reconstructed B candidate, respectively. In the $B^0 \to J/\psi K^0_L$ case, candidate K^0_L mesons are selected using information recorded in the ECL and/or the KLM. Since the K^0_L energy cannot be measured, we determine only its direction. Thus $B^0 \to J/\psi K^0_L$ candidates are identified by the value of p^*_B calculated using a two-body decay kinematic assumption.

The M_{bc} distribution for signal candidates with a stringent ΔE requirement ($|\Delta E| < 40$ MeV for $J/\psi K^0_S$, $|\Delta E| < 30$ MeV for $\psi(2S)K^0_S$, and $|\Delta E| < 25$ MeV for $\chi_{c1}K^0_S$) as well as the p^*_B distribution for $J/\psi K^0_L$ candidates are shown in Fig. 7. The signal yields and purities are estimated for each f_{CP} mode and given in Table 2.

3.4.2. Flavor tagging. For the events in which we reconstructed $B^0 \to f_{CP}$ candidates, the neutral B flavor is identified from the decay products of the accompanying B meson. The available

Table 2. Signal yield ($N_{\rm sig}$), CP eigenvalue (η_{CP}), and purity for each $B^0 \to f_{CP}$ mode.

B decay mode	η_{CP}	$N_{\rm sig}$	Purity (%)
$J/\psi K_S^0$	-1	$12\,649 \pm 114$	97
$\psi(2S)(\ell^+\ell^-)K_S^0$	-1	904 ± 31	92
$\psi(2S)(J/\psi\pi^+\pi^-)K_S^0$	-1	1067 ± 33	90
$\chi_{c1}K_S^0$	-1	940 ± 33	86
$J/\psi K_L^0$	$+1$	$10\,040 \pm 154$	63

information is obtained from leptons, kaons, Λ baryons, and pions. Leptons directly coming from B decay and secondary leptons and strange particles in the cascade decays carry the mother b-flavor information. Low momentum tagging pions may come from $D^{*\pm}$ decays. In addition, there are high momentum pions originating from $\overline{B}^0 \to D^{(*)+}\pi^-$ or $D^{(*)^+}\rho^-$ decays. Both types of tagging pions give some information about b-flavor. The information from all the decay products is handled by a multi-dimensional likelihood approach with corresponding look-up tables [27].

To calibrate w, we select a flavor specific final state of neutral B meson decays such as semileptonic $\overline{B^0} \to D^{*+}\ell^-\bar{\nu}$ decays and hadronic $\overline{B^0} \to D^{(*+)}\pi^-$ and $D^{+*}\rho^-$ decays. We then determine the wrong tag fraction w by measuring the time evolution of the opposite-sign flavor asymmetry, as it exhibits a Δt dependence proportional to $(1-2w)\cos(\Delta m_d \Delta t)$. We also determine Δw, which is the difference in w between $q=+1$ and -1 events. For $B^0 \to J/\psi K_S^0$ decay, we obtain the effective tagging efficiency, $\varepsilon_{\rm eff} = \varepsilon(1-2w)^2 = (30.1 \pm 0.4)\%$, where ε is the tagging efficiency.

3.4.3. Δt determination and its resolution. In energy-asymmetric e^+e^- collisions at KEKB, the $\Upsilon(4S)$ is produced with a Lorentz boost of $\beta\gamma = 0.425$ nearly along the z-axis, which is defined as the direction anti-parallel to the e^+ beam at Belle. Since B mesons are approximately at rest with respect to the $\Upsilon(4S)$, we can measure Δt by measuring the displacement between the two B meson decay vertices in the z direction, Δz,

$$\Delta t \simeq \frac{\Delta z}{\beta\gamma c}. \tag{3.6}$$

The B meson decay vertex is reconstructed by a Lagrange multiplier approach, which minimizes the χ^2 calculated from the decay vertex position and the daughter particle tracks [28]. We call this procedure a "vertex fit". The vertex fit is carried out using daughter tracks with a sufficient (minimal) number of SVD hits and a constraint on the interaction-region profile in the plane perpendicular to the beam axis.

Because of the negligible flight length of J/ψ or $\psi(2S)$ mesons, the vertex reconstructed from their daughter lepton tracks can represent the $B^0 \to f_{CP}$ decay vertex; its resolution is found to be approximately 75 μm. On the other hand, the $B^0 \to f_{\rm tag}$ vertex is obtained with well-reconstructed tracks that are not assigned to f_{CP}. Here, high momentum leptons are always retained because they usually come directly from semileptonic B meson decays. Since $f_{\rm tag}$ may contain long-lived particles such as D^+, D^0, K_S^0, and so on, the vertex reconstructed using the daughter tracks coming from these intermediate particles can deviate from the true $B^0 \to f_{\rm tag}$ vertex. This effect is minimized by removing tracks that are identified by a large contribution to the vertex fit χ^2. The $f_{\rm tag}$ vertex position resolution is found to be approximately 165 μm.

In the Belle experiment, the contributions to Δt measurement error are divided into three categories: detector measurement error, the effect of secondary particles in f_{tag} vertex reconstruction, and the kinematical approximation, $\Delta t \simeq \Delta z/(\beta\gamma c)$. These three effects are convoluted on an event-by-event basis to obtain the Δt resolution function, which is used in a maximum likelihood fit to extract $\mathcal{S}$ and $\mathcal{A}$ as discussed in the next section.

3.4.4. Extracting CP violation parameters. We determine $\sin 2\phi_1$ and $\mathcal{A}$ from a maximum likelihood fit using Δt and q information obtained on an event-by-event basis from signal candidates. By taking the effect of incorrect flavor assignment into account, the probability density function (PDF) expected for the signal distribution is given by

$$\begin{aligned}\mathcal{P}_{\mathrm{sig}}(\Delta t) = {} & \frac{e^{-|\Delta t|/\tau_{B^0}}}{4\tau_{B^0}}\{1 - q\Delta w_l + q(1-2w_l) \\ & \times [(-\eta_{CP})\sin 2\phi_1 \sin(\Delta m_d \Delta t) + \mathcal{A}\cos(\Delta m_d \Delta t)]\}\,.\end{aligned} \tag{3.7}$$

The distribution is convoluted with the Δt resolution function $R_{\mathrm{sig}}(\Delta t)$, which takes into account the finite vertex resolution as described in Sect. 3.4.3. The background PDF $\mathcal{P}_{\mathrm{bkg}}(\Delta t)$ is determined by the events found in a sideband region well away from the signal region in M_{bc}–ΔE space as well as Monte Carlo (MC) events. A small component of broad outliers in the Δz distribution, caused by misreconstruction, is represented by a Gaussian function $\mathcal{P}_{\mathrm{ol}}(\Delta t)$ with $\sigma \approx 30$ ps. We determine the following likelihood value for each event indexed by i:

$$\begin{aligned}\mathcal{P}_i(\Delta t_i, q_i; \sin 2\phi_1, \mathcal{A}) = {} & (1 - f_{\mathrm{ol}}) f_{\mathrm{sig}} \int_{-\infty}^{\infty} \mathcal{P}_{\mathrm{sig}}(\Delta t') R_{\mathrm{sig}}(\Delta t_i - \Delta t') d(\Delta t') \\ & + (1 - f_{\mathrm{ol}}) f_{\mathrm{bkg}} \mathcal{P}_{\mathrm{bkg}}(\Delta t_i) + f_{\mathrm{ol}} P_{\mathrm{ol}}(\Delta t_i),\end{aligned} \tag{3.8}$$

where f_{ol} is the outlier fraction, f_{sig} and f_{bkg} are the signal and background probabilities calculated as functions of ΔE and M_{bc}. The CP violation parameters, $\sin 2\phi_1$ and $\mathcal{A}$, are determined by maximizing the likelihood function

$$L(\sin 2\phi_1, \mathcal{A}) = \prod_i \mathcal{P}_i(\Delta t_i, q_i; \sin 2\phi_1, \mathcal{A}), \tag{3.9}$$

where the product runs over all events. A fit to the candidate events results in the CP violation parameters [29],

$$\begin{aligned}\sin 2\phi_1 &= 0.667 \pm 0.023(\mathrm{stat}) \pm 0.012(\mathrm{syst}), \\ \mathcal{A} &= 0.006 \pm 0.016(\mathrm{stat}) \pm 0.012(\mathrm{syst}).\end{aligned} \tag{3.10}$$

The background-subtracted Δt distribution for $q = +1$ and $q = -1$ events and the asymmetry for events with good quality tags are shown in Fig. 8. The world average of $\sin 2\phi_1$ is now 0.68 ± 0.02, which is a firm SM reference.

3.4.5. Search for new physics using CP violation measurements in $b \to s$ penguin modes. B meson decays involving penguin diagrams are thought to be a sensitive probe for new physics (NP)

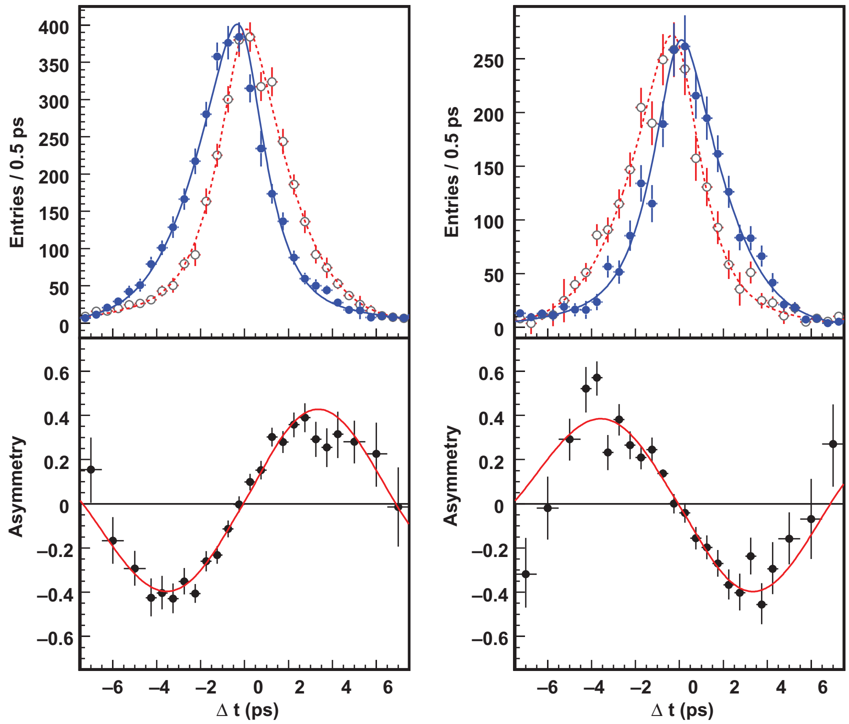

Fig. 8. The background-subtracted Δt distribution for $q = +1$ (red) and $q = -1$ (blue) events and asymmetry for events with good quality tags in $(c\bar{c})K_S^0$ (left) and $J/\psi K_L^0$ (right) decays.

beyond the SM because of the one-loop nature of penguins. NP could appear as deviations of CP violation parameters from the SM expectation. In this section, some highlight results for penguin modes are reviewed.

In SM $b \to s\bar{q}q$ hadronic B decays, the relevant coupling is $V_{tb}^* V_{ts}$ and the weak phase is the same as in the $b \to c\bar{c}s$ transition, e.g. $B^0 \to (c\bar{c})K^0$ decay. Therefore, the main point is to check whether the penguin CP violation results deviate from the SM expectation, $\mathcal{S} = -\eta_{CP} \sin 2\phi_1$ and $\mathcal{A} = 0$. In this context, the time-dependent CP-violating parameters are denoted as $\sin 2\phi_1^{\mathrm{eff}}$ and $\mathcal{A}$. The modes $B^0 \to \phi K^0$, $\eta' K^0$, and $K^0 K^0 K^0$ that involve only $b \to s\bar{s}s$ processes are of special interest, since the SM theoretical uncertainty for CP violation is small for these decay processes.

In the Belle experiment, attempts to perform measurements of time-dependent CP violation in $b \to s\bar{q}q$ induced decays with $B^0 \to \eta' K_S^0$ and ϕK_S^0 modes were made from the earliest stage of data taking, starting in 2002. In 2003, using a 152×10^6 $B\overline{B}$ data sample, the value of $\mathcal{S}$ in $B^0 \to \phi K_S^0$ flipped sign and exhibited a 3.5σ deviation from the S parameter measured in $B^0 \to (c\bar{c})K^0$ modes [30]. This was very striking and suggestive of an NP effect. In 2006, with a larger statistics data sample corresponding to 535×10^6 $B\overline{B}$, updated measurements were reported. These measurements added $B^0 \to \eta' K_L^0$ and ϕK_L^0 decays to the $B^0 \to \eta' K^0$ and ϕK^0 sample [31]. The results are summarized in Table 3. In $B^0 \to \eta' K^0$ decay, CP violation is observed with a statistical significance of 5.6σ. In all these three B decay modes, the large deviation from $B^0 \to (c\bar{c})K^0$ has disappeared.

In spite of the small theoretical uncertainty, experimentally, several contributions overlap in $B^0 \to \phi K^0$ because of the relatively wide natural widths of the resonances that contribute in the K^+K^- final state. In order to resolve these interfering contributions, Belle fits the time-dependent Dalitz distribution by expressing each contribution at the amplitude level for the $B^0 \to K^+K^-K_S^0$ candidate

Table 3. Measurements of CP violation parameters, $\sin 2\phi_1^{\rm eff}$ and $\mathcal{A}$, in $B^0 \to \eta' K^0$, ϕK^0, and $K_S^0 K_S^0 K_S^0$ modes with a 535×10^6 $B\overline{B}$ data sample. The first and second errors are statistical and systematic errors, respectively.

B decay mode	$\sin 2\phi_1^{\rm eff}$	$\mathcal{A}$
$\eta' K^0$	$+0.64 \pm 0.10 \pm 0.04$	$-0.01 \pm 0.07 \pm 0.05$
ϕK^0	$+0.50 \pm 0.21 \pm 0.06$	$+0.07 \pm 0.15 \pm 0.05$
$K_S^0 K_S^0 K_S^0$	$+0.30 \pm 0.32 \pm 0.08$	$-0.31 \pm 0.20 \pm 0.07$

Table 4. CP violation parameters in $B^0 \to K^+K^-K_S^0$ time-dependent Dalitz analysis, $\phi_1^{\rm eff}$ and $\mathcal{A}$. The first, second, and third errors are statistical, experimental systematic, and Dalitz model uncertainties, respectively.

B decay mode	$\phi_1^{\rm eff}$	$\mathcal{A}$
ϕK_S^0	$(32.2 \pm 9.0 \pm 2.6 \pm 1.4)^\circ$	$+0.04 \pm 0.20 \pm 0.10 \pm 0.02$
$f_0 K_S^0$	$(31.3 \pm 9.0 \pm 3.4 \pm 4.0)^\circ$	$-0.30 \pm 0.29 \pm 0.11 \pm 0.09$

events. With this technique, the extracted parameter is not $\sin 2\phi_1^{\rm eff}$ but rather the angle $\phi_1^{\rm eff}$ itself and $\mathcal{A}$. Therefore the result does not have a two-fold ambiguity between $\phi_1^{\rm eff}$ and $\pi/2 - \phi_1^{\rm eff}$. In $B^0 \to K^+K^-K_S^0$ decays, we find four solutions related to resonant amplitude interference. The preferred one is identified using external information related to $f_0(980)$ and f_X (assumed to be $f_0(1500)$) branching fractions. The obtained CP violation parameters are summarized in Table 4 [32]. These are consistent with the CP violation in $B^0 \to c\bar{c}K^0$ decays at the 1σ level.

Including other $b \to s$ mediated B decays, the precision of $\sin 2\phi_1^{\rm eff}$ is still statistically limited, typically $0.1 \sim 0.2$. Obtaining $\mathcal{O}(10^{-2})$ sensitivity requires an integrated luminosity of $\mathcal{O}(10\ {\rm ab}^{-1})$, and a Super B-factory experiment.

3.5. *Measurement of ϕ_2*

After the first observation of CP violation in B meson decays, which gave a measurement of ϕ_1, a precise measurement of ϕ_2 became the next target of CP violation measurements for the validation of the Kobayashi–Maskawa model. The first Belle measurement of CP asymmetry parameters in $B^0 \to \pi^+\pi^-$ decay [33] was reported in March 2002, representing the second decay mode (after $B \to c\bar{c}K^0$) with a time-dependent CP violation measurement.

The decay modes used for ϕ_2 measurements are those proceeding via $b \to u$ transition, such as $B^0 \to \pi^+\pi^-$, $B^0 \to \rho^+\pi^-$, $B^0 \to \rho^+\rho^-$. The $b \to u$ transition is shown in Fig. 9 (left) and includes the Cabibbo–Kobayashi–Maskawa (CKM) element, V_{ub}; it can be shown that the time dependent CP asymmetry is then given as $\mathcal{S} = \sin 2\phi_2$ and $\mathcal{A} \simeq 0$. However, an additional amplitude, a "penguin diagram" (Fig. 9 (right)), contributes and has a phase that is different from the tree diagram (V_{td} instead of V_{ub}). This causes a deviation of $\mathcal{S}$ from $\sin 2\phi_2$ and a non-zero $\mathcal{A}$.

The first ϕ_2 measurement was attempted using the $B^0 \to \pi^+\pi^-$ decay mode. This decay has the simplest two-body topology and was one of the first well established charmless B decays. The reconstruction of the decay is straightforward: a pair of oppositely charged pions with an invariant mass consistent with the B-meson mass ($M_{\rm bc} = m_B$) is selected; the B meson energy in CM is required to be consistent with the beam energy ($\Delta E = 0$). However, the selected sample suffers from a very large background from the $e^+e^- \to q\bar{q}$ ($q = u, d, s, c$) continuum process since the same kinematic

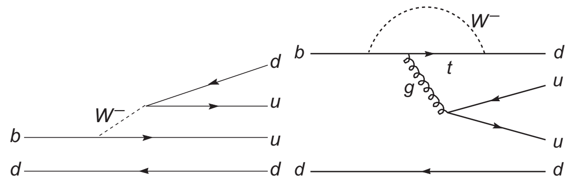

Fig. 9. Tree (left) and penguin (right) diagrams for $B^0 \to \pi^+\pi^-$ decay.

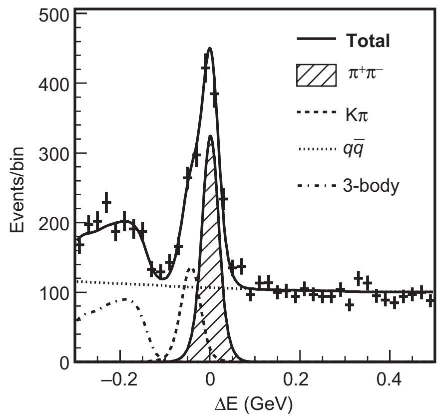

Fig. 10. ΔE distribution of $B^0 \to \pi^+\pi^-$ candidates. In order to enhance the signal, requirements are imposed on the two other variables, $M_{\rm bc}$ and $\mathcal{R}$.

properties can easily be faked by two oppositely charged pions fragmented from primary quarks and carrying about half of their momentum. Another significant background is from $B^0 \to K^+\pi^-$ decay, where the kaon is misidentified as a pion. The branching fraction for the former decay mode is about four times higher than that of $B^0 \to \pi^+\pi^-$. In this case, the reconstructed ΔE is shifted by -40 MeV and good K/π separation and good momentum resolution are important to reduce this background.

The continuum background is suppressed utilizing a difference in the global event topology for the two classes of events; continuum events have a two-jet like shape while $B\bar{B}$ events have an isotropic shape as the two B mesons are produced almost at rest in the CM. To quantify the event shape, we use a Fisher discriminant [34] combining modified Fox–Wolfram moments [35]. We form a likelihood $\mathcal{L}_s$ ($\mathcal{L}_b$) for signal (continuum background) using the Fisher discriminant and the angle between the flight direction of the B candidate and the beam direction in the CM, $\cos\theta_B$. The likelihood ratio $\mathcal{R} = \mathcal{L}_s/(\mathcal{L}_s + \mathcal{L}_b)$ is used as the final continuum suppression parameter. In the early analyses [33], we imposed a tight requirement on $\mathcal{R}$ by optimizing $S/\sqrt{S+B}$, where S and B are the expected number of signal and background events, respectively. In a later analysis [36], we optimized the $\mathcal{R}$ requirement depending on the flavor tagging quality.

The ΔE distribution of $B^0 \to \pi^+\pi^-$ candidates is shown in Fig. 10. Background events due to three-body decays populate the negative ΔE region but they do not contribute in the $B^0 \to \pi^+\pi^-$ signal region ($|\Delta E| < 0.064$ GeV).

The vertex reconstruction and the flavor tagging are performed in the same way as for the $\sin 2\phi_1$ measurements. The CP violation parameters are extracted from a fit to the Δt distribution for the events in the signal region in ΔE and $M_{\rm bc}$ ([5.271, 5.287] GeV/c^2). The PDFs include the signal, continuum background, and $B^0 \to K^+\pi^-$ background. The first result was reported using

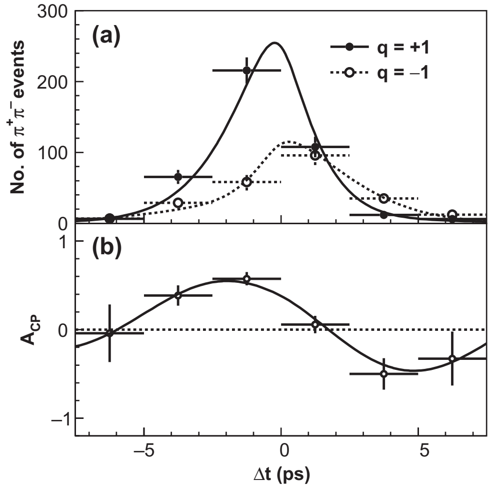

Fig. 11. Δt distribution for B^0 and $\bar{B}^0$ tagged $B \to \pi^+\pi^-$ events (top) and the CP asymmetry together with the fit result (bottom).

48×10^6 $B\overline{B}$ pairs: [33]

$$\mathcal{S}_{\pi\pi} = -1.21^{+0.38}_{-0.27}(\text{stat})^{+0.16}_{-0.13}(\text{syst})$$
$$\mathcal{A}_{\pi\pi} = +0.94^{+0.25}_{-0.31}(\text{stat}) \pm 0.09(\text{syst}). \tag{3.11}$$

In the latest analysis using 535×10^6 $B\overline{B}$ pairs [36], a stringent selection on K/π particle identification is not imposed and instead the $B^0 \to K^+\pi^-$ decays are included as a component in the fit to extract the CP violation parameters. This increases the signal detection efficiency by 23% and improves the measurement errors by 10%. The results are [36]

$$\mathcal{S}_{\pi\pi} = -0.61 \pm 0.10(\text{stat}) \pm 0.04(\text{syst})$$
$$\mathcal{A}_{\pi\pi} = +0.55 \pm 0.08(\text{stat}) \pm 0.05(\text{syst}). \tag{3.12}$$

The Δt distribution and the asymmetry together with fit results are shown in Fig. 11. A clear non-zero $\mathcal{A}_{\pi\pi}$, i.e. a clear direct CP violation, is seen (the asymmetry exhibits a significant cosine term). As shown above, the first measurement already indicated CP violation in decays with a significance of 2.9σ. The first evidence of direct CP violation in a B decay mode was reported with 3.2σ significance in January 2004 using a sample of 152×10^6 $B\overline{B}$ pairs [37]. Although this claim was not widely accepted at that time because the result of the BaBar collaboration showed a rather small $\mathcal{A}_{\pi\pi}$ value, the latest world average, $\mathcal{A}_{\pi\pi} = 0.38 \pm 0.06$ [38], establishes CP violation in $B^0 \to \pi^+\pi^-$ decays with a significance above 5σ.

The large direct CP violation indicates that the contribution of the penguin diagram is sizable and the deviation of $\mathcal{S}_{\pi\pi}$ from $\sin 2\phi_2$ may be significant. The angle ϕ_2 can be extracted using the isospin relation among branching fractions and CP asymmetries of $B^0 \to \pi^+\pi^-$, $B^0 \to \pi^0\pi^0$, and $B^+ \to \pi^+\pi^0$ decays; this was first proposed by M. Gronau and D. London [39]. The result, shown in Fig. 12, is obtained using the results for $\mathcal{S}_{\pi\pi}$ and $\mathcal{A}_{\pi\pi}$ given above and the world average values of branching fractions of the three $B \to \pi\pi$ modes and direct CP asymmetry in $B^0 \to \pi^0\pi^0$. Using this method, there are multiple discrete ambiguities for the angle ϕ_2. The solution that is closest to the global fit result [40] gives $\phi_2 = (97 \pm 11)^\circ$.

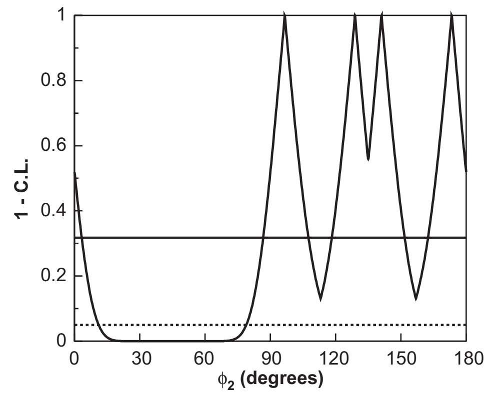

Fig. 12. 1-C.L. for a range of ϕ_2 values as obtained with an isospin analysis of $B \to \pi\pi$ decays. The solid and dashed lines indicate C.L. = 68.3% and 95%, respectively.

The final state in $B^0 \to \rho^+\pi^-$ decay is not a CP eigenstate, but the decay proceeds through the same quark diagrams as $B^0 \to \pi^+\pi^-$. Since B^0 and $\overline{B}^0$ can decay to $\rho^+\pi^-$, time-dependent CP violation can occur and provide information on ϕ_2. Here the final state is $\pi^+\pi^-\pi^0$ and the decay $B^0 \to \pi^+\pi^-\pi^0$ contains three intermediate states; $B^0 \to \rho^+\pi^-$, $\rho^-\pi^+$, and $\rho^0\pi^0$. These three amplitudes interfere and their magnitudes and relative strong phases can be extracted from a Dalitz plot amplitude analysis. Knowing the hadronic phases of these amplitudes in the Dalitz plane, a time-dependent Dalitz plot analysis allows the determination of ϕ_2 [41]. This method provides ϕ_2 without ambiguities (assuming large signal statistics) except for $\phi_2 \to \phi_2 + \pi$.

The reconstruction and continuum suppression are similar to the $B^0 \to \pi^+\pi^-$ analysis with an additional π^0 reconstructed in the $\pi^0 \to \gamma\gamma$ decay mode. CP violation parameters are obtained from a three-dimensional fit to the distribution of Δt and two Dalitz distribution parameters, $M^2_{\pi^+\pi^0}$ and $M^2_{\pi^-\pi^0}$. Belle performed the analysis using 449×10^6 $B\overline{B}$ pairs [42,43]. The amplitudes include $\rho(770)$ and higher mass resonances, $\rho(1450)$ and $\rho(1700)$. The time-dependent Dalitz plot distribution is parameterized with 27 real parameters describing the components that have different time- and Dalitz plot behaviors. CP violation parameters for $B^0 \to \rho^\pm\pi^\mp$, $B^0 \to \pi^0\pi^0$ decays and ϕ_2 are extracted from these parameters. We obtain $68^\circ < \phi_2 < 95^\circ$ at a 68.3% confidence level (C.L.) interval for the solution consistent with the global fit result. A large region ($0^\circ < \phi_2 < 5^\circ$, $23^\circ < \phi_2 < 34^\circ$, and $109^\circ < \phi_2 < 180^\circ$) also remains. With a larger data sample, a more restrictive constraint without ambiguities is expected from this measurement.

In the $B^0 \to \rho^+\rho^-$ mode a pseudoscalar decays into two vector particles and the final state is a mixture of CP-even and CP-odd amplitudes. In order to extract the fraction of each CP component, an angular analysis is required. Fortunately, the fraction of the longitudinal polarization turns out to be close to 100% [44–47], simplifying the measurement. The signal candidates are reconstructed in $\rho^\pm \to \pi^\pm\pi^0$ decays. Because of two π^0s in the final state, the combinatorial background due to fake π^0 candidates is very large. The results using 535×10^6 $B\overline{B}$ pairs are [48]:

$$\mathcal{A}_{\rho^+\rho^-} = +0.16 \pm 0.21(\text{stat}) \pm 0.07(\text{syst})$$
$$\mathcal{S}_{\rho^+\rho^-} = +0.19 \pm 0.30(\text{stat}) \pm 0.07(\text{syst}). \quad (3.13)$$

In this mode, ϕ_2 can be obtained using an isospin relation similar to that in the $B^0 \to \pi^+\pi^-$ case. Because the branching fraction for $B^0 \to \rho^0\rho^0$ is much smaller than those of $B^0 \to \rho^+\rho^-$ and

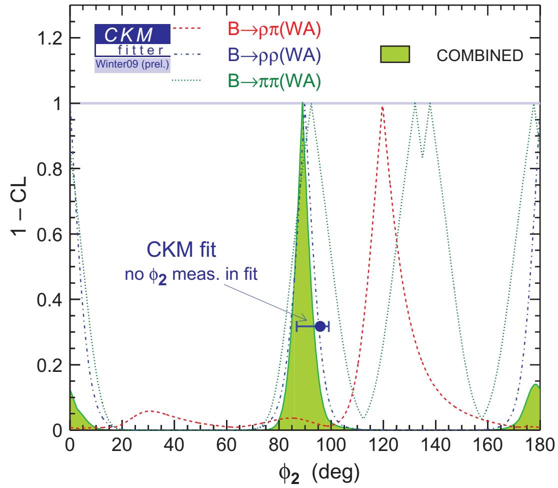

Fig. 13. 1-C.L. as a function of ϕ_2 from the average of the Belle and BaBar results for $B^0 \to \pi^+\pi^-$, $B^0 \to \rho\pi$, $B^0 \to \rho\rho$.

$B^+ \to \rho^+\rho^0$, the deviation of ϕ_2 from the measured value is small and some ambiguities are degenerate. So far only an upper limit on $\mathcal{B}(B^0 \to \rho^0\rho^0)$ has been obtained; this is used in the isospin analysis. The isospin analysis gives $62^\circ \le \phi_2 \le 106^\circ$ at the 68.3% C.L.

All of the above results and results from the BaBar collaboration can be combined to obtain the ϕ_2 constraint shown in Fig. 13 [40]. $\phi_2 = (89.0^{+4.4}_{-4.2})^\circ$ is obtained at a 68.3% C.L.

3.6. *Measurement of ϕ_3*

The angle ϕ_1 has been now measured with high precision (Sect. 3.4). Measurement of the angle ϕ_2 is more difficult due to theoretical uncertainties from the contributions of penguin diagrams (Sect. 3.5). Precise determination of the third angle of the unitarity triangle, ϕ_3, is possible using $B^\pm \to DK^\pm$ decays. However, it requires much more data than determinations of the other angles. The determination of ϕ_3 is theoretically clean due to the absence of loop contributions; ϕ_3 can be determined using tree-level processes only, exploiting the interference between $b \to c\bar{u}d$ and $b \to u\bar{c}d$ transitions that occurs when a process involves a neutral D meson reconstructed in a final state accessible to both D^0 and $\overline{D}^0$ decays. Therefore, ϕ_3 provides an SM benchmark, and its precise measurement is crucial in order to disentangle non-SM contributions to other processes, via global CKM fits.

Several different D decays have been studied in order to maximize the sensitivity to ϕ_3. The archetype is the use of D decays to CP eigenstates, a method proposed by M. Gronau, D. London, and D. Wyler (and called the GLW method) [49,50]. Belle makes use of CP-even modes (D_1), such as K^+K^-, and CP-odd modes (D_2), such as $K_S^0\pi^0$. To extract ϕ_3 using the GLW method, the following observables sensitive to CP violation are used: the asymmetries

$$\mathcal{A}_{1,2} \equiv \frac{\mathcal{B}(B^- \to D_{1,2}K^-) - \mathcal{B}(B^+ \to D_{1,2}K^+)}{\mathcal{B}(B^- \to D_{1,2}K^-) + \mathcal{B}(B^+ \to D_{1,2}K^+)} = \pm\frac{2r_B \sin\delta_B \sin\phi_3}{1 + r_B^2 \pm 2r_B\cos\delta_B\cos\phi_3} \tag{3.14}$$

and the ratios

$$\mathcal{R}_{1,2} \equiv \frac{\mathcal{B}(B^- \to D_{1,2}K^-) + \mathcal{B}(B^+ \to D_{1,2}K^+)}{\mathcal{B}(B^- \to D^0K^-) + \mathcal{B}(B^+ \to D^0K^+)} = 1 + r_B^2 \pm 2r_B\cos\delta_B\cos\phi_3, \tag{3.15}$$

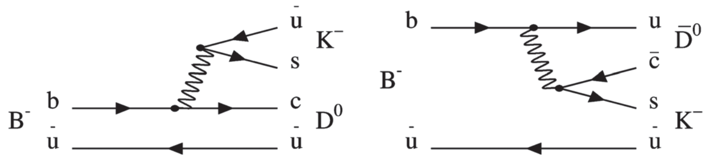

Fig. 14. Feynman diagrams for $B^- \to D^0 K^-$ and $B^- \to \overline{D}^0 K^-$.

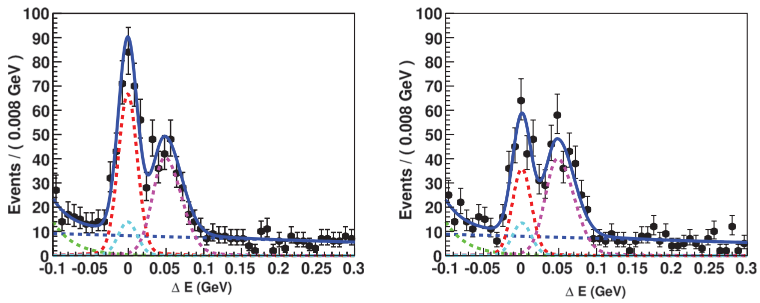

Fig. 15. Signals for $B^\pm \to D_1 K^\pm$ decays. The left (right) figure is for B^- (B^+) decays. The plotted variable, ΔE, peaks at zero for signal decays, while background from $B^\pm \to D\pi^\pm$ appears as a satellite peak at positive values.

Table 5. Results of the GLW analysis for $B^\pm \to DK^\pm$ mode.

$\mathcal{R}_1$	$1.03 \pm 0.07 \pm 0.03$
$\mathcal{R}_2$	$1.13 \pm 0.09 \pm 0.05$
$\mathcal{A}_1$	$+0.29 \pm 0.06 \pm 0.02$
$\mathcal{A}_2$	$-0.12 \pm 0.06 \pm 0.01$

where r_B is the ratio of the magnitudes of the two tree diagrams shown in Fig. 14 and δ_B is their strong-phase difference. The value of r_B is given by the product of the ratio of the CKM matrix elements $|V_{ub}^* V_{cs}|/|V_{cb}^* V_{us}| \sim 0.38$ and the color suppression factor, which altogether results in a value of around 0.1. In the expressions above, mixing and CP violation in the neutral D meson system are neglected. Among these four observables, $\mathcal{R}_{1,2}$ and $\mathcal{A}_{1,2}$, only three are independent (since $\mathcal{A}_1\mathcal{R}_1 = \mathcal{A}_2\mathcal{R}_2$). Recently, Belle updated their GLW analysis using their final data sample of 772×10^6 $B\overline{B}$ pairs (Belle Collaboration, preliminary results presented at Lepton Photon 2011 (BELLE-CONF-1112)). The analysis uses D^0 decays to K^+K^- and $\pi^+\pi^-$ as CP-even modes (Fig. 15), $K_S^0\pi^0$ and $K_S^0\eta$ as CP-odd modes. From Eqs. 3.14–3.15, the signs of the $\mathcal{A}_1$ and $\mathcal{A}_2$ asymmetries should be opposite, which is confirmed by experiment (Table 5).

The difficulties in the application of the GLW methods arise primarily due to the small magnitude of the CP asymmetry of the $B^\pm \to D_{CP} K^\pm$ decay, which may lead to significant systematic uncertainties in the observation of the CP violation. An alternative approach was proposed by D. Atwood, I. Dunietz, and A. Soni [51]. Instead of using D^0 decays to CP eigenstates, the ADS method uses Cabibbo-favored and doubly Cabibbo-suppressed decays: $\overline{D}^0 \to K^-\pi^+$ and $D^0 \to K^-\pi^+$. In the decays $B^+ \to [K^-\pi^+]_D K^+$ and $B^- \to [K^+\pi^-]_D K^-$, the suppressed B decay is followed by a Cabibbo-allowed D^0 decay, and vice versa. Therefore, the interfering amplitudes are of similar magnitude, and one can expect a large CP asymmetry. Unfortunately, the branching ratios of the decays

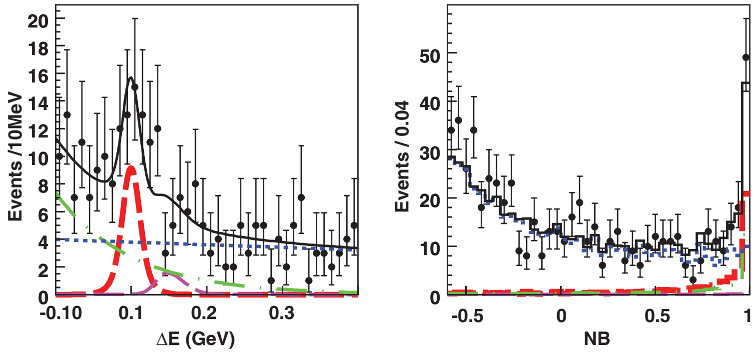

Fig. 16. Signal for $B^\pm \to DK^\pm$ decays from Belle ADS analysis. In these ΔE and NB (continuum suppression variable) distributions, $[K^+\pi^-]_D K^-$ components are shown by thicker dashed curves (red).

Table 6. Results of the Belle ADS analyses.

Mode	$\mathcal{R}_{\rm ADS}$	$\mathcal{A}_{\rm ADS}$
$B \to DK$	$0.0163^{+0.0044+0.0007}_{-0.0041-0.0013}$	$-0.39^{+0.26+0.04}_{-0.28-0.03}$
$B \to D^\star K,\, D^\star \to D\pi^0$	$0.010^{+0.008+0.001}_{-0.007-0.002}$	$+0.4^{+1.1+0.2}_{-0.7-0.1}$
$B \to D^\star K,\, D^\star \to D\gamma$	$0.036^{+0.014}_{-0.012} \pm 0.002$	$-0.51^{+0.33}_{-0.29} \pm 0.08$

mentioned above are small. The observable that is measured in the ADS method is the ratio of the suppressed and allowed branching fractions:

$$\mathcal{R}_{\rm ADS} = \frac{\mathcal{B}(B^\pm \to [K^\mp\pi^\pm]_D K^\pm)}{\mathcal{B}(B^\pm \to [K^\pm\pi^\mp]_D K^\pm)} = r_B^2 + r_D^2 + 2 r_B r_D \cos\phi_3 \cos\delta, \tag{3.16}$$

and

$$\mathcal{A}_{\rm ADS} = \frac{\mathcal{B}(B^- \to [K^+\pi^-]_D K^-) - \mathcal{B}(B^+ \to [K^-\pi^+]_D K^+)}{\mathcal{B}(B^- \to [K^+\pi^-]_D K^-) + \mathcal{B}(B^+ \to [K^-\pi^+]_D K^+)} \tag{3.17}$$

$$= 2 r_B r_D \sin\phi_3 \sin\delta / \mathcal{R}_{\rm ADS}, \tag{3.18}$$

where r_D is the ratio of the doubly Cabibbo-suppressed and Cabibbo-allowed D^0 decay amplitudes and δ is the sum of strong phase differences in B and D decays: $\delta = \delta_B + \delta_D$. The ADS analysis [52] using the full $\Upsilon(4S)$ data sample was reported by the Belle collaboration (Fig. 16). The analysis uses $B^\pm \to DK^\pm$ decays with D^0 decaying to $K^+\pi^-$ and $K^-\pi^+$ (and their charge-conjugated partners). The signal yield obtained is 56^{+15}_{-14} events, which corresponds to the first evidence of an ADS signal (with a significance of 4.1σ); the ratio of the suppressed and allowed modes is summarized in Table 6. Although the analyses with $B^\pm \to DK^\pm$ decays give the most precise results, different B decays have also been studied. The use of two additional decay modes, $D^* \to D\pi^0$ and $D^* \to D\gamma$, provides an extra handle on the extraction of ϕ_3 from $B^\pm \to D^* K^\pm$, which is becoming visible in the most recent results (Belle Collaboration, preliminary results presented at Lepton Photon 2011 (BELLE-CONF-1112)).

A Dalitz plot analysis of a three-body D meson final state allows one to obtain all the information required for determination of ϕ_3 in a single decay mode. Three-body final states such as $K_S^0\pi^+\pi^-$ have been suggested as promising modes (Ref. [53] and A. Bondar, unpublished work) for the extraction of ϕ_3. As in the GLW and ADS methods, the two amplitudes interfere if the D^0 and $\overline{D}^0$ mesons

Table 7. Results of Belle Dalitz plot analyses.

Mode	ϕ_3 (°)	δ_B (°)	r_B
$B \to DK$	$81^{+13}_{-15} \pm 5$	$137^{+13}_{-16} \pm 4$	$0.16 \pm 0.04 \pm 0.01$
$B \to D^{\star}K$	$74^{+19}_{-20} \pm 4$	$342^{+19}_{-21} \pm 3$	$0.20 \pm 0.07 \pm 0.01$

decay into the same final state $K^0_S\pi^+\pi^-$. Assuming no CP asymmetry in neutral D decays, the amplitude for $B^+ \to D[K_S\pi^+\pi^-]K^+$ decay as a function of Dalitz plot variables $m^2_+ = m^2_{K^0_S\pi^+}$ and $m^2_- = m^2_{K^0_S\pi^-}$ is

$$f_{B^+} = f_D(m^2_+, m^2_-) + r_B e^{i\phi_3 + i\delta_B} f_D(m^2_-, m^2_+), \tag{3.19}$$

where $f_D(m^2_+, m^2_-)$ is the amplitude of the $\overline{D}^0 \to K^0_S\pi^+\pi^-$ decay. Similarly, the amplitude for $B^- \to D[K_S\pi^+\pi^-]K^-$ decay is

$$f_{B^-} = f_D(m^2_-, m^2_+) + r_B e^{-i\phi_3 + i\delta_B} f_D(m^2_+, m^2_-). \tag{3.20}$$

The $\overline{D}^0 \to K^0_S\pi^+\pi^-$ decay amplitude f_D can be determined from a large sample of flavor-tagged $\overline{D}^0 \to K^0_S\pi^+\pi^-$ decays produced in continuum e^+e^- annihilation. Once f_D is known, a simultaneous fit to B^+ and B^- data allows the contributions of r_B, ϕ_3, and δ_B to be separated. The method has only two-fold ambiguity: (ϕ_3, δ_B) and $(\phi_3 + 180°, \delta_B + 180°)$ solutions cannot be distinguished. To test the consistency of the fit, the same procedure was applied to the $B^\pm \to D^{(*)}\pi^\pm$ control samples and the $B^\pm \to D^{(*)}K^\pm$ signal. A combined unbinned maximum likelihood fit to the B^+ and B^- samples with free parameters r_B, ϕ_3, and δ_B yields the values given in Table 7. Combining $B^\pm \to DK^\pm$ and $B^\pm \to D^*K^\pm$, we obtain [54] the value $\phi_3 = (78^{+11}_{-12} \pm 4 \pm 9)°$, where the sources of uncertainties are statistical, systematic, and due to imperfect knowledge of the amplitude model that describes $D \to K^0_S\pi^+\pi^-$ decays. The last source of uncertainty can be eliminated by binning the Dalitz plot (Refs. [53,55,56] and A. Bondar, unpublished work), using information on the average strong phase difference between D^0 and $\overline{D}^0$ decays in each bin that can be determined using quantum correlated $\psi(3770)$ data. Results have been published recently by CLEO-c [57]. The measured strong phase difference is used to obtain a model-independent result [58]:

$$\phi_3 = (77 \pm 15 \pm 4 \pm 4)°, \tag{3.21}$$

where the last uncertainty is due to the statistical precision of the CLEO-c results.

4. Measurement of $|V_{cb}|$ and $|V_{ub}|$, semileptonic, and leptonic B decays

4.1. *Introduction*

The Cabibbo–Kobayashi–Maskawa (CKM) matrix elements $|V_{cb}|$ and $|V_{ub}|$ are determined from semileptonic $B \to X\ell\nu$ $(\ell = e, \mu)$ decays to charmed and charmless final states, respectively (Fig. 17). These decays are chosen because semileptonic decays proceed via leading-order weak interactions and thus are free of possible non-Standard Model contributions. Their branching fractions are sizable compared to purely leptonic $B \to \ell\nu$ decays, and have hadronic uncertainties that are well controlled by various theoretical techniques.

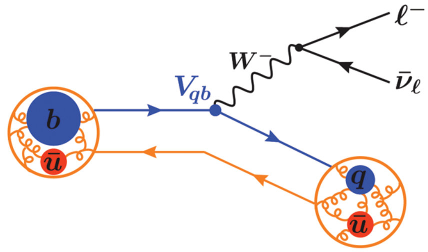

Fig. 17. Illustration of the semileptonic B meson decay $B \to X\ell\nu$.

In this section, we also discuss purely leptonic and semileptonic B decays involving a heavy τ lepton. At present these decays are not relevant for the determination of $|V_{cb}|$ and $|V_{ub}|$ but are studied because of their sensitivity to the charged Higgs boson and other manifestations of new physics.

There are two orthogonal approaches to measuring semileptonic decays and determining $|V_{cb}|$ and $|V_{ub}|$: Analyses can either be *exclusive*, i.e., these reconstruct only a specific semileptonic final state, such as $D^*\ell\nu, \pi\ell\nu, \ldots$. Alternatively, the analysis can be *inclusive*, which means that it is sensitive to all semileptonic final states, $X_c\ell\nu$ or $X_u\ell\nu$, in a given region of phase space, where X_c and X_u refer to a hadronic system with charm or without charm, respectively.

Exclusive and inclusive analyses are affected by different experimental uncertainties. In addition, different and largely independent theoretical approaches are used to describe the QCD contributions in exclusive and inclusive decays. Since both approaches rely on different experimental techniques and involve different theoretical approximations, they complement each other and provide largely independent determinations of comparable accuracy for $|V_{cb}|$ and $|V_{ub}|$. This in turn provides a crucial cross check of the methods and our understanding of semileptonic B decays in general.

4.2. $|V_{cb}|$

4.2.1. $|V_{cb}|$ *from exclusive semileptonic decays.* The determination of $|V_{cb}|$ from exclusive decays is based on the $B \to D^*\ell\nu$ or $B \to D\ell\nu$ decay modes. Experimentally, one has to measure the differential decay rate as a function of the velocity transfer w, defined as

$$w = \frac{P_B \cdot P_{D^{(*)}}}{m_B m_{D^{(*)}}} = \frac{m_B^2 + m_{D^{(*)}}^2 - q^2}{2 m_B m_{D^{(*)}}}, \tag{4.1}$$

where m_B and $m_{D^{(*)}}$ are the masses of the B and the charmed mesons, P_B and $P_{D^{(*)}}$ are their four-momenta, and $q^2 = (P_\ell + P_\nu)^2$. The point $w = 1$ is referred to as zero recoil, because there the charmed meson is at rest in the B meson frame. To determine $|V_{cb}|$, the experimental analyses extrapolate the decay rate to $w = 1$, as theory can determine the decay form factors with greater accuracy at this kinematic point. When neglecting the lepton mass, i.e., considering only electrons and muons, the differential decay rate of $B \to D^*\ell\nu$ as a function of w is given by [59]

$$\frac{d\Gamma}{dw} = \frac{G_F^2 m_{D^*}^3}{48\pi^3}(m_B - m_{D^*})^2 \sqrt{w^2 - 1}\, \chi(w) \mathcal{F}^2(w) |V_{cb}|^2. \tag{4.2}$$

Here, G_F is Fermi's constant equal to $(1.166\,37 \pm 0.000\,01) \times 10^{-5}\,\mathrm{GeV}^{-2}$ and $\chi(w)$ is a known phase space factor,

$$\chi(w) = (w+1)^2 \left[1 + 4\frac{w}{w+1}\frac{1 - 2wr + r^2}{(1-r)^2}\right], \tag{4.3}$$

where $r = m_{D^*}/m_B$. The dynamics of the decay are contained in the form factor $\mathcal{F}(w)$, which can be parameterized by the normalization $\mathcal{F}(1)$, the slope $\rho^2_{D^*}$, and the amplitude ratios $R_1(1)$ and $R_2(1)$ in the framework of the heavy quark effective theory (HQET) [60].

A similar expression can be derived for the differential rate of the decay $B \to D\ell\nu$,

$$\frac{d\Gamma}{dw} = \frac{G_F^2 m_D^3}{48\pi^3}(m_B + m_D)^2(w^2-1)^{3/2}\mathcal{G}^2(w)|V_{cb}|^2. \tag{4.4}$$

As the D meson is a pseudoscalar, the form factor $\mathcal{G}(w)$ of this decay is simpler than $\mathcal{F}(w)$ and can be parameterized by the normalization $\mathcal{G}(1)$ and the slope ρ^2_D only [60].

In the limit of infinite quark masses, the form factors $\mathcal{F}(w)$ and $\mathcal{G}(w)$ coincide with the Isgur–Wise function [61], which is normalized to unity at zero recoil, $w = 1$. Corrections to the heavy quark limit have been calculated in the framework of lattice QCD (LQCD). In LQCD, the QCD action is discretized on a Euclidean spacetime lattice and calculations are performed numerically on computers using Monte Carlo methods. Physical results are then recovered in the limit of zero lattice spacing. Because lattice results are obtained from QCD first principles, they can be improved to arbitrary precision, given sufficient computing resources.

The form factor values at $w = 1$ are the main theoretical input needed for the determination of $|V_{cb}|$ from exclusive decays and also the main source of theoretical uncertainty. The current LQCD value of $\mathcal{F}(1)$, describing the decays $B \to D^*\ell\nu$, is [62]

$$\mathcal{F}(1) = 0.908 \pm 0.017. \tag{4.5}$$

The LQCD $B \to D\ell\nu$ form factor at zero recoil is calculated to be [63]

$$\mathcal{G}(1) = 1.074 \pm 0.024. \tag{4.6}$$

The Belle measurement of $B^0 \to D^{*-}\ell^+\nu$ [64] is based on 772×10^6 $B\bar{B}$ events, resulting in about 120 000 reconstructed decays. In this analysis the decay chain $D^{*-} \to \bar{D}^0\pi^-$ followed by $\bar{D}^0 \to K^+\pi^-$ is reconstructed and D^* candidates are combined with a charged lepton ℓ ($\ell = e, \mu$) with momentum between 0.8 GeV and 2.4 GeV. As the analysis makes no requirement on the second B meson in the event, the direction of the neutrino is not precisely known. However, using the $\cos\theta_{BY}$ variable,

$$\cos\theta_{BY} = \frac{2E_B E_Y - m_B^2 - m_Y^2}{2P_B P_Y}, \tag{4.7}$$

with $Y = D^*\ell$, the B momentum vector is constrained to a cone centered on the $D^*\ell$ direction. By averaging over the possible B directions one can approximate the neutrino momentum and calculate the kinematic variables of the decay (w and three decay angles). The parameters of the form factor $\mathcal{F}(w)$ are obtained by fitting these four kinematic distributions. The very large data sample led to much reduced statistical and systematic uncertainties.

The result of the Belle analysis (after rescaling input parameters to their most recent values [23]) is

$$\mathcal{F}(1)|V_{cb}| = (34.7 \pm 0.2(\text{stat}) \pm 1.0(\text{syst})) \times 10^{-3}, \tag{4.8}$$

where the dominant systematic uncertainties stem from charged track reconstruction. Assuming the form factor normalization of Eq. 4.5, we obtain

$$|V_{cb}| = (38.2 \pm 1.1(\mathrm{exp}) \pm 0.7(\mathrm{th})) \times 10^{-3}. \tag{4.9}$$

The experimental uncertainty is at the level of 3.0% while the theoretical uncertainty from lattice QCD amounts to 1.9%.

In addition, the decay $B \to D\ell\nu$ has been studied at Belle using 10.8×10^6 $B\bar{B}$ events [65]. For the determination of $|V_{cb}|$, the decay $B \to D^*\ell\nu$ is preferred over $B \to D\ell\nu$ for both theoretical and experimental reasons: On the theory side, the rate at zero recoil is lower for $B \to D\ell\nu$ than for $B \to D^*\ell\nu$ due to the factor $(w^2-1)^{3/2}$ in the expression for the width (instead of $\sqrt{w^2-1}$ in the D^* case). Experimentally, due to the presence of the slow pion in the decay $D^* \to D\pi$, the D^* signal is cleaner than the D signal and backgrounds in the analysis of $B \to D\ell\nu$ are typically the limiting factor.

The result of the Belle analysis (after rescaling input parameters to their most recent values [23]) is

$$\mathcal{G}(1)|V_{cb}| = (40.8 \pm 4.4(\mathrm{stat}) \pm 5.2(\mathrm{syst})) \times 10^{-3}, \tag{4.10}$$

with the dominant systematic uncertainties from background estimation. Assuming the $\mathcal{G}(1)$ value from Eq. 4.6, we obtain

$$|V_{cb}| = (38.0 \pm 6.3(\mathrm{exp}) \pm 0.8(\mathrm{th})) \times 10^{-3}. \tag{4.11}$$

This determination of $|V_{cb}|$ is consistent with the $B \to D^*\ell\nu$ value but has a significantly larger uncertainty.

4.2.2. $|V_{cb}|$ from inclusive semileptonic decays. The theoretical tool for calculating the inclusive semileptonic decay width $\Gamma(B \to X_c\ell\nu)$ of the B meson is the operator product expansion (OPE). In this framework, a simplified form reads [66,67]

$$\Gamma(B \to X_c\ell\nu) = \frac{G_F^2 m_b^5}{192\pi^3}|V_{cb}|^2 \left(1 + \frac{c_5(\mu)\,\langle O_5\rangle(\mu)}{m_b^2} + \frac{c_6(\mu)\,\langle O_6\rangle(\mu)}{m_b^3} + \mathcal{O}\left(\frac{1}{m_b^4}\right)\right), \tag{4.12}$$

where the expansion parameter is the b-quark mass m_b. At leading order in $1/m_b$, the OPE result coincides with the parton model, i.e., with the decay width of a (hypothetical) free b-quark. Corrections to the free b-quark decay arise at order $1/m_b^2$: the term $\langle O_5\rangle(\mu)$ denotes the expectation values of local dimension 5 operators, which depend on the renormalization scale μ. A detailed analysis shows that only two operators appear at $\mathcal{O}(1/m_b^2)$: the kinetic operator, related to the kinetic energy of the b-quark inside the B hadron, and the chromomagnetic operator, related to the B^*–B hyperfine mass splitting. At $\mathcal{O}(1/m_b^3)$, new operators appear. These expectation values of local operators describe basic hadronic properties of the B meson and do not depend on the observable (here $\Gamma(B \to X_c\ell\nu)$) calculated using the OPE. As they contain soft hadronic physics, they cannot be calculated by perturbative QCD.

These matrix elements are multiplied by the Wilson coefficients $c_5, c_6, \ldots$, which encode the short-distance QCD contributions to the process and thus can be calculated in perturbation theory as a series in powers of α_s. Hence, the OPE factorizes the calculable and the non-calculable contributions to the semileptonic width. Even more interestingly, the hadronic matrix elements in the non-calculable part also appear in similar OPE expressions for other inclusive observables in semileptonic B decays. By measuring these additional observables, one can determine the non-perturbative OPE parameters, substitute them into the expression of the semileptonic width, and measure $|V_{cb}|$ with a total precision of about 1–2%. This is the basic idea underlying the global fit analysis of $|V_{cb}|$ discussed in this section.

These other observables are the (truncated) moments of the lepton energy E_ℓ (in the B rest frame) and the hadronic mass squared m_X^2 spectra in $B \to X\ell\nu$. The quantity m_X^2 is the invariant mass squared of the hadronic system X_c accompanying the lepton–neutrino pair. The lepton energy moments are defined as

$$\langle E_\ell^n \rangle_{E_{\text{cut}}} = \frac{R_n(E_{\text{cut}})}{R_0(E_{\text{cut}})}, \tag{4.13}$$

where E_{cut} is the lower lepton energy threshold and

$$R_n(E_{\text{cut}}) = \int_{E_\ell > E_{\text{cut}}} E_\ell^n \frac{d\Gamma}{dE_\ell} dE_\ell. \tag{4.14}$$

Here, $d\Gamma/dE_\ell$ is the partial semileptonic width as a function of the lepton energy. The hadronic mass moments are

$$\langle m_X^{2n} \rangle_{E_{\text{cut}}} = \frac{S_n(E_{\text{cut}})}{S_0(E_{\text{cut}})}, \tag{4.15}$$

with

$$S_n(E_{\text{cut}}) = \int_{E_\ell > E_{\text{cut}}} m_X^{2n} \frac{d\Gamma}{dm_X^2} dm_X^2. \tag{4.16}$$

Here the integration over the $B \to X_c\ell\nu$ phase space is restricted by the requirement $E_\ell > E_{\text{cut}}$. These observables can be expanded in OPEs similar to Eq. 4.12, containing the *same* non-perturbative parameters.

In practice, the semileptonic width and moments in $B \to X_c\ell\nu$ have been calculated in two theoretical frameworks, referred to by the name of the renormalization scheme used for the quark masses (though this is not the only difference in the calculations): The calculations in the *kinetic scheme* are now available at next-to-next-to-leading (NNLO) order in α_s [66,68]. At leading order in the OPE, the non-perturbative parameters are the quark masses m_b and m_c. At $\mathcal{O}(1/m_b^2)$ the parameters are μ_π^2 and μ_G^2, and at $\mathcal{O}(1/m_b^3)$ the parameters ρ_D^3 and ρ_{LS}^3 appear. Independent expressions have been obtained in the *1S scheme* [67]. Here, the long-distance parameters are m_b at leading order, λ_1 and λ_2 at $\mathcal{O}(1/m_b^2)$ and ρ_1, τ_{1-3} at $\mathcal{O}(1/m_b^3)$. Note that the numerical values of the quark masses in the two schemes cannot be compared directly due to their different definitions.

Belle has measured moments of inclusive observables in $B \to X_c\ell\nu$ decays [69,70]. The lepton energy E_ℓ and hadronic mass squared m_X^2 spectra in $B \to X_c\ell\nu$ are based on 152×10^6 $\Upsilon(4S) \to B\bar{B}$ events. These analyses first fully reconstruct the decay of one B meson (B_{tag}) in the event in a hadronic mode (or a hadronic tag). The tracks and clusters associated with B_{tag} are removed from the event. The semileptonic decay of the second B meson in the event (B_{sig}) is then identified by searching for a charged lepton among the remaining particles in the event. In the lepton energy

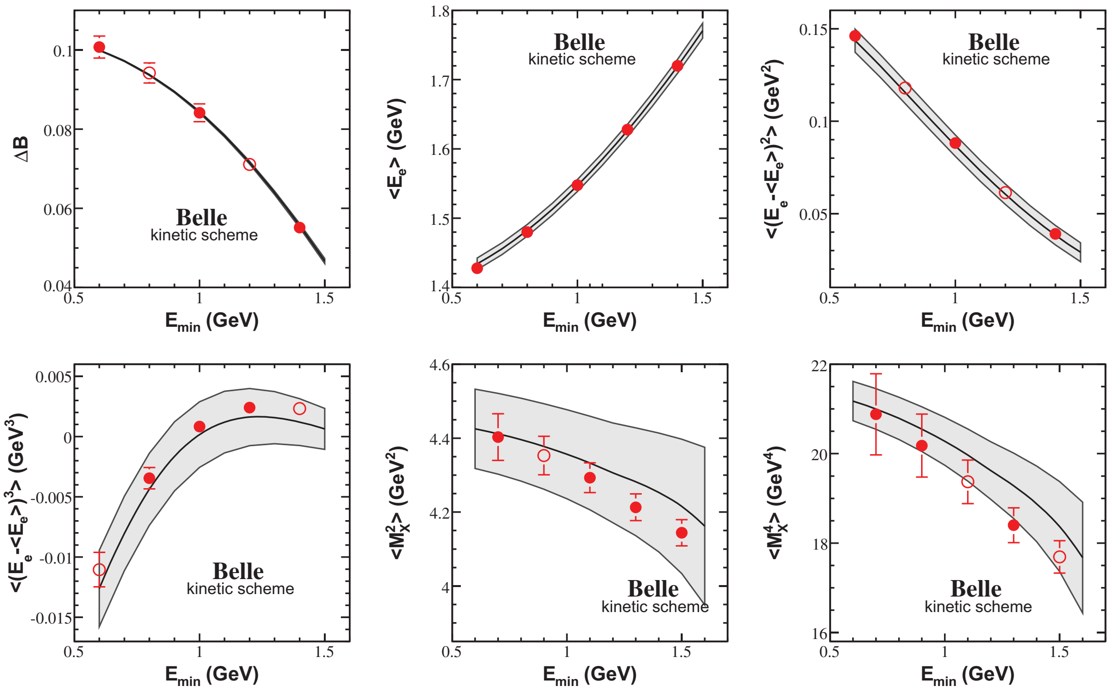

Fig. 18. Global fit of moments in $B \to X_c \ell \nu$ decays measured at Belle to theoretical expressions obtained in the kinetic scheme. The error bars show the experimental uncertainties. The error bands represent the theory error. Filled circles are data points used in the fit, and open circles are unused measurements.

analysis [69], the electron momentum spectrum p_e^* in the B meson rest frame is measured down to 0.4 GeV/c. In the hadronic mass study [70], all remaining particles in the event, after excluding the charged lepton (either an electron or muon), are combined to reconstruct the hadronic X system. The m_X^2 spectrum is measured for lepton energies above 0.7 GeV in the B meson rest frame.

The observed spectra are distorted by resolution and acceptance effects and cannot be used directly to obtain the moments. In the Belle analyses, acceptance and finite resolution effects are corrected by unfolding the observed spectra using the singular value decomposition (SVD) algorithm [71]. Belle measures the lepton energy moments $\langle E_\ell^k \rangle$ for $k = 0, 1, 2, 3, 4$ and minimum lepton energies ranging from 0.4 to 2.0 GeV. Moments of the hadronic mass $\langle m_X^k \rangle$ are measured for $k = 2, 4$ and minimum lepton energies between 0.7 and 1.9 GeV.

To determine $|V_{cb}|$, Belle performs fits [72] to 14 lepton energy moments, 7 hadronic mass moments, and 4 moments of the photon energy spectrum in $B \to X_s \gamma$ based on OPE expressions derived in the kinetic [66,68,73] and 1S schemes [67] (Fig. 18). Both theoretical frameworks are considered independently and yield very consistent results: The fit to the Belle data in the kinetic scheme yields

$$|V_{cb}| = (41.58 \pm 0.90) \times 10^{-3}, \tag{4.17}$$

while in the 1S scheme we obtain

$$|V_{cb}| = (41.56 \pm 0.68) \times 10^{-3} . \tag{4.18}$$

While the result in the 1S scheme is more precise (1.6% uncertainty compared to 2.2% in the kinetic scheme), it should be noted that the assumptions on the dominant theory error are significantly different.

4.3. $|V_{ub}|$

4.3.1. $|V_{ub}|$ *from exclusive* $B \to X_u \ell \nu$ *decays.* The absolute value of V_{ub}, one of the least known CKM elements, can be determined from rate measurements of exclusive charmless semileptonic decays, such as $B \to \pi \ell \nu$, $B \to \rho \ell \nu$ and $B \to \omega \ell \nu$. Of these, $B^0 \to \pi^- \ell^+ \nu$ decay has been the most extensively studied both theoretically and experimentally. The decay rates and $|V_{ub}|$ are related as

$$\frac{d\Gamma(B^0 \to \pi^- \ell^+ \nu)}{dq^2} = \frac{G_F^2}{24\pi^3} |V_{ub}|^2 p_\pi^3 |f_+(q^2)|^2, \tag{4.19}$$

where G_F is the Fermi coupling constant, and $f_+(q^2)$ is the $B \to \pi$ transition form factor, which is calculated in lattice QCD and by QCD sum rules. Compared to the inclusive measurements, described below, the exclusive measurements are relatively straightforward experimentally, but suffer from large theoretical uncertainties in the form factors, which must be determined from non-perturbative QCD calculations.

The Belle collaboration has measured $B \to \pi/\rho/\omega \ell \nu$ decays [74–76]. The most recent measurement of the $B^0 \to \pi^- \ell^+ \nu$ decay [76] uses a data sample containing 657×10^6 $B\bar{B}$ pairs, and has the best precision for the $|V_{ub}|$ determination. In this analysis, signals are reconstructed by combining an oppositely charged pion and lepton (either electron or muon), originating from a common vertex. For the reconstruction of the undetected neutrino, the missing energy and momentum in the c.m. frame are defined as $E_{\text{miss}} \equiv 2E_{\text{beam}} - \Sigma_i E_i$ and $\vec{p}_{\text{miss}} \equiv -\Sigma_i \vec{p}_i$, respectively, where E_{beam} is the beam energy in the c.m. frame, and the sums include all charged and neutral particle candidates in the event. We require $E_{\text{miss}} > 0\,\text{GeV}$, and the neutrino 4-momentum is taken to be $p_\nu = (|\vec{p}_{\text{miss}}|, \vec{p}_{\text{miss}})$, since the determination of $\vec{p}_{\text{miss}}$ is more accurate than that of the missing energy. As in the analysis of $B^0 \to D^{*-} \ell^+ \nu$, using the variable $\cos\theta_{BY}$ [Eq. (4.7)], the B momentum vector is constrained to lie on a cone centered on the $\pi^- \ell^+$ direction; signals can then be selected by requiring $|\cos\theta_{BY}| < 1$. Background from continuum $e^+e^- \to q\bar{q}(q = u, d, s, c)$ jets are reduced using an event topology requirement based on the second Fox–Wolfram moment. Signals are extracted, for each of 13 q^2 bins ranging from 0 to 26 GeV^2/c^2, by fitting the two-dimensional distribution of the beam energy constrained mass $M_{\text{bc}} = \sqrt{E_{\text{beam}}^2 - |\vec{p}_\pi + \vec{p}_\ell + \vec{p}_\nu|^2}$ and the energy difference $\Delta E = E_{\text{beam}} - (E_\pi + E_\ell + E_\nu)$. Figure 19 shows the obtained q^2 distribution. The total branching fraction, integrated over the entire q^2 region, is

$$\mathcal{B}(B^0 \to \pi^- \ell^+ \nu) = (1.49 \pm 0.04(\text{stat}) \pm 0.07(\text{syst})) \times 10^{-4}. \tag{4.20}$$

The value of $|V_{ub}|$ can be determined from the measured differential q^2 distribution using Eq. (4.19). Following the procedure proposed by the FNAL/MILC collaboration [77], $|V_{ub}|$ can be extracted from a simultaneous fit to experimental and lattice QCD results from the FNAL/MILC collaboration, as shown in Fig. 20. In this approach, q^2 is transformed to a dimensionless quantity z, and both the experimental and lattice QCD distributions are fit to a third-order polynomial with $|V_{ub}|$ determined as a relative normalization between the lattice QCD and experimental results. We find

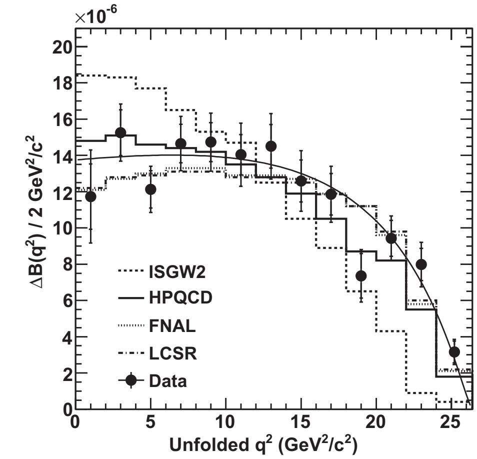

Fig. 19. Measured q^2 distribution for the $B^0 \to \pi^- \ell \nu$ decay. The curve represents a fit to an empirical form factor parameterization. The four histograms show various form factor predictions (dashed: ISGW2; plain: HPQCD; dotted: FNAL; dot-dashed: LCSR).

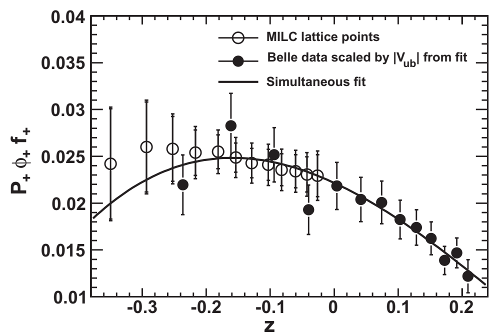

Fig. 20. $|V_{ub}|$ extraction from a simultaneous fit to experimental (closed circles) and FNAL/MILC lattice QCD results (open circles).

Table 8. Summary of $|V_{ub}|$ results from a recent $B^0 \to \pi^- \ell \nu$ measurement by Belle.

Theory	q^2 (GeV$^2/c^4$)	$\lvert V_{ub}\rvert$ ($\times 10^{-3}$)
LCSR [78]	<16	$3.64 \pm 0.11^{+0.60}_{-0.40}$
HPQCD [79]	>16	$3.55 \pm 0.13^{+0.62}_{-0.41}$
FNAL [63]	>16	$3.78 \pm 0.14^{+0.65}_{-0.43}$
FNAL/MILC [77]	all regions	3.43 ± 0.33

$|V_{ub}| = (3.43 \pm 0.33) \times 10^{-3}$, as shown in Table 8. The table also lists $|V_{ub}|$ values determined using only a fraction of the overall phase space, leading to less precise but statistically compatible results. The form factor $f_+(q^2)$ predictions are based on the light cone sum rule (LCSR) and lattice QCD (LQCD), which can be applied in the regions $q^2 < 16\,\mathrm{GeV}^2/c^4$ and $q^2 > 16\,\mathrm{GeV}^2/c^4$, respectively.

4.3.2. $|V_{ub}|$ from inclusive $B \to X_u \ell \nu$ decays. For inclusive $B \to X_u \ell \nu$ decays, the theoretical description relies on the operator product expansion (OPE), as in the case of inclusive $B \to X_c \ell \nu$ decays. However, $B \to X_u \ell \nu$ decays are about 50 times less abundant than $B \to X_c \ell \nu$ decays, and

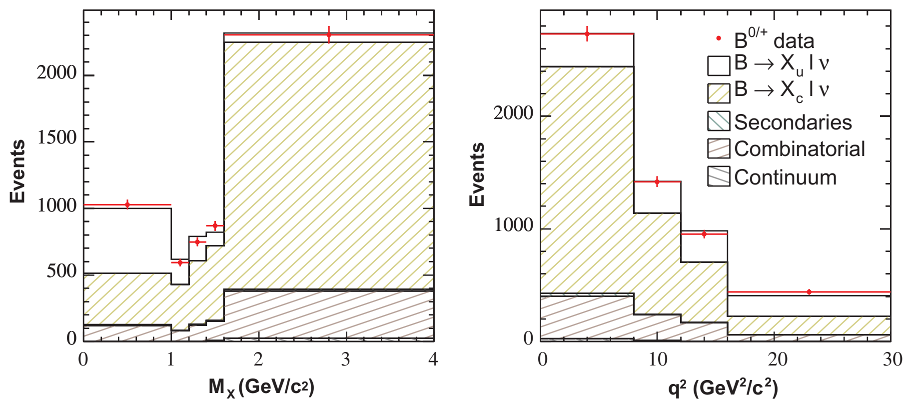

Fig. 21. Projections of the $m_X - q^2$ fit in bins of m_X (left) and q^2 (right).

thus the experimental sensitivity to $B \to X_u \ell \nu$ and $|V_{ub}|$ is highest in the region of phase space that is less impacted by the dominant background from $B \to X_c \ell \nu$ decays. In this phase space region, however, non-perturbative corrections are kinematically enhanced, and as a result non-perturbative dynamics become an O(1) effect. Extracting $|V_{ub}|$ requires the use of theoretical parameterizations called *shape functions (SF)* to describe the unmeasured regions of phase space.

A classical method is to measure the lepton momentum spectrum at the end-point of the spectrum ($p_\ell^{cm} > 2.3\text{GeV}/c$), where the $b \to c$ decay is forbidden. This method allows the measurement of $|V_{ub}|$ with small data samples, but suffers from a large extrapolation error, because only a limited portion of the phase space ($\sim$10% of the total) is measured. Belle reported a result using this method in 2005 [80]. The high luminosity data at Belle enable us to also measure kinematic variables such as the invariant mass of the X_u hadronic system, m_X, and the four-momentum transfer of the B meson to the X_u system, q. This enables us to control the experimental and theoretical errors by optimizing the region of phase space for the measurement. Belle reported the first measurement using $m_x - q^2$ for the inclusive $B \to X_u \ell \nu$ decay [81].

More recently, Belle reported a measurement of the partial branching fraction of $B \to X_u \ell \nu$ decays with a lepton momentum threshold of 1 GeV/c using a multivariate data mining technique, with a data sample containing $657 \times 10^6 B\bar{B}$ pairs [82]. This method allows us to access $\sim 90\%$ of the $B \to X_u \ell \nu$ phase space and minimizes the dependence on an SF. The measurement is made by fully reconstructing one B meson (B_{tag}) in hadronic decays, and measuring the semileptonic decay of the other B meson (B_{sig}) with a high momentum electron or muon. The $B \to X_u \ell \nu$ decays are selected based on a nonlinear multivariate boosted decision tree (BDT), which incorporates a total of 17 discriminating variables, such as the kinematical quantities of candidate semileptonic decays, number of kaons in the event, M_{bc} of B_{tag}, etc. The candidates passing the selection of the BDT classifier are analyzed in a two-dimensional fit in the (m_X, q^2) plane. The hadronic invariant mass m_X is calculated from the measured momenta of all charged tracks and neutral clusters that are not associated to B_{tag} reconstruction or used as a lepton candidate. The momentum transfer is calculated as $q = p_{\Upsilon(4S)} - p_{B_{\text{tag}}} - p_X$. Figure 21 shows the one-dimensional projections of the (m_X, q^2) distribution with a lepton momentum requirement of $p_\ell^{*B} > 1.0\text{GeV}/c$, fitted with distributions for the $B \to X_u \ell \nu$ signal, $B \to X_c \ell \nu$ and other backgrounds mainly from secondary and misidentified leptons. The partial branching fraction for $p_\ell^{*B} > 1.0\text{GeV}/c$ is

$$\Delta\mathcal{B}(B \to X_u \ell \nu;\ p_\ell^{*B} > 1.0\text{GeV}/c) = 1.963 \times (1 \pm 0.088(\text{stat}) \pm 0.081(\text{syst})) \times 10^{-3}. \quad (4.21)$$

Table 9. $|V_{ub}|$ values obtained using the inclusive $B \to X_u \ell nu$ measurement by Belle and input parameters (m_b and μ_π^2). The errors quoted on $|V_{ub}|$ correspond to experimental and theoretical uncertainties, respectively.

Theory	m_b (GeV)	μ_π^2 (GeV^2)	$|V_{ub}|$ ($\times 10^{-3}$)
BLNP [83]	4.588 ± 0.025	$0.189^{+0.046}_{-0.057}$	$4.47 \pm 0.27^{+0.19}_{-0.21}$
DGE [84]	4.194 ± 0.043	—	$4.60 \pm 0.27^{+0.11}_{-0.13}$
GGOU [85]	4.560 ± 0.023	0.453 ± 0.036	$4.54 \pm 0.27^{+0.10}_{-0.11}$
ADFR [86]	4.194 ± 0.043	—	$4.48 \pm 0.30^{+0.19}_{-0.19}$

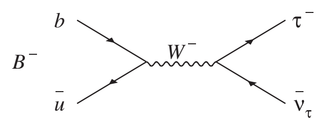

Fig. 22. A Feynman diagram for the SM $B^- \to \tau^- \bar{\nu}_\tau$ process.

A $|V_{ub}|$ value is obtained from the partial branching fraction using $|V_{ub}|^2 = \Delta\mathcal{B}_{u\ell\nu}/(\tau_B \Delta R)$, where ΔR is the predicted $B \to X_u \ell\nu$ partial rate in the given phase space region, and τ_B is the average B lifetime. Table 9 presents $|V_{ub}|$ results based on different theoretical prescriptions that predict ΔR. Here the results were obtained by the Heavy Flavor Averaging Group (HFAG) using the most recent calculations and input parameters [38]. The results are consistent within their stated theoretical uncertainties, and have an overall uncertainty of $\sim$7%.

As described above, there is a tension between the $|V_{ub}|$ values extracted from the exclusive and inclusive methods, which are subject to further clarification with improved experimental and theoretical errors in the future.

4.4. *Purely leptonic $B^- \to \ell^- \bar{\nu}_\ell (\ell = e, \mu, or\ \tau)$ decays*

In the SM, $B^- \to \ell^- \bar{\nu}_\ell$ decays to purely leptonic final states ($\ell = e,\ \mu$, or τ) occur via annihilation of the two quarks in the initial state, b and $\bar{u}$, to a W^- boson (Fig. 22). The branching fraction for a $B^- \to \ell^- \bar{\nu}_\ell$ decay is given by

$$\mathcal{B}(B^- \to \ell^- \bar{\nu}_\ell) = \frac{G_F^2 m_B m_\ell^2}{8\pi} \left(1 - \frac{m_\ell^2}{m_B^2}\right)^2 f_B^2 |V_{ub}|^2 \tau_B, \tag{4.22}$$

where G_F is the weak interaction coupling constant, m_ℓ and m_B are the lepton and B^+ meson masses, respectively, τ_B is the B^- lifetime, $|V_{ub}|$ is the magnitude of a CKM matrix element, and f_B is the B^- meson decay constant. All these input parameters have been directly measured with good precision except for f_B. The value of f_B can be obtained using LQCD calculations. Since LQCD calculations are based on first principles of QCD, it is possible to calculate the SM expectation for $\mathcal{B}(B^- \to \ell^- \bar{\nu}_\ell)$ with high precision. Therefore, measurement of f_B via $B^- \to \ell^- \bar{\nu}_\ell$ decays can provide a stringent test of the LQCD, within the framework of the SM.

On the other hand, particles from physics beyond the SM, for example, a charged Higgs boson in supersymmetry or a generic two-Higgs doublet model, may take the place of the W^- in Fig. 22 and modify the branching fraction. Moreover, in the minimum flavor violation NP scheme, it is expected that the relative branching fractions of charged lepton modes will remain the same as those predicted

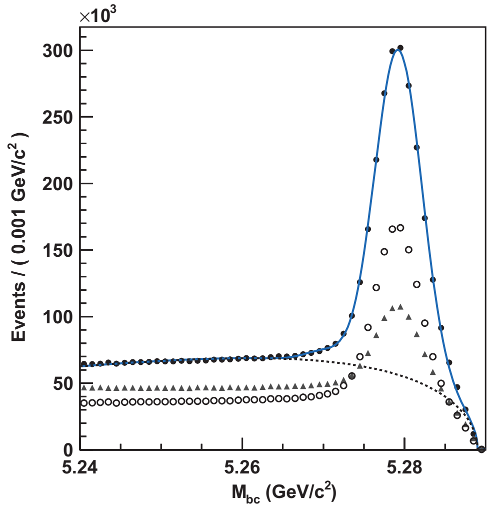

Fig. 23. M_{bc} distributions for the B_{tag} candidate events. The triangles, open circles, and solid circles represent the distributions obtained by applying the original tagging algorithm [87] to the previous data set, applying improved hadronic tagging to the previous data set, and applying improved tagging to the latest fully reprocessed data set, respectively. The solid and dotted curves show the sum and the background component, respectively, of the fit to the full data sample.

by the SM. Accordingly, measuring the branching fractions of $B^- \to \ell^- \bar{\nu}_\ell$ ($\ell = e,\ \mu$, or τ) modes and their relative ratios can provide a very sensitive probe for NP beyond the SM.

Due to helicity suppression, the branching fraction [Eq. (4.22)] is proportional to the square of the charged lepton mass, m_ℓ^2. As a result, the SM branching fractions for $e^- \bar{\nu}_e$ and $\mu^- \bar{\nu}_\mu$ modes are suppressed in comparison to the $\tau^- \bar{\nu}_\tau$ mode by factors of $\sim 10^7$ and ~ 200, respectively. At the time of this report, there exists evidence for $B^- \to \tau^- \bar{\nu}_\tau$ from Belle [87,88] and BaBar[89,90], but no evidence has yet been found for the $B^- \to e^- \bar{\nu}_e$ and $B^- \to \mu^- \bar{\nu}_\mu$ modes.

4.4.1. $B^- \to \tau^- \bar{\nu}_\tau$. While the large mass of the τ lepton significantly enhances the branching fraction of $B^- \to \tau^- \bar{\nu}_\tau$ compared to other modes, the presence of one or more neutrinos from the τ decay make it difficult to cleanly detect $B^- \to \tau^- \bar{\nu}_\tau$ decays. In the process $e^+ e^- \to \Upsilon(4S) \to B\overline{B}$, signal sensitivity is greatly improved by completely reconstructing or "tagging" one B meson (B_{tag}); the signature of the signal is then searched for in the other B meson (B_{sig}). Experimentally, two different tagging methods have been applied to measure $\mathcal{B}(B^- \to \tau^- \bar{\nu}_\tau)$: reconstructing a full decay chain of a hadronic final state ("hadronic tagging") or reconstructing all particles except for a neutrino in semileptonic $B_{\mathrm{tag}} \to D^{(*)} \ell \nu$ decays ("semileptonic tagging").

4.4.2. Hadronic tagging analysis. The first evidence for $B^- \to \tau^- \bar{\nu}_\tau$ decays was obtained in a hadronic tagging analysis by Belle [87] using 449×10^6 $B\overline{B}$ events, which obtained $\mathcal{B}(B^- \to \tau^- \bar{\nu}_\tau) = (1.79^{+0.56+0.46}_{-0.49-0.51}) \times 10^{-4}$. Recently, Belle has updated the hadronic tagging analysis of $B^- \to \tau^- \bar{\nu}_\tau$, analyzing the full Belle data sample containing 772×10^6 $B\overline{B}$ events [91].

In the most recent analysis, the data sample is fully reprocessed with much improved tracking and slightly improved neutral cluster detection. A new hadronic tagging algorithm using a Bayesian artificial neural network has been developed and applied to the analysis [92]. As a result of all these improvements, the statistics of the B_{tag} sample has increased by nearly a factor of

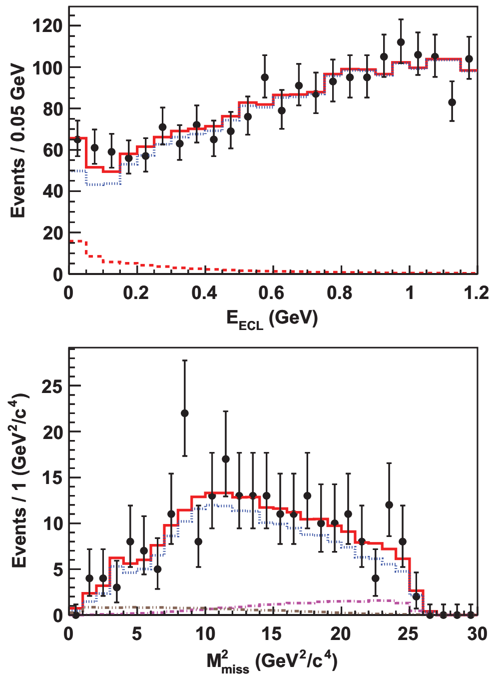

Fig. 24. Distributions of E_{ECL} (top) and M^2_{miss} (bottom) combined for all the τ^- decays. The M^2_{miss} distribution is shown for the signal region $E_{\mathrm{ECL}} < 0.2$ GeV. The solid circles with error bars are data. The solid histograms show the projections of the fits. The dashed and dotted histograms show the signal and background components, respectively.

three. Figure 23 shows the M_{bc} distribution of B_{tag} candidate events, in comparison with that from the previous analysis.

Once the B_{tag} candidates are selected, we search for $B^- \to \tau^-\bar{\nu}_\tau$ decays using the particles not belonging to B_{tag} in these events. The τ^- lepton is identified in four decay modes: $\tau^- \to e^-\bar{\nu}_e\nu_\tau,\ \mu^-\bar{\nu}_\mu\nu_\tau,\ \pi^-\nu_\tau$, and $\pi^-\pi^0\nu_\tau$. Signal candidate events are required to have only one track with charge opposite to B_{tag}. The charged tracks are required to be consistent with being either an electron, muon, or pion. For the $\tau^- \to \pi^-\pi^0\nu_\tau$ mode, with $\pi^0 \to \gamma\gamma$, the invariant mass of the $\pi^-\pi^0$ system must be within 0.15 GeV/c^2 of the nominal ρ^- mass. There should be no other detected particles after removing the particles from the B_{tag} and the charged tracks and π^0s from the B_{sig}. In particular, events containing extra π^0 and K^0_L candidates are rejected.

The signal yield is evaluated by fitting the two-dimensional distribution of E_{ECL} and M^2_{miss}, where E_{ECL} is the sum of the energies of neutral clusters that are not associated with either the B_{tag} or the π^0 candidate in the $\tau^- \to \pi^-\pi^0\nu_\tau$ decay and M^2_{miss} is the missing mass squared defined by $M^2_{\mathrm{miss}} = (E_{\mathrm{CM}} - E_{B_{\mathrm{tag}}} - E_{B_{\mathrm{sig}}})^2 - |\vec{p}_{B_{\mathrm{tag}}} + \vec{p}_{B_{\mathrm{sig}}}|^2$ with the energies and momenta measured in the CM frame. To reduce background, we require $M^2_{\mathrm{miss}} > 0.7$ (GeV/c^2)^2. Figure 24 shows the projections of the result of the fit on E_{ECL} and M^2_{miss} where the four τ decay modes are combined. The preliminary fitted signal yield is $62\,^{+23}_{-22} \pm 6$ events and the branching fraction $\mathcal{B}_{\mathrm{had}}$ (in the hadronic tagging analysis) is

$$\mathcal{B}_{\mathrm{had}}(B^- \to \tau^-\bar{\nu}_\tau) = (0.72\,^{+0.27}_{-0.25} \pm 0.11) \times 10^{-4}. \tag{4.23}$$

The signal significance is 3.0σ including systematic uncertainty. This result is consistent with the previous measurement considering the overlap of the event samples.

4.4.3. Semileptonic tagging analysis. In the semileptonic tagging analysis of $B^- \to \tau^- \bar{\nu}_\tau$, $B_{\rm tag}$ is reconstructed in $B^+ \to \overline{D}^{*0} \ell^+ \nu$ and $B^+ \to \overline{D}^0 \ell^+ \nu$ decays, where ℓ is an electron or muon. Since semileptonic tagging imposes fewer constraints on the $B_{\rm sig}$ kinematics, only τ^- decays to $\ell^- \bar{\nu}_\ell \nu_\tau$ ($\ell = e, \mu$) and $\pi^- \nu_\tau$ are used for $B_{\rm sig}$ reconstruction. Except for $\overline{D}^0$ or $\overline{D}^{*0}$, one ℓ^+ for $B_{\rm tag}$, and one ℓ^- or π^- for $B_{\rm sig}$, we allow no other charged track or neutral particle in the event.

One of the main variables to suppress background events is the cosine of the angle, $\cos\theta_{B,D^{(*)}\ell}$, between the momentum of $B_{\rm tag}$ and that of $\overline{D}^{(*)0}$ and ℓ^+ system. This variable is defined in the same way as the variable $\cos\theta_{BY}$ discussed in the previous section, but with $Y = \overline{D}^{(*)0} \ell^+$. Correctly reconstructed $B_{\rm tag}$ candidates populate the physical range $-1 \le \cos\theta_{B,D^{(*)}\ell} \le 1$. Signal candidates are selected based on $P_\ell^{\rm cm}$ (the lepton momentum of $B_{\rm tag}$ in the CM frame), $\cos\theta_{B,D^{(*)}\ell}$, and $P_{\rm sig}^{\rm cm}$ (the CM-frame momentum of the charged track from $B_{\rm sig}$). The selection criteria depend on the τ decay mode of $B_{\rm sig}$. After all selections, the signal yield ($n_{\rm s}$) is obtained by fitting the $E_{\rm ECL}$ distribution. From a combined fit to the three τ^- decay modes, $n_{\rm s} = 143\,^{+36}_{-35}$ events is obtained. The signal significance is found to be 3.6σ including the systematic uncertainty. The branching fraction $\mathcal{B}_{\rm SL}$ (in the semileptonic tagging analysis) is

$$\mathcal{B}_{\rm SL}(B^- \to \tau^- \bar{\nu}_\tau) = (1.54\,^{+0.38+0.29}_{-0.37-0.31}) \times 10^{-4}. \tag{4.24}$$

4.4.4. The combined result. The two results, $\mathcal{B}_{\rm had}$ and $\mathcal{B}_{\rm SL}$, are combined after taking the correlation in the systematic uncertainties between the two results into account[2]. The signal significance for the combined result is 4.0σ and the average branching fraction is

$$\mathcal{B}(B^- \to \tau^- \bar{\nu}_\tau) = (0.96 \pm 0.22 \pm 0.13) \times 10^{-4}. \tag{4.25}$$

The result is consistent with the SM expectation obtained from other experimental constraints. Using this result along with the input values found from the most recent world averages[23], we obtain $f_B |V_{ub}| = (7.4 \pm 0.8 \pm 0.5) \times 10^{-4}$ GeV. This result sets stringent constraints on the parameters of various models involving charged Higgs bosons.

4.4.5. $B^- \to \ell^- \bar{\nu}_\ell$ ($\ell = e, \mu$). As discussed above, the $B^- \to e^- \bar{\nu}_e$ and $B^- \to \mu^- \bar{\nu}_\mu$ decays are suppressed compared to $B^- \to \tau^- \bar{\nu}_\tau$ due to helicity suppression. On the other hand, these decays have a clear experimental signature: the monochromatic energy of the charged lepton in the rest frame of the signal B. Two methods have been applied to measure these decays: a loose reconstruction analysis and a hadronic tagging analysis.

In the loose reconstruction analysis, where a data sample containing 277×10^6 $B\overline{B}$ pairs is used[93], the signal candidates are selected mainly via a tight requirement on p_ℓ^B, which is the charged lepton momentum (magnitude) in the signal B rest frame. The signal yield is then obtained by fitting the $M_{\rm bc}$ distribution, where $M_{\rm bc}$ is calculated by including all detected particles in the event except for the signal charged lepton. No significant excess of signal in any mode is found. We set the following upper limits on the corresponding branching fractions at the 90% C.L.:

$$\mathcal{B}(B^- \to e^- \bar{\nu}_e) < 0.98 \times 10^{-6}, \tag{4.26}$$

$$\mathcal{B}(B^- \to \mu^- \bar{\nu}_\mu) < 1.7 \times 10^{-6}. \tag{4.27}$$

[2] The semileptonic tag result, $\mathcal{B}_{\rm SL}$, is rescaled by using the updated branching fraction of a background mode so that a consistent set of input parameters is used in the combined fit.

The hadronic tagging analysis is based on a method similar to that described in Sect. 4.4.2 and uses the full data set of Belle containing 772×10^6 $B\overline{B}$ pairs. After selecting signal candidates primarily using the $M_{\rm bc}$ and ΔE variables of the $B_{\rm tag}$ and requiring that the $B_{\rm sig}$ be consistent with $B^- \to \ell^-\bar{\nu}_\ell$, including a requirement on $E_{\rm ECL}$, the expected background in the signal region, $2.6 < p_\ell^B < 2.7$ GeV/c, is much less than one event. The background estimate is determined by examining data and MC events in the sideband of p_ℓ^B below the signal region.

The signal yield is obtained by counting the events in the p_ℓ^B signal region. No events are found in any mode and we set 90% C.L. upper limits on the branching fractions using the POLE [94] program taking the uncertainty in signal efficiency and the expected background with its uncertainty into account. The preliminary upper limits (at 90% C.L.) for the branching fractions $\mathcal{B}_{\rm had}$ (by hadronic tagging analysis) are [95]:

$$\mathcal{B}_{\rm had}(B^- \to e^-\bar{\nu}_e) < 3.5 \times 10^{-6}, \tag{4.28}$$

$$\mathcal{B}_{\rm had}(B^- \to \mu^-\bar{\nu}_\mu) < 2.5 \times 10^{-6}. \tag{4.29}$$

Although the constraints are not as stringent as those obtained in the loose reconstruction analysis, the amount of background is much smaller, nearly zero; hence it is anticipated that the sensitivity may improve almost linearly with the increase of statistics. Therefore, the hadronic tagging analysis will be very interesting in the next-generation super B-factory experiments such as Belle II.

4.5. $B \to D^{(*)}\tau\nu$ decays

Compared to ordinary semileptonic decays $\overline{B}^0 \to D^{*+}\ell^-\bar{\nu}_\ell$ with $\ell = e$ or μ, $B \to D^{(*)}\tau^-\bar{\nu}_\tau$ decays, occurring through a quark-level $b \to c\tau^-\bar{\nu}_\tau$ process, are suppressed because of the large τ mass. The predicted branching fractions, based on the SM, are approximately 1.4% and 0.7% for $B \to D^*\tau^-\bar{\nu}_\tau$ and $B \to D\tau^-\bar{\nu}_\tau$ decays, respectively [96]. On the other hand, the large τ lepton mass makes them sensitive to interactions with a charged Higgs, where the H^+ may replace the virtual W, thereby modifying the branching fraction. Therefore, these $B \to D^{(*)}\tau^-\bar{\nu}_\tau$ modes can be a very effective probe to search for indirect evidence of charged Higgs or other NP hypotheses beyond the SM. Moreover, compared with $B^- \to \tau^-\bar{\nu}_\tau$, these decay modes provide more observables to search for NP, e.g. the polarization of the τ lepton. On the experimental side, however, it is very difficult to measure these modes because of the multiple neutrinos in the final state, the low lepton momenta, and the large associated background contamination.

The first observation of $B \to D^{(*)}\tau^-\bar{\nu}_\tau$ decays was reported by Belle in the $\overline{B}^0 \to D^{*+}\tau^-\bar{\nu}_\tau$ mode using an event sample of 535×10^6 $B\bar{B}$ pairs [97]. In contrast to the hadronic tagging analysis (see Sect. 4.4.2), a loose reconstruction of the accompanying B ($B_{\rm tag}$), where all particles not belonging to the signal decay chain are included without taking subdecay information into account, was used and tighter kinematic constraints were applied for improved background suppression. The signal yield was obtained by fitting the distribution of the beam-constrained mass $M_{\rm bc}$ of the $B_{\rm tag}$. A clear signal excess of 60^{+12}_{-11} events was observed with a significance of 5.2σ including systematic uncertainties. The measured branching fraction was $\mathcal{B}(\overline{B}^0 \to D^{*+}\tau^-\bar{\nu}_\tau) = (2.02^{+0.40}_{-0.37} \pm 0.37)\%$.

Belle has also published measurements of other $B \to D^{(*)}\tau^-\bar{\nu}_\tau$ decay modes. Analyzing a data sample of 657×10^6 $B\overline{B}$ pairs, using a similar analysis to that described above, 446^{+58}_{-56} events of the $B^- \to D^{*0}\tau^-\bar{\nu}_\tau$ decay mode are observed with a significance of 8.1σ and 146^{+42}_{-41} events of the

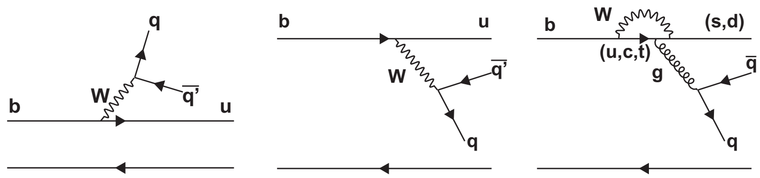

Fig. 25. Feynman diagrams for the quark-level transitions that dominantly contribute to charmless hadronic B decays: (left) color allowed and (middle) color suppressed $b \to u$ tree diagrams, and (right) $b \to (s, d)g$ penguin diagrams.

$B^- \to D^0\tau^-\bar{\nu}_\tau$ decay mode are obtained, providing the first evidence of this mode with a significance of 3.5σ [98]. The branching fractions are $\mathcal{B}(B^- \to D^{*0}\tau^-\bar{\nu}_\tau) = (2.12^{+0.28}_{-0.27} \pm 0.29)\%$ and $\mathcal{B}(B^- \to D^0\tau^-\bar{\nu}_\tau) = (0.77 \pm 0.22 \pm 0.12)\%$.

A preliminary branching fraction of the $\overline{B}^0 \to D^+\tau^-\bar{\nu}_\tau$ mode is measured by an analysis that uses a hadronic tagging method similar to the one described in Sect. 4.4.2: $\mathcal{B}(\overline{B}^0 \to D^+\tau^-\bar{\nu}_\tau) = (1.01\ {}^{+0.46+0.13}_{-0.41-0.11} \pm 0.10)\%$ [99], where the third error comes from the branching fraction uncertainty of the normalization mode, $\overline{B}^0 \to D^+\ell^-\bar{\nu}_\ell$. The branching fractions of the other $B \to D^{(*)}\tau^-\bar{\nu}_\tau$ decay modes are also obtained in this analysis; the results are consistent with published results [97,98].

Recently, BaBar has claimed that the branching fractions of $B \to D^*\tau^-\bar{\nu}_\tau$ and $B \to D\tau^-\bar{\nu}_\tau$ are larger than SM expectations at a combined significance of 3.4σ [100]. We note that all the branching fractions of $B \to D^{(*)}\tau^-\bar{\nu}_\tau$ modes measured by Belle are also larger than the SM-predicted values [96]. It will be interesting to see the final Belle results on these modes using improved hadronic tagging and the full data sample of 772×10^6 $B\overline{B}$ pairs.

5. Rare *B* decays

5.1. Charmless hadronic decays

Charmless hadronic B decays give rise to final states with two or more hadrons that do not contain any charm quark. These decays are suppressed in the SM, mostly proceeding via the CKM-suppressed $b \to u$ tree level transition and $b \to (s, d)g$ penguin diagrams, as shown in Fig. 25. Compared to the CKM-favored $b \to c$ transition such as $B^0 \to J/\psi K^0$, the golden channel for determining the angle ϕ_1 of the unitarity triangle (Sect. 3), their branching fractions are about two to four orders of magnitude lower. By virtue of this suppression, charmless decays provide a good window to probe new physics beyond the SM. For instance, these rare decays have the potential to reveal the contribution of heavy, non-SM virtual particles in penguin loops. Branching fraction calculations within the SM—whether they are based on QCD factorization [101–103], SU(3) flavor symmetry [104–108], or perturbative QCD [109–111]—suffer from large theoretical uncertainties. However, one can examine physics observables in which theory errors as well as common experimental systematic uncertainties largely cancel out. Such observables include direct CP asymmetries, ratios of branching fractions, and longitudinal polarization fractions (in the case in which the decay final states consist of two vector particles). In this section, we summarize Belle's results on charmless B decays, which have resulted in close to 100 journal publications.

5.1.1. Experimental methodology. Before examining various categories of charmless decays, we wish to describe the important experimental considerations. As these decays are suppressed in the

SM one needs to be extremely careful in devising selection algorithms to select candidate events and fitting methods used for extracting the final signal yields. We identify B mesons using two kinematical variables: the beam-energy constrained mass, $M_{\rm bc} \equiv \sqrt{E_{\rm beam}^2 - |\vec{p}_B|^2}$, and the energy difference $\Delta E \equiv E_B - E_{\rm beam}$, where $E_{\rm beam}$ is the beam energy, and E_B and $\vec{p}_B$ are the energy and momentum of B candidates in the CM frame, respectively. The dominant background contribution is from $e^+e^- \to q\bar{q}$ ($q = u, d, s, c$) continuum processes. To suppress this background, we use variables based on the event topology; these selections rely on the fact that B decays are nearly isotropic, in contrast to jet-like continuum events. In some analyses, additional discrimination is provided by variables pertaining to the nature of B decay, e.g., the flight-length difference along the beam direction between the signal and recoil B decay. All this information is combined into either a likelihood ratio or a neural network to optimize the sensitivity. B decays proceeding via a CKM-favored $b \to c$ transition can have a final state that is either the same as our signal or mis-reconstructed. Since branching fractions for $b \to c$ decays are much larger and the charm mesons involved are quite narrow, we suppress their contributions by applying a veto on the reconstructed invariant mass of daughter particles of the charm meson. Backgrounds from other B decays, especially those due to particle misidentification, pose a special challenge. The ΔE and charged-hadron identification variables help in discriminating such backgrounds. The final signal yield is extracted by means of an unbinned maximum likelihood fit to the discriminating variables, $M_{\rm bc}$, ΔE, and continuum suppression variable (in some analyses we have used an optimized and tight requirement on the latter using the expected signal significance from Monte Carlo simulations as a figure of merit). For decays involving narrow or non-zero spin resonances in the final state, we employ the invariant mass and helicity angle distributions to further enhance the sensitivity of our results.

5.1.2. Results on charmless decays. Charmless hadronic B decays can be roughly divided into "two-body", "quasi-two-body (Q2B)", and "three-body" categories. Although two-body decays are easily identifiable by the presence of two long-lived final state particles, such as $K\pi$, the latter two classes of decays are somewhat intertwined. For instance, when one performs the Dalitz plot analysis of a three-body final state, one can access information on related Q2B decays along with the three-body nonresonant decay. The Dalitz plot approach is the most appropriate method when dealing with broad intermediate resonances, e.g., $\rho(770)$. However, if the intermediate resonances are narrow or the resonances decaying to the same final state do not interfere, we can use a Q2B approach where the interference is accounted for as an additional source of systematic error. Since the aforementioned distinction between the two categories is not "black and white", we begin the discussion with two-body decays, then Q2B decays are described together with intermediate resonance final states from three-body Dalitz analyses, and finally we move on to results on three-body nonresonant and inclusive final states.

Two-body decays

B meson decays to two stable hadrons are kinematically easy to identify, having average momenta larger than a typical B decay. The kinematics also provides a good handle on the continuum background. A formidable challenge is posed by the feed-across background arising due to particle misidentification (mostly, kaons misidentified as pions). We tackle this issue by performing a simultaneous fit to the event samples that can cross feed into each other.

Table 10 summarizes the branching fraction and CP asymmetry results for various charmless two-body B decays from Belle. The most notable result here has been the observation

Table 10. Data samples used ($N_{B\overline{B}}$), branching fractions ($\mathcal{B}$), 90% confidence-level upper limits on $\mathcal{B}$ (UL), and direct *CP* asymmetries (A_{CP}) obtained for various charmless two-body B decays. The two uncertainties quoted here and elsewhere are statistical and systematic, respectively.

Final state	$N_{B\overline{B}}(10^6)$	$\mathcal{B}(10^{-6})$	UL (10^{-6})	A_{CP}	Ref.
K^+K^-	772	$0.10 \pm 0.08 \pm 0.04$	0.20		[112]
$K^+\overline{K}^0$	772	$1.11 \pm 0.19 \pm 0.05$		$+0.014 \pm 0.168 \pm 0.002$	[112]
$K^0\overline{K}^0$	772	$1.26 \pm 0.19 \pm 0.05$			[112]
$K^+\pi^-$	772	$20.00 \pm 0.34 \pm 0.60$		$-0.069 \pm 0.014 \pm 0.007$	[112]
$K^+\pi^0$	772	$12.62 \pm 0.31 \pm 0.56$		$+0.043 \pm 0.024 \pm 0.002$	[112]
$K^0\pi^+$	772	$23.97 \pm 0.53 \pm 0.71$		$-0.011 \pm 0.021 \pm 0.006$	[112]
$K^0\pi^0$	772	$9.68 \pm 0.46 \pm 0.50$			[112]
$\pi^+\pi^-$	772	$5.04 \pm 0.21 \pm 0.18$			[112]
$\pi^+\pi^0$	772	$5.86 \pm 0.26 \pm 0.38$		$+0.025 \pm 0.043 \pm 0.007$	[112]
$\pi^0\pi^0$	275	$2.3^{+0.4+0.2}_{-0.5-0.3}$		$+0.44^{+0.53}_{-0.52} \pm 0.17$	[120]
$p\overline{p}$	449		0.41		[121]
$p\overline{\Lambda}$	449		0.49		[121]
$\Lambda\overline{\Lambda}$	449		0.69		[121]

of a non-zero difference of *CP* violation asymmetry in the $B^0 \to K^+\pi^-$ and $B^+ \to K^+\pi^0$ decays: $\Delta A_{K\pi} = A_{CP}(K^+\pi^0) - A_{CP}(K^+\pi^-) = +0.112 \pm 0.027 \pm 0.007$ [112]. This discrepancy, also called the $\Delta A_{K\pi}$ *puzzle*, may be explained either by a large contribution from the color-suppressed tree diagram [105,113] or a new physics contribution in the electroweak penguin [114–118]. Before concluding on this issue, we must improve the uncertainties on *CP* violation results for the decay $B^0 \to K^0\pi^0$. This would allow us to precisely test the prediction of an isospin sum rule [119] given by $A_{CP}(K^+\pi^-) + A_{CP}(K^0\pi^+)\frac{\Gamma(K^0\pi^+)}{\Gamma(K^+\pi^-)} - A_{CP}(K^+\pi^0)\frac{2\Gamma(K^+\pi^0)}{\Gamma(K^+\pi^-)} - A_{CP}(K^0\pi^0)\frac{2\Gamma(K^0\pi^0)}{\Gamma(K^+\pi^-)} = 0$, where Γ is the partial width. Belle's latest update [112] reports a sum of $-0.270 \pm 0.132 \pm 0.060$ with 1.9σ significance.

Quasi-two-body (Q2B) decays

Q2B analyses assume that the intermediate resonances decaying to the same final state (such as $\rho(770)$ and $f_0(980)$ decaying to $\pi^+\pi^-$) do not interfere. This treatment allows us to compare branching fraction results with measurements from earlier experiments, in which the effects of interference were treated as a part of the systematic error. The extent and nature of the background (as most charmless B decays suffer from a low signal-to-background ratio) and of the nonresonant signal component strongly influence our analysis strategy. The helicity angle plays an important role in such Q2B analyses when the intermediate resonances have a non-zero spin; we can use it either as a simple selection criterion or to extract physics observables, such as the fraction of longitudinal polarization f_L, directly from the fit. The helicity angle θ_H for a resonance is defined as the angle between the momentum vector of one of its daughter particles and the direction opposite to the B-meson momentum in the resonance rest frame [122].

In the discussions that follow, the decays have been grouped according to their spin. For each spin grouping, the results for branching fractions, direct *CP* asymmetries, and longitudinal polarization fractions (where applicable) are listed in the accompanying tables. In Table 11 we start with final states comprising at least an η, or η' meson that is reconstructed in the two channels $\eta \to \gamma\gamma$ and

Table 11. Data samples used ($N_{B\overline{B}}$), branching fractions ($\mathcal{B}$), 90% confidence-level upper limits on $\mathcal{B}$ (UL), and direct CP asymmetries (A_{CP}) obtained for various charmless Q2B decays with an η or η' meson in the final state.

Final state	$N_{B\overline{B}}$ (10^6)	$\mathcal{B}$ (10^{-6})	UL (10^{-6})	A_{CP}	Ref.
ηK^+	772	$2.12 \pm 0.23 \pm 0.11$		$-0.38 \pm 0.11 \pm 0.01$	[123]
ηK^0	772	$1.27^{+0.33}_{-0.29} \pm 0.08$			[123]
$\eta\pi^+$	772	$4.07 \pm 0.26 \pm 0.21$		$-0.19 \pm 0.06 \pm 0.01$	[123]
$\eta\pi^0$	152	$1.2 \pm 0.7 \pm 0.1$	2.5		[124]
$\eta\eta$	152	$0.7^{+0.7}_{-0.4} \pm 0.1$	2.0		[124]
$\eta' K^+$	386	$69.2 \pm 2.2 \pm 3.7$		$+0.028 \pm 0.028 \pm 0.021$	[125]
$\eta' K^0$	386	$58.9^{+3.6}_{-3.5} \pm 4.3$			[125]
$\eta'\pi^+$	386	$1.76 \pm 0.67^{+0.62}_{-0.15}0.14$		$+0.20^{+0.37}_{-0.36} \pm 0.04$	[125]
$\eta'\pi^0$	386	$2.79 \pm 1.02^{+0.96}_{-0.25}0.34$			[125]
$\eta'\eta$	535		4.5		[126]
$\eta'\eta'$	535		6.5		[126]
ηK^{*+}	449	$19.3^{+2.0}_{-1.9} \pm 1.5$		$+0.03 \pm 0.10 \pm 0.01$	[127]
ηK^{*0}	449	$15.2 \pm 1.2 \pm 1.0$		$+0.17 \pm 0.08 \pm 0.01$	[127]
$\eta\rho^+$	449	$4.1^{+1.4}_{-1.3} \pm 0.4$	6.5	$-0.04^{+0.34}_{-0.32} \pm 0.01$	[127]
$\eta\rho^0$	449	$0.84^{+0.56}_{-0.51} \pm 0.19$	1.9		[127]
$\eta' K^{*+}$	535		2.9		[126]
$\eta' K^{*0}$	535		2.6		[126]
$\eta'\rho^+$	535		5.8		[126]
$\eta'\rho^0$	535		1.3		[126]
$\eta'\omega$	535		2.2		[126]
$\eta'\phi$	535		0.5		[126]

$\eta \to \pi^+\pi^-\pi^0$, or $\eta' \to \eta\pi^+\pi^-$ and $\eta' \to \rho^0\gamma$, respectively. Among the highlighted results are the first observation of $B^0 \to \eta K^0$, and evidence for direct CP violation in the decays $B^+ \to \eta K^+$ and $B^+ \to \eta\pi^+$ with significances of 3.8σ and 3.0σ, respectively [123]. The latter results call for a large interference between the $b \to s$ penguin process and the CKM-suppressed, color-favored $b \to u$ tree transition, both of which contribute to $B^+ \to \eta h^+$ $(h = K, \pi)$.

The branching fractions and CP asymmetries for other Q2B decays without an η or η' meson in the final state are summarized in Table 12. Most of the results are obtained as a by-product of a three-body Dalitz plot analysis. The systematic uncertainties in the table include the experimental systematic as well as Dalitz-plot model dependence, where applicable. We report the first evidence of CP violation in the Q2B decay $B^+ \to \rho^0 K^+$ exceeding the 3σ level. Note that this was the first evidence for direct CP violation in a charged meson decay, a phenomenon that was already observed in decays of neutral K [137–139] and B [112,140] mesons, and very recently in D^0 decays [141,142].

In Table 13 we present results obtained from the vector–vector final states. One naively expects $B \to VV$ decays to be dominated by longitudinal polarization amplitudes since $f_L = 1 - 4m_V/m_B \sim 0.9$ [149,150], where m_V (m_B) is the mass of the vector (B) meson. Contrary to this expectation, it is found out that the decays dominated by the $b \to s$ penguin transition such as $B \to \phi K^*$ have f_L values closer to 0.5. However, decays proceeding via the $b \to u$ tree diagram, notably $B \to \rho\rho$, follow the expected trend. This so-called *polarization puzzle* could be explained by

Table 12. Data samples used ($N_{B\overline{B}}$), branching fractions ($\mathcal{B}$), 90% confidence-level upper limits on $\mathcal{B}$ (UL), and direct CP asymmetries (A_{CP}) obtained for various charmless Q2B decays without an η or η' meson in the final state.

Final state	$N_{B\overline{B}}$ (10^6)	$\mathcal{B}$ (10^{-6})	UL (10^{-6})	A_{CP}	Ref.
$f_0(980)K^0$	388	$7.6 \pm 1.7^{+0.9}_{-1.3}$			[128]
$f_0(980)K^+$	386	$8.78 \pm 0.82^{+0.85}_{-1.76}$		$-0.077 \pm 0.065^{+0.046}_{-0.026}$	[129]
$f_2(1270)K^+$	386	$1.33 \pm 0.30^{+0.23}_{-0.34}$		$-0.59 \pm 0.22 \pm 0.04$	[129]
$f_2(1270)K^0$	388		2.5		[128]
$K_0^*(1430)^+\pi^-$	388	$49.7 \pm 3.8^{+6.8}_{-8.2}$			[128]
$K_0^*(1430)^0\pi^+$	386	$51.6 \pm 1.7^{+7.0}_{-7.5}$		$+0.076 \pm 0.038^{+0.028}_{-0.022}$	[129]
$K^{*+}\pi^-$	388	$8.4 \pm 1.1^{+1.0}_{-0.9}$		$-0.21 \pm 0.11 \pm 0.07$	[128]
$K^{*0}\pi^+$	386	$9.67 \pm 0.64^{+0.81}_{-0.89}$		$-0.149 \pm 0.064 \pm 0.022$	[129]
$K^{*0}\pi^0$	85	$0.4^{+1.9}_{-1.7} \pm 0.1$	3.5		[130]
ωK^+	388	$8.1 \pm 0.6 \pm 0.6$		$+0.05^{+0.08}_{-0.07} \pm 0.01$	[131]
ωK^0	388	$4.4^{+0.8}_{-0.7} \pm 0.4$			[131]
$\omega\pi^+$	388	$6.9 \pm 0.6 \pm 0.5$		$-0.02 \pm 0.09 \pm 0.01$	[131]
$\omega\pi^0$	388	$0.5^{+0.4}_{-0.3} \pm 0.1$	2.0		[131]
ϕK^+	152	$9.60 \pm 0.92^{+1.05}_{-0.84}$		$+0.01 \pm 0.12 \pm 0.05$	[132]
ϕK^0	85	$9.0^{+2.2}_{-1.8} \pm 0.7$			[133]
$\phi\pi^+$	657	$0.08^{+0.09+0.06}_{-0.08-0.03}$	0.33		[134]
$\phi\pi^0$	657	$-0.07^{+0.06+0.04}_{-0.04-0.08}$	0.15		[134]
$\phi(1680)K^+$	152		0.8		[132]
ρ^-K^+	85	$15.1^{+3.4+2.4}_{-3.3-2.6}$		$+0.22^{+0.22+0.06}_{-0.23-0.02}$	[130]
ρ^0K^+	386	$3.89 \pm 0.47^{+0.43}_{-0.41}$		$+0.30 \pm 0.11^{+0.11}_{-0.05}$	[129]
ρ^0K^0	388	$6.1 \pm 1.0^{+1.1}_{-1.2}$			[128]
$\rho^+\pi^0$	152	$13.2 \pm 2.3^{+1.4}_{-1.9}$		$+0.06 \pm 0.17^{+0.04}_{-0.05}$	[135]
$\rho^0\pi^+$	32	$8.0^{+2.3}_{-2.0} \pm 0.7$			[136]
$\rho^0\pi^0$	449	$3.0 \pm 0.5 \pm 0.7$			[42]
$\rho^\mp\pi^\pm$	449	$22.6 \pm 1.1 \pm 4.4$			[42]

the presence of new particles in the penguin loop [151–156]. However, large SM corrections appear to be a more plausible explanation.

Three-body decays

As was discussed above, the Dalitz-plot method is the most robust analysis technique for a three-body decay, especially for $B \to 3$ pseudoscalars. This method has greater complexity but at the same time provides a better understanding of the underlying physics. A subtle point here is that one needs a good deal of statistics before carrying out a full-fledged Dalitz plot analysis. As the integrated luminosity continued to increase at Belle, starting with measurements of inclusive branching fractions and charge asymmetries, various rare decay analyses slowly evolved into a detailed study of the three-body phase space, e.g., $B^+ \to K^+\pi^+\pi^-$. At times, study of Q2B final states served as an intermediate step. The choice of analysis technique is mostly dictated by the luminosity, expected signal and background, and the understanding of the intermediate resonances involved. Table 14 summarizes results on the branching fraction and CP asymmetry for various decays with three-body mesonic final states.

Table 13. Data samples used ($N_{B\overline{B}}$), branching fractions ($\mathcal{B}$), 90% confidence-level upper limits on $\mathcal{B}$ (UL), longitudinal polarization fraction (f_L), and direct CP asymmetries (A_{CP}) obtained for various charmless Q2B decays with vector–vector final states.

Final state	$N_{B\overline{B}}(10^6)$	$\mathcal{B}(10^{-6})$	UL (10^{-6})	f_L	A_{CP}	Ref.
$K^{*0}K^{*0}$	657		0.2			[143]
$K^{*0}\overline{K}^{*0}$	657	$0.26^{+0.33+0.10}_{-0.29-0.08}$	0.8			[143]
$K^{*0}\rho^+$	275	$8.9 \pm 1.7 \pm 1.2$		$0.43 \pm 0.11^{+0.05}_{-0.02}$		[144]
$K^{*0}\rho^0$	657	$2.1^{+0.8+0.9}_{-0.7-0.5}$	3.4			[145]
ωK^{*0}	657	$1.8 \pm 0.7^{+0.3}_{-0.2}$		$0.56 \pm 0.29^{+0.18}_{-0.08}$		[146]
ϕK^{*+}	85, 257	$6.7^{+2.1+0.7}_{-1.9-1.0}$		$0.52 \pm 0.08 \pm 0.03$	$-0.02 \pm 0.14 \pm 0.03$	[133,147]
ϕK^{*0}	85, 257	$10.0^{+1.6+0.7}_{-1.5-0.8}$		$0.45 \pm 0.05 \pm 0.02$	$+0.02 \pm 0.09 \pm 0.02$	[133,147]
$\rho^+\rho^-$	275	$22.8 \pm 3.8^{+2.3}_{-2.6}$		$0.94^{+0.03}_{-0.04} \pm 0.03$		[45]
$\rho^+\rho^0$	85	$31.7 \pm 7.1^{+3.8}_{-6.7}$		$0.95 \pm 0.11 \pm 0.02$	$+0.00 \pm 0.22 \pm 0.03$	[44]
$\rho^0\rho^0$	657	$0.4 \pm 0.4^{+0.2}_{-0.3}$	1.0			[148]

Table 14. Data samples used ($N_{B\overline{B}}$), branching fractions ($\mathcal{B}$), 90% confidence-level upper limits on $\mathcal{B}$ (UL), and direct CP asymmetries (A_{CP}) obtained for various charmless decays with three-body mesonic final states.

Final state	$N_{B\overline{B}}$ (10^6)	$\mathcal{B}$ (10^{-6})	UL (10^{-6})	A_{CP}	Ref.
$K^+K^+\pi^-$	85		2.4		[157]
$K^+K^-K^+$	152	$30.6 \pm 1.2 \pm 2.3$			[132]
$K^+K^-K^0$	85	$28.3 \pm 3.3 \pm 4.0$			[157]
$K^+K^-\pi^+$	85	$9.3 \pm 2.3 \pm 1.1$	13		[157]
$K^+K^0_SK^0_S$	85	$13.4 \pm 1.9 \pm 1.5$			[157]
$K^+\pi^+\pi^-$ nonres.	386	$16.9 \pm 1.3^{+1.7}_{-1.6}$			[129]
$K^+\pi^+\pi^-$	386	$48.8 \pm 1.1 \pm 3.6$		$+0.049 \pm 0.026 \pm 0.020$	[129]
$K^+\pi^-\pi^0$ nonres.	85	$5.7^{+2.7+0.5}_{-2.5-0.4}$	9.4		[130]
$K^+\pi^-\pi^0$	85	$36.6^{+4.2}_{-4.3} \pm 3.0$		$+0.07 \pm 0.11 \pm 0.01$	[130]
$K^-\pi^+\pi^+$	85		4.5		[157]
$K^0K^-\pi^+$	85		18		[157]
$K^0\pi^+\pi^-$ nonres.	388	$19.9 \pm 2.5^{+1.7}_{-2.0}$			[128]
$K^0\pi^+\pi^-$	388	$47.5 \pm 2.4 \pm 3.7$			[128]
$K^0_SK^0_SK^0_S$	85	$4.2^{+1.6}_{-1.3} \pm 0.8$			[157]
$K^0_SK^0_S\pi^+$	85		3.2		[157]
$\omega K^+\pi^-$ nonres.	657	$5.1 \pm 0.7 \pm 0.7$			[146]
$\phi\phi K^+$	449	$3.2^{+0.6}_{-0.5} \pm 0.3$		$+0.01^{+0.19}_{-0.16} \pm 0.02$	[158]
$\phi\phi K^0$	449	$2.3^{+1.0}_{-0.7} \pm 0.2$			[158]
$\rho^0K^+\pi^-$	657	$2.8 \pm 0.5 \pm 0.5$			[145]
$\rho^0\pi^+\pi^-$	657	$5.9^{+3.5}_{-3.4} \pm 2.7$	12		[148]
$f_0(980)K^+\pi^-$	657	$1.4 \pm 0.4^{+0.3}_{-0.4}$	2.1		[145]
$f_0(980)\pi^+\pi^-$	657	$0.3^{+1.9}_{-1.8} \pm 0.9$	3.8		[148]

A great deal of effort has also been applied to studying charmless three-body baryonic decays. Quite often Belle has reported results before its sister experiment, BaBar, in these kind of studies. In Table 15 we attempt to summarize the results obtained in these baryonic decays. An intriguing

Table 15. Data samples used ($N_{B\overline{B}}$), branching fractions ($\mathcal{B}$), 90% confidence-level upper limits on $\mathcal{B}$ (UL), and direct CP asymmetries (A_{CP}) obtained for various charmless decays with three-body baryonic final states.

Final state	$N_{B\overline{B}}$ (10^6)	$\mathcal{B}$ (10^{-6})	UL (10^{-6})	A_{CP}	Ref.
$p\overline{p}\pi^+$	449	$1.57^{+0.17}_{-0.15} \pm 0.12$		$-0.17 \pm 0.10 \pm 0.02$	[159]
$p\overline{p}K^+$	449	$5.00^{+0.24}_{-0.22} \pm 0.32$		$-0.02 \pm 0.05 \pm 0.02$	[159]
$p\overline{p}K^0$	535	$2.51^{+0.35}_{-0.29} \pm 0.21$			[160]
$p\overline{p}K^{*+}$	535	$3.38^{+0.73}_{-0.60} \pm 0.39$		$-0.01 \pm 0.19 \pm 0.02$	[160]
$p\overline{p}K^{*0}$	535	$1.18^{+0.29}_{-0.25} \pm 0.11$		$-0.08 \pm 0.20 \pm 0.02$	[160]
$p\overline{\Lambda}\pi^0$	449	$3.00^{+0.61}_{-0.53} \pm 0.33$		$+0.01 \pm 0.17 \pm 0.04$	[161]
$p\overline{\Lambda}\pi^-$	449	$3.23^{+0.33}_{-0.29} \pm 0.29$		$-0.02 \pm 0.10 \pm 0.03$	[161]
$p\overline{\Lambda}K^-$	85		0.82		[162]
$p\overline{\Sigma}^0\pi^-$	85	$3.97^{+1.00}_{-0.80} \pm 0.56$			[162]
$\Lambda\overline{\Lambda}\pi^+$	152		2.80		[163]
$\Lambda\overline{\Lambda}K^+$	152	$2.91^{+0.90}_{-0.70} \pm 0.38$			[163]

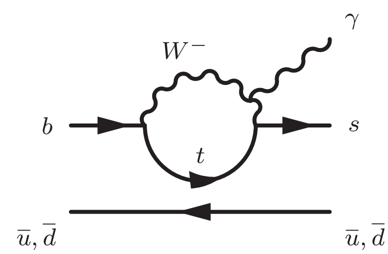

Fig. 26. Feynman diagram for the $b \to s\gamma$ process.

feature of the results is the peaking of baryon–antibaryon pair mass distributions toward threshold. These enhancements have generated much theoretical interest [164–168].

5.2. *Radiative penguin decays*

Decay processes of a b quark that emit a photon are not allowed at the tree level in the SM, and require a so-called radiative "penguin" loop (Fig. 26). The dominant contribution in the SM is from a loop with a top quark and a weak boson. However, these heavy SM particles may be replaced by hypothetical particles such as a charged Higgs boson or supersymmetric particles. In such a scenario, the decay rate or other observables could be drastically modified. Hence, radiative decays have been extensively studied to search for and to constrain physics beyond the SM.

5.2.1. Inclusive $B \to X_s\gamma$ measurement. At the hadron level, the quark-level $b \to s\gamma$ transition is represented by a radiative B meson decay into a high energy photon and an inclusive hadronic final state with a unit strangeness denoted by the symbol X_s. The clean signature of the high energy photon makes it possible to measure the decay rate without reconstructing the X_s. The SM transition rate is calculated including next-to-next-to-leading logarithmic corrections to 7% precision [169].

A large and dominant background to $B \to X_s\gamma$ is from the π^0s (and to a lesser extent η) in the $e^+e^- \to q\overline{q}$ continuum, which subsequently decay into a pair of photons. Although this background is several orders of magnitude larger than the inclusive photon signal, backgrounds that are not from a B meson decay can be statistically subtracted by using the off-resonance data sample taken at

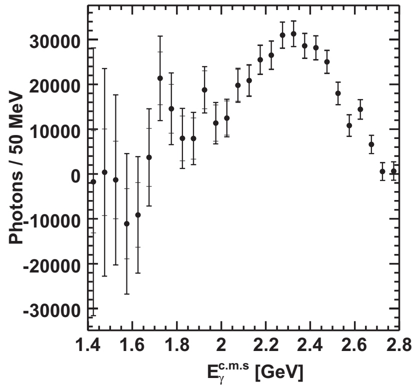

Fig. 27. Photon energy spectrum from $B \to X_s\gamma$.

60 MeV below the $\Upsilon(4S)$ resonance. However, since only 10% of integrated luminosity is taken off-resonance, this continuum background remains the main source of the statistical and systematic error. The remaining backgrounds are from B meson decays, where the photon backgrounds are dominantly (in order of their importance) from the π^0s, ηs, radiative decays of other hadrons, final state radiation and electron bremsstrahlung, and mis-reconstructed K_L^0s and (anti-)neutrons. The inclusive π^0 and η production rate from a B meson is directly measured in data, and used to subtract the corresponding background contribution, while other sub-dominant contributions are subtracted using MC expectations after correcting for the measured data-MC differences. The photon energy spectrum, which is monochromatic if $b \to s\gamma$ is strictly a two-body process, is broadened by QCD corrections and the Fermi motion of the b quark in the B meson [170,171]. The measured spectrum in the $\Upsilon(4S)$ rest frame is further broadened by the small momentum of the B meson and the detector resolution. The branching fraction has to be integrated over the entire photon energy range. It becomes more difficult to do so for lower energies as the signal contribution becomes smaller and the background becomes insurmountably large. It is now customary to compare the extrapolated branching fraction in the range $E_\gamma > 1.6$ GeV to theoretical predictions. Experimental efforts to lower this bound have been the focus of most past $B \to X_s\gamma$ measurements. Using 657×10^6 $B\overline{B}$ events, Belle measured $B \to X_s\gamma$ with $E_\gamma > 1.7$ GeV [172]. This should cover $(98.5 \pm 0.4)\%$ of the spectrum above 1.6 GeV [171]. The spectrum is shown in Fig. 27 and the branching fraction was measured to be

$$\mathcal{B}(B \to X_s\gamma;\ E_\gamma > 1.7\ \text{GeV}) = (3.45 \pm 0.15(\text{stat}) \pm 0.40(\text{syst})) \times 10^{-4}, \tag{5.1}$$

where the errors are statistical and systematic. Together with BaBar's measurement, the world average [38] extrapolated for $E_\gamma > 1.6$ GeV is $\mathcal{B}(B \to X_s\gamma) = (3.55 \pm 0.24(\text{exp}) \pm 0.09(\text{model}) \times 10^{-4}$, where the first error is a combined experimental (statistical and systematic) uncertainty and the second is the model error in the extrapolation. This can be compared with the theory prediction [169] of $\mathcal{B}(B \to X_s\gamma) = (3.15 \pm 0.23) \times 10^{-4}$. The results are consistent, and have been used to constrain new physics scenarios. For example, the charged Higgs mass is bounded to be above 295 GeV.

5.2.2. Exclusive radiative B decays with $b \to s\gamma$. Exclusive radiative B meson decay modes, such as $B \to K^*(892)\gamma$ [173], have been more precisely measured, since one can fully constrain and effectively suppress the background of the decay kinematics using the beam-energy constrained mass (M_{bc}) and the energy difference (ΔE). However, theoretical predictions suffer from large uncertainties in the exclusive form factors, which cannot be reliably determined [174–176].

The $B \to K^*(892)\gamma$ constitutes about 15% of the total $B \to X_s\gamma$ branching fraction. Since the B meson has spin zero and the photon has spin one and is longitudinally polarized, the X_s system cannot be a single kaon (with spin zero), a resonance, or an S-wave $K\pi$ system. Of the higher kaonic resonances, only $B \to K_2^*(1430)\gamma$ [177] and $B \to K_1(1270)\gamma$ [178] have been measured. In particular, higher kaonic resonances around 1.4 GeV have a complicated structure, and among these the $K_1(1270)$ contribution was found to be dominant [179]. In the multi-body final states, many modes have been measured: $B \to K\pi\pi\gamma$ [177], $B \to K\eta\gamma$ [180], $B \to K\eta'\gamma$ [181], $B \to K\rho\gamma$ [177], $B \to K\phi\gamma$ [182], and $B \to \Lambda\overline{p}\gamma$ [183].

One way to reduce the theoretical uncertainty is to take ratios or asymmetries. In particular, the time-dependent CP asymmetry for a radiative decay into a self-conjugate final state has a unique feature. In the SM, the final state, e.g. $K_S^0\pi^0\gamma$, is not a CP eigenstate since the photon is dominantly left-handed from $\overline{B}^0$ (with a b quark) decay and thus does not mix with the decay from B^0 (with a $\overline{b}$ quark) with a right-handed photon. The spin flip is suppressed by the quark mass ratio $2m_s/m_b$ and hence the time-dependent CP asymmetry is also suppressed in the SM to a few per cent [184]. Therefore, this asymmetry in the $b \to s\gamma$ process is sensitive to non-SM right-handed currents.

In $B \to K^*(892)^0\gamma$, the rate to the $K_S^0(\to \pi^+\pi^-)\pi^0\gamma$ final state is only 1/9 of that for $K^+\pi^-\gamma$. The time-dependent asymmetry is measured by extrapolating the K_S^0 momentum from the K_S^0 decay vertex to the interaction region. Therefore, the detection efficiency and statistics of the final signal sample are not large. The coefficient to the sine term is measured with 535×10^6 $B\overline{B}$ to be [185]

$$\mathcal{S}_{K^{*0}\gamma} = -0.32^{+0.36}_{-0.33}(\text{stat}) \pm 0.05(\text{syst}). \tag{5.2}$$

This study can be extended to $B^0 \to P^0Q^0\gamma$, where P^0 and Q^0 are any pseudoscalars [186], or to the $P^0V^0\gamma$ state if the spin parity of the P^0V^0 system is determined. Time-dependent asymmetries have been measured for $K_S^0\pi^0\gamma$, $K_S^0\rho^0\gamma$, and $K_S^0\phi\gamma$ states, although none of them is yet able to constrain the right-handed current. This study is one of the promising modes in the search for physics beyond the SM with the high statistics data samples expected at Belle II.

5.2.3. Radiative B decays with $b \to d\gamma$. The $b \to d\gamma$ penguin loop is suppressed with respect to $b \to s\gamma$ by $|V_{td}/V_{ts}|^2$, and therefore is sensitive to this ratio. It is particularly interesting because a more precise determination of $|V_{td}/V_{ts}|$ was not available until the B_s mixing rate was measured [187] and even after that it provided an independent test of this ratio of CKM parameters.

Since the dominant diagram is suppressed, there are more contributions from subleading diagrams. These could lead to a large direct CP violation or large isospin asymmetry, although they also modify the determination of $|V_{td}/V_{ts}|$. On the other hand, time-dependent asymmetry is expected to be even smaller, since the phase from V_{td} in mixing and $b \to d\gamma$ transition cancel [184,188]. Contributions from non-SM physics can therefore be relatively enhanced and may be more clearly visible than in the $b \to s\gamma$ case.

Because of the similarity of the kinematics, the large $b \to s\gamma$ process is a severe background to the suppressed $b \to d\gamma$ process. In the reconstruction of an exclusive decay mode, particle identification devices are crucial to separate the kaon in $b \to s\gamma$ from the pion in $b \to d\gamma$. Exclusive $b \to d\gamma$ decay modes such as $B \to \rho\gamma$ and $B \to \omega\gamma$ have been searched for since the start of Belle, and were finally observed with 386×10^6 $B\overline{B}$ pairs in a combined measurement [189]. Charged and

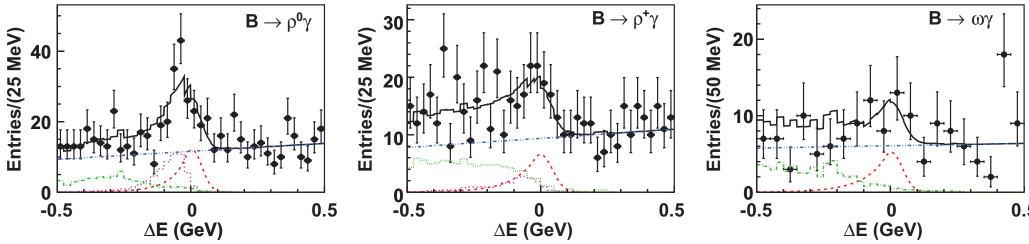

Fig. 28. ΔE distributions of $B^0 \to \rho^0\gamma$ (left), $B^+ \to \rho^+\gamma$ (middle), and $B^0 \to \omega\gamma$ (right).

neutral modes are combined assuming isospin symmetry $\mathcal{B}(B^+ \to \rho^+\gamma) = 2\mathcal{B}(B^0 \to \rho^0\gamma)$ and $\mathcal{B}(B^0 \to \rho^0\gamma) = \mathcal{B}(B^0 \to \omega\gamma)$. The latest result with 657×10^6 $B\overline{B}$ pairs is shown in Fig. 28 and the combined branching fraction is measured to be [190]

$$\mathcal{B}(B \to (\rho, \omega)\gamma) = (1.14 \pm 0.20(\text{stat})^{+0.10}_{-0.12}(\text{syst})) \times 10^{-6}. \tag{5.3}$$

As $B \to \rho\gamma$ is suppressed compared to $B \to K^*\gamma$ by $|V_{td}/V_{ts}|^2$, known kinematic corrections, and less-known form factor ratios and corrections for subleading diagrams, the result is combined with a corresponding analysis on $B \to K^*\gamma$ to constrain $|V_{td}/V_{ts}|$. The result is

$$|V_{td}/V_{ts}| = 0.195^{+0.020}_{-0.019}(\text{exp}) \pm 0.015(\text{theo}), \tag{5.4}$$

where the first error is a combined statistical and systematic uncertainty and the second error is the theory uncertainty on the ratio.

The $B^0 \to \rho^0\gamma$ signal is found to be stronger than $B^+ \to \rho^+\gamma$. This corresponds to a large isospin asymmetry, which is defined as $\Delta(\rho\gamma) = \frac{\tau_{B^0}}{2\tau_{B^+}}\mathcal{B}(B^+ \to \rho^+\gamma)/\mathcal{B}(B^0 \to \rho^0\gamma) - 1$. The isospin asymmetry is calculated as

$$\Delta(\rho\gamma) = -0.48^{+0.21}_{-0.19}(\text{stat})^{+0.08}_{-0.09}(\text{syst}). \tag{5.5}$$

BaBar also measures this ratio and finds the same tendency; the combined isospin asymmetry is $\sim 3\sigma$ away from the SM expectation, which could be at most $\sim$10%. As the statistical error is still large, the high statistics expected at Belle II will be necessary to clarify this tension.

5.3. *Electroweak penguin decays*

The $b \to s(d)l^+l^-$ transitions proceed at lowest order in the SM via Z/γ penguin diagrams or a W box diagram (Fig. 29). The $b \to s(d)\nu_l\overline{\nu}_l$ transitions also proceed through similar diagrams, except for the γ penguin diagram. NP mediated by SUSY particles or a possible fourth generation may contribute to the penguin loop or box diagram and as a result branching fractions and other properties could be modified [191–193]. Such NP contributions may change the Wilson coefficients that parameterize the strength of the short distance interactions. This is similar to $b \to s(d)\gamma$, but has a richer structure. The decay $B \to K^*l^+l^-$ is of particular interest since its large branching fraction facilitates the examination of various observables that are sensitive to NP. For instance, the lepton forward–backward asymmetry (A_{FB}), the K^* polarization (F_L), and the $K^*l^+l^-$ isospin asymmetry (A_I) as functions of dilepton mass squared (q^2) differ from the SM expectations in various NP models [194–197].

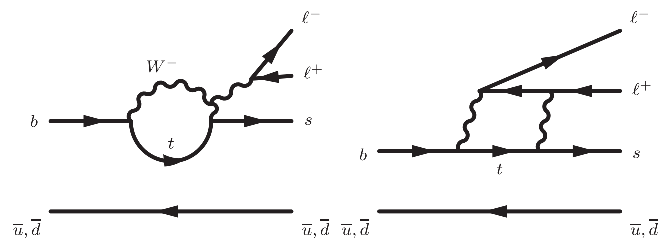

Fig. 29. Feynman diagrams for the $b \to sl^+l^-$ process.

The neutral pure leptonic decays $B^0 \to l^+l^-$ and $B^0 \to \nu_l\overline{\nu}_l$ proceed mainly through the box and Z boson mediated annihilation diagrams, which are equivalent to the diagrams for $b \to dl^+l^-$ and $b \to d\nu_l\overline{\nu}_l$. In the SM these decays are also helicity suppressed and, compared to the charged purely leptonic decays (see Sect. 4.3), the branching fractions are about three orders of magnitude smaller for the corresponding generation [198]. The SM branching fraction of $B^0 \to \nu_l\overline{\nu}_l$ is at the level of 10^{-20} [199]. The lepton-flavor-violating decay $B^0 \to e^\pm\mu^\mp$ is not an electroweak penguin decay and is forbidden in the SM, but can occur in the Pati–Salam model [200] or supersymmetric models [201–203], and can be searched for simultaneously. A positive signal for any of these decay modes with the current Belle data sample would demonstrate NP in the loop.

5.3.1. Exclusive $b \to s(d)\, l^+l^-$ decays. The study of the decay $B \to K^{(*)}l^+l^-$ started at the beginning of Belle and was updated several times. We reported the first observations of $B \to Kl^+l^-$ [204] and $B \to K^*l^+l^-$ [205] with 31.3×10^6 and 152×10^6 $B\overline{B}$ pairs, respectively. In 2006, Belle published the first measurements of the forward–backward asymmetry and the ratios of Wilson coefficients A_9/A_7 and A_{10}/A_7 using $386 \times 10^6 B\overline{B}$ pairs [206]. An unbinned maximum likelihood fit to q^2 and $\cos\theta_l$ was used to extract the ratios of the Wilson coefficients, where θ_l is the angle between the momenta of a negative (positive) lepton and the B ($\overline{B}$) meson in the dilepton rest frame.

The latest analysis in 2008 [207] used 657×10^6 $B\overline{B}$ pairs; more observables were measured. Candidate $B \to K^{(*)}l^+l^-$ decays were reconstructed in 10 channels: $K^+\pi^-$, $K_S^0\pi^+$, $K^+\pi^0$ for K^*, K^+, and K_S^0 for K, with e^+e^- and $\mu^+\mu^-$ lepton pairs. The dilepton mass of each candidate was required to be outside of the J/ψ and $\psi(2S)$ mass regions to avoid the large charmonium background, and above the π^0 mass for e^+e^- pairs to avoid the π^0 Dalitz decay, photon conversion, and the pole at $q^2 = 0$. Two major backgrounds were considered: the continuum and $B\overline{B}$ events in which both B mesons decay semileptonically. These backgrounds were suppressed by imposing requirements on the signal–continuum and signal–$B\overline{B}$ likelihood ratios.

After requiring the candidate ΔE to lie in the signal region, the signal yields in each q^2 bin were extracted from an unbinned likelihood fit to $M_{\rm bc}$ and the $K\pi$ mass ($M_{K\pi}$) for the $K^*l^+l^-$ mode and $M_{\rm bc}$ only for the Kl^+l^- mode. The corresponding branching fractions were thus obtained. The F_L and A_{FB} parameters were extracted from fits to $\cos\theta_{K^*}$ and $\cos\theta_l$ in the signal region, where θ_{K^*} is the angle between the kaon direction and the direction opposite to the B meson in the K^* rest frame. The signal PDFs for the $\cos\theta_{K^*}$ and $\cos\theta_l$ variables are the product of the following two functions,

$$\left[\tfrac{3}{2}F_L\cos^2\theta_{K^*} + \tfrac{4}{3}(1-F_L)(1-\cos^2\theta_{K^*})\right] \times \epsilon(\cos\theta_{K^*})$$

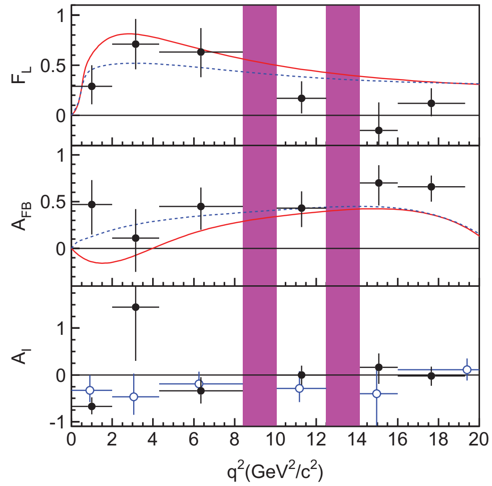

Fig. 30. The q^2 dependence of F_L (top), A_{FB} (middle), and A_I (bottom) in six bins. The results for $B \to K^* l^+ l^-$ are the filled circles and those for $B \to K l^+ l^-$ are open circles (A_I only).

and

$$\left[\tfrac{3}{4} F_L (1 - \cos^2\theta_l) + \tfrac{3}{8}(1 - F_L)(1 + \cos^2\theta_l) + A_{FB}\cos\theta_l\right] \times \epsilon(\cos\theta_l),$$

where $\epsilon(\cos\theta_{K^*})$ and $\epsilon(\cos\theta_l)$ are the reconstruction efficiencies. For the $B \to K l^+ l^-$ modes, F_L is set to 1. Furthermore, this analysis also reported the isospin asymmetry defined as

$$A_I = \frac{(\tau_{B^+}/\tau_{B^0}) \times \mathcal{B}(K^{(*)0} l^+ l^-) - \mathcal{B}(K^{(*)\pm} l^+ l^-)}{(\tau_{B^+}/\tau_{B^0}) \times \mathcal{B}(K^{(*)0} l^+ l^-) + \mathcal{B}(K^{(*)\pm} l^+ l^-)},$$

where τ_{B^+}/τ_{B^0} is the ratio of B^+ to B^0 lifetimes. These observables were measured for the first time in six q^2 bins as shown in Fig. 30. Although the uncertainties in the A_{FB} values are still large, the positive central values in all q^2 bins suggested a non-zero $A_{FB}(q^2)$. This phenomenon would have been an undeniable signature of NP, but unfortunately did not persist with larger data samples at the LHC hadron collider [208]. Two more observables, the direct CP-violating asymmetry and the lepton flavor ratio of the muon to electron modes, were also measured. The latter is sensitive to Higgs emission and could be larger than the SM expectation in the two Higgs doublet model at large $\tan\beta$ [209].

The observed values are $A_{CP}(K^* l^+ l^-) = -0.10 \pm 0.10 \pm 0.01$ and $A_{CP}(K l^+ l^-) = 0.04 \pm 0.10 \pm 0.02$, consistent with no asymmetry, and $R_{K^*} = 0.83 \pm 0.18 \pm 0.08$ and $R_K = 1.03 \pm 0.19 \pm 0.06$, similar to the SM values. The measurements of so many observables demonstrate the richness and potential of the $B \to K^{(*)} l^+ l^-$ decay.

A search for the exclusive $b \to d l^+ l^-$ process, $B \to \pi l^+ l^-$ ($\pi = \pi^+$ or π^0), was performed using $657 \times 10^6 B\overline{B}$ pairs [210]. No obvious signal was observed and upper limits on the branching fractions at the 90% C.L. were obtained: $\mathcal{B}(B^+ \to \pi^+ l^+ l^-) < 4.9 \times 10^{-8}$ and $\mathcal{B}(B^0 \to \pi^0 l^+ l^-) < 15.4 \times 10^{-8}$. These limits are approaching the SM expectations, which are $O(10^{-8})$.

5.3.2. Inclusive $B \to X_s l^+ l^-$ decay. The inclusive measurement of the $b \to s l^+ l^-$ process is experimentally challenging, but can be compared with theoretically clean predictions. The standard technique is to analyze $B \to X_s l^+ l^-$ events with a semi-inclusive approach, where the X_s is reconstructed in 18 different combinations of either a K^+ or K_S^0 combined with 0 to 4 pions, of which up to one π^0 is allowed. This set of final states covers around 62% of X_s decay states. The missing states were taken into account in the signal efficiency obtained from MC simulations.

The first observation of $B \to X_s l^+ l^-$ was reported by Belle using 65.4×10^6 $B\overline{B}$ pairs in 2003 [211]. The latest Belle results in 2009 used 657×10^6 $B\overline{B}$ pairs [212]. As in the exclusive analysis, signal candidates were selected with ΔE and then the $M_{\rm bc}$ distribution is used to extract the signal yield. The dilepton mass was required to be outside of the J/ψ and $\psi(2S)$ regions and the low mass region below $0.2\,{\rm GeV}/c^2$. The signal yields were extracted from an unbinned maximum likelihood fit to the $M_{\rm bc}$ distribution. In addition to the dominant backgrounds from $B\overline{B}$ pairs and continuum, an effort was made to investigate the peaking background and include it in the fit. Two kinds of peaking background were considered: charmonium peaking background and hadronic peaking background. The former includes the residual of $B \to J/\psi X_s$, $B \to \psi(2S) X_s$ events after the J/ψ and $\psi(2S)$ vetoes, and a possible contribution from higher ψ resonances, such as the $\psi(3770)$, $\psi(4140)$, and $\psi(4160)$. The hadronic peaking background contains $B \to X_s hh$ and $B \to X_s h l \nu$ events in which one or two hadrons are misidentified as leptons. The peaking backgrounds were estimated directly from data or simulations and the corresponding yields were fixed in the fit. Finally, the last component considered is the self-cross-feed background, in which the B daughter particles are not correctly selected. Its probability density function was modeled as a histogram with the ratio of the normalization of the self-cross-feed background to signal fixed to the MC simulation value in the fit. The probability density function for the dominant background was modeled by an ARGUS function with the parameters floated in the fit. A simultaneous fit to the $X_s l^+ l^-$ and $X_s e^\pm \mu^\mp$ samples was performed with the same ARGUS parameters for the dominant background.

The branching fractions of $B \to X_s l^+ l^-$ were reported as a function of M_{X_s} and q^2 separately. Fit results for the total sample and a subset with $M_{X_s} > 1.0\,{\rm GeV}/c^2$ are shown in the top two plots of Fig. 31, and the differential branching fractions as functions of M_{X_s} and q^2 are shown in the bottom two plots. The differential distributions are compared with the SM expectation[3], and found to be in good agreement. The branching fraction of $B \to X_s l^+ l^-$ in the entire M_{X_s} range was obtained by summing the branching fraction in each M_{X_s} region and correcting for the $X_s l^+ l^-$ fraction in the J/ψ, $\psi(2S)$, and $M_{X_s} > 2.0\,{\rm GeV}/c^2$ regions. The branching fraction with the dilepton mass above $0.2\,{\rm GeV}/c^2$ is thus measured to be $\mathcal{B}(B \to X_s l^+ l^-) = (3.33 \pm 0.80^{+0.19}_{-0.24}) \times 10^{-6}$. We also reported the branching fractions separately for the electron and muon modes using the same analysis procedure, $\mathcal{B}(B \to X_s e^+ e^-) = (4.56 \pm 1.15^{+0.33}_{-0.40}) \times 10^{-6}$ and $\mathcal{B}(B \to X_s \mu^+ \mu^-) = (1.91 \pm 1.02^{+0.16}_{-0.18}) \times 10^{-6}$.

5.3.3. Searches for B^0 decays to invisible final states. Searches for B^0 decays to invisible final states are rather challenging. The same strategy used in the $B^+ \to \tau^+ \nu_\tau$ analysis was applied to identify the signal (Sect. 4.4.2). Candidate events were selected by fully reconstructing a B^0 meson and requiring no additional charged, π^0, or K_L^0 particles in the rest of the event. The signal can

[3] The exclusive $K^{(*)} l^+ l^-$ was modeled according to Refs. [195,213], while nonresonant $X_s l^+ l^-$ with X_s mass above $1.0\,{\rm GeV}/c^2$ was based on a model described by Refs. [195,214] and the Fermi motion model [215, 216], followed by JETSET [217] to hadronize the system with a strange quark and a spectator quark.

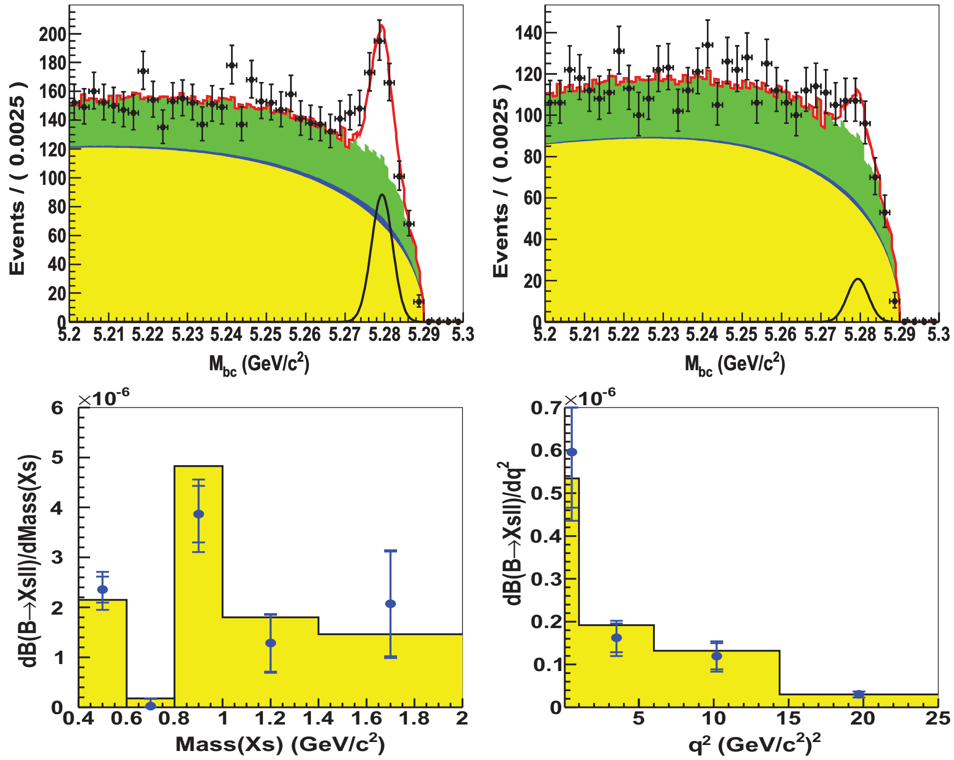

Fig. 31. The top two plots show the M_{bc} distributions with the fit curves superimposed for the entire sample (left) and for $1.0\ \mathrm{GeV}/c^2 < M_{X_s} < 2.0\ \mathrm{GeV}/c^2$ (right). Points with error bars are data; the dominant background, peaking background, and self-cross-feed components are the yellow, green, and blue solid shaded areas, respectively. The bottom plots show the $d\mathcal{B}/dM_{X_s}$ (left) and $d\mathcal{B}/dq^2$ (right) distributions for data (points) and the SM expectation (histograms).

be identified by requiring no or very little extra calorimeter energy (E_{ECL}) in the event. Furthermore, two variables were used to distinguish the signal and the continuum background: $\cos\theta_B$ and $\cos\theta_T$, where the latter is the cosine of the angle of the B_{tag} thrust axis with respect to the beam axis in the CM frame. The continuum was suppressed by making requirements on $\cos\theta_T$ and $\cos\theta_B$.

The signal yield was extracted from an unbinned extended likelihood fit to E_{ECL} and $\cos\theta_B$. Candidate events in the fit were categorized as signal, $B\overline{B}$, and non-B backgrounds, where the latter includes the continuum and a small $e^+e^- \to \tau^+\tau^-$ background. Using a sample of 657×10^6 $B\overline{B}$ pairs, the signal yield obtained in the fit was $8.9^{+6.3}_{-5.5}$ events. Since no significant signal was observed, we provide the branching fraction upper limit including systematics at the 90% C.L. of $\mathcal{B}(B^0 \to \text{invisible}) < 1.3 \times 10^{-4}$ [218]. The expected upper limit from the MC study is 1.1×10^{-4}.

5.3.4. Search for $B^0 \to l^+l^-$. The results of searches for the decays $B^0 \to e^+e^-$, $\mu^+\mu^-$ and $e^\pm\mu^\mp$ (collectively denoted by $B^0 \to l^+l^-$) were reported at the beginning of Belle using only 85×10^6 $B\bar{B}$ pairs [219]. Since the background for the two energetic leptons is relatively small, the Belle analysis was able to suppress the background effectively while maintaining a high reconstruction efficiency. After all the selection criteria, no events were found in any of the three modes [219]. The upper limits are: $\mathcal{B}(B^0 \to e^+e^-) < 1.9 \times 10^{-7}$, $\mathcal{B}(B^0 \to \mu^+\mu^-) < 1.6 \times 10^{-7}$, and $\mathcal{B}(B^0 \to e^\pm\mu^\mp) < 1.7 \times 10^{-7}$. Furthermore, a lower bound on the mass of the Pati–Salam leptoquark model of 46 TeV/c^2 was obtained using the upper limit for the $e\mu$ mode.

6. Tau physics

The tau lepton is an extremely convenient probe to search for NP beyond the SM because of the well-understood mechanisms that govern its production and decay in electroweak interactions. With its large mass, it is the only lepton that can decay into hadrons, thus providing a clean environment to study QCD effects in the 1 GeV energy region. Tau physics at Belle is categorized by two themes; NP searches and SM precision measurements. To probe NP, we search for lepton-flavor violating (LFV) decays, CPV in the charged lepton sector, and the electric dipole moment (EDM) of the tau lepton. For SM precision measurements, we measure the τ lepton mass, the branching fractions of various hadronic decay modes, and their invariant mass distributions. In this section, we summarize the results obtained from the world's largest data sample (about 10^9 $\tau^+\tau^-$ pairs) accumulated at the Belle experiment.

6.1. New physics searches

6.1.1. Tau lepton flavor violation. An observation of LFV would be a clear signature of NP since LFV in charged leptons has a negligibly small probability in the SM, $O(10^{-54}) - O(10^{-52})$, even if neutrino oscillations are taken into account [220–222]. Since the τ is the most massive charged lepton, it has many possible LFV decay modes. Belle has examined as many decay modes as possible in the LFV searches, since the specific mechanisms of NP are unknown.

Models including supersymmetry (SUSY), which is the most popular scenario beyond the SM, can naturally induce LFV at one loop. In many SUSY models, including see-saw extensions and grand unified theories, $\tau \to \mu\gamma$ is expected to have the largest branching fraction of all the possible τ LFV decays. In some cases, however, such as the Higgs-mediated scenario, τ decay into $\mu\eta$ or $\mu\mu\mu$ can become more probable. By measuring the branching fractions for various τ LFV decays, one may be able to determine the NP model favored by nature. Among the various modes studied in Belle, we focus here on three possibilities, $\tau \to \ell\gamma$, $\ell\ell'\ell''$, and ℓP^0, where ℓ stands for e or μ and P^0 is π^0, η, or η'.

In an LFV analysis, in order to evaluate the signal yield, two independent variables are used: the reconstructed mass of the signal and the difference between the sum of energies of the signal τ daughters and the beam energy (ΔE) in the CM frame. In the $\tau \to \mu\gamma$ case, these variables are defined as

$$M_{\mu\gamma} = \sqrt{E_{\mu\gamma}^2 - P_{\mu\gamma}^2}, \tag{6.1}$$

$$\Delta E = E_{\mu\gamma}^{\mathrm{CM}} - E_{\mathrm{beam}}^{\mathrm{CM}}, \tag{6.2}$$

where $E_{\mu\gamma}$ and $P_{\mu\gamma}$ are the sum of the energies and the magnitude of the vector sum of the momenta for the μ and the γ, respectively. The superscript CM indicates that the variable is defined in the CM frame, e.g. $E_{\mathrm{beam}}^{\mathrm{CM}}$ is the beam energy in the CM frame. For signal, $M_{\mu\gamma}$ and ΔE should be in the vicinity of $M_{\mu\gamma} \sim m_\tau$ and $\Delta E \sim 0$ (GeV), while for the background, $M_{\mu\gamma}$ and ΔE will smoothly vary without any special peaking structure. Taking into account the resolution of the detector and the correlation between $M_{\mu\gamma}$ and ΔE, we use an elliptical signal region. To avoid bias, we perform a blind analysis: the data in the signal region are blinded when determining the selection criteria and the systematic uncertainties. After fixing these quantities, we open the blind and evaluate the number of signal events in the signal region.

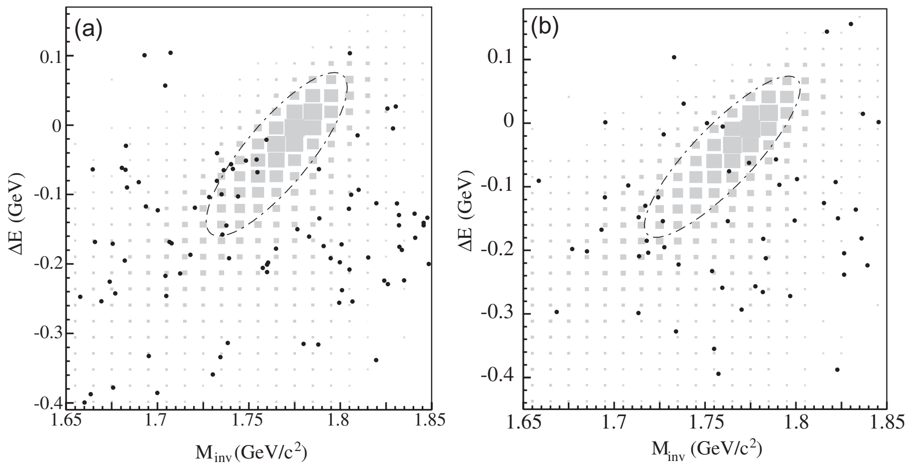

Fig. 32. $M_{\mu\gamma}$–ΔE distributions in the search for (a) $\tau \to \mu\gamma$ and (b) $\tau \to e\gamma$ [223]. The black dots and shaded boxes show the data and signal MC, respectively, and the ellipse is the 2σ signal region.

$\tau \to \ell\gamma$

We have searched for $\tau \to \ell\gamma$ with a data set corresponding to produced 4.9×10^8 $\tau^+\tau^-$ pairs [223]. The main background (BG) is from $\tau \to \ell\nu_\ell\nu_\tau$ + extra γ events and radiative di-muon (for $\mu\gamma$) or Bhabha (for $e\gamma$) events. The observed $M_{\mu\gamma}$–ΔE distributions are shown in Figs. 32(a) and (b) for $\tau \to \mu\gamma$ and $\tau \to e\gamma$, respectively. The signal yield is evaluated from an extended unbinned maximum-likelihood fit to the $M_{\mu\gamma}$–ΔE distribution. We found no excess in the signal region. We thus obtain an upper limit on the branching fraction for $\tau \to \mu\gamma$ $(e\gamma)$ of 4.5×10^{-8} (1.2×10^{-7}) at 90% C.L.

$\tau \to \ell\ell'\ell''$

The decays $\tau \to \ell\ell'\ell''$ have been searched for with nearly the entire data sample of 7.2×10^8 $\tau^+\tau^-$ pairs obtained by Belle [224]. Figures 33(a) and (b) show the three-lepton invariant mass versus ΔE ($M_{\ell\ell\ell}$–ΔE) distributions for the $\tau^- \to e^-e^+e^-$ and $\tau^- \to \mu^-\mu^+\mu^-$ candidates after selection, respectively. No events in the signal region have been found in any of the six modes; the 90% C.L. upper limits on the branching fractions in units of 10^{-8} are given in Table 16. The obtained upper limits are two or three times more restrictive than those obtained previously [225,226].

$\tau \to \ell P^0$ ($P^0 = \pi^0, \eta, \eta'$)

Early Belle results on the search for the τ decays into a lepton and a neutral pseudoscalar (π^0, η, η'), were based on a data sample of 3.6×10^8 $\tau^+\tau^-$ pairs; the resulting upper limits were in the range $(0.8 - 2.4) \times 10^{-7}$ at 90% C.L. [227]. Recently, we have updated the results with a data set two times larger. By studying the backgrounds in detail, we obtain on average about 1.5 times higher efficiency than in our previous study while maintaining a background level in the signal region of less than one event in all modes. The results are summarized in Table 17. A single event is found in $\tau \to e\eta(\to \gamma\gamma)$ while no events are observed in other modes. The obtained 90% C.L. ULs on the branching fraction are in the range $(2.2 - 4.4) \times 10^{-8}$.

In total, Belle has completed searches for 46 lepton-flavor-violating τ decay modes using nearly the entire data sample of 1000 fb^{-1} except for the ongoing analysis of the $\ell\gamma$ modes. No evidence for LFV decays has been observed in any of the modes studied and we set 90% C.L. ULs on the

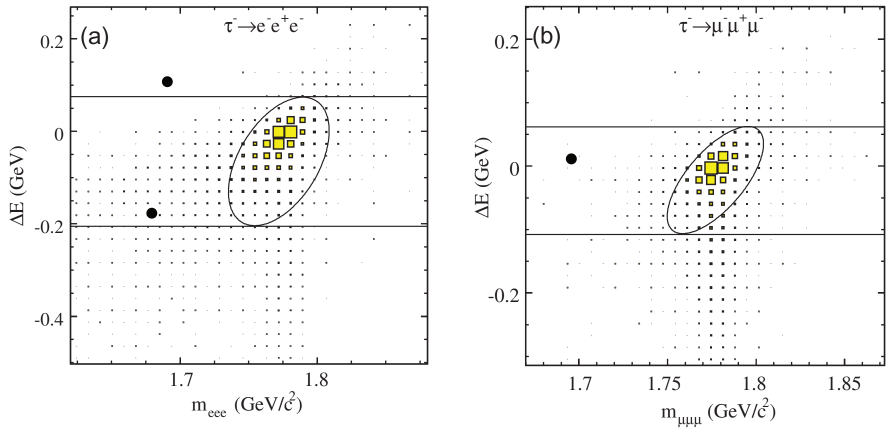

Fig. 33. $M_{\ell\ell\ell}$–ΔE distributions for (a) $\tau^- \to e^-e^+e^-$ and (b) $\tau^- \to \mu^-\mu^+\mu^-$ modes [224]. The black dots and shaded boxes show the data and signal MC, respectively. The ellipse is the signal region. The region formed by the two parallel lines, excluding the signal ellipse region, is the side-band region used to evaluate the expected number of backgrounds in the signal region.

Table 16. Summary of the efficiency (Eff.), the expected number of BG events ($N_{BG}^{\rm exp}$), and the upper limit on the branching fraction (UL) at 90% C.L. for $\tau^- \to \ell^-\ell'^+\ell''^-$.

Mode	Eff. (%)	$N_{BG}^{\rm exp}$	UL (10^{-8})	Mode	Eff. (%)	$N_{BG}^{\rm exp}$	UL (10^{-8})
$e^-e^+e^-$	6.0	0.21 ± 0.15	2.7	$e^-\mu^+\mu^-$	6.1	0.10 ± 0.04	2.7
$e^-e^+\mu^-$	9.3	0.04 ± 0.04	1.8	$\mu^-e^+\mu^-$	10.1	0.02 ± 0.02	1.7
$e^-\mu^+e^-$	11.5	0.01 ± 0.01	1.5	$\mu^-\mu^+\mu^-$	7.6	0.13 ± 0.06	2.1

Table 17. Summary of the efficiency (Eff.), the expected number of BG events ($N_{BG}^{\rm exp}$), and the upper limit on the branching fraction (UL) for $\tau \to \ell P^0$, where (comb.) means the combined result from subdecay modes.

Mode	Eff. (%)	$N_{BG}^{\rm exp}$	UL (10^{-8})	Mode	Eff. (%)	$N_{BG}^{\rm exp}$	UL (10^{-8})
$\mu\eta(\to\gamma\gamma)$	8.2	0.63 ± 0.37	3.6	$e\eta(\to\gamma\gamma)$	7.0	0.66 ± 0.38	8.2
$\mu\eta(\to\pi\pi\pi^0)$	6.9	0.23 ± 0.23	8.6	$e\eta(\to\pi\pi\pi^0)$	6.3	0.69 ± 0.40	8.1
$\mu\eta$(comb.)			2.3	$e\eta$(comb.)			4.4
$\mu\eta'(\to\pi\pi\eta)$	8.1	$0.00^{+0.16}_{-0.00}$	10.0	$e\eta'(\to\pi\pi\eta)$	7.3	0.63 ± 0.45	9.4
$\mu\eta'(\to\gamma\rho^0)$	6.2	0.59 ± 0.41	6.6	$e\eta'(\to\gamma\rho^0)$	7.5	0.29 ± 0.29	6.8
$\mu\eta'$(comb.)			3.8	$e\eta'$(comb.)			3.6
$\mu\pi^0$	4.2	0.64 ± 0.32	2.7	$e\pi^0$	4.7	0.89 ± 0.40	2.2

branching fractions at the $O(10^{-8})$ level. The current status of τ LFV searches in B-factory experiments and in the CLEO experiment is summarized in Fig. 34. The sensitivity for LFV searches has been improved by two orders of magnitude in comparison with the CLEO results. This is due to the effective background rejection as well as the increase in the size of the data sample. In the near future, SuperKEKB/Belle II at KEK will reach a sensitivity at the $O(10^{-9})$–$O(10^{-10})$ level and explore a wider region of parameters in various NP scenarios.

6.1.2. CP-violating τ decays. To date CPV has been observed only in the K and B meson systems. In the SM, all observed CPV effects can be explained by a single irreducible complex phase in the CKM quark mixing matrix. It is important to look for other CP-violating effects where SM CPV is not expected in order to find NP. One such system is the τ lepton. In hadronic τ decays, no

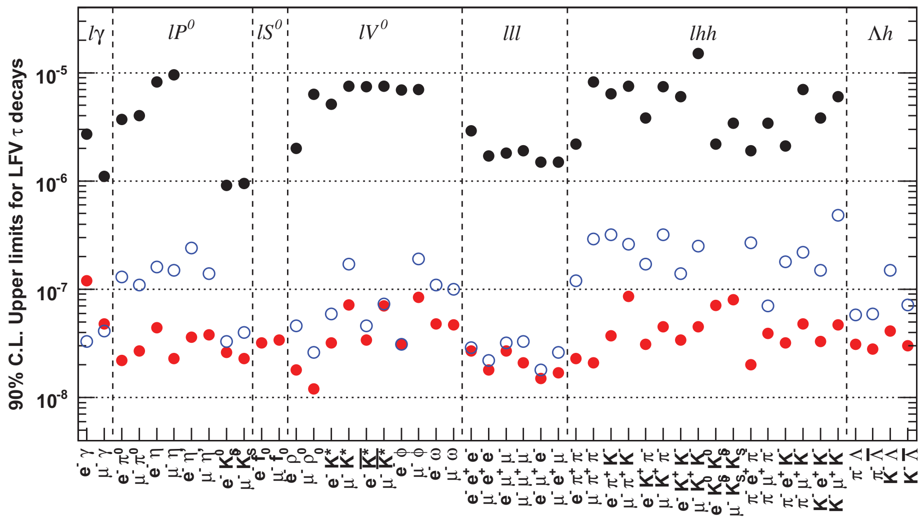

Fig. 34. Current 90% C.L. upper limits for the branching fraction of τ LFV decays obtained in the CLEO, BaBar, and Belle experiments. Red, blue, and black circles show Belle, BaBar, and CLEO results, respectively.

CP-violating effects from the SM are expected except for cases in which the decay products contain K_S^0 mesons. In other words, the τ decay is an ideal place to look for other CP-violating effects that could originate from new physics scenarios, such as the minimal supersymmetric model [228,229] or from multi-Higgs-doublet models [230].

If there is a CP-violating NP amplitude in a τ decay, interference between the SM and NP amplitudes should occur. Even in this case, as was emphasized by J.H. Kühn and E. Mirkes [231], one cannot observe the CPV effects as a difference of the total decay rates between τ^- and τ^+, but instead one needs to measure the difference between the decay-angular distributions of the hadronic system for τ^- and τ^+. The analysis of the decay-angular distribution is therefore crucial.

We searched for CP violation in $\tau^\pm \to K_S^0\pi^\pm\nu_\tau$ using a 699 fb^{-1} data sample [232]. In order to search for CP violation in the angular distribution, we define the CP asymmetry observable as the difference between the mean value of the product of the decay angles $\cos\beta\cos\phi$ in the $K_S^0\pi^\pm$ system for τ^- and τ^+:

$$A^{\mathrm{CP}} = \langle \cos\beta \cdot \cos\psi \rangle_{\tau^-} - \langle \cos\beta \cdot \cos\psi \rangle_{\tau^+},$$

where β (ψ) is the angle between the direction of the K_S^0 (τ) and the direction of the e^+e^- CM system measured in the $K_S^0\pi^\pm$ rest frame.

We obtain 3.2×10^5 $\tau^\pm \to K_S^0\pi^\pm\nu_\tau$ candidates. The $K_S^0\pi^\pm$ invariant mass distribution shown in Fig. 35 clearly indicates that, in addition to the $K^*(890)$ resonance, other resonant contributions are also needed to explain the full spectrum (see Sect. 6.2.3 for more details). The measured CP asymmetry A^{CP} is shown in Fig. 36 as a function of $K_S^0\pi^\pm$ invariant mass after correcting for known detector effects. The result indicates that there is no CP asymmetry at the 1% level. Then we obtain the upper limit for the CP-violating scalar coupling constant η_s [232] to be

$$|\mathrm{Im}(\eta_s)| < (0.012 - 0.026),$$

at the 90% C.L. Our study achieved ten times higher sensitivity than the previous CLEO results shown by the inverted red triangles in Fig. 36.

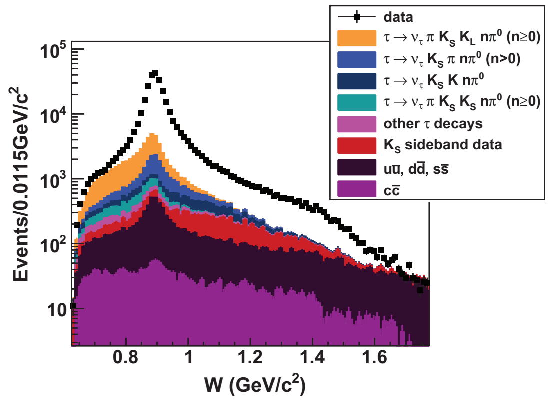

Fig. 35. Invariant mass spectrum of the $K_S^0\pi^\pm$ system in $\tau \to K_S^0\pi^\pm\nu_\tau$ candidates [232].

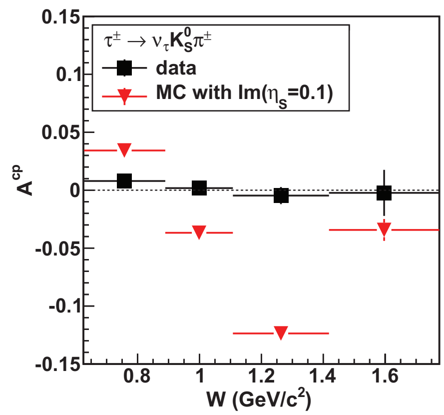

Fig. 36. Measured CP-violating asymmetry A^{CP} as a function of the $K_S^0\pi^\pm$ invariant mass W after subtraction of background (black squares) [232]. The inverted red triangles show the expected asymmetry when $\Im(\eta_S) = 0.1$. Note that the previous CLEO result [233] corresponds to $\Im(\eta_S) \le 0.19$.

6.1.3. Tau electric dipole moment. If an elementary particle has a non-zero electric dipole moment (EDM), this is a clear indication of violation of the T-reversal symmetry and thus violation of CP invariance according to the CPT theorem. The current limit for the τ EDM (d_τ) is several orders of magnitude less restrictive than that for the electron, muon, or neutron. Measurement of d_τ is difficult because of τ's short lifetime. However, improvements in sensitivity are interesting both theoretically and experimentally. As explained below, one can measure the τ EDM by using the correlation of decay product momenta in the process $e^+e^- \to \tau^+\tau^-$.

The matrix element for the process $e^+e^- \to \tau^+\tau^-$, is given by the sum of the SM term $\mathcal{M}^2_{\mathrm{SM}}$, the EDM term $|d_\tau|^2\mathcal{M}^2_{d^2}$, and the interference between them:

$$\mathcal{M}^2 = \mathcal{M}^2_{\mathrm{SM}} + \mathrm{Re}(d_\tau)\mathcal{M}^2_{\mathrm{Re}} + \mathrm{Im}(d_\tau)\mathcal{M}^2_{\mathrm{Im}} + |d_\tau|^2\mathcal{M}^2_{d^2},$$

where $\mathrm{Re}(d_\tau)$ ($\mathrm{Im}(d_\tau)$) is the real (imaginary) part of the EDM. These interference terms $\mathcal{M}^2_{\mathrm{Re/Im}}$ contain the following combination of spin-momentum correlations:

$$\mathcal{M}^2_{\mathrm{Re}} \propto (\boldsymbol{S}_+ \times \boldsymbol{S}_-)\cdot\hat{\boldsymbol{k}}, \quad (\boldsymbol{S}_+ \times \boldsymbol{S}_-)\cdot\hat{\boldsymbol{p}},$$
$$\mathcal{M}^2_{\mathrm{Im}} \propto (\boldsymbol{S}_+ - \boldsymbol{S}_-)\cdot\hat{\boldsymbol{k}}, \quad (\boldsymbol{S}_+ - \boldsymbol{S}_-)\cdot\hat{\boldsymbol{p}},$$

where $\boldsymbol{S}_\pm$ is a $\tau^\pm$ spin vector, and $\hat{\boldsymbol{k}}$ and $\hat{\boldsymbol{p}}$ are the unit vectors of the τ^- and e^- momenta in the CM system, respectively. These terms are CP-odd since they change sign under a CP transformation.

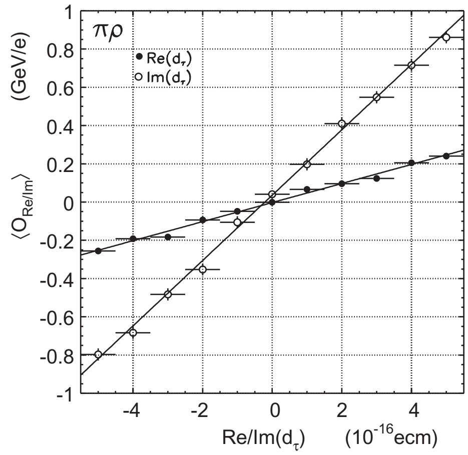

Fig. 37. Correlation between the τ EDM and the optimal observable obtained by MC simulation for $\tau^+\tau^- \to (\pi\nu_\tau)(\rho\nu_\tau)$ [235]. Black dots and circles indicate the relations for the real and imaginary parts, respectively.

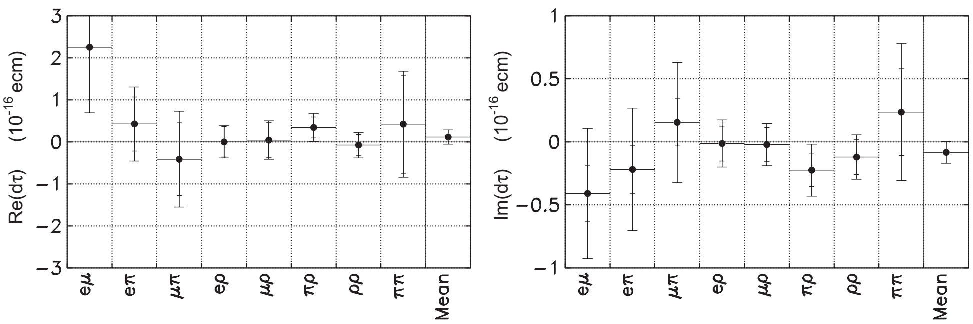

Fig. 38. Results on the τ EDM for 8 modes and the weighted mean for the (a) real and (b) imaginary parts.

One could evaluate the value of the matrix elements if the values of $\boldsymbol{S}_\pm$ and $\hat{\boldsymbol{k}}$ could be measured on an event-by-event basis from the τ-decay products. Although one cannot know them completely due to missing neutrinos from τ decays, one can obtain the most probable values of $\boldsymbol{S}_\pm$ and $\hat{\boldsymbol{k}}$ by calculating approximate averages from measurements of the momenta of τ decay products. In the analysis, we employ the method of optimal observables [234]. In this method, the observables $\mathcal{O}_{\text{Re}}$ and $\mathcal{O}_{\text{Im}}$ are

$$\mathcal{O}_{\text{Re}} = \frac{\mathcal{M}^2_{\text{Re}}}{\mathcal{M}^2_{\text{SM}}}, \quad \mathcal{O}_{\text{Im}} = \frac{\mathcal{M}^2_{\text{Im}}}{\mathcal{M}^2_{\text{SM}}},$$

evaluated using the most probable values of $\boldsymbol{S}_\pm$ and $\hat{\boldsymbol{k}}$. The means of $\mathcal{O}_{\text{Re}}$, $\mathcal{O}_{\text{Im}}$ are proportional to the EDM value and have maximal sensitivity. The relation between the mean values and the EDM d^τ is shown in Fig. 37 for the $\tau^+\tau^- \to (\pi\nu_\tau)(\rho\nu_\tau)$ mode.

We carried out the EDM analysis with a $29.5\,\text{fb}^{-1}$ data sample collected by the Belle detector [235]. In order to obtain the maximal sensitivity, we measured the EDM in 8 modes, $\tau^+\tau^- \to (e\nu_e\nu_\tau)(\mu\nu_\mu\nu_\tau)$, $(e\nu_e\nu_\tau)(\pi\nu_\tau)$, $(\mu\nu_\mu\nu_\tau)(\pi\nu_\tau)$, $(e\nu_e\nu_\tau)(\rho\nu_\tau)$, $(\mu\nu_\mu\nu_\tau)(\rho\nu_\tau)$, $(\pi\nu_\tau)(\pi\nu_\tau)$, $(\pi\nu_\tau)(\rho\nu_\tau)$, and $(\rho\nu_\tau)(\rho\nu_\tau)$. The values of EDM obtained from the mean values of the optimal observables are shown in Fig. 38. All results are consistent with zero EDM.

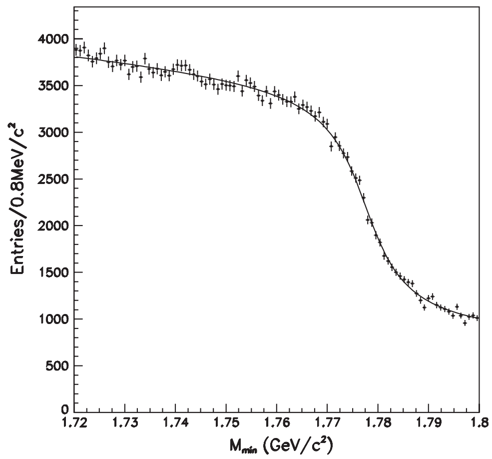

Fig. 39. Pseudomass distribution $M_{\min}$ for $\tau^{\pm} \to 3\pi^{\pm}\nu_{\tau}$ candidates [236].

We obtain mean values for $\mathrm{Re}(d_\tau)$ and $\mathrm{Im}(d_\tau)$ by taking the weighted mean of 8 modes to be

$$\mathrm{Re}(d_\tau) = (1.15 \pm 1.70) \times 10^{-17} e\mathrm{cm}, \quad \mathrm{Im}(d_\tau) = (-0.83 \pm 0.86) \times 10^{-17} e\mathrm{cm}.$$

The 95% C.L. intervals are

$$-2.2 \times 10^{-17} < \mathrm{Re}(d_\tau) < 4.5 \times 10^{-17} e\mathrm{cm}, \quad -2.5 \times 10^{-17} < \mathrm{Im}(d_\tau) < 0.8 \times 10^{-17} e\mathrm{cm}.$$

These limits are ten times more restrictive than previous experiments.

6.2. Precision measurements

6.2.1. Tau lepton mass. A precise measurement of the τ lepton mass is very important to test electroweak theory and lepton universality, since the decay width is proportional to the τ lepton mass to the fifth power. For a long time the world average for the tau mass was dominated by a single precise measurement carried out at the e^+e^- threshold by the BES experiment in 1996.

Belle measured [236] the τ mass by using a pseudomass method and showed that a precision similar to that obtained in the threshold region can be obtained with completely different systematic errors. Figure 39 shows the pseudomass distribution obtained by Belle, where a few hundred thousand $\tau^{\pm} \to \pi^{\pm}\pi^{-}\pi^{+}\nu_{\tau}$ events are used. The pseudomass is defined by

$$M_{\min} = \sqrt{M_x^2 + 2(E_{\mathrm{beam}} - E_x)(E_x - P_x)},$$

where M_x, P_x, E_x are the mass, absolute momentum, and energy of the 3π system, respectively. We obtain

$$m_\tau = (1776.61 \pm 0.13(\mathrm{stat}) \pm 0.35(\mathrm{syst})\mathrm{MeV}/c^2$$

for the τ mass and

$$|m_{\tau^+} - m_{\tau^-}|/m_\tau < 2.8 \times 10^{-4} \quad \text{at 90\% C.L.},$$

the most stringent limit for the relative mass difference between positive and negative τ leptons.

Measurements with a similar precision were subsequently carried out by BaBar with the pseudo-mass method [237] and by KEDR with the threshold-scan method [238]. The current status of τ mass measurements is summarized in Fig. 40.

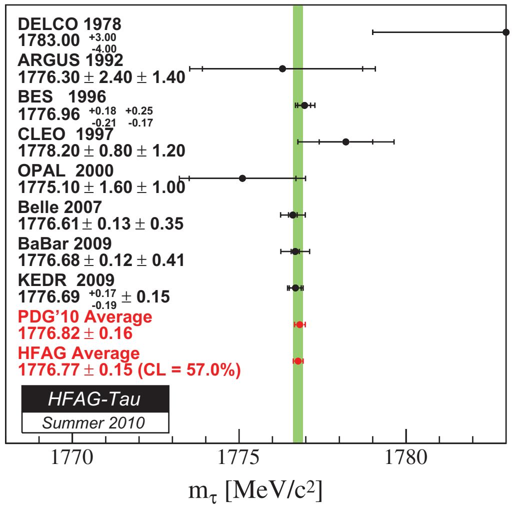

Fig. 40. Summary of the τ mass measurements.

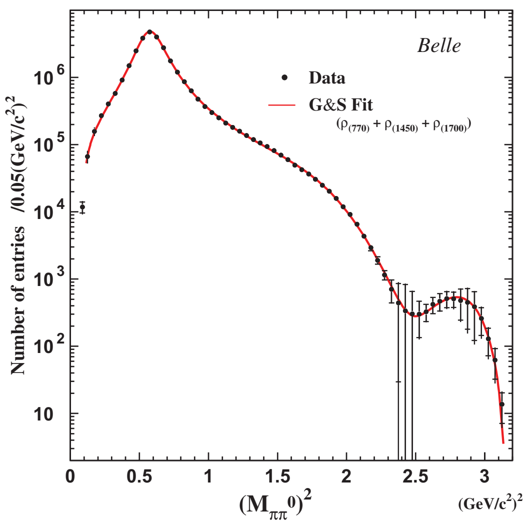

Fig. 41. Unfolded $\pi^{\pm}\pi^0$ mass spectrum for $\tau^{\pm} \to \pi^{\pm}\pi^0\nu_\tau$. Solid circles are the data and the solid curve is a fit. The error bars include both statistical and systematic uncertainties [239].

6.2.2. Spectral function in $\tau^{\pm} \to \pi^{\pm}\pi^0\nu_\tau$ decay. Among the decay channels of the τ lepton, $\tau^{\pm} \to \pi^{\pm}\pi^0\nu_\tau$ has the largest branching fraction. From the conservation of vector current (CVC), the $\pi^-\pi^0$ mass spectrum can be related to the cross section for the process $e^+e^- \to \pi^+\pi^-$ and thus can be used to improve the theoretical error on the anomalous magnetic moment of the muon $a_\mu = (g_\mu - 2)/2$.

Using a sample of 5 430 000 $\tau^{\pm} \to \pi^{\pm}\pi^0\nu_\tau$, Belle measures the branching fraction and the $\pi\pi^0$ mass spectrum [239], which are important for obtaining the theoretical value of $g_\mu - 2$. After unfolding using the singular-value-decomposition method [71], the $\pi\pi^0$ mass spectrum obtained is shown in Fig. 41, where the shapes for $\rho(770)$, $\rho(1450)$, and $\rho(1700)$ resonances and their interference pattern are measured very precisely. Figure 42 is the pion form factor in the $\rho(770)$ region obtained from the mass spectra in Fig. 41. The measured branching fraction is

$$\mathcal{B}(\tau^{\pm} \to \pi^{\pm}\pi^0\nu_\tau) = (25.24 \pm 0.04(\text{stat}) \pm 0.40(\text{syst}))\%.$$

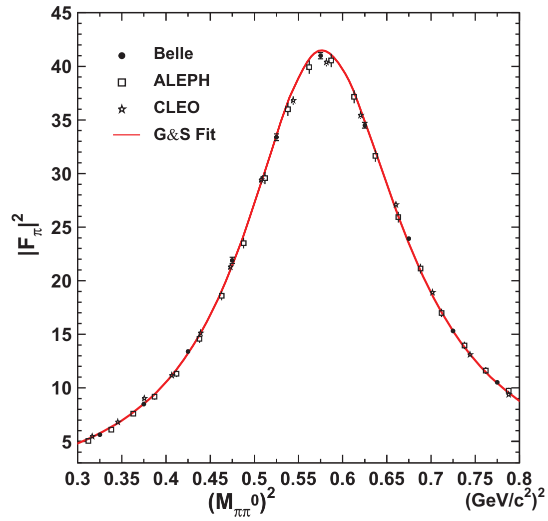

Fig. 42. Pion form factor $|F_\pi(s)|^2$ in the $\rho(770)$ region extracted from the mass spectra in Fig. 41.

It is known that there is a significant difference in the value of $a_\mu^{2\pi}$ obtained from e^+e^- and τ data. A lengthy discussion is ongoing about a possible source of this difference [240]. Belle τ data are in very good agreement with the recent measurement of the $e^+e^- \to \pi^+\pi^-$ cross section from initial-state radiation (ISR) data by BaBar[241]. In addition, it has been pointed by F. Jegerlehner [242,243] that $\gamma - \rho$ interference, which is present only in e^+e^- and does not contribute in the τ decay, plays an important role. After taking this interference effect into account, the discrepancy between the e^+e^- and τ data disappears; i.e. the hadronic term of $(g_\mu - 2)$ from the e^+e^- data is $a_\mu^{\text{had}}[e] = 690.8(4.7) \times 10^{-10}$, while including the τ data it becomes $a_\mu^{\text{had}}[e,\ \tau] = 691.0(4.7) \times 10^{-10}$ [242]. Note that without the $\rho - \gamma$ interference correction, $a_\mu^{\text{had}}[e,\ \tau]$ was $a_\mu^{\text{had}}[e,\ \tau] = 696.6(4.7) \times 10^{-10}$.

The resulting difference between theory and experiment for a_μ is greater than 3σ, which strengthens the difference further. Recently there have been efforts to evaluate a_μ^{had} in lattice QCD [244,245]. The reported values scatter in the range from $a_\mu^{\text{had}} = 641 \times 10^{-10}$ to 748×10^{-10} with an error of $(30 - 64) \times 10^{-10}$. The error is one order of magnitude larger than that obtained so far from e^+e^- and/or τ data.

6.2.3. Observation of decays with three kaons. Using a data sample of 401 fb^{-1} corresponding to 3.6×10^8 $\tau^+\tau^-$ pairs, Belle reported the first observation of decays with three charged kaons in the final state [246]. We select events in which a K^+K^- pair comes from the ϕ meson and, after taking into account a serious peaking background from $\tau^- \to \phi\pi^-\nu_\tau$, report the branching fraction, $\mathcal{B}(\tau^- \to \phi K^-\nu_\tau) = (4.05 \pm 0.25 \pm 0.26) \times 10^{-5}$. In addition, we observe $\tau^- \to \phi\pi^-\nu_\tau$ and $\tau^- \to \phi\pi^-\pi^0\nu_\tau$ decays, which is a serious peaking background for the three kaon process. Later BaBar confirmed the existence of this decay with a branching fraction consistent with ours [247].

6.2.4. Study of $\tau^- \to K_S\pi^-\nu_\tau$. A data sample of 351 fb^{-1} has been used to study the $K_S\pi^-\nu_\tau$ final state [248]. As a result of the analysis, 53 110 lepton-tagged signal events have been selected. The measured branching fraction, $\mathcal{B}(\tau^- \to K_S\pi^-\nu_\tau) = (0.404 \pm 0.002 \pm 0.013)\%$, is the most precise of all the published measurements. Although the Belle result is consistent with the other results within errors, the central value is somewhat lower than all of them. An analysis of the

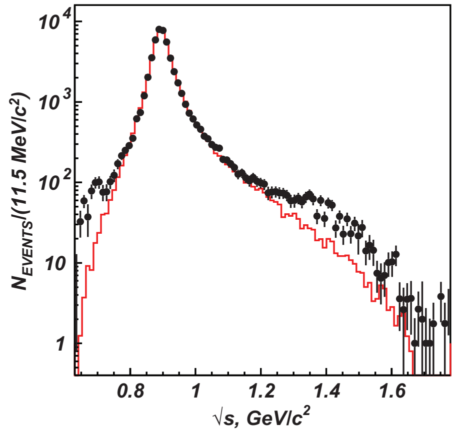

Fig. 43. The $K_S\pi$ mass distribution. Points with error bars are data while the histogram shows the fitted result for the spectrum expected in a model incorporating only $K^*(892)$. The background is already subtracted.

Table 18. The branching fractions of various decay modes with an η meson. The upper limits are at the 90% C.L.

Decay mode	$\mathcal{B}$
$K^-\eta\nu_\tau$, 10^{-4}	$1.58 \pm 0.05 \pm 0.09$
$\pi^-\pi^0\eta\nu_\tau$, 10^{-3}	$1.35 \pm 0.03 \pm 0.07$
$K^-\pi^0\eta\nu_\tau$, 10^{-5}	$4.6 \pm 1.1 \pm 0.4$
$K^0_S\pi^-\eta\nu_\tau$, 10^{-5}	$4.4 \pm 0.7 \pm 0.3$
$K^{*-}\eta\nu_\tau$, 10^{-4}	$1.34 \pm 0.12 \pm 0.09$
$K^-K^0_S\eta\nu_\tau$, 10^{-6}	<4.5
$K^0_S\pi^-\pi^0\eta\nu_\tau$, 10^{-5}	<2.5
$K^-\eta\eta\nu_\tau$, 10^{-6}	<3.0
$\pi^-\eta\eta\nu_\tau$, 10^{-6}	<7.4
$(K^-\pi^0\eta\nu_\tau)_{\text{nonres}}$, 10^{-5}	<3.5

$K_S\pi^-$ invariant mass spectrum shown in Fig. 43 reveals the dominant contribution from $K^*(892)^-$ with additional contributions of higher states at 1400 MeV. A satisfactory fit is obtained only if the existence of a broad scalar state, $K_0^*(800)$, is assumed. For the first time the $K^*(892)^-$ mass and width have been measured in τ decay: $M = (895.47 \pm 0.20 \pm 0.44 \pm 0.59)$ MeV, $\Gamma = (46.2 \pm 0.6 \pm 1.0 \pm 0.7)$ MeV, where the third uncertainty is from the model. The $K^*(892)^-$ mass is significantly higher than the world average value based on various hadronic experiments and is much closer to the world average for the neutral $K^*(892)$.

6.2.5. Measurement of hadronic τ decays with an η meson. Using a data sample of 490 fb^{-1} we have studied hadronic τ decay modes involving an η meson. Candidate η mesons are reconstructed from their decays into $\gamma\gamma$ and $\pi^+\pi^-\pi^0$ [249]. Table 18 lists the measured branching fractions or the upper limits. In all cases the number of observed events is significantly higher and the results are more precise than previous measurements by CLEO [250–252] and ALEPH [253]. For the $K^-\eta\eta\nu_\tau$ decay mode, our result is the first measurement. For $\pi^-\pi^0\eta\nu_\tau$, the invariant mass spectrum and the branching fraction are consistent with a prediction based on the conserved vector current (CVC) theorem [254].

Table 19. Comparison of the branching fractions of three hadron decay modes from Belle and BaBar.

Decay mode	BaBar	Belle
$\pi^-\pi^+\pi^-\nu_\tau$, %	$8.83 \pm 0.01 \pm 0.13$	$8.42 \pm 0.00^{+0.26}_{-0.25}$
$K^-\pi^+\pi^-\nu_\tau$, %	$0.273 \pm 0.002 \pm 0.009$	$0.330 \pm 0.001^{+0.016}_{-0.017}$
$K^-K^+\pi^-\nu_\tau$, %	$0.1346 \pm 0.0010 \pm 0.0036$	$0.155 \pm 0.001^{+0.006}_{-0.005}$
$K^-K^+K^-\nu_\tau$, 10^{-5}	$1.58 \pm 0.13 \pm 0.12$	$3.29 \pm 0.17^{+0.19}_{-0.20}$

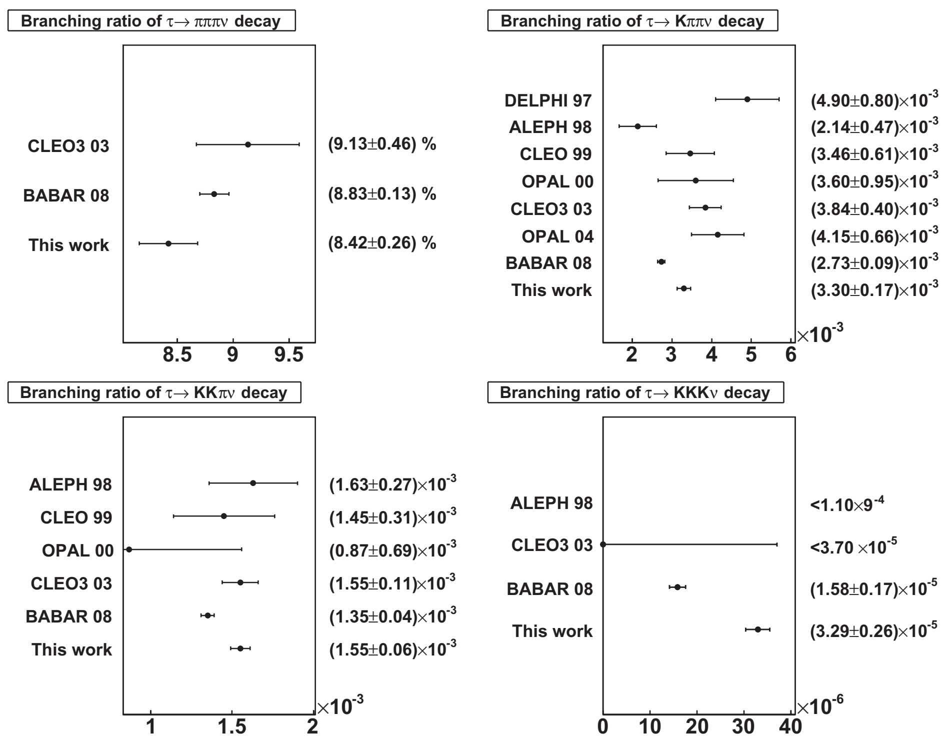

Fig. 44. Summary of the branching fraction measurements for three-prong τ decays.

6.2.6. Decays with three hadrons in the final state. With a data sample of 666 fb^{-1} Belle has also studied various decay modes of the τ lepton with three hadrons in the final state [255]. The results of this analysis for the branching fractions of various three-prong modes are listed in Table 19 together with recent results from BaBar [247]. Note that, for the $\pi^-\pi^+\pi^-\nu_\tau$ and $K^-\pi^+\pi^-\nu_\tau$ modes, the branching fractions listed do not include any K^0 contribution, while the result for $K^-K^+K^-\nu_\tau$ includes $\phi K^-\nu_\tau$.

In Fig. 44, our results are compared with the previous measurements. For all modes studied, the precision of the branching fraction measurements for both BaBar [247] and Belle is significantly better than previous results. The accuracy of our results is comparable to that of BaBar, but the central values show striking differences in all channels other than $\pi^-\pi^+\pi^-\nu_\tau$. For this mode, our result is 1.4σ lower than that of BaBar, while for the other modes the branching fractions obtained by Belle are higher by 3.0σ, 3.0σ, and 5.4σ than those of BaBar for the $K^-\pi^+\pi^-\nu_\tau$, $K^-K^+\pi^-\nu_\tau$, and $K^-K^+K^-\nu_\tau$ modes, respectively.

6.2.7. Summary of precise measurements. These measurements, as well as additional measurements of missing modes, are very important for obtaining separately the inclusive branching fractions of vector, axial-vector, and strange decay modes and corresponding spectral functions.

For the rare decay modes with branching fractions of less than 10^{-2}, there is a significant improvement compared to the previous experiments.

7. D^0 mixing and CPV

The neutral D meson system is one of the four flavored neutral particle–antiparticle systems that can exhibit oscillations. Particle–antiparticle mixing causes an initial (at time $t = 0$) pure D^0 meson state to evolve in time to a linear combination of D^0 and $\overline{D}^0$ states:

$$|D^0(t)\rangle = \left[|D^0\rangle \cos\text{h}\left(\frac{ix+y}{2}\Gamma t\right) + \frac{q}{p}|\bar{D}^0\rangle \sin\text{h}\left(\frac{ix+y}{2}\Gamma t\right)\right] \times e^{-(im-\frac{\Gamma}{2})t}, \tag{7.1}$$

where the two parameters that describe the D^0–$\overline{D}^0$ mixing, x and y, are defined as the mass and width difference of the two mass eigenstates $|D_{1,2}\rangle = p|D^0\rangle \pm q|\overline{D}^0\rangle$:

$$x = \frac{m_1 - m_2}{\Gamma},\ y = \frac{\Gamma_1 - \Gamma_2}{2\Gamma},\ \Gamma = \frac{\Gamma_1 + \Gamma_2}{2}, \tag{7.2}$$

and Γ is the mean decay width. The coefficients p and q are complex, satisfying the normalization condition $|p|^2 + |q|^2 = 1$. The time-dependent decay rates for $D^0 \to f$ (favored) and $D^0 \to \overline{f}$ (suppressed) decays are given by:

$$\begin{aligned}\Gamma(D^0(t) \to f) = |\mathcal{A}_f|^2 e^{-\Gamma t}\Bigg(&\frac{1+|\lambda_f|^2}{2}\cos\text{h}(y\Gamma t) - \text{Re}[\lambda_f]\sin\text{h}(y\Gamma t)\\ &+\frac{1-|\lambda_f|^2}{2}\cos(x\Gamma t) + \text{Im}[\lambda_f]\sin(x\Gamma t)\Bigg),\end{aligned} \tag{7.3}$$

$$\begin{aligned}\Gamma(D^0(t) \to \overline{f}) = |\overline{\mathcal{A}}_{\overline{f}}|^2 \left|\frac{q}{p}\right|^2 e^{-\Gamma t}\Bigg(&\frac{1+|\lambda_{\overline{f}}^{-1}|^2}{2}\cos\text{h}(y\Gamma t) - \text{Re}[\lambda_{\overline{f}}^{-1}]\sin\text{h}(y\Gamma t)\\ &-\frac{1-|\lambda_{\overline{f}}^{-1}|^2}{2}\cos(x\Gamma t) - \text{Im}[\lambda_{\overline{f}}^{-1}]\sin(x\Gamma t)\Bigg),\end{aligned} \tag{7.4}$$

where $\lambda_f = \frac{q}{p}\frac{\overline{\mathcal{A}}_f}{\mathcal{A}_f}$ and $\lambda_{\overline{f}} \equiv \frac{q}{p}\frac{\overline{\mathcal{A}}_{\overline{f}}}{\mathcal{A}_{\overline{f}}}$. The time evolution of neutral D meson decays is exponential with lifetime $\tau_{D^0} = 1/\Gamma$, modulated by the mixing parameters x and y (see the expressions above). Time-dependent measurements of D^0 and $\overline{D}^0$ decays thus enable us to measure the mixing parameters x and y. Since the dependence on x and y depends on the final state, different decay modes exhibit different sensitivities to the parameters x and y.

Out of the four flavored neutral meson systems, the neutral D meson system is the only one in which down-type quarks are involved in the box diagram loop (see Fig. 45). The neutral pion is its own antiparticle and the top quark decays before it forms a hadron and therefore cannot oscillate. Hence studies of charm mixing offer a unique probe of NP via flavor changing neutral currents in the down-type quark sector. In the SM, mixing in the neutral D meson system can proceed through a double weak boson exchange (short distance contributions) represented by box diagrams, or through intermediate states that are accessible to both D^0 and $\overline{D}^0$ (long distance effects), as represented in

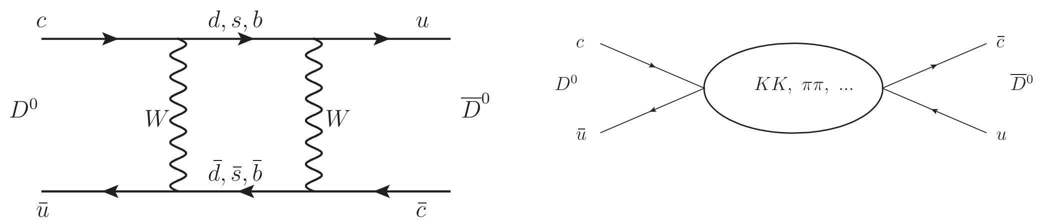

Fig. 45. Short distance (left) and long distance (right) contributions to D^0–$\overline{D}^0$ mixing in the Standard Model.

Fig. 45. The potentially large long distance contributions are non-perturbative and therefore difficult to estimate, so the predictions for the mixing parameters x and y within the SM span several orders of magnitude between 10^{-8} and 10^{-2} [256,257]. Due to large uncertainties in the SM mixing predictions, it is difficult to identify NP contributions (a clear hint would be if x is found to be much larger than y); however, measurements can still provide useful and competitive constraints on many NP models, as will be discussed later.

The study of CP violation in decays of charmed hadrons also holds the potential for uncovering NP. In the SM, direct CP violation can occur in singly Cabibbo suppressed (SCS; $c \to du\overline{d}$, $c \to su\overline{s}$) decays, but not in Cabibbo favored (CF; $c \to su\overline{d}$) or doubly Cabibbo suppressed (DCS; $c \to du\overline{s}$) decays. This is due to the fact that the final state particles in SCS decays contain at least one quark–antiquark pair of the same flavor, which makes a contribution from penguin-type or box amplitudes induced by virtual b-quarks possible in addition to the tree amplitudes. However, the contribution of these second order amplitudes is strongly suppressed by the small combination of CKM matrix elements $V_{cb}V_{ub}^*$. Therefore, in processes involving charmed hadrons, mainly the first two generations of quarks are involved. From the Wolfenstein parameterization of the CKM matrix [22] one can see that the elements related to the first two generations of the quarks are nearly real. Of course, by using the unitarity of the matrix one can still parameterize and estimate the imaginary part of those elements. For example, examining the phase difference between the decays $D^0(\bar{D}^0) \to K^+K^-$, one finds that it is $2\arg(V_{cs}V_{us}^*)$, which can be expressed using the unitarity and the Wolfenstein parameterization as $2A^2\lambda^4\eta \approx 10^{-3}$. Hence the expected CPV asymmetries in the charm sector are of the order of 10^{-3}, which is small compared to the measured CP asymmetries in the bottom sector. Recently, with the experimental precision reaching the per mille level, some authors [258] have argued that the asymmetries could be much larger than naively expected. Nevertheless, at the current level of experimental sensitivity, the measurements of the CPV in the charm sector are mainly a search for a significant effect, which would point to so-far unknown NP processes.

7.1. Experimental techniques of D^0–$\overline{D}^0$ mixing and CP symmetry violation

Often, the flavor of initially produced neutral D mesons needs to be tagged in order to identify D^0–$\overline{D}^0$ transitions and CP violation. The flavor is tagged by requiring that neutral D mesons originate from $D^{*+} \to D^0\pi^+$ decays, where the charge of the pion accompanying D^0 tags the flavor of the neutral D meson at production. Another common property of the measurements described below is the selection of D meson candidates based on the CM momentum, typically $p^* > 2.5$ GeV/c for data taken at the $\Upsilon(4S)$ resonance. This requirement completely removes charmed mesons arising from possibly CP-violating B meson decays that have a displaced production vertex. Hence the Belle charm samples consist entirely of $e^+e^- \to c\bar{c}$ continuum data.

The most precise constraints on the mixing parameters x and y are obtained using the time dependence of D^0 decays. In time-dependent measurements, the D^0 decay time is determined according to $t = m_{D^0}(\vec{L} \cdot \vec{p}_{D^0})/|\vec{p}_{D^0}|^2$, where $\vec{L}$ is the vector joining the D^0's production and decay vertices, and $\vec{p}_{D^0}$ and m_{D^0} are its momentum and nominal mass. The reconstructed tracks of D^0 decay products are refitted to a common vertex to determine the D^0 decay point, and then the D^0's production point is determined from the kinematic fit of the D^0 momentum vector with the beam spot profile. The decay-time uncertainty σ_t is evaluated event-by-event from the covariance matrices of the production and decay vertices. Typically, for decays with two charged tracks in the final state, $\langle\sigma_t\rangle \sim \tau_{D^0}/2$. Candidates with badly reconstructed decay time (with large σ_t) are excluded from the analysis.

The mixing parameters are extracted by performing a fit to the decay-time distribution using the following PDF:

$$\mathcal{P}(t) = \int_{-\infty}^{+\infty} \Gamma_{\text{sig}}(t'; x, y) R_{\text{sig}}(t - t')dt' + \mathcal{P}_{\text{bkg}}(t), \tag{7.5}$$

where the signal contribution is a convolution of the (final state dependent) time-dependent decay rate (Γ_{sig}) and the detector resolution function (R_{sig}). To reduce the systematic uncertainties related to the parameterization of the resolution function, kinematically similar decays (from high statistics control samples) are usually used to determine the resolution function parameters directly from data. The background $\mathcal{P}_{\text{bkg}}(t)$ is parameterized using an exponential (to describe the background candidates originating from mis-reconstructed charm decays) and a δ function (to describe random combinations of final state particles), each convolved with its corresponding resolution function. The parameters of the background PDF are determined using events populating the sideband region in the invariant mass of D^0 candidates.

Experimental determinations of CPV can be divided into those using the decay time distribution of certain decays to determine the unknown parameters and those using the decay time-integrated methods. The unknown CPV parameters often follow from the parameterization below:

$$\left|\frac{\bar{A}_{\bar{f}}}{A_f}\right|^2 \equiv 1 + A_D^f, \quad \left|\frac{q}{p}\right|^2 \equiv 1 + A_M, \quad \Im\left[\frac{q}{p}\frac{\bar{A}_f}{A_f}\right] \equiv \left|\frac{q}{p}\frac{\bar{A}_f}{A_f}\right| \sin\phi. \tag{7.6}$$

$A_D^f \neq 0$ is the asymmetry from CPV in decays to a final state f, $A_M \neq 0$ is from CPV in the mixing, and $\sin\phi \neq 0$ is a manifestation of CPV in the interference between decays without mixing.

While in charged D meson processes only the CPV in decays is present, neutral charmed mesons may include contributions from all three types of violation.

All measurements are performed blindly, i.e. the selection criteria are determined using samples of simulated events or data events that are statistically independent from those used to perform the measurement, in order to avoid possible biases.

7.2. *Time-dependent measurements of D^0–$\overline{D}^0$ mixing and CP violation*

7.2.1. Decays to CP eigenstates. Belle found the first evidence for D^0–$\overline{D}^0$ mixing [259] in a data sample of 540 fb^{-1} using the ratios of lifetimes extracted from a sample of D^0 mesons produced through the process $D^{*+} \to D^0\pi^+$, which decay to $K^-\pi^+$, K^-K^+, or $\pi^-\pi^+$. The time-dependent decay rates of the CF mode, $K^-\pi^+$, and the SCS modes h^-h^+ ($h = K$ or π) are obtained from the time-dependent decay rates given in the previous section:

$$\Gamma(D^0(t) \to K^-\pi^+, \overline{D}^0(t) \to K^+\pi^-) \propto e^{-t/\tau_{D^0}} \tag{7.7}$$

$$\Gamma(D^0(t), \overline{D}^0(t) \to h^+h^-) \propto e^{-(1+y_{CP})t/\tau_{D^0}}, \tag{7.8}$$

where we assume that $x, y \ll 1$ and $|\overline{\mathcal{A}}_f/\mathcal{A}_f| = 1$ ($|\overline{\mathcal{A}}_f/\mathcal{A}_f| \ll 1$) for D^0 meson decays to h^-h^+ ($K^-\pi^+$). For $D^0 \to h^+h^-$ decays, linear terms in xt and yt are the first terms in the Taylor expansion of the exponential function above. The lifetime difference between decays to the CP eigenstates h^-h^+ and CP-mixed state $K^-\pi^+$, y_{CP}, is defined as

$$y_{CP} \equiv \frac{\tau_{K^\mp\pi^\pm}}{\tau_{h^+h^-}} - 1 = y\cos\phi - \frac{1}{2}A_M x \sin\phi. \tag{7.9}$$

The lifetimes $\tau_{K\pi}$ and τ_{hh} are the effective lifetimes extracted from samples of D^0 mesons decaying to the CP mixed final state $K^-\pi^+$, and CP even final states K^-K^+ and $\pi^-\pi^+$. If $|q/p| = 1$ and $\phi = \arg(q/p) = 0(\pi)$, CP symmetry in mixing and interference between mixing and decay is conserved, and hence the parameter y_{CP} corresponds to the mixing parameter y. In these time-dependent measurements of neutral D mesons decaying to CP eigenstates, indirect CP violation is also probed by comparing the lifetimes of D^0 and $\overline{D}^0$ mesons decaying to CP eigenstates:

$$A_\Gamma = \frac{\tau^{\overline{D}^0}_{h^+h^-} - \tau^{D^0}_{h^+h^-}}{\tau^{\overline{D}^0}_{h^+h^-} + \tau^{D^0}_{h^+h^-}} = \frac{1}{2}A_M y\cos\phi - x\sin\phi. \tag{7.10}$$

By performing a simultaneous fit to the decay-time distributions of around 0.15 (1.2) million reconstructed tagged D^0 decays with purity above 90% to h^-h^+ ($K^-\pi^+$), Belle found $y_{CP} = (1.13 \pm 0.32 \pm 0.25)\%$ and $A_\Gamma = (0.01 \pm 0.30 \pm 0.15)\%$. Figure 46 shows the decay-time distributions with fit results superimposed as well as the decay-time dependent ratio of D^0 decays to CP-even eigenstates K^-K^+ and $\pi^-\pi^+$ to the CP mixed final state $K^-\pi^+$, as measured by Belle [259]. In case of $y_{CP} = 0$, this ratio would be constant, which is inconsistent with Belle's data at 3.2σ. No evidence for indirect CP violation is found.

7.2.2. Decays to hadronic wrong sign decays. Belle also performed a search for neutral D meson mixing and CP violation in a time-dependent study of DCS $D^0 \to K^+\pi^-$ decays [260] based on $400\,\mathrm{fb}^{-1}$ of data. These decays (also referred to as wrong sign decays) can proceed both through mixing followed by a CF decay, $D^0 \to \overline{D}^0 \to K^+\pi^-$, or directly through a DCS decay such as $D^0 \to K^+\pi^-$. To distinguish the two processes, an analysis of the decay time distribution is performed. The most general form (e.g. allowing for direct CP violation in DCS decays, mixing and interference between mixing and decay) for the time-dependent decay rates of the two-body wrong sign decays $D^0 \to K^+\pi^-$ or $\overline{D}^0 \to K^-\pi^+$ to second order in x and y is given by:

$$\begin{aligned}\Gamma\begin{pmatrix}D^0(t) \to K^+\pi^- \\ \overline{D}^0(t) \to K^-\pi^+\end{pmatrix} &\propto e^{-t/\tau_{D^0}}\,\Big(R_D(1 \pm A_D)\,. \\ &\quad + \sqrt{R_D(1 \pm A_D)}\left[\frac{1 \pm A_M}{1 \mp A_M}\right]^{1/4}(y'\cos\phi \mp x'\sin\phi)\frac{t}{\tau_{D^0}} \\ &\quad + \frac{1}{4}\left[\frac{1 \pm A_M}{1 \mp A_M}\right]^{1/2}(x'^2 + y'^2)\frac{t^2}{\tau^2_{D^0}}\Big),\end{aligned} \tag{7.11}$$

where R_D is the ratio of DCS to CF decay rates, and the parameters x' and y' are rotated mixing parameters, which are rotated by an unknown strong phase difference between the DCS and CF

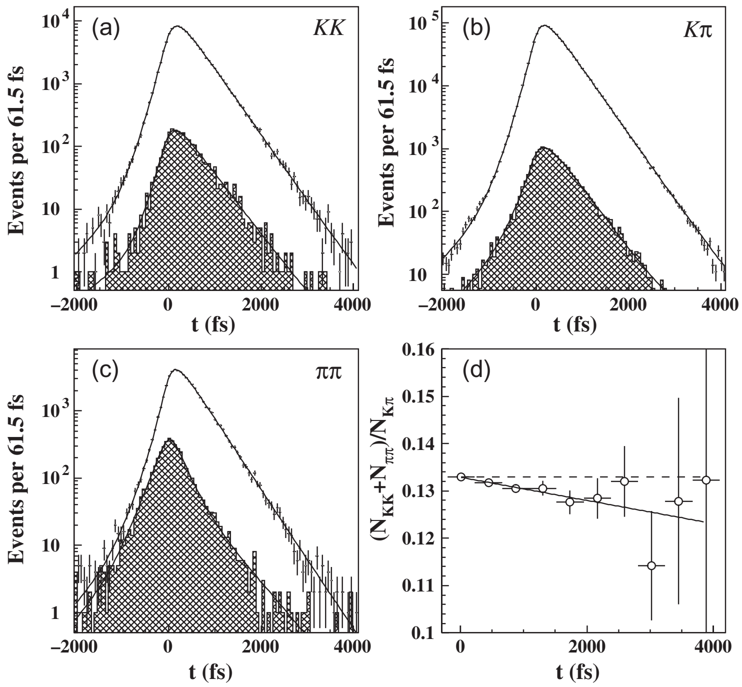

Fig. 46. Results of the simultaneous fit to decay-time distributions of (a) $D^0 \to K^+K^-$, (b) $D^0 \to K^-\pi^+$, and (c) $D^0 \to \pi^+\pi^-$ decays. The cross-hatched area represents background contributions, the shape of which was fitted using D^0 invariant mass sideband events. (d) Ratio of decay-time distributions between $D^0 \to K^+K^-$, $\pi^+\pi^-$, and $D^0 \to K^-\pi^+$ decays. The solid line is a fit to the data points.

amplitudes, $\delta_{K\pi}$: $x' = x\cos\delta_{K\pi} + y\sin\delta_{K\pi}$ and $y' = y\cos\delta_{K\pi} - x\sin\delta_{K\pi}$. The three terms in the time-dependent decay rates of wrong sign decays are due to the DCS amplitude, the interference between the DCS and CF amplitudes, and the CF amplitude, respectively. In addition to the wrong sign decays, the Cabibbo favored (or right sign) $D^0 \to K^-\pi^+$ decays are reconstructed in order to determine the resolution function parameters, as well as the distribution of wrong sign signal events in D^0 invariant mass and mass difference distributions, which are fitted to extract the number of correctly reconstructed wrong sign decays.

From a fit to the decay-time distribution of around 4×10^3 signal wrong sign decays (and with purity around 50%) Belle found $x'^2 = (0.18^{+0.21}_{-0.23}) \times 10^{-3}$ and $y' = (0.6^{+0.4}_{-3.9}) \times 10^{-3}$ assuming no CP violation (setting $A_D = A_M = \phi = 0$ in Eq. 7.11). The errors in x'^2 and y' include both statistical and systematic uncertainties. A projection of this fit superimposed on the data is shown in Fig. 47 and the non-mixing point ($x'^2 = y' = 0$) is found to be excluded at 95% C.L. In a second fit, CP-violating parameters are allowed to float and no evidence for either direct or indirect CPV is found. Belle obtains the following 95% C.L. intervals for CP-violating parameters: $A_D \in (-76, 107) \times 10^{-3}$ and $A_M \in (-995, 1000) \times 10^{-3}$.

7.2.3. Self-conjugated three-body decays. Several intermediate resonances can contribute to a hadronic three-body decay of a neutral D meson. For example, $D^0 \to K^0_S\pi^+\pi^-$ decays can proceed via $D^0 \to K^{*-}\pi^+$ (CF amplitude), $D^0 \to K^0_S\rho^0$ (SCS amplitude and CP eigenstate), $D^0 \to K^{*+}\pi^-$ (DCS amplitude), and others. In the isobar model, the instantaneous amplitudes for D^0 and $\overline{D}^0$ decays to the three-body final state f are parameterized as a sum of Breit–Wigner resonances and a constant nonresonant term (in the case of no direct CP violation, e.g., there is no difference

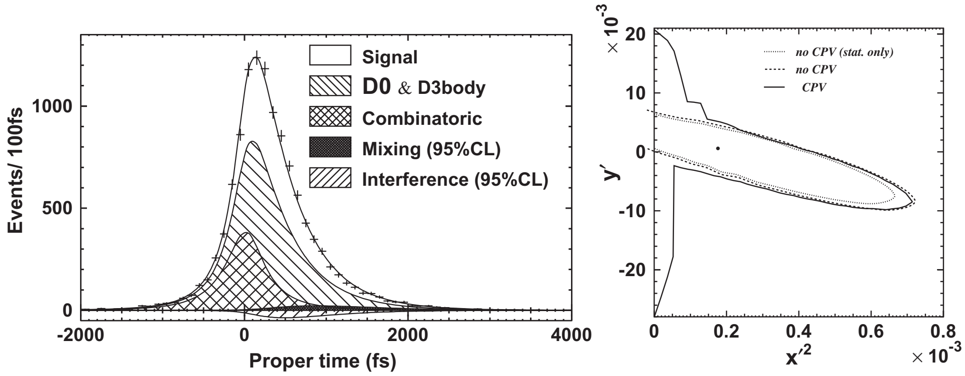

Fig. 47. (Left) The decay-time distribution for wrong sign (WS) events. Superimposed on the data (points with error bars) are projections of the decay-time fit when no CPV is assumed. The mixing and interference terms are shown at the 95% C.L. upper limits. (Right) 95% C.L. regions for (x'^2, y'). The point is the best fit result assuming CP conservation. The dotted (dashed) curve is the statistical (statistical and systematic) contour for no CPV. The solid curve is the statistical and systematic contour in the CPV-allowed case.

between amplitudes and phases in D^0 and $\overline{D}^0$ decays):

$$\mathcal{A}_f(s_+, s_-) = \sum_r a_r e^{i\phi_r} \mathcal{A}_r(s_+, s_-) + a_{\rm NR} e^{i\phi_{\rm NR}}, \tag{7.12}$$

$$\overline{\mathcal{A}}_f(s_+, s_-) = \sum_r a_r e^{i\phi_r} \mathcal{A}_r(s_-, s_+) + a_{\rm NR} e^{i\phi_{\rm NR}}, \tag{7.13}$$

where $\sqrt{s_\pm}$ is the invariant mass of a pair of final state particles (e.g. $K_S^0\pi^\pm$), and the sum runs over possible intermediate resonances r. The time-dependent decay rate for D^0 decays is thus given by (the corresponding expression for $\overline{D}^0$ decays is obtained by multiplying the equation below by $|p/q|^2$):

$$\begin{aligned}\frac{d\Gamma(D^0 \to f)}{ds_+ ds_- dt} \propto{}& |\mathcal{A}_1(s_+, s_-)|^2 e^{-\frac{t}{\tau}(1+y)} + |\mathcal{A}_2(s_+, s_-)|^2 e^{-\frac{t}{\tau}(1-y)} \\ &+ 2{\rm Re}[\mathcal{A}_1(s_+, s_-)\mathcal{A}_2^*(s_+, s_-)] \cos\left(x\frac{t}{\tau}\right) e^{-\frac{t}{\tau}} \\ &+ 2{\rm Im}[\mathcal{A}_1(s_+, s_-)\mathcal{A}_2^*(s_+, s_-)] \sin\left(x\frac{t}{\tau}\right) e^{-\frac{t}{\tau}},\end{aligned} \tag{7.14}$$

where $\mathcal{A}_{1,2}(s_+, s_-) = \frac{1}{2}\left(\mathcal{A}_f(s_+, s_-) \pm \frac{q}{p}\overline{\mathcal{A}}_f(s_+, s_-)\right)$. Different regions in the $s_+ - s_-$ plane (also called the Dalitz plot) exhibit different forms of time dependence, as can be seen from the above decay rate; therefore, the time-dependent Dalitz plot analysis of neutral D meson decays to a self-conjugated three-body final state enables us to measure the x and y parameters simultaneously. In the case where the analysis is performed separately for D^0 and $\overline{D}^0$ samples, indirect CP violation can be probed by measuring the amplitude and phase of q/p. This method of measuring the mixing parameters x and y was pioneered by CLEO in $D^0 \to K_S^0\pi^+\pi^-$ decays [261], and was applied by Belle to $D^0 \to K_S^0\pi^+\pi^-$ decays [262] using a data sample of 540 fb^{-1} in which around 530 000 signal events are reconstructed with a purity of around 95%.

The decay amplitude is not a priori known and has to be extracted from the data. This is done by first performing a time-integrated Dalitz plot analysis in which a model for the decay amplitude ($\mathcal{A}(s_+, s_-)$) that describes the observed decay kinematics best is obtained. Belle finds that a

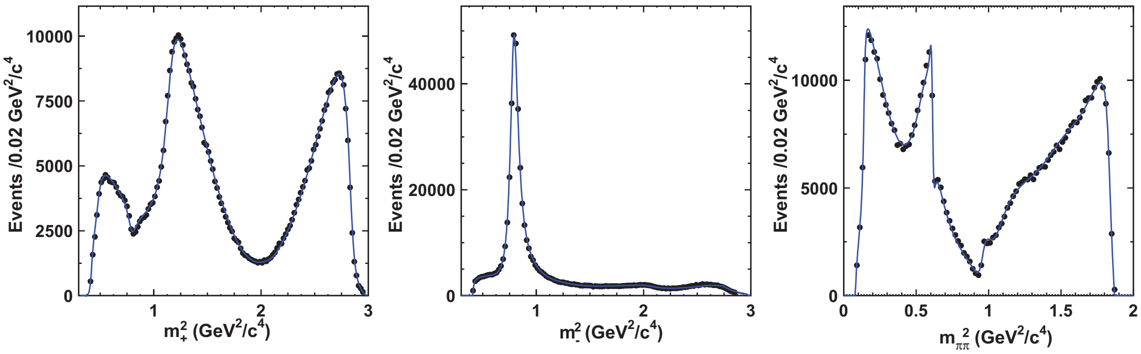

Fig. 48. Projections of the Dalitz distribution (points with error bars) and the fit result (curve) for $D^0 \to K_S^0\pi^+\pi^-$ decays [262]. Here, $m_\pm^2$ corresponds to $m^2(K_S^0\pi^\pm)$ for D^0 decays and to $m^2(K_S^0\pi^\mp)$ for $\overline{D}^0$ decays.

good description of the Dalitz plot is obtained when 18 quasi-two-body resonances and a nonresonant term are used (see Fig. 48 for the results of the fit). Once the decay amplitude composition is determined, a time-dependent Dalitz analysis is performed to determine the mixing parameters. In a fit with conserved CP symmetry ($|q/p| = 1$ and $\phi = 0$) the mixing parameters are found to be: $x = (0.80 \pm 0.29^{+0.09+0.10}_{-0.07-0.14})\%$ and $y = (0.33 \pm 0.24^{+0.08+0.06}_{-0.12-0.08})\%$, excluding the non-mixing point with 95% C.L. The errors quoted are the statistical, systematic error arising from experimental sources (e.g. modeling of background, resolution function, etc.) and the systematic error arising from the decay model (determined by using alternative models with different parameterizations, excluding resonances with small contributions, etc.). In a fit allowing for *CPV*, the $|q/p|$ and ϕ parameters are found to be consistent with no CP violation: $|q/p| = 0.86^{+0.30+0.06}_{-0.29-0.03} \pm 0.08$ and $\phi = (-14^{+16+5+2}_{-18-3-4})^\circ$.

Large fractions of $D^0 \to K_S^0K^+K^-$ decays proceed via $D^0 \to K_S^0\phi$ (CP-odd) and $D^0 \to K_S^0a_0(980)$ (CP-even) decays. Belle took advantage of this fact and performed a measurement of the y_{CP} mixing parameter integrated over the Dalitz plot using an untagged sample of $D^0 \to K_S^0K^+K^-$ decays [263]. We measure the effective lifetimes of D^0 mesons, $\tau_{\mathrm{ON,OFF}}$, in two different regions of K^+K^- invariant mass (at the ϕ peak (ON) and in ϕ sidebands (OFF)), which are given by $\tau_{\mathrm{ON,OFF}} = (1 + (1 - 2f_{\mathrm{ON,OFF}})y_{CP})\tau_{D^0}$, where $f_{\mathrm{ON,OFF}}$ is the CP-even fraction in the ON or OFF region calculated using the decay model obtained by BaBar [264]. The obtained value of $y_{CP} = (0.11 \pm 0.61 \pm 0.52)\%$ is consistent with y_{CP} obtained in $D^0 \to hh$ decays.

7.3. *World average and constraints on new physics models*

Various measurements of D^0–$\overline{D}^0$ mixing performed in different decay modes can be combined to obtain the world average values of x and y. The Charm subgroup of the Heavy Flavor Averaging Group has done this by performing a global χ^2 fit from measurements of relevant observables [38] performed by the Belle[4], BaBar, CDF, LHCb, CLEO-c, Focus, and FNAL E791 experiments. The world average values are found to be

$$x = (0.63 \pm {}^{+0.19}_{-0.20})\%, \tag{7.15}$$

[4] In the world average fit, HFAG also includes Belle's time-integrated measurement of the mixing rate $R_M = (x^2 + y^2)/$ in $D^0 \to K^+\ell\nu_\ell$ [265], which is not described in detail in this report.

$$y = (0.75 \pm 0.12)\%, \tag{7.16}$$

and

$$\left|\frac{q}{p}\right| = (0.88 \pm {}^{+0.18}_{-0.16}), \tag{7.17}$$

$$\phi = (-10.1 \pm {}^{+9.5}_{-8.9})^{\circ}. \tag{7.18}$$

The non-mixing point, $(x, y) = (0, 0)$, is excluded at the 10.2 standard deviation level while the $|q/p|$ and ϕ values are consistent with conservation of CP symmetry in mixing and interference between mixing and decay.

Golowich et al. [266] studied the implications of existing D^0–$\overline{D}^0$ measurements on many NP models. In many scenarios they found strong constraints that surpass those from other search techniques and provide an important test of flavor changing neutral currents in the up-quark sector. One simple extension to the SM that they studied is the addition of a fourth family of fermions. The obtained constraint on the CKM mixing parameters $V_{cb'}V^*_{ub'}$ (b' is the down-quark of the fourth generation) is an order of magnitude more restrictive than those obtained from unitarity considerations of the CKM matrix.

7.4. Time-integrated measurements of CPV in charm

In the time-integrated measurements one usually determines the asymmetry of the partial decay widths,

$$A^f_{CP} \equiv \frac{\Gamma(D \to f) - \Gamma(\bar{D} \to \bar{f})}{\Gamma(D \to f) + \Gamma(\bar{D} \to \bar{f})}. \tag{7.19}$$

The measured asymmetry

$$A^f_{\text{rec}} = \frac{N(D^+ \to f) - N(D^- \to \bar{f})}{N(D^+ \to f) + N(D^- \to \bar{f})}, \tag{7.20}$$

where N denotes the number of detected decays, receives a contribution from several non-CP violating sources, the detector-induced asymmetries due to a possible asymmetry in the acceptance of positively and negatively charged pions and kaons, or the different acceptances for neutral kaons and their antiparticles. In addition, the physical forward–backward asymmetry in the process $e^+e^- \to c\bar{c}$ affects the measured asymmetry, as we will see in the following. All these effects must be carefully determined using control data samples in order to achieve an accuracy at the level of $\mathcal{O}(10^{-3})$, the level of uncertainty of A_{CP} measurements in various final states reached by the Belle experiment. The existing MC simulation tools cannot be used for corrections at this level of accuracy.

Currently the best sensitivity on A_{CP} at Belle has been achieved in the decays $D^+ \to \pi^+ K^0_S$. This decay mode is a mixture of CF ($D^+ \to \pi^+\bar{K}^0$) and DCS ($D^+ \to \pi^+ K^0$) decay. If NP processes with unknown CP-violating phases would contribute, the CPV in the decays may be significantly different from zero. The measured asymmetry in these decays can be written as

$$A^{K_S\pi^+}_{\text{rec}} = A^{K_S\pi^+}_{CP} + A^{\pi^+}_{\epsilon}(p_{\pi^+}, \cos\theta_{\pi^+}) + A_{FB}(\cos\theta^*), \tag{7.21}$$

where $A^{K_S\pi^+}_{CP}$ is the physical CPV asymmetry, $A^{\pi^+}_{\epsilon}$ the detector-induced asymmetry between the π^+ and π^- reconstruction efficiencies, and A_{FB} the contribution of the forward–backward asymmetry. The latter is an odd function of the D meson polar angle in the CM $\cos\theta^*$ (see e.g. Ref. [23]), while the first term is independent of any kinematic variables. The detector-induced asymmetry depends

Table 20. Measured time-integrated CPV asymmetries in the D meson system.

Decay mode	$\mathcal{L}$ (fb^{-1})	A_{CP} (%)	Comment	Ref.
$D^0 \to K_S^0\pi^0$	791	$-0.28 \pm 0.19 \pm 0.10$		[269]
$D^0 \to K_S^0\eta$		$+0.54 \pm 0.51 \pm 0.16$		
$D^0 \to K_S^0\eta'$		$+0.98 \pm 0.67 \pm 0.14$		
$D^0 \to \pi^+\pi^-$	540	$+0.43 \pm 0.52 \pm 0.12$		[270]
$D^0 \to K^+K^-$		$-0.43 \pm 0.30 \pm 0.11$		
$D^0 \to \pi^+\pi^-\pi^0$	532	$+0.43 \pm 1.30$		[271]
$D^0 \to K^+\pi^-\pi^0$	281	-0.6 ± 5.3		[272]
$D^0 \to K^+\pi^-\pi^+\pi^-$		-1.8 ± 4.4		
$D^+ \to K_S^0\pi^+$	977	$-0.363 \pm 0.094 \pm 0.067$	signif. asymmetry due to K_S^0	[267]
$D^+ \to \phi\pi^+$	955	$+0.51 \pm 0.28 \pm 0.05$	universality of A_{FB} in D_s^+ and D^+ decays to $\pi^+\phi$ tested	[273]
$D^+ \to \eta\pi^+$	791	$+1.74 \pm 1.13 \pm 0.19$	$D^+ \to K^+\eta^{(\prime)}$	[274]
$D^+ \to \eta'\pi^+$	791	$-0.12 \pm 1.12 \pm 0.17$	also observed	
$D^+ \to K_S^0K^+$	673	$-0.16 \pm 0.58 \pm 0.25$		[275]
$D_s^+ \to K_S^0\pi^+$	673	$+5.45 \pm 2.50 \pm 0.33$		[275]
$D_s^+ \to K_S^0K^+$		$+0.12 \pm 0.36 \pm 0.22$		[275]

on the momentum and the polar angle of the charged track in the laboratory frame. In bins of these variables the measured asymmetry can be corrected for $A_\epsilon^{\pi^+}$ using samples of $D^0 \to K^-\pi^+\pi^0$ and $D^+ \to K^-\pi^+\pi^+$ decays. The measured asymmetries for these decays are

$$A_{\text{rec}}^{K\pi\pi} = A_{FB} + A_\epsilon^{K^-} + A_\epsilon^{\pi_1^+} + A_\epsilon^{\pi_2^+}$$
$$A_{\text{rec}}^{K\pi\pi^0} = A_{FB} + A_\epsilon^{K^-} + A_\epsilon^{\pi_1^+}, \tag{7.22}$$

assuming negligible CP violation in the Cabibbo favored D meson decays and the universality of the forward–backward asymmetry for different types of charmed mesons[5]. By inspecting Eqs. (7.22) one finds that in the difference of the measured asymmetries in $D^0 \to K^-\pi^+\pi^0$ and $D^+ \to K^-\pi^+\pi^+$ some of the detector-induced asymmetries and the forward–backward contribution cancel and hence one can determine $A_\epsilon^{\pi^+}$. In turn, $A_\epsilon^{\pi^+}$ is then used to correct $A_{\text{rec}}^{K_S\pi^+}$ in bins of the charged pion momentum and polar angle, and to extract $A_{CP}^{K_S\pi^+}$ [267]. However, in the $D^+ \to h^+K_S^0$ decay modes, one needs additional corrections due to the presence of a neutral kaon in the final state. In such D^+ meson decay modes either a K^0 or $\bar{K}^0$ is produced, which interact differently in the detector material. However, in the final state a K_S^0 is reconstructed, and hence this affects the value of the asymmetry. A separate dedicated study [268] was performed and the appropriate correction factor applied to the asymmetry. Furthermore, because of the CP violation in the neutral kaon system, the asymmetry expected in this final state with K_S^0 is $A^{K_S} = (-0.332 \pm 0.006)\%$. The Belle result is given in Table 20 and is in good agreement with the expectation due to CP violation in the neutral kaon system.

Belle searched extensively for non-zero time-integrated CP asymmetries in a number of other decay modes and achieved the best sensitivity in many of these. The results (see Table 20) are consistent with no CPV at levels varying from $\mathcal{O}(10^{-2})$ to $\mathcal{O}(10^{-3})$.

[5] Within the SM only Cabibbo suppressed decays of charmed mesons have two possible amplitudes with different weak and strong phases—the tree and the penguin amplitude—which is a necessary condition for non-zero CPV in decays.

7.5. *Conclusions*

With the world's largest sample of recorded charmed hadron decays Belle has experimentally observed mixing phenomena in the last remaining neutral meson system, D^0. The mixing parameters in this system are nowadays becoming a precision measurement, with world average values [38] of $x = (0.63 \pm ^{+0.19}_{-0.20})\%$ and $y = (0.75 \pm 0.12)\%$. Further measurements and advances in theoretical predictions are required to determine whether the observed values are consistent with the SM or receive contributions from NP. Furthermore, an extensive search for CPV in the charm sector was carried out. The measurement methods that were developed allowed for the observation of a significant CPV asymmetry in decay modes with a neutral kaon in the final state and sensitivities to possible time-integrated CP asymmetries at the per mille level in a variety of decay modes. No significant indirect CP violation has been observed so far.

8. *B* physics at the $\Upsilon(5S)$

The $\Upsilon(10\,860)$ ($M = 10\,876 \pm 11\,\mathrm{MeV}/c^2$, $\Gamma = 55 \pm 28\,\mathrm{MeV}$) [23] is generally interpreted as the $\Upsilon(5S)$, the fourth excitation of the vector bound state of $b\bar{b}$, and is just above $B_s^* \bar{B}_s^*$ threshold. The Belle experiment collected a total of 121.4 fb^{-1} at the $\Upsilon(10\,860)$ peak energy and a total of 27.6 fb^{-1} at off-peak CM energies nearby, between 10.683 and 11.021 GeV. The on-resonance data sample corresponds to 37 million resonance events and includes 7.1 million B_s events. These data were analyzed to pursue investigations of B_s meson properties, hadronization to B_q and B_s events (q is a u- or d-quark), energy dependence of various types of events, and possible new bottomonia and bottomonium-like states. Published on-peak results are based on two subsets, 1.86 fb^{-1} and 23.6 fb^{-1} (including the 1.86 fb^{-1}), as well as the full set of 121.4 fb^{-1}, which will be referred to as sets 2FB, 24FB, and 121FB, respectively.

The $e^+e^- \to \Upsilon(10\,860)$ is an excellent venue for studying several aspects of B_s decay; given clean, efficiently triggered events with precisely known CM energy, collected by a well-understood detector, the Belle experiment has been uniquely positioned to measure absolute branching fractions, access modes that include photons in the final state, and do comparative studies of B and B_s mesons with minimal systematic uncertainties.

8.1. $B_s^{(*)}$ *masses: method of full reconstruction*

At the energy of the $\Upsilon(10\,860)$, three types of B_s events are allowed: $B_s\bar{B}_s$, $B_s^*\bar{B}_s^*$, and $B_s\bar{B}_s^*$ (and $\bar{B}_s B_s^*$) events. Each is an exclusive 2-body decay, so the energy of the daughter $B_s^{(*)}$ in the collision CM frame is fully constrained. The method of "full reconstruction," where all decay products are detected and measured, was used with great success for B_q at the $\Upsilon(4S)$. The reconstruction of B_s in $B_s\bar{B}_s$ events is analogous: each B_s carries energy equal to the beam energy (in the collision CM system), so upon reconstructing a candidate, the quantity ΔE accumulates at $\Delta E = 0\,\mathrm{GeV}$ and M_{bc} at the true B_s mass, m_{B_s}. In the decay $B_s^* \to B_s\gamma$, the photon carries away essentially all of the released energy, which is equal to the mass difference, $\delta M \approx 50\,\mathrm{MeV}/c^2$. In a $B_s^*\bar{B}_s$ event, the $\bar{B}_s$ (B_s^*) carries energy $\sim E_{\mathrm{beam}} - \delta Mc^2/2$ ($\sim E_{\mathrm{beam}} + \delta Mc^2/2$). The daughter B_s from $B_s^* \to B_s\gamma$ carries energy $\sim E_{\mathrm{beam}} - \delta Mc^2/2$. Thus, for both of these B_ss, one can expect reconstructed decays to accumulate around $\Delta E = -\delta Mc^2/2$ and $M_{\mathrm{bc}} = m_{B_s} + \delta M/2$. Carrying the process another step further, both B_ss in $B_s^*\bar{B}_s^*$ events accumulate at $\Delta E = -\delta Mc^2$ and $M_{\mathrm{bc}} = m_{B_s} + \delta M = m_{B_s^*}$. Given the Belle detector's momentum resolution, these three event types accumulate in well-separated regions of

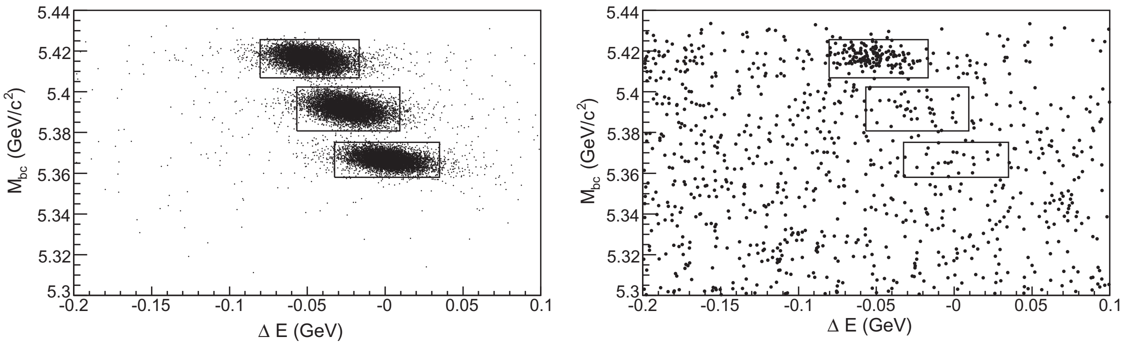

Fig. 49. Illustration of the full reconstruction method, $B_s \to D_s\pi$. Distributions in ΔE and $M_{\rm bc}$ of candidates, (left) Monte Carlo simulation, (right) data, 24FB set. Also shown are signal regions for $B_s^*\bar{B}_s^*$ (upper signal box), $B_s^*\bar{B}_s$ (middle box), and $B_s\bar{B}_s$ (lower box) events [276].

ΔE and $M_{\rm bc}$, as shown in Fig. 49 for $B_s \to D_s^-\pi^+$ candidates, signal Monte Carlo simulations, and data [276].

As can be seen from Fig. 49, the $B_s^*\bar{B}_s^*$ events dominate in the data. As explained above, the $M_{\rm bc}$ distribution peaks at m_{B_s} (with very minor corrections). The $B_s^* - B_s$ mass difference is found from the mean ΔE of the candidates; the B_s candidate mass reconstructed as $M'_{\rm bc} = \sqrt{(E^*_{\rm beam} + \langle\Delta E\rangle)^2 - (p^*_{\rm cand})^2}$ accumulates at the B_s mass. The modes $\bar{B}_s \to D_s^+\pi^-\{D_s \to \phi(\to K^+K^-)\pi^-, K^{*0}(\to K^+K^-)K^-, K_S(\to \pi^+\pi^-)K^-\}$ were reconstructed for this measurement. $B_s^*\bar{B}_s^*$ candidates are selected by requiring $-0.08 < \Delta E < -0.02$ GeV. From the 24FB data set we measure [276]

$$m_{B_s^*} = 5416.4 \pm 0.4 \pm 0.5\,\mathrm{MeV}/c^2$$
$$m_{B_s} = 5364.4 \pm 1.3 \pm 0.7\,\mathrm{MeV}/c^2.$$

8.2. *Event composition at the* $\Upsilon(10\,860)$ *peak*

To study production and decay rates of B_s, their abundance and properties in $\Upsilon(10\,860)$ events are needed. This evaluation proceeds in three steps. First, we measure the hadronic $b\bar{b}$ cross section [277]. We then find the fraction of $b\bar{b}$ events containing B_s [277]. Finally, we measure the relative rates to the three possible event types [276].

8.2.1. $\sigma(e^+e^- \to b\bar{b})$. As is the case at the $\Upsilon(4S)$, $b\bar{b}$ events at the $\Upsilon(10\,860)$ (where "$b\bar{b}$" includes both resonance and $b\bar{b}$ continuum events, which are indistinguishable) are readily distinguished statistically from the continuum of lighter quarks $e^+e^- \to q\bar{q}$ ($q = u, d, s, c$) via their distribution in R_2, the ratio of the second and zeroth Fox–Wolfram moments [35], a measure of "jettiness" that tends to be lower for the more isotropic $b\bar{b}$ events. The R_2 distribution for the 2FB data and a scaled continuum sample are shown in Fig. 50. We found $\sigma_{e^+e^-\to b\bar{b}} = (3.01 \pm 0.02 \pm 0.16) \times 10^2$ pb [277], which constitutes ≈10% of the total hadronic cross section. This value was averaged with the corresponding result from CLEO [278] to obtain the PDG average of $\sigma_b = (3.02 \pm 0.14) \times 10^2$ pb [23].

8.2.2. $\sigma(e^+e^- \to B_s\bar{B}_s)/\sigma(e^+e^- \to b\bar{b})$. The fraction ($f_s$) of $b\bar{b}$ events that hadronize to B_s ($B_s^{(*)}\bar{B}_s^{(*)}$) may be determined through measurement of the inclusive rate $\mathcal{B}(\Upsilon(10\,860) \to D_sX) \equiv \mathcal{B}_\Upsilon$. The B_s decays predominantly via the spectator mechanism, as do the lighter B mesons, and as

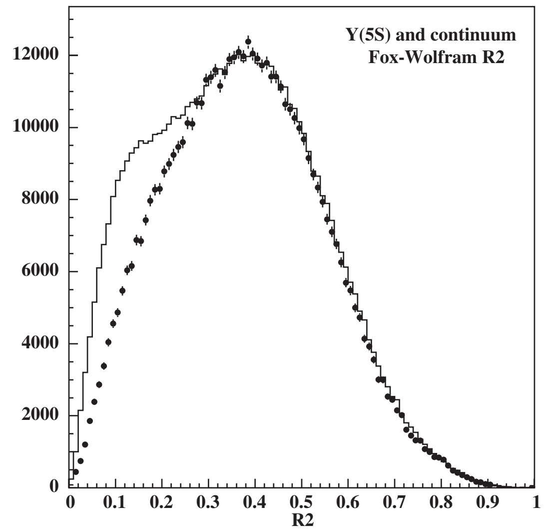

Fig. 50. Distribution in R_2, (histogram) data set 2FB, at the $\Upsilon(10\,860)$ and (points) continuum below $\Upsilon(4S)$, scaled.

such we can assume a direct correspondence between $B \to DX$ and $B_s \to D_s X$ for a large fraction of the decays. Based on our understanding of the mechanisms of B decay and the measured branching fractions $\mathcal{B}(B \to DX)$ and $\mathcal{B}(B \to D_s X)$, a reasonable estimate may be made [279]: $\mathcal{B}(B_s \to D_s X) = (92 \pm 11)\%$. The inclusive rate of $\Upsilon(5S) \to D_s X$ is an average over B_s, B_d, and B_u, weighted by abundance:

$$\frac{\mathcal{B}(\Upsilon(5S) \to D_s X)}{2} = f_s \cdot \mathcal{B}(B_s \to D_s X) + (1 - f_s)\frac{\mathcal{B}(\Upsilon(4S) \to D_s X)}{2} \tag{8.1}$$

where f_s is the fraction of B_s and we assume that B_d and B_u are produced equally and that non-B production is negligible. The distributions of D_s in normalized momentum $x \equiv p_{D_s}/\sqrt{E^2_{\text{beam}} - m^2_{D_s}}$ for $\Upsilon(5S)$ and scaled continuum data are shown in Fig. 51. The measured value, $\mathcal{B}(\Upsilon(5S) \to D_s X)/2 = (22.6 \pm 1.2 \pm 2.8)\%$ for the 2FB data set, is fed into Eq. (8.1) and solved to obtain [277] $f_s = (16.4 \pm 1.4 \pm 4.1)\%$, which corresponds to $(4.95 \pm 1.31) \times 10^4$ B_s events/fb^{-1}. The same analysis may be performed for D^0 to obtain an independent value of f_s, albeit with larger uncertainties; $\mathcal{B}(B_s \to D^0 X) \ll \mathcal{B}(B_q \to D^0 X)$. The results are combined to obtain [277] $f_s = (18.0 \pm 1.3 \pm 3.2)\%$. The Belle result is averaged with the corresponding CLEO result [278] to obtain the PDG average [23]

$$f_s = (19.5^{+3.0}_{-2.3})\%.$$

The same method applied to the 121FB set yields

$$f_s = (17.1 \pm 3.0)\%.$$

8.2.3. $B_s^* \bar{B}_s^* : B_s^* \bar{B}_s : B_s B_s$. As described in Sect. 8.1, reconstructed B_s signals from the three event types are well separated in ΔE and M_{bc}. These three modes account for 100% of B_s events, so the fraction comprised by each is derived from a simultaneous fit to ΔE and M_{bc} that yields all three signals. For this measurement we use $B_s \to D_s^- \pi^+$, the mode with the greatest statistical significance. To date, statistically significant signals have been observed in the $B_s^* \bar{B}_s^*$ and B_s^*

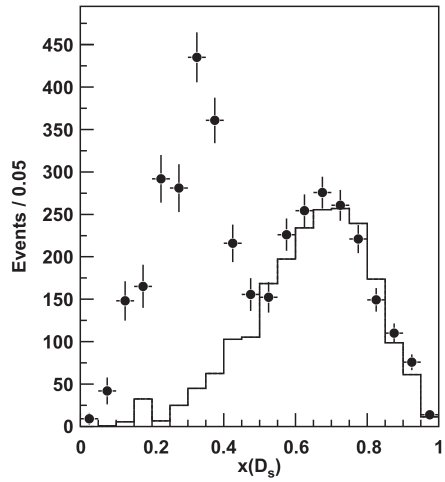

Fig. 51. Distribution of D_s in $x \equiv p_{D_s}/\sqrt{E^2_{\text{beam}} - m^2_{D_s}}$, (points) $\Upsilon(10\,860)$ and (histogram) scaled continuum [277].

$\bar{B}_s + B_s \bar{B}^*_s$ channels in the 24FB data set, from which we obtain [276]

$$f_{B^*_s B^*_s} \equiv \frac{\sigma(e^+e^- \to B^*_s \bar{B}^*_s)}{\sigma(e^+e^- \to B^{(*)}_s \bar{B}^{(*)}_s)} = (90.1^{+3.8}_{-4.0} \pm 0.2)\%$$

$$f_{B^*_s B_s} \equiv \frac{\sigma(e^+e^- \to B^*_s \bar{B}_s + B_s \bar{B}^*_s)}{\sigma(e^+e^- \to B^{(*)}_s \bar{B}^{(*)}_s)} = (7.3^{+3.3}_{-3.0} \pm 0.1)\%.$$

The value $f_{B^*_s B^*_s} = (87.0 \pm 1.7)\%$ from the 121FB data set (unpublished)[6] is used in evaluating branching fractions from the 121FB set.

8.2.4. $B^{(*)}\bar{B}^{(*)}(\pi)(\pi)$. The well-tuned methods of B reconstruction at the $\Upsilon(4S)$ (Sect. 4.4.2) have been applied to study the more complicated assortment of B events at the $\Upsilon(10\,860)$ [280]. The following final states that include non-strange B mesons are energetically allowed: $B^{(*)}_q \bar{B}^{(*)}_q$, $B_q \bar{B}^{(*)}_q \pi$, $B_q \bar{B}_q \pi\pi$. The relative rates can improve our understanding of hadronization dynamics. Neutral and charged Bs are reconstructed in the following modes and submodes: $B^+ \to J/\psi K^+$, $\bar{D}^0\pi^+$; $B^0 \to J/\psi K^{*0}$, $D^-\pi^+$; $J/\psi \to e^+e^-$, $\mu^+\mu^-$; $K^{*0} \to K^+\pi^-$; $\bar{D}^0 \to K^+\pi^-$, $K^+\pi^+\pi^-\pi^-$; $D^- \to K^+\pi^-\pi^-$. As with the fully reconstructed B_s, the signal events populate the $(\Delta E, M_{\text{bc}})$ plane in clusters depending on the type of event. Figure 52(a) shows the projections in M_{bc} of the distributions for the various event types. The distribution of candidates in data, after background subtraction, are shown in Fig. 52(b). While the distributions for events containing additional pions overlap each other, it is clear from the data that their contribution is relatively small and that the majority of the rate is due to two-body events, $B^{(*)}\bar{B}^{(*)}$. It is also noted that there is an accumulation of events in the region of high M_{bc}, where $B\bar{B}\pi\pi$ events would accumulate, according to the MC simulation. The fractions of $b\bar{b}$ events fragmenting to $B\bar{B}$, $B^*\bar{B}$, and $B^*\bar{B}^*$ are measured to be $(5.5^{+1.0}_{-0.9} \pm 0.4)\%$, $(13.7 \pm 1.3 \pm 1.1)\%$, and $(37.5^{+2.1}_{-1.9} \pm 3.0)\%$, respectively. The events where M_{bc} is above the two-body limit are grouped together as "large M_{bc}" and found to comprise $(17.5^{+1.8}_{-1.6} \pm 1.3)\%$.

[6] This result is obtained by Belle using 121.4 fb^{-1} of data and the method described in Ref. [276].

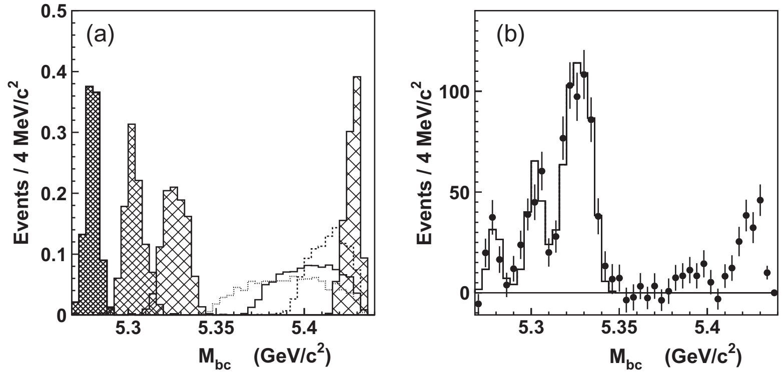

Fig. 52. (a) Distributions in M_{bc} for reconstructed $B^0 \to D^-\pi^+$, for $B\bar{B}$, $B\bar{B}^* + B^*\bar{B}$, $B^*\bar{B}^*$, and $B\bar{B}\pi\pi$ channels (cross-hatched histograms, left to right) and for the three-body channels $B\bar{B}^*\pi + B^*\bar{B}\pi$ (plain histogram), $B\bar{B}\pi$ (dotted), and $B^*\bar{B}^*\pi$ (dashed). The distributions are normalized to unity. (b) M_{bc} distribution in data after background subtraction. The sum of the five studied B decays (points with error bars) and results of the fit (histogram) used to extract the two-body channel fractions are shown.

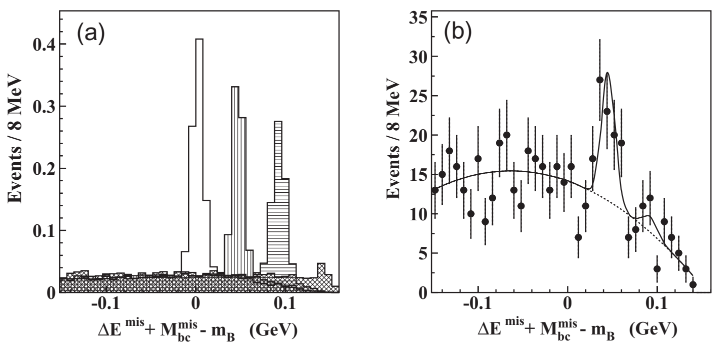

Fig. 53. (a) The $\Delta E_{\mathrm{miss}} + M_{\mathrm{bc,miss}} - m_B$ distribution normalized per reconstructed B meson for MC simulated $B^+ \to J/\psi K^+$ decays in the (peaks from left to right) $B\bar{B}\pi^+$, $B\bar{B}^*\pi^+ + B^*\bar{B}\pi^+$, $B^*\bar{B}^*\pi^+$, and $B\bar{B}\pi\pi$ channels. (b) The $\Delta E_{\mathrm{miss}} + M_{\mathrm{bc,miss}} - m_B$ data distribution for right-sign $B^{-/0}\pi^+$ combinations for all five studied B modes. The curve shows the result of the fit [280].

Events containing one or more additional pions may be identified by pairing reconstructed Bs with additional charged pions in the event and examining the residual, or *missing*, event energy and momentum, E_{miss} and $\vec{P}_{\mathrm{miss}}$, which by inference are carried by the opposing $B^{(*)}$ and up to one additional pion. From these we reconstruct ΔE_{miss} and $M_{\mathrm{bc,miss}}$. Projections onto $\Delta E_{\mathrm{miss}} + M_{\mathrm{bc,miss}} - m_B$ for various simulated event types are shown in Fig. 53(a). The corresponding distribution in data, with the fit result, is shown in Fig. 53(b). The fractions of $b\bar{b}$ events hadronizing to three-body modes $B\bar{B}\pi$, $B\bar{B}^*\pi$, and $B^*\bar{B}^*\pi$ are found to be $(0.0 \pm 1.2 \pm 0.3)\%$, $(7.3^{+2.3}_{-2.1} \pm 0.8)\%$, and $(1.0^{+1.4}_{-1.3} \pm 0.4)\%$, respectively. Paradoxically, no evidence for $B\bar{B}\pi\pi$ was observed, so this channel does not account for the remaining $(9.2^{+3.0}_{-2.8} \pm 1.0)\%$ of the "large M_{bc}" contribution observed in $\Upsilon(10\,860) \to BX$. The residual is quantitatively consistent with initial state radiation, $e^+e^- \to e^+e^-\gamma,\ e^+e^- \to b\bar{b}$, where about half the $b\bar{b}$ form the $\Upsilon(4S)$ resonance [280].

8.3. B_s decays

To a large degree, the general properties of the B_s meson parallel those of the non-strange B mesons. Like its lighter cousins, the B_s is expected to decay predominantly by a spectator process, where the lighter valence quark has no role in the weak interaction, and its spectator-dominated properties

Table 21. Branching fractions with statistical and systematic uncertainties. A third uncertainty, due to f_s, is quoted where it is separated from other systematics. The data set analyzed is identified in the rightmost column.

Mode	$\mathcal{B}(10^{-4})$	Data set
Single-D_s modes		
$D_s^- \pi^+$	$36.7^{+3.5+4.3}_{-3.3-4.2} \pm 4.9$	24FB
$D_s^{*-} \pi^+$	$24^{+5}_{-4} \pm 3 \pm 4$	24FB
$D_s^- \rho^+$	$85^{+13}_{-12} \pm 11 \pm 13$	24FB
$D_s^{*-} \rho^+$	$118^{+22}_{-20} \pm 17 \pm 18$	24FB
$c\bar{c}s\bar{s}$ modes		
$J/\psi\eta$	$5.10 \pm 0.50 \pm 0.25^{+1.14}_{-0.79}$	121FB
$J/\psi\eta'$	$3.71 \pm 0.61 \pm 0.18^{+0.83}_{-0.57}$	121FB
$J/\psi f_0(980)$	$1.16^{+0.31+0.15+0.26}_{-0.19-0.17-0.18}$	121FB
$J/\psi f_0(1370)$	$0.34^{+0.11+0.03+0.08}_{-0.14-0.02-0.05}$	121FB
$D_s^{*+} D_s^{*-}$	$200 \pm 30 \pm 50$	121FB
$D_s^{*+} D_s^- + c.c.$	$180 \pm 20 \pm 40$	121FB
$D_s^+ D_s^-$	$58^{+11}_{-9} \pm 13$	121FB
$D_s^{(*)+} D_s^{(*)-}$ sum	$430 \pm 40 ^{+60}_{-50} \pm 90$	121FB
$h\bar{h}$ modes		
K^+K^-	$0.38^{+0.10}_{-0.09} \pm 0.05 \pm 0.05$	24FB
$K^0\bar{K}^0$	<0.66(90% C.L.)	24FB
$K^-\pi^+ + c.c.$	<0.26(90% C.L.)	24FB
$\pi^+\pi^-$	<0.12(90% C.L.)	24FB
$\phi\gamma$	$0.57^{+0.18+0.12}_{-0.15-0.11}$	24FB
$\gamma\gamma$	<870(90% C.L.)	24FB

such as lifetime are expected to be similar. This is serendipitous at the B-factory, allowing many of the techniques developed for analysis of Bs at the $\Upsilon(4S)$ to be applied to B_s at the Υ(5S). Furthermore, close correspondences between the hadronic final states in spectator decays of B_s and B_d allow for sensitive tests of quark–hadron duality and of hadronic models that may reduce theoretical uncertainties limiting precision CKM tests in B physics.

Being electrically neutral, the B_s experiences mixing and may thus address questions of interest regarding CP violation and roles for physics beyond the Standard Model. Notably, B_s experiences a much higher rate of mixing than B_d, and very little CP violation in the SM.

All branching fractions described in this section are listed in Table 21. The branching fractions measured in the 24FB set are evaluated using $f_{B_s^* B_s^*} = (90.1^{+3.8}_{-4.0})\%$, $f_s = (19.5^{+3.0}_{-2.3})\%$, and $\sigma_{e^+e^-\to b\bar{b}} = 0.302 \pm 0.014$ nb (a weighted average from Refs. [277,278]). The results based on the 121FB set have used $N_{B_s^{(*)}\bar{B}_s^{(*)}} = (7.1 \pm 1.3) \times 10^6 = \mathcal{L} \times \sigma_{e^+e^-\to b\bar{b}} \times f_s$ and $f_{B_s^* B_s^*} = (87.1 \pm 3.0)\%$.

8.3.1. Modes with single D_s. The decays $B_s \to D_s^{(*)-} h^+$, where h is a light non-strange meson, proceed dominantly via a CKM-favored spectator process. The D_s are reconstructed in the modes $\phi(\to K^+K^-)\pi^-$, $K^{*0}(\to K^+K^-)K^-$, and $K_S(\to \pi^+\pi^-)K^-$ and $\rho^\pm$ in $\pi^\pm\pi^0$. As described in Sect. 8.1, the signal is extracted by fitting the distributions in ΔE and $M_{\rm bc}$ (and decay angles, for $B_s \to D_s^{*-}\rho^+$). Shown in Fig. 54 (left) is the projection into $M_{\rm bc}$ for $B_s \to D_s^-\pi^+$ candidates in the 24FB set. The branching fraction for modes other than $D_s^-\pi^+$ are obtained using only the $B_s^*\bar{B}_s^*$ sample and the value of $f_{B_s^* B_s^*}$ measured with $D_s^-\pi^+$ [276,281].

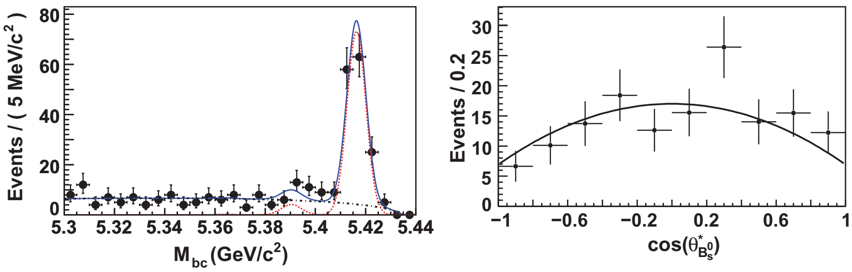

Fig. 54. (Left) $M_{\rm bc}$ distribution of $B_s \to D_s^- \pi^+$ candidates with ΔE in the $B_s^* \bar{B}_s^*$ signal region $[-80, -17]$ MeV, 24FB data set [276]. The different fitted components are shown with dashed curves for the signal, dotted curves for the $B_s \to D_s^{*-}\pi^+$ background, and dash-dotted curves for the continuum. (Right) Fitted distribution of the cosine of the angle between the B_s momentum and the beam axis in the CM frame for the $\Upsilon(5S) \to B_s^* \bar{B}_s^*$ signal.

The distribution of the angle between the B_s momentum and the beam axis in the CM frame, $\theta^*_{B_s}$, is of theoretical interest [282] and is presented in Fig. 54 (right) for the signal events in the $B_s^* \bar{B}_s^*$ region. A fit of the distribution to $1 + a\cos^2\theta^*_{B_s}$ returns χ^2/n.d.f. $= 8.74/8$ with $a = -0.59^{+0.18}_{-0.16}$. We naively expect $a = -0.27$ by summing over all the possible polarization states.

For $B_s \to D_s^{*-}\rho^+$, a pseudoscalar decay to two vectors, the distributions in the helicity angles $\theta_{D_s^{*-}}$ and θ_{ρ^+} depend on the relative contribution from the different helicity states, which depends on the detailed hadronization mechanism for the decay; for example, the factorization hypothesis predicts that longitudinal polarization dominates: $f_L \approx 88\%$ [283]. A four-dimensional fit yields $77.7^{+14.6}_{-13.3}$ (7.4σ) signal events and $f_L = 1.05^{+0.08+0.03}_{-0.10-0.04}$ [281].

8.3.2. Flavor-neutral channels. An interesting characteristic of B_s stems from the fact that it experiences an appreciable rate to the flavor-neutral combination $c\bar{c}s\bar{s}$, via a tree-level CKM-favored process. The massiveness of the participating quarks and proximity to mass threshold argue for the applicability of predictions at the limit $m_{(b,c)} \to \infty$ with $(m_b - 2m_c) \to 0$ and N_c(number of colors) $\to \infty$, where the $c\bar{c}s\bar{s}$ final states are CP-even and the $D_s^{*\pm}D_s^{\mp}$ and $D_s^{*+}D_s^{*-}$ modes (along with $D_s^+D_s^-$) saturate the width difference $\Delta\Gamma_s^{CP}$ between the two CP-eigenstates [284]. This parameter equals $\Delta\Gamma_s/\cos\phi_s$, where $\Delta\Gamma_s$ is the decay width difference between the mass eigenstates, and ϕ_s is the CP-violating phase in B_s–$\overline{B}_s$ mixing[7]. Thus the summed branching fraction $\mathcal{B}(B_s^0 \to D_s^{(*)+}D_s^{(*)-})$ gives a constraint in the $\Delta\Gamma_s$–ϕ_s parameter space. Both parameters can receive contributions from NP; see, e.g., Refs. [287–289]. Assuming negligible CP violation ($\phi_s \approx 0$), the branching fraction is related to $\Delta\Gamma_s$ via

$$\Delta\Gamma_s/\Gamma_s = 2\mathcal{B}/(1-\mathcal{B}). \tag{8.2}$$

The quantity of interest, the summed branching fraction $\mathcal{B} = \mathcal{B}(B_s \to D_s^{(*)+}D_s^{(*)-}$, is more easily measured in $e^+e^- \to \Upsilon(5\mathrm{S})$ than at a hadron machine because the decay $D_s^* \to D_s\gamma$ can be fully reconstructed.

The final Belle result is based on the 121FB set [290]. It includes the first measurement of the fraction of longitudinal polarization (f_L) of $B_s^0 \to D_s^{*+}D_s^{*-}$. The final states reconstructed consist of $D_s^+D_s^-$, $D_s^{*+}D_s^- + D_s^{*-}D_s^+$ ($\equiv D_s^{*\pm}D_s^{\mp}$), and $D_s^{*+}D_s^{*-}$, where $D_s^{*+} \to D_s^+\gamma$, $D_s^+ \to \phi\pi^+$,

[7] Specifically, $\phi_s = \arg(-M_{12}/\Gamma_{12})$, where M_{12} and Γ_{12} are the off-diagonal elements of the B_s–$\overline{B}_s$ mass and decay matrices; see Refs. [285,286].

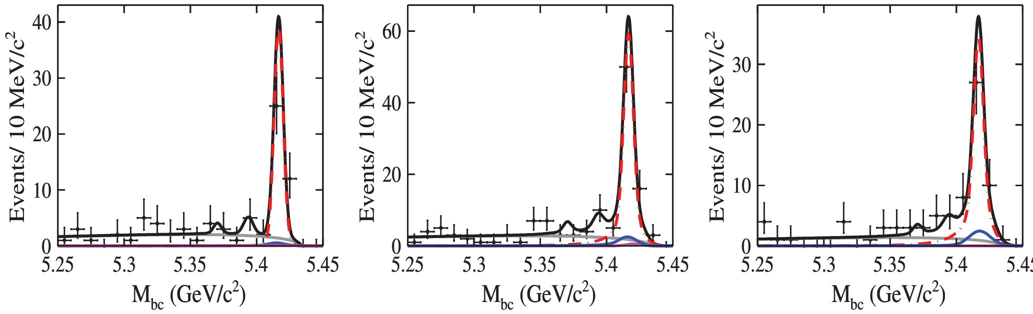

Fig. 55. M_{bc} projections and fit results, (left) $B_s^0 \to D_s^+ D_s^-$, (center) $B_s^0 \to D_s^{*\pm} D_s^{\mp}$, (right) $B_s^0 \to D_s^{*+} D_s^{*-}$. The red dashed curves show CR+WC signal; the blue and purple solid curves show CF; the gray solid curves show background; and the black solid curves show the total.

$K_S^0 K^+$, $\overline{K}^{*0} K^+$, $\phi\rho^+$, $K_S^0 K^{*+}$, and $\overline{K}^{*0} K^{*+}$, $K_S^0 \to \pi^+\pi^-$, $K^{*0} \to K^+\pi^-$, $K^{*+} \to K_S^0\pi^+$, $\phi \to K^+K^-$, $\rho^+ \to \pi^+\pi^0$, and $\pi^0 \to \gamma\gamma$.[8]

Events containing candidates satisfying $5.25\,\text{GeV}/c^2 < M_{\text{bc}} < 5.45\,\text{GeV}/c^2$ and $-0.15\,\text{GeV} < \Delta E < 0.10\,\text{GeV}$ are selected. Approximately half the selected events have multiple $B_s^0 \to D_s^{(*)+} D_s^{(*)-}$ candidates. These typically arise from photons produced via $\pi^0 \to \gamma\gamma$ that are wrongly assigned as D_s^* daughters. For these events we select the candidate that minimizes a χ^2 constructed from the reconstructed D_s^+ and (if present) D_s^{*+} masses.

Signal yields are measured by performing a two-dimensional unbinned maximum-likelihood fit to the M_{bc}–ΔE distributions. The combinatorial effects of analyzing multiple multi-body decays present a particular challenge in this analysis. The signal PDFs have three components: correctly reconstructed (CR) decays; "wrong combination" (WC) decays in which a non-signal track or γ is included in place of a true daughter track or γ; and "cross-feed" (CF) decays in which a $D_s^{*\pm} D_s^{\mp}$ ($D_s^{*+} D_s^{*-}$) is reconstructed as a $D_s^+ D_s^-$ ($D_s^+ D_s^-$ or $D_s^{*\pm} D_s^{\mp}$), or a $D_s^+ D_s^-$ ($D_s^{*\pm} D_s^{\mp}$) is reconstructed as a $D_s^{*\pm} D_s^{\mp}$ or $D_s^{*+} D_s^{*-}$ ($D_s^{*+} D_s^{*-}$). In the former case, the γ from $D_s^{*+} \to D_s^+\gamma$ is lost and ΔE is shifted down by 100–150 MeV; this is called "CF-down." In the latter case, an extraneous γ is included and ΔE is shifted up by a similar amount; this is called "CF-up." In both cases M_{bc} remains almost unchanged. The small contributions from $B_s\overline{B}_s$ and $B_s\overline{B}_s^*$ events are fixed relative to $B_s^*\overline{B}_s^*$ according to our measurement on $B_s^0 \to D_s^-\pi^+$ decays (see footnote to Sect. 8.2.3). The fitted signal yields from $B_s^*\overline{B}_s^*$ only are used to determine the branching fractions.

The projections of the fit are shown in Fig. 55. The branching fraction for channel i is calculated as $\mathcal{B}_i = Y_i/(\varepsilon_{MC}^i \cdot N_{B_s\overline{B}_s} \cdot f_{B_s^*\overline{B}_s^*} \cdot 2)$, where Y_i is the fitted CR yield, and ε_{MC}^i is the MC signal efficiency with intermediate branching fractions [23] included. The statistical significance is calculated as $\sqrt{-2\ln(\mathcal{L}_0/\mathcal{L}_{\text{max}})}$, where $\mathcal{L}_0$ and $\mathcal{L}_{\text{max}}$ are the values of the likelihood function when the signal yield Y_i is fixed to zero and when it is floated, respectively. We include systematic uncertainties (discussed below) in the significance by smearing the likelihood function by a Gaussian having a width equal to the total systematic error related to the signal yield.

Inserting the total $\mathcal{B}$ from Table 21 into Eq. 8.2 gives

$$\Delta\Gamma_s/\Gamma_s = 0.090 \pm 0.009 \pm 0.023, \tag{8.3}$$

[8] Charge-conjugate modes are implicitly included.

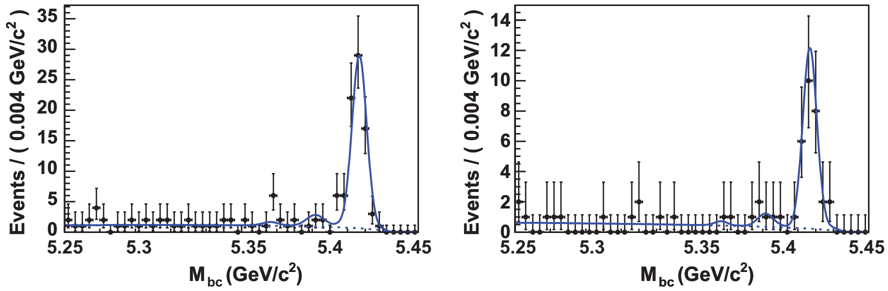

Fig. 56. Projections in M_{bc}, based on the 121FB data set at $\Upsilon(10\,860)$: (left) $B_s \to J/\psi\eta(\gamma\gamma)$, (right) $B_s \to J/\psi\eta(\pi^+\pi^-\pi^0)$. Solid curves show projections of fit results. Backgrounds are represented by the blue dotted curves. Two small bumps around 5.37 and 5.39 GeV$/c^2$ are contributions from $B_s^0\bar{B}_s^0$ and $B_s^*\bar{B}_s^0$ production channels, due to the overlap of the ΔE signal regions.

where the first error is statistical and the second is systematic. This result has precision similar to that of other recent measurements [291,292]. The central value is consistent with, but lower than, the theoretical prediction [287]; the difference may be due to the unknown CP-odd component in $B_s^0 \to D_s^{*+}D_s^{*-}$, and contributions from three-body final states. With more data these unknowns can be measured. The former is estimated to be only 6% for analogous $B^0 \to D^{*+}D_s^{*-}$ decays [293], but the latter can be significant: Ref. [294] calculates $\Delta\Gamma(B_s \to D_s^{(*)}D^{(*)}K^{(*)})/\Gamma_s = 0.064 \pm 0.047$. This calculation predicts $\Delta\Gamma_s/\Gamma_s$ from $D_s^{(*)+}D_s^{(*)-}$ alone to be 0.102 ± 0.030, which agrees well with our result.

To measure f_L, we perform an unbinned ML fit to the helicity angles θ_1 and θ_2, which are the angles between the daughter γ momentum and the opposite of the B_s momentum in the D_s^{*+} and D_s^{*-} rest frames, respectively. The angular distribution is $\left(|A_+|^2 + |A_-|^2\right)\left(\cos^2\theta_1 + 1\right)\left(\cos^2\theta_2 + 1\right) + |A_0|^2 4\sin^2\theta_1\sin^2\theta_2$, where A_+, A_-, and A_0 are the three polarization amplitudes in the helicity basis. The fraction $f_L = |A_0|^2/(|A_0|^2 + |A_+|^2 + |A_-|^2)$. We obtain [290]

$$f_L = 0.06\,^{+0.18}_{-0.17} \pm 0.03, \tag{8.4}$$

where the first error is statistical and the second is systematic. Reconstruction of B_s decays to well-defined CP final states are of interest for studies of CP violation. In the SM, mixing-mediated CP violation occurs in neutral mesons due to the complex argument of the product of CKM matrix elements participating in the mixing “box diagram.” For B_s the relevant product is $V_{\rm tb}^{*2}V_{\rm ts}^2$, which is real, so no significant asymmetry is expected. Searches for CP asymmetry in decays of B_s thus present an opportunity to reveal NP. Such measurements will require the reconstruction of a sizable sample of CP-defined final states.

The decays $B_s \to J/\psi\eta^{(\prime)}$ ($CP = +1$) proceed by the same process as $B \to J/\psi K^0$, so the branching fractions may be estimated based on the measured branching fractions [23], $\mathcal{B}(B_d^0 \to J/\psi K^0) = 8.71 \times 10^{-4}$: $\mathcal{B}(B_s \to J/\psi\eta) \approx 3.5 \times 10^{-4}$, and $\mathcal{B}(B_s \to J/\psi\eta') \approx 4.9 \times 10^{-4}$. The decays are reconstructed in the following modes: $J/\psi \to e^+e^-,\ \mu^+\mu^-$; $\eta \to \gamma\gamma, \pi^+\pi^-\pi^0$; $\eta' \to \eta\pi^+\pi^-, \rho^0\gamma$. The signals are extracted via a 2-dimensional fit in ΔE and $M_{\rm bc}$. Projections in $M_{\rm bc}$ are shown in Fig. 56.

The same $b \to c\bar{c}s$ process can also produce the decay $B_s^0 \to J/\psi f_0(980)$, another promising channel for CP studies, with the clear advantage of being an all-charged final state with no angular analysis required because of the $J^P = 0^+$ quantum numbers of the $f_0(980)$. The mode was reconstructed as $B_s \to J/\psi\pi^+\pi^-$, $\{J/\psi \to \mu^+\mu^-, e^+e^-\}$, analyzing the 121FB set. The fit to data include the $f_0(980)$ and another resonance in the $\pi\pi$ mass spectrum at $\sim 1.4\,\mathrm{GeV}^2$, f_X (Fig. 57).

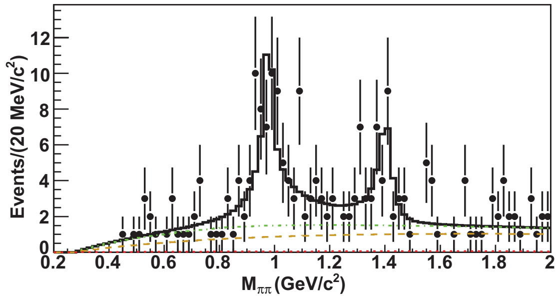

Fig. 57. Pion pair mass distribution for $B_s \to J/\psi\pi^+\pi^-$ candidates in the 121FB set, for $-79.7\,\text{MeV} < \Delta E < -19.7\,\text{MeV}$. The solid line represents the total PDF. The dash-dotted curve represents the total background, the dashed curve shows other J/ψ background, and the dotted curve the nonresonant component.

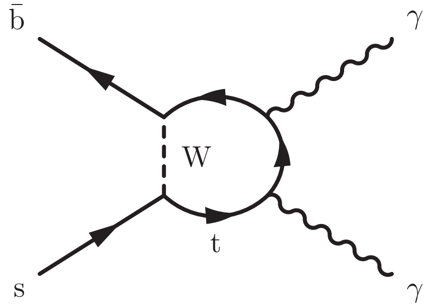

Fig. 58. Diagram describing the dominant processes for $B_s \to \gamma\gamma$.

The f_X mass, measured at $1.405 \pm 0.015^{+0.001}_{-0.007}\,\text{GeV}/c^2$, is consistent with that of the $f_0(1370)$. The nonresonant yield is consistent with zero.

We have also searched for the 2-body CP-eigenstate modes $B_s \to K^+K^-$, $K^0\bar{K}^0$, and $\pi^-\pi^+$, as well as the flavored mode $B_s \to K^-\pi^+$, in the 24FB data set [295]. The findings for K^+K^- and $K^0\bar{K}^0$ were the first absolute branching fraction and first reported limit, respectively.

8.3.3. Radiative decays. Radiative penguin decays, which produce a photon via a one-loop Feynman diagram, are a promising venue to search for physics beyond the SM because particles at mass scales not yet directly accessible at accelerators can contribute to such loop effects. The $B_s \to \phi\gamma$ mode is a radiative process described within the SM by a $\bar{b} \to \bar{s}\gamma$ penguin diagram; it is the counterpart of the $B \to K^*(892)\gamma$ decay. In the SM, the $B_s \to \phi\gamma$ branching fraction has been computed with $\sim$30% uncertainty to be about 40×10^{-6} [296,297]. This channel was first observed at Belle, with ϕ reconstructed in the mode K^+K^- [298]. For photon selection, major sources of background in the signal region included $\pi^0 \to \gamma\gamma$ and $\eta \to \gamma\gamma$ as well as calorimeter hits that were out of time with the beam crossing. Based on the 24FB set, we reported $\mathcal{B}(B_s \to \phi\gamma) = (57^{+18}_{-15}(\text{stat})^{+12}_{-11}(\text{syst})) \times 10^{-6}$, which is in agreement with both the SM predictions and with extrapolations from measured $B^+ \to K^*(892)^+\gamma$ and $B^0 \to K^*(892)^0\gamma$ decay branching fractions [298].

8.3.4. Modes suppressed in the Standard Model. The $B_s \to \gamma\gamma$ mode is described in the SM by a penguin annihilation diagram (Fig. 58), and its branching fraction has been calculated to be in the range $(0.5\text{–}1.0) \times 10^{-6}$ [299–301]. Belle has searched for this mode in the 24FB data set [298]. No

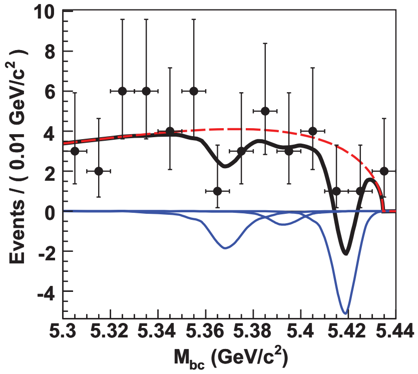

Fig. 59. $M_{\rm bc}$ projection and fit for the $B_s \to \gamma\gamma$ search 24FB data set.

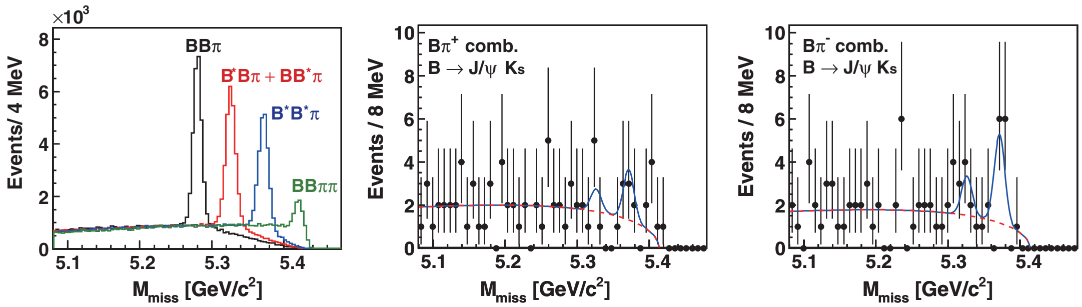

Fig. 60. Distributions in $M_{\rm miss}$ of tagged $B^0\pi$ candidates for (left) simulated $B\bar{B}\pi$, $B\bar{B}^*\pi$, and $B^*\bar{B}^*\pi$ events and 121.4 fb^{-1} of data, (center) $B^0\pi^+$ and (right) $B^0\pi^-$.

significant signal was observed (Fig. 59), and a 90% C.L. upper limit of $\mathcal{B}(B_s \to \gamma\gamma) < 8.7 \times 10^{-6}$ was obtained. This limit significantly improves on the previously reported one and is only an order of magnitude larger than the SM prediction, providing the possibility of observing this decay at a future Super B-factory [302,303].

8.4. *Measurement of* $\sin 2\phi_1$

The method of full B reconstruction, used to study the assortment of B events at the $\Upsilon(5S)$ [280], has been applied to a novel tag to measure $\sin 2\phi_1$ [304]. Three-body final states $B^{(*)0}\{\to B^0(\gamma)\}B^{(*)-}\pi^+$ $(+c.c.)$ are identified through full reconstruction of a neutral B in a CP-eigenstate and a charged pion. The event residue, consisting of a charged B and up to two photons, is characterized through "missing mass," calculated through energy and momentum conservation:

$$E_{\rm miss} = E_{\rm beam} - E_{B^0\pi}; \quad \vec{p}_{\rm miss} = -\vec{p}_{B^0\pi}; \quad MM(B^0\pi) = M_{\rm miss} = \sqrt{E^2_{\rm miss} - \vec{p}^{\,2}_{\rm miss}}.$$

The missing mass distributions are well separated for $B\bar{B}\pi\pi$, $B\bar{B}\pi$, $B\bar{B}^*\pi$, and $B^*\bar{B}^*\pi$ events, as can be seen in Fig. 60 (left). The sign of the charged pion tags the initial flavor of the neutral B and enables a *time-independent* measurement of CP asymmetry, which is related to $\sin 2\phi_1$ as:

$$A_{BB\pi} \equiv \frac{N_{BB\pi^-} - N_{BB\pi^+}}{N_{BB\pi^-} + N_{BB\pi^+}} = \frac{\mathcal{S}x + \mathcal{A}}{1 + x^2}$$

where $\mathcal{S} = -\eta_{CP}\sin 2\phi_1$ (η_{CP} is the CP-eigenvalue of the B^0 mode), $x = \Delta m/\Gamma$, and $\mathcal{A}$, a measure of direct CP violation, is zero in the SM.

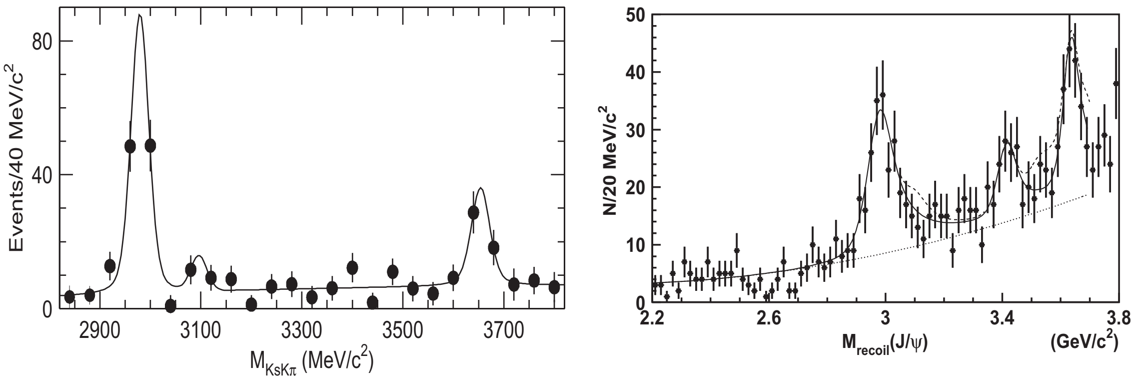

Fig. 61. Left: The $K_S K^{\pm}\pi^{\mp}$ mass distribution from $B \to K K_S K^{\pm}\pi^{\mp}$ decays [307]. The large peak on the left is the η_c; the smaller peaks on the right are the J/psi (around 3.1 GeV) and $\eta_c(2S)$ signals. Right: The J/ψ recoil mass spectrum in inclusive $e^+e^- \to J/\psi\ X$ processes [308]. A fit with η_c, χ_{c0}, and $\eta_c(2S)$ contributions is shown as a solid curve. The dashed curve in the figure corresponds to the case where the contributions of the J/ψ, χ_{c1}, χ_{c2}, and $\psi(2S)$ are set at their 90% C.L. upper limit values. The dotted curve is the background function.

Neutral Bs are reconstructed in the following modes and submodes: $B^0 \to J/\psi K_S$; $J/\psi \to e^+e^-$, $\mu^+\mu^-$. Figure 60 shows the distributions in $M_{\rm miss}$ for (center) $B^0\pi^+$ and (right) $B^0\pi^-$ combinations, respectively, where the fits yield a total of 21.5 ± 6.8 events. The asymmetry is found to be $A_{BB\pi} = 0.28 \pm 0.28$, corresponding to $\sin 2\phi_1 = 0.57 \pm 0.58 \pm 0.06$. This result establishes a new time-independent method of measuring $\sin 2\phi_1$. The value is consistent with measurements in $\Upsilon(4S)$ data.

9. New resonances

9.1. Charmonium physics

In e^+e^- collisions at CM energies near $\sqrt{s} \simeq 10.58$ GeV, there are a number of ways to produce final states that contain a $c\bar{c}$ quark pair. These include: i) B-meson decays, in which $b \to c\bar{c}s$ is a favored transition; ii) $\gamma\gamma$ fusion, which is proportional to the square of the quark charge and, thus, favors production of $c\bar{c}$ and $u\bar{u}$ pairs over $s\bar{s}$ and $d\bar{d}$ pairs; iii) near-threshold s-channel $c\bar{c}$ production via initial-state radiation; and iv) $c\bar{c}$ associated production with J/ψ mesons in e^+e^- annihilation, which Belle found to be the dominant mechanism for J/ψ productions in e^+e^- annihilation near $\sqrt{s} = 10$ GeV. Belle exploited all four of these processes to make a series of interesting discoveries related to the spectroscopy and interactions of $c\bar{c}$ charmonium mesons.

9.1.1. First observation of the $\eta_c(2S)$. Prior to 2002, the only "positive" observation of the $\eta_c(2S)$, the first radial excitation of the charmonium ground state meson, η_c, was a peak in the γ energy spectrum from exclusive $\psi(2S) \to \gamma X$ decays reported by the Crystal Ball Experiment [305]. However, this result was somewhat suspicious since the hyperfine $\psi(2S)$–$\eta_c(2S)$ mass splitting inferred from the measured mass value, $\Delta M_{\rm hfs}(2S) = 92 \pm 5$ MeV, is substantially higher than the theoretical expectation of $\Delta M^{\rm theory}_{\rm hfs}(2S) \simeq 58 \pm 8$ MeV; see, e.g., Ref. [306]. In 2002, Belle reported the observation of a higher-mass $\eta_c(2S)$ candidate in the $\eta_c(2S) \to K_S K^{\pm}\pi^{\mp}$ mass distribution produced via the $B \to K\eta_c(2S)$, $\eta_c(2S) \to K_S K^{\pm}\pi^{\mp}$ decay chain (see Fig. 61 (left)) [307]. Belle subsequently observed a signal at the same mass in the J/ψ recoil mass spectrum for inclusive $e^+e^- \to J/\psi X$ processes [308], shown in the right-hand panel of Fig. 61.

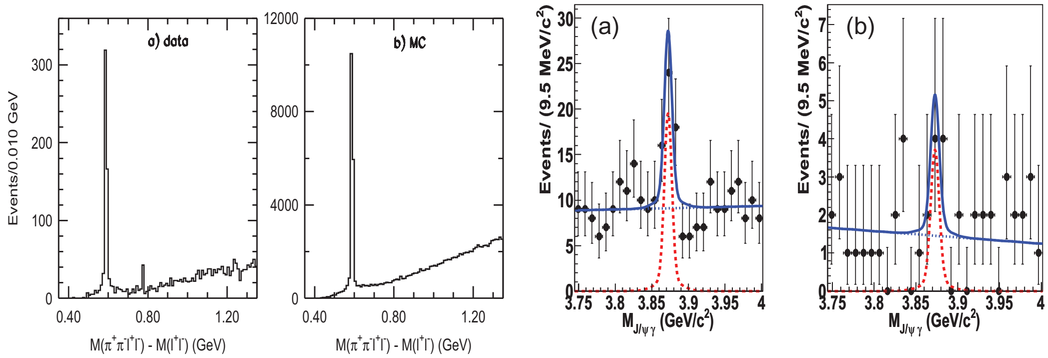

Fig. 62. Left: $\Delta M = M(\pi^+\pi^-\ell^+\ell^-) - M(\ell^+\ell^-)$ distributions for $B \to K\pi^+\pi^- J/\psi$, $J/\psi \to \ell^+\ell^-$ decays for a) data and b) inclusive $B \to J\psi X$ MC [310]. The peak near $\Delta M \simeq 0.6\,\text{GeV}$ is due to $\psi' \to \pi^+\pi^- J/\psi$ decays; the peak at $\Delta M \simeq 0.75\,\text{GeV}$ in the data, which does not show up in the MC, is due to $X(3872) \to \pi^+\pi^- J/\psi$. Right: $M(\gamma J/\psi)$ distributions for a) $B^+ \to K^+\gamma J/\psi$ and b) $B^0 \to K^0\gamma J/\psi$ decays [314].

The original Belle $\eta_c(2S)$ signal has since been confirmed by a number of reports, including a higher statistics Belle study of $B \to K K_S K^\pm \pi^\mp$ decays [309]. The current PDG world-average hyperfine splitting value, $\Delta M^{\text{PDG}}_{\text{hfs}}(2S) = 49 \pm 4\,\text{MeV}$ [23], is close to theoretical expectations and inconsistent with the Crystal Ball result, which is now generally thought to have been incorrect.

9.1.2. The X(3872). The $X(3872)$ was first observed by Belle [310] as a small narrow peak in the $\pi^+\pi^- J/\psi$ invariant mass spectrum from $B \to K\pi^+\pi^- J/\psi$ decays shown in the leftmost panel of Fig. 62. It was subsequently confirmed by CDF, D0, and BaBar [311–313]. Other $X(3872)$ decay modes that have been identified include the radiative decay, $X(3872) \to \gamma J/\psi$ [314,315], which establishes its charge conjugation parity as $C = +1$, subthreshold decays to $\omega J\psi$ [316,317], and the decay to open charm, $X(3872) \to D^{*0}\bar{D}^0$ [318–320]. The Belle signals for $X(3872) \to \gamma J/\psi$ are shown in the right panel of Fig. 62. Angular correlation studies by CDF [321] and Belle [322] indicate a preferred quantum number assignment of $J^{PC} = 1^{++}$, although 2^{-+} cannot be ruled out. The only available 1^{++} $c\bar{c}$ charmonium assignment for the $X(3872)$ is the χ'_{c1}. However, the 3872 MeV mass value is significantly lower than the expected χ'_{c1} mass of 3905 MeV, a value that is pegged to the measured $3929 \pm 6\,\text{MeV}$ mass of its $J = 2$ multiplet partner, the χ'_{c2}, which was discovered by Belle in 2006 (see below). A χ'_{c1} mass of 3872 MeV would imply that the mass splitting for the radially excited $\chi_{cJ}(2P)$ multiplet is larger than that for the $\chi_{cJ}(1P)$ multiplet, contrary to expectations from potential models and lattice QCD (C. Davies, private communication). There are similar problems for the $J^{PC} = 2^{-+}$ assignment, for which the only available $c\bar{c}$ level is the η_{c2}, the $^1D_2$ state. In this case, the 3872 MeV mass value is too high compared to the expected value of 3837 MeV, an expectation that is tightly constrained by the measured mass of its $^3D_1$ multiplet partner, the well established $\psi(3770)$.

The lack of a natural charmonium assignment and the close proximity of the $X(3872)$ mass, $3871.68 \pm 0.17\,\text{MeV}$ [23], to the $D^{*0}\bar{D}^0$ mass threshold, $3871.94 \pm 0.35\,\text{MeV}$ [23], has led to speculations that the $X(3872)$ is a loosely bound $D^{*0}\bar{D}^0$ molecule-like structure; see, e.g., Ref. [323], although other interpretations have been proposed; see, e.g., Refs. [324,325].

9.1.3. The Y(3940). The $Y(3940)$ was first observed by Belle as the near-threshold peak in the $\omega J/\psi$ invariant mass distribution in $B \to K\omega J/\psi$ decays [326], as shown in the left panel of

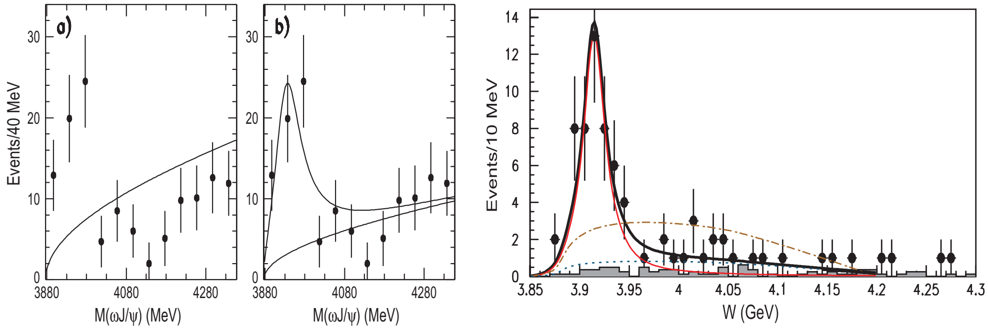

Fig. 63. Left: The points with error bars show the $M(\omega J/\psi)$ distribution for $B \to K\omega J/\psi$ decays. The curve in a) shows results of a fit to a phase-space-like threshold function. The curve in b) shows the results of a fit with a Breit–Wigner resonance function included [326]. Right: The $\omega J/\psi$ invariant mass distributions for the two-photon fusion process $\gamma\gamma \to \omega J/\psi$ [328]. The bold solid curve shows results of a fit including a resonance (thinner solid curve) and the dot-dashed curve shows a fit to a phase-space-only distribution; the histogram shows J/ψ sideband data.

Fig. 63. This observation was subsequently confirmed by BaBar [327]. The Belle experiment reported a similar peak in the near-threshold $\omega J/\psi$ mass distribution produced in the two-photon process $\gamma\gamma \to \omega J/\psi$ [328] (see Fig. 63 (right)). Although the mass of the $Y(3940)$ is well above the open-charm threshold, decays to $D\bar{D}$ [329,330] and $D^*\bar{D}$ [318] have not been seen; in the latter case, a 90% C.L. upper limit of $\mathcal{B}(Y(3940) \to D^*\bar{D}) < 1.4\mathcal{B}(Y(3940) \to \omega J/\psi)$ has been established. This limit and the rate of production in two-photon processes, implies that the partial width to $\omega J/\psi$ is large, namely $\Gamma(Y(3940) \to \omega J/\psi) > 1$ MeV, which is very large for charmonium.

Belle's $\gamma\gamma \to Y(3940) \to \omega J/\psi$ observation was confirmed by BaBar, which also included results of an angular analysis that favors a $J^{PC} = 0^{++}$ quantum number assignment [331]. The only available 0^{++} $c\bar{c}$ assignment is the χ'_{c0}, for which the mass value is somewhat high, but, perhaps, acceptable. The $\chi'_{c0} \to D^*\bar{D}$ decay mode is forbidden by parity, but $\chi'_{c0} \to D\bar{D}$ is allowed and expected to be a strongly favored mode [332], so the lack of any prominent signal for it is a mystery [329,330].

9.1.4. The Z(3930) candidate for the χ'_{c2} charmonium state. The left panel of Fig. 64 shows the $D\bar{D}$ invariant mass distribution for the process $\gamma\gamma \to D\bar{D}$ measured by Belle [333], where a strong peak near 3930 MeV is evident. The right panel shows the $|\cos\theta^*|$ distribution for events in the ± 20 MeV mass interval centered at 3930 MeV, where θ^* is the CM angle between the D meson direction and the beamline. Small values of $|\cos\theta^*|$ are favored, which is consistent with expectations for a $J = 2$ resonance (shown in the figure as a solid curve). The mass, angular distribution, and the strong decay to $D\bar{D}$ are all consistent with expectations for the χ'_{c2}, i.e., the radially excited 2^3P_2 charmonium state.

9.1.5. The $X(3940)$. Belle discovered a third meson state with mass near 3940 MeV, the $X(3940)$, produced in association with a J/ψ in e^+e^- annihilation. The left panel of Fig. 65 shows the distribution of masses recoiling from the J/ψ in inclusive $e^+e^- \to J/\psi\, X$ reactions [334]. With a partial reconstruction technique, Belle was able to isolate samples of exclusive $e^+e^- \to J/\psi D\bar{D}$ and $J/\psi D^*\bar{D}$ events. The $D\bar{D}$ and $D^*\bar{D}$ invariant mass distributions for these samples are shown in the right panels of Fig. 65. There is no sign of the $X(3940)$ in the $D\bar{D}$ events, but there is a distinct signal for $X(3940) \to D^*\bar{D}$.

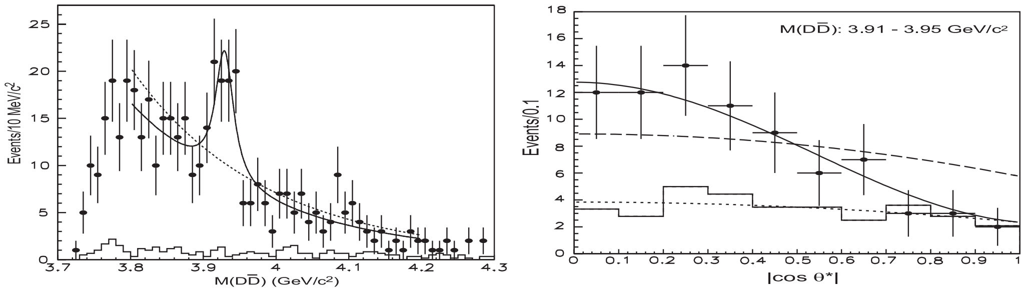

Fig. 64. Left: Invariant mass distributions for $D\bar{D}$ pairs produced via the $\gamma\gamma \to D\bar{D}$ two-photon process. The curves show fits to the data with (solid) and without a resonance term (dashed) [333]. Right: The yield of events with $3.91 < M(D\bar{D}) < 3.95\,\mathrm{GeV}$ versus $|\cos\theta^*|$. The curves are expectations for $J = 2$ (solid) and $J = 0$ (dashed); the histogram shows the $M(D\bar{D})$ sideband yield [333].

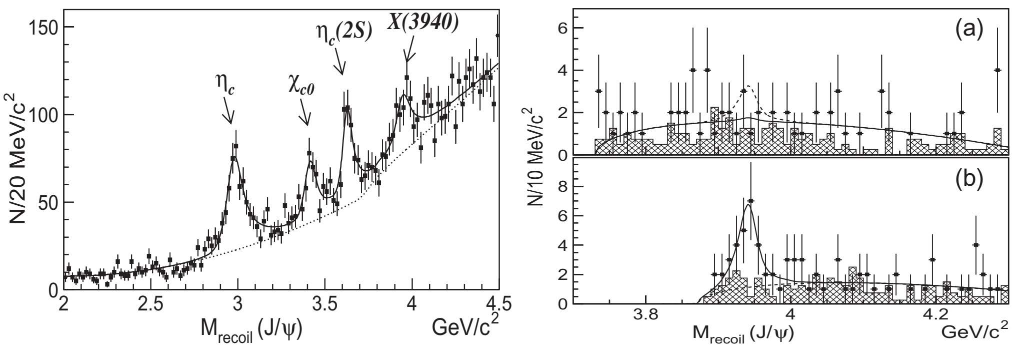

Fig. 65. Left: The distribution of masses recoiling from the J/ψ in inclusive $e^+e^- \to J/\psi\, X$ reactions [334]. The solid curve shows the result of a fit that includes η_c, χ_{c0}, $\eta_c(2S)$, and $X(3940)$ resonance terms as well as a smooth background function that has a step at the $D\bar{D}$ threshold (dotted curve). Right: The a) $D\bar{D}$ and b) $D^*\bar{D}$ invariant mass distributions from exclusive $e^+e^- \to J/\psi D^{(*)}\bar{D}$ annihilation [334]. The curves are fits that include possible resonance terms and the histograms are backgrounds determined from the D-meson sidebands. The dashed curves show: a) the 90% C.L. upper limit on the signal; b) the background function.

To address the question of whether or not the $X(3940)$ is the same state as the $Y(3940)$, a search [334] was made for $e^+e^- \to J/\psi\omega J/\psi$. No signal for $X(3940) \to \omega J/\psi$ was seen and a 90% C.L. lower limit $\mathcal{B}(X(3940) \to D^*\bar{D}) > 1.7\mathcal{B}(X(3940) \to \omega J/\psi)$ was established, which is inconsistent with the corresponding upper limit for the $Y(3940)$ discussed above. This implies that the $Y(3940)$, produced in B decays and decaying to $\omega J/\psi$, and the $X(3940)$, produced in association with a J/ψ and decaying to $D\bar{D}^*$, are distinct states. The only $c\bar{c}$ assignment available for the $X(3940)$ is the $\eta_c(3S)$, for which decays to $D^*\bar{D}$ are expected to be dominant and decays to $D\bar{D}$ are forbidden by parity. However, the ${}^3S_1$ triplet partner state of the $\eta_c(3S)$ is the well established $\psi(4040)$, with a mass of $4040 \pm 4\,\mathrm{MeV}$ [23]. Assigning the $X(3940)$ as the $\eta_c(3S)$ would mean $\Delta M_{hfs}(3S) = 98 \pm 8\,\mathrm{MeV}$, i.e., twice as large as $\Delta M_{hfs}(2S)$ (see above) and in strong disagreement with theoretical expectations.

9.1.6. Anomalous $J^{PC} = 1^{--}$ states seen in initial-state-radiation processes. In 2005, BaBar reported the discovery of a striking $\pi^+\pi^- J/\psi$ peak near 4260 MeV in the initial-state-radiation process $e^+e^- \to \gamma_{isr}\pi^+\pi^- J/\psi$ [335]. This observation was subsequently confirmed by CLEO [336] and Belle [337]. The cross section for $e^+e^- \to \pi^+\pi^- J/\psi$ from the Belle paper is shown in the left panel of Fig. 66, where a prominent signal for the $Y(4260)$ with a peak cross section of $\sim 70\,\mathrm{pb}$ is

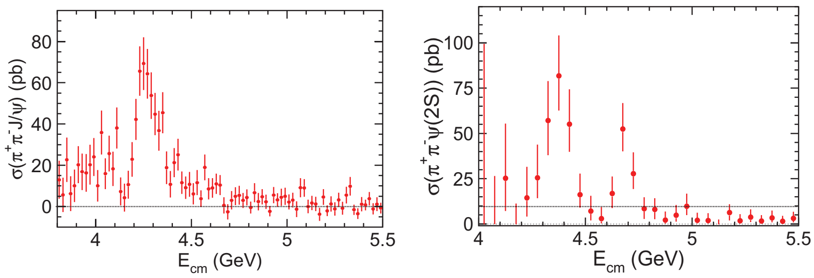

Fig. 66. The cross sections for left: $e^+e^- \to \pi^+\pi^- J/\psi$ [337] and right: $e^+e^- \to \pi^+\pi^-\psi(2S)$ [341].

evident. Curiously, the total cross section for e^+e^- annihilation into open charmed mesons shows no sign of a peak at 4260 MeV; the total cross section for open charm at the $Y(4260)$ peak is about 3 pb [338], which, taken together with the measured natural width $\Gamma_{\mathrm{tot}}[Y(4260)] = 95 \pm 14$ MeV, implies a 90% C.L. lower limit on the partial width $\Gamma(Y(4260) \to \pi^+\pi^- J/\psi) > 1.6$ MeV [339]. This is much larger than values that are typical for 1^{--} charmonium states (e.g., $\Gamma(\psi(3770) \to \pi^+\pi^- J/\psi) = 53 \pm 8$ keV).

BaBar also reported a similar peak in the $\pi^+\pi^-\psi(2S)$ cross section at 4325 MeV [340]. With higher statistics, Belle confirmed this (now called the $Y(4360)$), and found a second, higher mass peak, the $Y(4660)$ [341] (see the right panel of Fig. 66). Here too, there are no evident accompanying structures in the open charm cross sections near these masses. Another peculiar feature is that, with the currently available statistics, there are no signs of the $Y(4260)$ in the $\pi^+\pi^-\psi(2S)$ channel or of the $Y(4360)$ or $Y(4660)$ in the $\pi^+\pi^- J/\psi$ channel.

9.1.7. The electrically charged Z^- charmonium-like meson candidates. In 2008, Belle reported peaks in the $\psi'\pi^-$ and $\chi_{c1}\pi^-$ invariant mass distributions in $B \to \psi'\pi^- K$ (Fig. 67 (left) [342,343] and $B \to \chi_{c1}\pi^- K$ (Fig. 67 (right) [344], respectively. If these peaks are meson resonances, they would necessarily have a minimal quark content of $c\bar{c}d\bar{u}$ and be unmistakably exotic. Although in both cases the peaks have greater than 5σ statistical significance, the experimental situation remains uncertain since none of these peaks have yet been confirmed by other experiments. Analyses by BaBar of the same channels neither confirm nor contradict the Belle claims [345,346].

9.1.8. Studies of open charmed hadron pair-production via initial-state-radiation. The observation of the $Y(4260)$ motivated a Belle program of measurements of exclusive e^+e^- cross sections for charmed hadron pairs near threshold. Belle presented the first measurements of exclusive cross sections for the production of charmed-hadron pairs in electron–positron annihilation in the vicinity of the threshold for open-charm production performed at CM energies near the $\Upsilon(4S)$ resonance using the initial-state-radiation process. The continuous energy spectrum of this radiation allows investigating the production of charmonium with quantum numbers $J^{PC} = 1^{--}$ over the whole energy range. The electromagnetic suppression of hard photon radiation is compensated by an enormous integrated luminosity collected at the B-factories, and selection criteria specific for the ISR processes provide high efficiency at considerable suppression of the background. Taken together, these factors resulted in measurements that are competitive in precision with the CLEOc [336] and BESII [347] experimental data in which charmed-hadron cross sections were measured using e^+e^- energy scans without electromagnetic suppression.

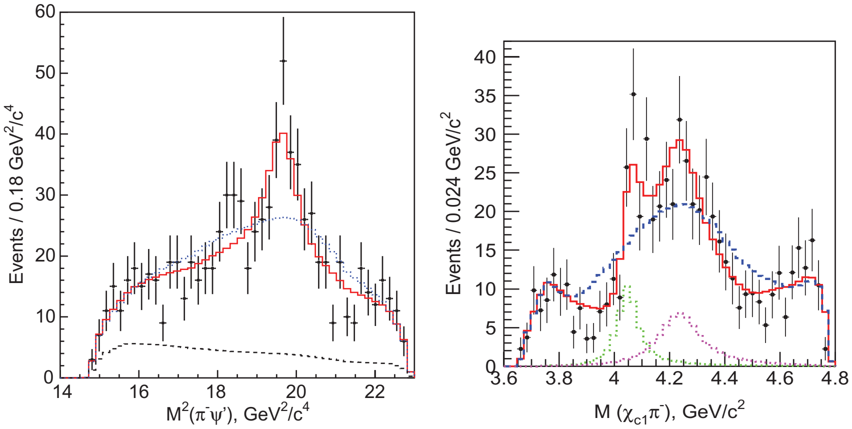

Fig. 67. Left: The $M^2_{\psi'\pi^-}$ projection of the Dalitz plot with the K^* bands removed is shown as data points [343]. The histograms show the corresponding projections of the Dalitz-plot fits with (red solid) and without (blue dotted) a $Z^- \to \psi'\pi^-$ resonance term. The dashed histogram is the background. Right: The data points show the $M_{\chi_{c1}\pi^-}$ projection of the Dalitz plot with the K^* bands removed. The histograms show the corresponding projections of the fits with (red solid) and without (blue dotted) two $Z^- \to \chi_{c1}\pi^-$ resonance terms, the dotted histograms represent the contribution of the two $\chi_{c1}\pi^-$ resonances.

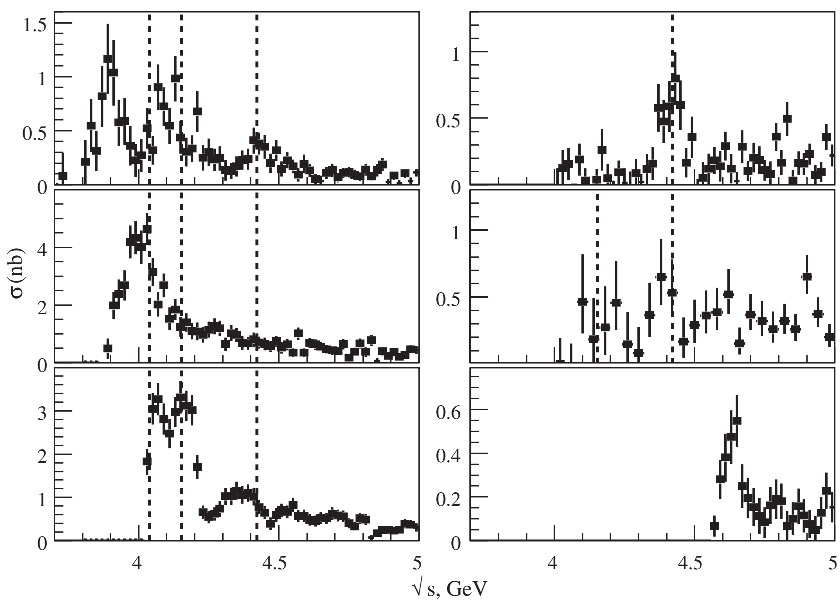

Fig. 68. Exclusive cross sections for charmed-hadron pair production measured in Belle [348–352]. Left: $D\bar{D}$, $D = D^0$ or D^+ (upper); D^+D^{*-} (middle); $D^{*+}D^{*-}$ (lower). Right: $D^0D^-\pi^+$ (upper); $D^0D^{*-}\pi^+$ (middle); $\Lambda_c^+\Lambda_c^-$ (lower). The vertical dashed lines indicate the mass values of the established 1^{--} charmonium states: $\psi(4040)$, $\psi(4160)$, and $\psi(4415)$.

The exclusive e^+e^- cross sections to $D\overline{D}$ ($D = D^0$ or D^+), D^+D^{*-}, $D^{*+}D^{*-}$, $D^0D^-\pi^+$, and $D^0D^{*-}\pi^+$ final state using ISR [348–351], shown in Fig. 68, have no evident peaks that can be associated with any of the above-mentioned Y states, contrary to expectations for conventional $J^{PC} = 1^{--}$ charmonium states with such large masses and total widths.

In 2008, the Belle collaboration reported the observation of a significant near-threshold peak, called the $X(4630)$, in the $e^+e^- \to \Lambda_c^+\Lambda_c^-$ exclusive cross section shown in the lower right-hand panel of Fig. 68 [352]. It remains unclear whether or not this observed peak is a resonance. In particular, peaks near the baryon–antibaryon pair mass threshold are observed in many processes, including three-body baryon decays of B-mesons [162]. The mass and width of the $X(4630)$ peak determined under the assumption that the $X(4630)$ is due to a resonance are $M = (4634 \pm 10)$ MeV/c^2 and $\Gamma = (92 \pm 40)$ MeV. These values agree within errors with the mass and the full width of the $Y(4660)$ peak seen in the $Y(4660) \to \pi^+\pi^-\psi'$ decay channel [341] as mentioned above. Such a coincidence (including quantum numbers) may not be accidental, although the possibility that the $X(4630)$ and $Y(4660)$ peaks have different origins cannot be ruled out. Among possible conventional interpretations, it has been suggested that the $X(4630)$ is the $\psi(5S)$ or $\psi(6S)$ 1^{--} charmonium state [353], or a threshold effect caused by the presence of the $\psi(3D)$ state with mass slightly below the $\Lambda_c^+\Lambda_c^-$ threshold.

9.1.9. Summary. This section has highlighted only a fraction of the charmonium and charmonium-related results from Belle. In addition to the observations described above, Belle reported a number of other observations related to charmonium. A near-threshold peak was found in the $D^*\bar{D}^*$ $e^+e^- \to J/\psi D^*\bar{D}^*$ annihilation process [354]. A Belle search for the $Y(4140)$—a $\phi J/\psi$ resonance reported by CDF [355]—in the $\phi J/\psi$ mass distribution produced via the $\gamma\gamma \to \phi J/\psi$ two-photon process found no evidence for the $Y(4140)$ but, instead, uncovered a 3.2σ significant peak at higher mass that was dubbed the $X(4350)$ [356]. Belle cross section measurements of exclusive processes of the type $e^+e^- \to J/\psi\eta_c$ [308] and $e^+e^- \to J/\psi D^{(*)}\bar{D}^{(*)}$ [357] found order-of-magnitude disagreements with NRQCD predictions [358–360] and have had a profound impact on subsequent developments in the theory; see, e.g., Ref. [361]. A recent study of the $\gamma\chi_{c1}$ mass distribution in the B-meson decay process $B \to K\gamma\chi_{c1}$ found strong evidence for the long-sought-for ψ_{c2}, the ${}^3D_2$ charmonium state (V. Bhardwaj et al. (Belle Collaboration), manuscript in preparation).

In the original physics program planned for Belle outlined in the Belle Letter of Intent (M.T. Cheng et al. (Belle Collaboration), KEK-Report 94-2 (1994), unpublished), no mention was made of charmonium physics or searches for non-conventional, multi-quark meson states. Somewhat unexpectedly, thanks in part to the huge data samples provided by the KEKB collider, Belle turned out to be a powerful instrument for both conventional charmonium physics, and for uncovering a new class of charmonium-like states that have yet to be understood [362].

9.2. Bottomonium(-like) states

As described in the previous section, most of the new charmonium states discovered in recent years at the B-factories do not seem to have a simple $c\bar{c}$ structure. Although the masses of these states are above the corresponding thresholds for decay into a pair of open charm mesons, they decay readily into J/ψ or $\psi(2S)$ and pions, which is unusual for $c\bar{c}$ states. In addition, their masses and decay modes are not in agreement with the predictions of potential models, which, in general, describe $c\bar{c}$ states very well. For these reasons, some of these charmonium-like states are probably more complex than simple quark–antiquark states and are candidates for exotic objects such as hybrid, molecular, or tetraquark states. Recently, Belle has made a series of exciting discoveries of new states in the bottomonium sector using its unique data sample taken around the $\Upsilon(5S)$ resonance.

Bottomonium refers to bound states of $b\bar{b}$ quarks and is considered an excellent laboratory to study QCD at low energy. The spin-singlet states $h_b(nP)$ and $\eta_b(nS)$ alone provide information concerning the spin–spin (or hyperfine) interaction in bottomonium. Measurements of the $h_b(nP)$ masses would provide unique access to the P-wave hyperfine splitting, $\Delta M_{hfs}(nP) \equiv < M(n^3P_J) > - M(n^1P_1)$, the difference between the spin-weighted average mass of the P-wave triplet states ($\chi_{bJ}(nP)$ or

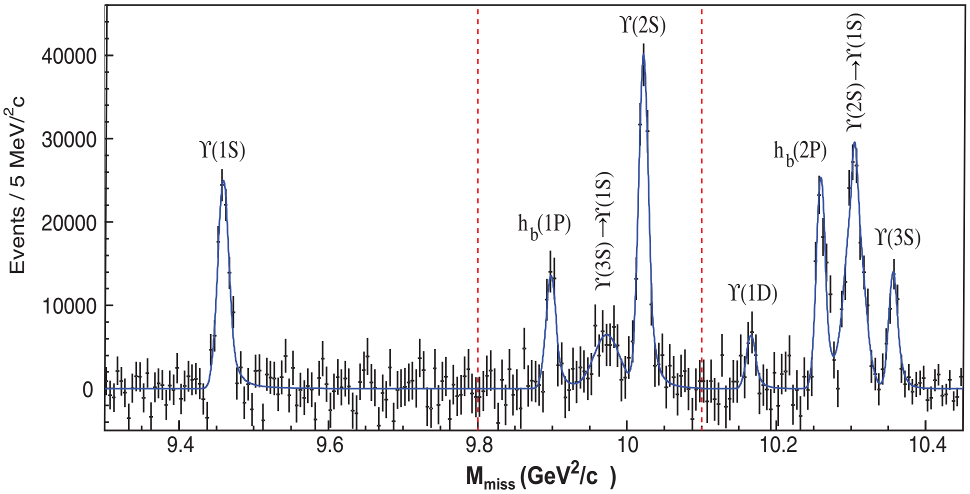

Fig. 69. The inclusive M_{miss} spectrum with the combinatorial background subtracted (points with error bars) and the signal component of the fit function overlaid (smooth curve). The vertical lines indicate boundaries of the fit regions. The expected high-statistics reference signals, $\Upsilon(5S) \to \Upsilon(nS)\pi^+\pi^-$ where $n = 1, 2, 3$, as well as the newly observed $h_b(1P)$ and $h_b(2P)$ states are seen.

n^3P_J) and that of corresponding $h_b(nP)$, or n^1P_1. These splittings are predicted to be close to zero. Recently, CLEO observed the process $e^+e^- \to h_c(1P)\pi^+\pi^-$ at a rate comparable to that for $e^+e^- \to J/\psi\pi^+\pi^-$ in data taken at the $\psi(4160)$ resonance. Such a large rate was unexpected because the production of $h_c(1P)$ requires a c-quark spin-flip, while production of J/ψ does not. Belle previously reported anomalously high rates for $e^+e^- \to \Upsilon(nS)\pi^+\pi^-$ ($n = 1, 2, 3$) at energies near the $\Upsilon(5S)$ mass [363]. If the $\Upsilon(nS)$ signals are attributed entirely to $\Upsilon(5S)$ decays, the measured partial decay widths $\Gamma[\Upsilon(5S) \to \Upsilon(nS)\pi^+\pi^-] \sim 0.5$ MeV are about two orders of magnitude larger than typical widths for di-pion transitions among the four lower $\Upsilon(nS)$ states. Using the large data sample collected at energies near the $\Upsilon(5S)$ resonance and motivated by the suggestive CLEO result, Belle decided to investigate the missing $h_b(mP)$ singlet bottomonium states [364].

We do not expect the $h_b(mP)$ states to have a large dominant exclusive decay mode, which would allow their reconstruction with high efficiency. Instead, they are reconstructed inclusively using the missing mass (recoil mass) of the $\pi^+\pi^-$ pair. The $\pi^+\pi^-$ missing mass is defined as $M^2_{\text{miss}} \equiv (P_{\Upsilon(5S)} - P_{\pi^+\pi^-})^2$, where $P_{\Upsilon(5S)}$ is the 4-momentum of the $\Upsilon(5S)$ determined from the beam momenta and $P_{\pi^+\pi^-}$ is the 4-momentum of the $\pi^+\pi^-$ system. The $\pi^+\pi^-$ transitions between $\Upsilon(nS)$ states provide high-statistics reference signals as shown in Fig. 69. The $h_b(nP)$ states are also very clearly, and for the first time, observed here. The measured masses of the $h_b(1P)$ and $h_b(2P)$, $M = (9898.3 \pm 1.1^{+1.0}_{-1.1})$ MeV/c^2 and $M = (10259.8 \pm 0.6^{+1.4}_{-1.0})$ MeV/c^2 respectively, correspond to hyperfine splittings that are consistent with zero. The processes $\Upsilon(5S) \to h_b(mP)\pi^+\pi^-$, which require a heavy-quark spin flip, are then found to have rates that are comparable to those for the heavy-quark spin conserving transitions $\Upsilon(5S) \to \Upsilon(nS)\pi^+\pi^-$. These observations differ from a priori theoretical expectations and strongly suggest that exotic mechanisms contribute to $\Upsilon(5S)$ decays.

To understand the $\Upsilon(nS)$ and $h_b(mP)$ production mechanism at the $\Upsilon(5S)$ resonance, it is necessary to study in detail the resonant structure of the $\Upsilon(5S) \to \Upsilon(nS)\pi^+\pi^-$ and $\Upsilon(5S) \to h_b(mP)\pi^+\pi^-$ transitions [365]. In the case of $\Upsilon(5S) \to \Upsilon(nS)\pi^+\pi^-$, the $\Upsilon(nS)$ is reconstructed in the $\mu^+\mu^-$ channel and one examines the $\pi^\pm\Upsilon(nS)$ mass spectra. This is illustrated for the $\Upsilon(2S)$

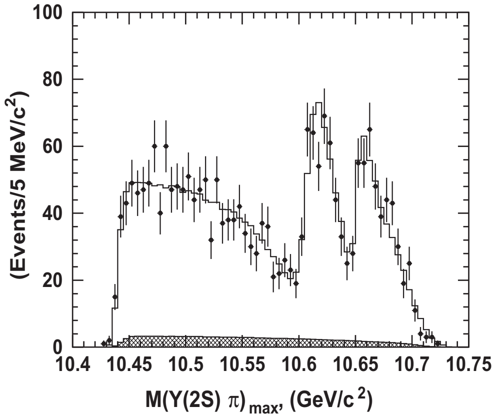

Fig. 70. Comparison of fit results (open histograms) with experimental data (points with error bars) for events in the $\Upsilon(2S)$ signal regions. $M(\Upsilon(2S)\pi)_{\max}$ is the maximum invariant mass of the two $\Upsilon(2S)\pi$ combinations. The hatched histogram shows the background component.

Table 22. Comparison of results on $Z_b(10\,610)$ and $Z_b(10\,650)$ parameters (mass and width in MeV, relative normalization and phase in degrees) obtained from $\Upsilon(5S) \to \Upsilon(nS)\pi^+\pi^-$ $(n = 1, 2, 3)$ and $\Upsilon(5S) \to h_b(mP)\pi^+\pi^-$ $(m = 1, 2)$ analyses.

Final state	$\Upsilon(1S)\pi^+\pi^-$	$\Upsilon(2S)\pi^+\pi^-$	$\Upsilon(3S)\pi^+\pi^-$	$h_b(1P)\pi^+\pi^-$	$h_b(2P)\pi^+\pi^-$
$M[Z_b(10\,610)]$	$10\,611 \pm 4 \pm 3$	$10\,609 \pm 2 \pm 3$	$10\,608 \pm 2 \pm 3$	$10\,605 \pm 2^{+3}_{-1}$	$10\,599^{+6+5}_{-3-4}$
$\Gamma[Z_b(10\,610)]$	$22.3 \pm 7.7^{+3.0}_{-4.0}$	$24.2 \pm 3.1^{+2.0}_{-3.0}$	$17.6 \pm 3.0 \pm 3.0$	$11.4^{+4.5+2.1}_{-3.9-1.2}$	$13^{+10+9}_{-8\ -7}$
$M[Z_b(10\,650)]$	$10\,657 \pm 6 \pm 3$	$10\,651 \pm 2 \pm 3$	$10\,652 \pm 1 \pm 2$	$10\,654 \pm 3^{+1}_{-2}$	$10\,654^{+2+3}_{-3-2}$
$\Gamma[Z_b(10\,650)]$	$16.3 \pm 9.8^{+6.0}_{-2.0}$	$13.3 \pm 3.3^{+4.0}_{-3.0}$	$8.4 \pm 2.0 \pm 2.0$	$20.9^{+5.4+2.1}_{-4.7-5.7}$	$19 \pm 7^{+11}_{-7}$
Rel. norm.	$0.57 \pm 0.21^{+0.19}_{-0.04}$	$0.86 \pm 0.11^{+0.04}_{-0.10}$	$0.96 \pm 0.14^{+0.08}_{-0.05}$	$1.39 \pm 0.37^{+0.05}_{-0.15}$	$1.6^{+0.6+0.4}_{-0.4-0.6}$
Rel. phase	$58 \pm 43^{+4}_{-9}$	$-13 \pm 13^{+17}_{-8}$	$-9 \pm 19^{+11}_{-26}$	187^{+44+3}_{-57-12}	$181^{+65\ +74}_{-105-109}$

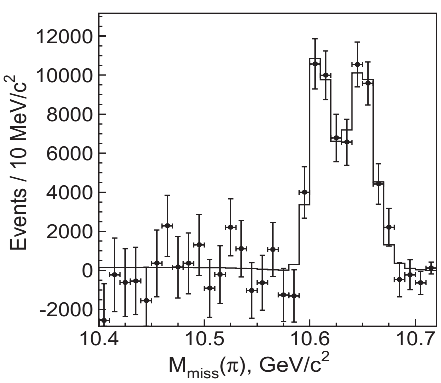

Fig. 71. Comparison of fit results for events in the $h_b(1P)$ signal region. The $Z_b(10\,610)$ and $Z_b(10\,650)$ are clearly observed in both cases; the result of the fit is represented by the histogram.

case in Fig. 70. Two charged bottomonium-like resonances, the $Z_b(10\,610)$ and $Z_b(10\,650)$, are observed (Table 22). A similar structure is found (Fig. 71) for the $h_b(mP)\pi^+\pi^-$ decay, where this time the appropriate observable is $M_{\mathrm{miss}}(\pi^\mp)$, the missing mass of the opposite sign pion as the decays are reconstructed inclusively using the missing mass of the $\pi^+\pi^-$ pair. Production of the Z_bs saturates the $\Upsilon(5S) \to h_b(mP)\pi^+\pi^-$ transitions and accounts for the high inclusive $h_b(mS)$ production rate. All channels yield consistent results and weighted averages over all five channels give $M = 10\,607.2 \pm 2.0\,\mathrm{MeV}/c^2$, $\Gamma = 18.4 \pm 2.4\,\mathrm{MeV}$ for the $Z_b(10\,610)$ and $M = 10\,652.2 \pm 1.5\,\mathrm{MeV}/c^2$, $\Gamma = 11.5 \pm 2.2\,\mathrm{MeV}$ for the $Z_b(10\,650)$, where statistical and systematic errors are added in quadrature. The $Z_b(10\,610)$ production rate is similar to that of the $Z_b(10\,650)$ for each of the five decay channels. Analyses of charged pion angular distributions favor the $J^P = 1^+$ spin-parity assignment for both the $Z_b(10\,610)$ and $Z_b(10\,650)$.

These states defy a standard bottomonium assignment. In principle, a bottomonium particle's electric charge is zero; therefore, the minimal quark content of the $Z_b(10\,610)$ and $Z_b(10\,650)$ is a four-quark combination. Theoretical interpretations of these hidden-bottom meson resonances were proposed immediately after their observation. The proximity (within a few MeV/c^2) of the measured masses of these unexpected new states to the open beauty thresholds, $B\bar{B}^*$ ($10\,604.6\,\mathrm{MeV}/c^2$) and $B^*\bar{B}^*$ ($10\,650.2\,\mathrm{MeV}/c^2$), suggests a "molecular" nature of these new states, which can in turn explain most of their observed properties. In the case of a molecule, it would be natural to expect that $Z_b^0(10\,610)$ and $Z_b^0(10\,650)$ states to decay respectively to $B\bar{B}^*$ and $B^*\bar{B}^*$ final states at substantial rates. Recently, Belle reported preliminary results on the analysis of three-body $\Upsilon(5S) \to BB^*\pi$ ($B^+\bar{B}^{*0}\pi^-$, $B^-B^{*0}\pi^+$, $B^0B^{*-}\pi^+$ and $\bar{B}^0B^{*+}\pi^-$) and $\Upsilon(5S) \to B^*B^*\pi$ ($B^{*+}\bar{B}^{*0}\pi^-$ and $B^{*-}B^{*0}\pi^+$) including an observation of the $\Upsilon(5S) \to Z_b^{\pm}(10\,610)\pi^{\mp} \to [B\bar{B}^*]^{\pm}\pi^{\mp}$ and $\Upsilon(5S) \to Z_b^{\pm}(10\,650)\pi^{\mp} \to [B^*\bar{B}^*]^{\pm}\pi^{\mp}$ decays as intermediate channels. Evidence (with a significance of 4.9σ) for a neutral $Z_b^0(10\,610)$ decaying to $\Upsilon(2S)\pi^0$ has been also obtained by Belle in a Dalitz plot analysis of $\Upsilon(5S) \to \Upsilon(2S)\pi^0\pi^0$ using their full $\Upsilon(5S)$ data sample [366]. Its measured mass, $M(Z_b^0(10\,610)) = 10\,609^{+8}_{-6} \pm 6\,\mathrm{MeV}/c^2$, is consistent with the mass of the corresponding charged state, the $Z_b^{\pm}(10\,610)$.

The Z_b states have also been interpreted as cusps at the $B^*\bar{B}$ and $B^*\bar{B}^*$ thresholds and as tetraquark states.

After observing that the decay $\Upsilon(5S) \to h_b(nP)\pi^+\pi^-$ proceeds via the Z_b intermediate resonances, Belle [367] exploited this information to look for the $\eta_b(1, 2S)$ resonances in the processes $e^+e^- \to h_b(nP)\pi^+\pi^-$, $h_b(nP) \to \eta_b(mS)\gamma$. Here only the π^+, π^-, and γ are reconstructed and the requirement $10.59\,\mathrm{GeV}/c^2 < M_{\mathrm{miss}}(\pi^{\pm}) < 10.67\,\mathrm{GeV}/c^2$ helps to reduce the background significantly. The $M_{\mathrm{miss}}(\pi^+\pi^-)$ spectra are fitted for different $M^{(n)}_{\mathrm{miss}}(\pi^+\pi^-\gamma)$ bins to measure the $h_b(nP)$ yield. The $h_b(nP)$ yield peaks at $M^{(n)}_{\mathrm{miss}}(\pi^+\pi^-\gamma)$ values corresponding to $m_{\eta_b(mS)}$ due to the $h_b(nP) \to \eta_b(mS)\gamma$ transitions (Fig. 72).

The $h_b(1P) \to \eta_b(1S)\gamma$ and $h_b(2P) \to \eta_b(1S)\gamma$ transitions are observed for the first time and first evidence for the $\eta_b(2S)$ is obtained using the $h_b(2P) \to \eta_b(2S)\gamma$ transition. The mass and width parameters of the $\eta_b(1S)$ and $\eta_b(2S)$ are measured to be $m_{\eta_b(1S)} = (9402.4 \pm 1.5 \pm 1.8)\,\mathrm{MeV}/c^2$, $m_{\eta_b(2S)} = (9999.0 \pm 3.5^{+2.8}_{-1.9})\,\mathrm{MeV}/c^2$, and $\Gamma_{\eta_b(1S)} = (10.8^{+4.0+4.5}_{-3.7-2.0})\,\mathrm{MeV}$. Our value of the $\eta_b(1S)$ mass is about 11 MeV higher than the previous world average and the hyperfine splittings are $57.9 \pm 2.3\,\mathrm{MeV}$ and $24.3^{+4.0}_{-4.5}\,\mathrm{MeV}$ for the $1S$ and $2S$ states, respectively, consistent with theoretical predictions.

9.3. *Others*

In addition to $c\bar{c}$ and $b\bar{b}$ states, Belle has also studied charmed mesons and baryons. They are copiously produced at KEKB either directly in e^+e^- collisions or as products of B meson decays. At the 10.53 GeV CM energy, the cross section for prompt $c\bar{c}$ pair production exceeds that of $b\bar{b}$, assuring large samples of ground and excited charmed states hadronizing from the produced $c\bar{c}$ quarks. Charm hadrons are usually studied inclusively; however, such an approach often suffers from large

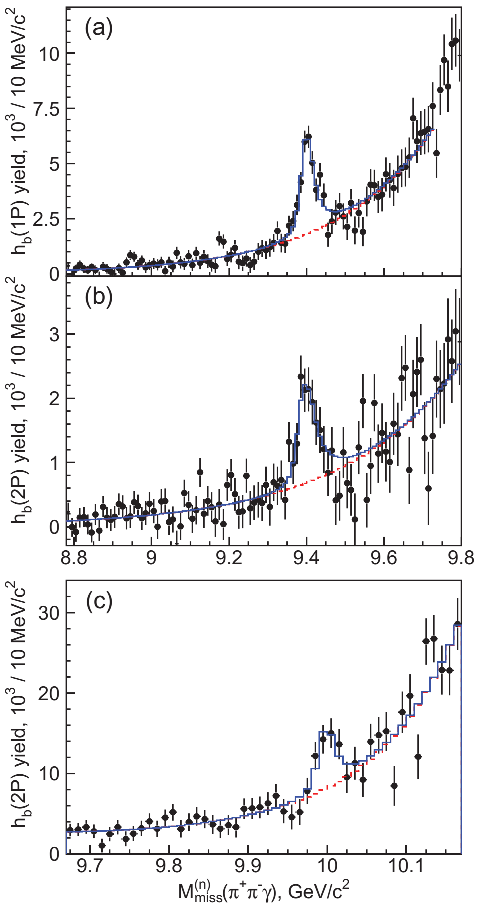

Fig. 72. The $h_b(1P)$ yield versus $M^{(1)}_{\text{miss}}(\pi^+\pi^-\gamma)$ (a), and $h_b(2P)$ yield versus $M^{(2)}_{\text{miss}}(\pi^+\pi^-\gamma)$ in the $\eta_b(1S)$ region (b) and in the $\eta_b(2S)$ region (c). The solid (dashed) histogram presents the fit result (background component of the fit function).

background. Charm production in B decays is governed by the Cabibbo-favored $b \to c$ transition. The restricted kinematics of $\Upsilon(4S) \to B\bar{B}$ production enables selection of clean B samples. The fixed spin of the parent B constrains the possible quantum numbers of daughter particles, simplifying spin-parity determinations. However, charmed states with high spin and highly excited charm states are suppressed in B decays.

9.3.1. Charmed mesons. The spectra of quark–antiquark systems are predicted using potential models, which attempt to model QCD features by describing the interquark potential [368,369]. Charmed mesons, having $c\bar{u}$, $c\bar{d}$, or $c\bar{s}$ quark content, are heavy-light systems for which the models employ heavy quark symmetry (HQS). In the limit of an infinitely heavy-quark mass, heavy-light mesons become similar to a hydrogen atom, which gives many theoretical simplifications. However, since the c quark mass is finite, HQS is only an approximate symmetry. An important consequence of its breaking is the $D_{(s)} - D^*_{(s)}$ splitting. The orbitally excited P-wave multiplet ($L = 1$), denoted $D^{**}_{(s)}$, is expected to consist of a broad $J^P = (0^+, 1^+)$ doublet having total light-quark angular momentum $j_q = \frac{1}{2}$ and a narrow $(1^+, 2^+)$ doublet with $j_q = \frac{3}{2}$.

Before the advent of the B-factories, in addition to the ground state $D_{(s)}$ and $D^*_{(s)}$ mesons, only the narrow $D^{**}_{(s)}$ doublets were established: $(D_1(2420), D^*_2(2460))$ and $(D_{s1}(2536), D^*_{s2}(2573))$; the broad ones remained missing. The discovery of two narrow and unexpected states, the $D^*_{s0}(2317)^+$

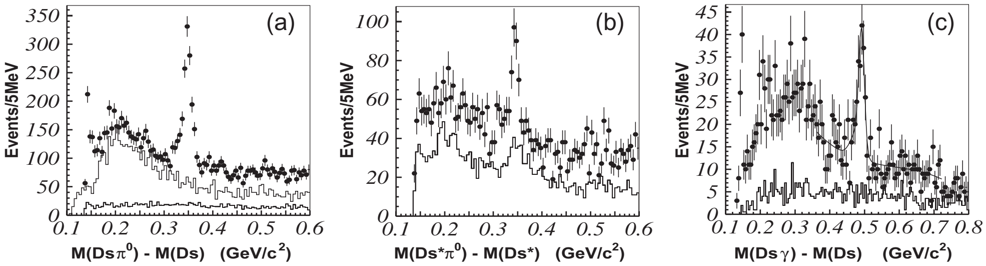

Fig. 73. Distributions of $\Delta M(D_s\pi^0)$ (left), $\Delta M(D_s^*\pi^0)$ (middle), and $\Delta M(D_s\gamma)$ (right). Histograms show data from the D_s and/or π^0 sideband regions.

Table 23. Parameters of $D_{s0}^*(2317)$ and $D_{s1}(2460)$, compared with PDG parameters of $j_q = \frac{3}{2}$ states.

$J^P(j_q)$	D_s^{**}	Decay modes	Mass (MeV/c^2)	Width (MeV/c^2)
$0^+(\frac{1}{2})$	$D_{s0}^*(2317)$	$D_s\pi$	$2317.2 \pm 0.5 \pm 0.9$	<4.6
$1^+(\frac{1}{2})$	$D_{s1}(2460)$	$D_s^*\pi$, $D_s\gamma$	$2456.5 \pm 1.3 \pm 1.3$	<5.5
$1^+(\frac{3}{2})$	$D_{s1}(2536)$	D^*K	2535.3 ± 0.2	<2.3
$2^+(\frac{3}{2})$	$D_{s2}^*(2573)$	DK	2572.6 ± 0.9	20 ± 5

and $D_{s1}(2460)^+$, began a renaissance in charm spectroscopy [370–372]. They were found in the $D_s^+\pi^0$ and $D_s^{*+}\pi^0$ final states, respectively, and were produced inclusively in the $c\bar{c}$ continuum. Spectra of the $\Delta M(D_s^{(*)}\pi^0) \equiv M(D_s^{(*)}\pi^0) - M(D_s^{(*)})$ mass difference measured by Belle are shown in Fig. 73; prominent peaks at $\Delta M(D_s\pi^0) \approx 350$ MeV/c^2 and $\Delta M(D_s^*\pi^0) \approx 350$ MeV/c^2 are the $D_{s0}^*(2317)$ and $D_{s1}(2460)$, respectively. Their masses and upper limits on their widths, measured from fits to the $\Delta M(D_s^{(*)}\pi^0)$, are summarized in Table 23.

Observation of radiative $D_s\gamma$ (Fig. 73) and di-pion $D_s\pi^+\pi^-$ decays of the $D_{s1}(2460)$ ruled out a $J^P = 0^\pm$ assignment. For the $D_{s0}^*(2317)$ no decay channel was found apart from the discovery mode. Such a decay pattern was consistent with spin-parity assignments of 0^+ and 1^+ for the $D_{s0}^*(2317)$ and $D_{s1}(2460)$ respectively, as expected for the P-wave $c\bar{s}$ doublet with $j_q = \frac{1}{2}$. However, the measured masses were much lower than predicted by potential models and, thus, decays to $D^{(*)}K$, expected to be dominant, were not permitted kinematically. Instead, the dominant decays into isospin-violating modes resulted in very small widths. All this triggered exotic interpretations of these mesons as DK molecules, multiquark states, mixtures of a P-wave $c\bar{s}$ meson with a $c\bar{s}q\bar{q}$ tetraquark, or chiral partners of $D_s^{(*)}$ [373–375].

To clarify the nature of these states, Belle searched for them in exclusive $B \to \bar{D}D_{sJ}$ decays, where D_{sJ} denotes any excited charmed-strange meson [376]. These reactions proceed via $\bar{b} \to \bar{c}W^+ \to \bar{c}c\bar{s}$, which is the dominant $c\bar{s}$ production mechanism in B decays; here D_s^{**} with $j_q = \frac{1}{2}$ are expected to be more readily produced than $j_q = \frac{3}{2}$ states. Thus, one expected to observe the $D_{s0}^*(2317)$ and $D_{s1}(2460)$ in $B \to \bar{D}D_{sJ}$, if they were the missing $c\bar{s}$ doublet. The D_{sJ} final states studied were $D_s^{(*)}\pi^0$, $D_s^{(*)}\gamma$, and $D_s^{(*)}\pi^+\pi^-$. Figure 74 shows the distributions of D_{sJ} invariant mass for B candidates satisfying the ΔE and M_{bc} signal region requirements, and for the channels with significant signals found: $D_{s0}^*(2317) \to D_s\pi^0$, $D_{s1}(2460) \to D_s^*\pi^0$, and $D_{s1}(2460) \to D_s\gamma$. The $D_{s1}(2460)$ helicity angle distribution for the $D_{s1}(2460) \to D_s\gamma$ mode (Fig. 74) showed that the data were consistent with the $J = 1$ hypothesis. Study of the D_{sJ} production rates in $B \to \bar{D}D_{sJ}$ decays seems to support the interpretation of the $D_{s0}^*(2317)$ and $D_{s1}(2460)$ as the orbitally excited

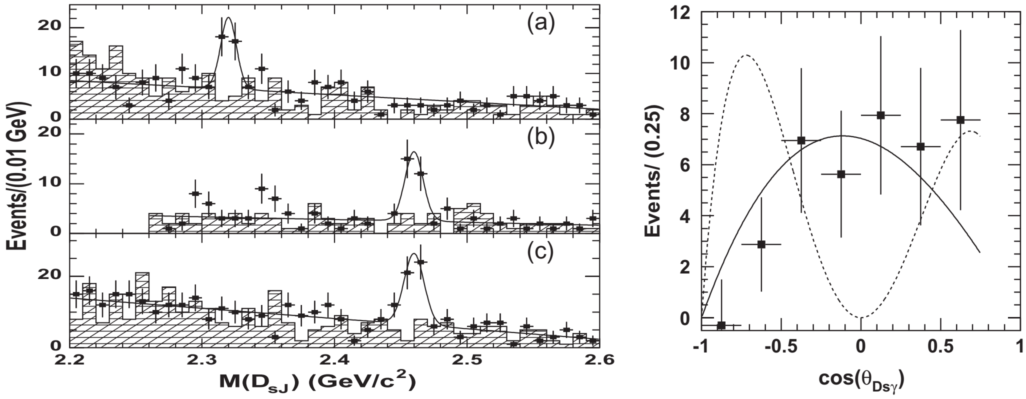

Fig. 74. Left: $M(D_{sJ})$ distributions for D_{sJ} final states: $D_s\pi^0$ (top), $D_s^*\pi^0$ (middle), $D_s\gamma$ (bottom). Hatched histograms show the ΔE sidebands. Right: the $D_{s1}(2460) \to D_s\gamma$ helicity distribution. Data points are compared with MC predictions for $J = 1$ (solid line) and $J = 2$ (dashed) assignments.

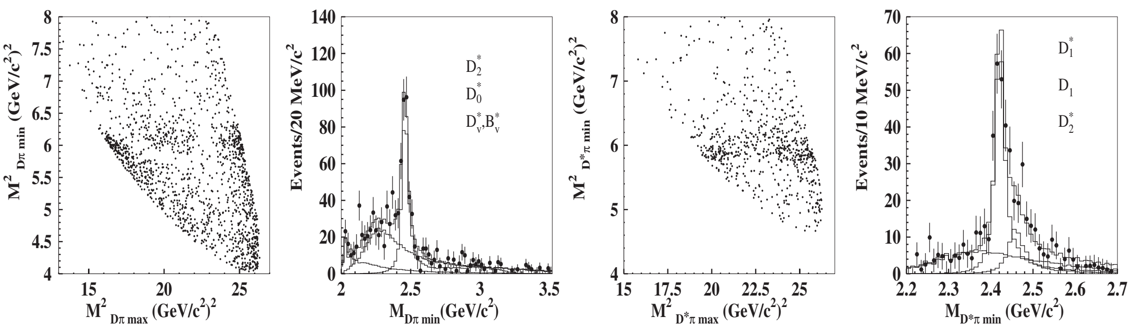

Fig. 75. Dalitz distributions for $B^- \to D^+\pi^-\pi^-$ (first from the left) and $B^- \to D^{*+}\pi^-\pi^-$ (third) signal region candidates. The corresponding $M(D^+\pi^-)_{\min}$ and $M(D^{*+}\pi^-)_{\min}$ projections, with background subtracted, are shown as the second and fourth plots, respectively. Hatched histograms show the fitted resonance contributions. The open histogram is the coherent sum of all contributions.

$c\bar{s}$ $j_q = \frac{1}{2}$ doublet. Although some of the models managed to reproduce the low masses of these states [377], our understanding of $c\bar{s}$ spectroscopy still seems to be incomplete.

On the other hand, the corresponding $j_q = \frac{1}{2}$ doublet in the $c\bar{u}$ spectrum, discovered by Belle about the same time as the narrow D_s^{**} states, has properties that perfectly match potential model predictions. The D^{**} mesons, expected to decay dominantly into $D^{(*)}\pi$ final states, were studied at Belle in a full Dalitz plot analysis of $B^+ \to D^{(*)-}\pi^+\pi^+$ decays [378]. To distinguish between the two identical final-state pions, $D^{(*)-}\pi^+$ combinations having minimal and maximal mass values were used as the Dalitz plot variables. The $M^2(D^{(*)}\pi)_{\min}$ versus $M^2(D^{(*)}\pi)_{\max}$ plots for B candidates within the ΔE–M_{bc} signal region are shown in Fig. 75. Non-uniformly distributed events indicate intermediate resonances emerging in the $M^2(D\pi)_{\min}$ spectrum. The fitted resonance contributions to the $M(D^{(*)-}\pi^+)_{\min}$ projection are shown in Fig. 75. The $D\pi$ system was found to be composed of a tensor D_2^{*0} and broad scalar state D_0^{*0}, while the $D^*\pi$ system consists of a narrow axial D_1, a tensor D_2^*, as well as a broad axial D_1'. The two broad states, observed for the first time, were consistent with the $j_q = \frac{1}{2}$ P-wave $c\bar{u}$ doublet. The measured parameters of the D^{**0} states are summarized in Table 24; the differences between the D^{**} and D_s^{**} properties are striking. Belle also performed a similar analysis for the D^{**+}s produced in $B^0 \to \bar{D}^{(*)0}\pi^+\pi^-$ [379].

Table 24. Parameters of the D^{**} mesons.

$J^P(j_q)$	D^{**}	Decay modes	Mass (MeV/c^2)	Width (MeV/c^2)
$0^+(\frac{1}{2})$	$D_0^*(2400)$	$D\pi$	$2308 \pm 17 \pm 15 \pm 28$	$276 \pm 21 \pm 18 \pm 60$
$1^+(\frac{1}{2})$	$D_1'(2420)$	$D^*\pi$	$2427 \pm 26 \pm 20 \pm 15$	$384^{+107}_{-75} \pm 24 \pm 70$
$1^+(\frac{3}{2})$	$D_1(2420)$	$D^*\pi$	$2421.4 \pm 1.5 \pm 0.4 \pm 0.8$	$23.7 \pm 2.7 \pm 0.2 \pm 4.0$
$2^+(\frac{3}{2})$	$D_2^*(2460)$	$D^{(*)}\pi$	$2461.6 \pm 2.1 \pm 0.5 \pm 3.3$	$45.6 \pm 4.4 \pm 6.5 \pm 1.6$

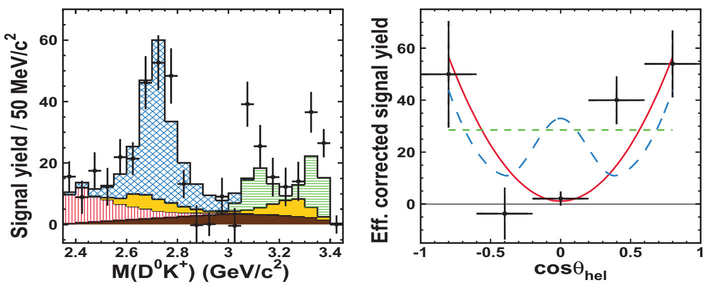

Fig. 76. Left: Background-subtracted $M(D^0K^+)$ distribution for $B^+ \to \bar{D}^0D^0K^+$ with a contribution from $D_{s1}^*(2700)^+$ (blue histogram), reflections from $\psi(3770)$ (green) and $\psi(4160)$ (yellow) decaying to $\bar{D}^0D^0$, nonresonant contributions (brown and red). Right: $D_{s1}^*(2700)$ helicity distribution compared to predictions for $J = 0$ (green), 1 (red), and 2 (blue) spin assignments.

Studies performed by Belle allowed one to investigate the important implications of HQS breaking. Theory predicts that the two 1^+ mesons, with $j_q = \frac{1}{2}$ and $j_q = \frac{3}{2}$, decay into $D^*\pi$ in an S and a D wave, respectively. Due to the finite c-quark mass, the observed (physical) 1^+ states can be a mixture of such pure states and, thus, the resulting D_1' and D_1 amplitudes are superpositions of S- and D-wave amplitudes. The corresponding mixing angle was measured to be non-zero [378]. Similarly, mixing between the two $c\bar{s}$ axial states can be expected. An angular analysis performed for the $D_{s1}(2536)^+ \to D^{*+}K_S^0$ mode showed that, contrary to the HQS prediction of a pure D-wave decay, the S-wave decay dominates [380].

Potential models also predict multiplets of higher orbital and radial excitations of charmed mesons. The first example of such a $c\bar{s}$ meson, the $D_{s1}^*(2700)^+$, was observed in the D^0K^+ final state produced in doubly-charmed $B^+ \to \bar{D}^0D^0K^+$ decays [329]. Its mass was measured to be $2708 \pm 9^{+11}_{-10}\,\mathrm{MeV}/c^2$, while its width is $108 \pm 23^{+36}_{-31}\,\mathrm{MeV}/c^2$. The $D_{s1}^*(2700)^+$'s spin-parity of 1^- was established from a study of its helicity angle. The $M(D^0K^+)$ spectrum together with the measured intermediate resonance contributions, as well as the $D_{s1}^*(2700)$ helicity distribution, are shown in Fig. 76. Observation of the $D_{s1}^*(2700) \to D^*K$ decay with a rate comparable to that for DK, suggests that the $D_{s1}^*(2700)$ is a D_s^* radial excitation [381].

9.3.2. Charmed baryons. Charmed baryons provide a laboratory for the study of the dynamics of a light diquark in the environment of a heavy quark and allow one to test many theoretical predictions [382,383]. For the charmed baryons with cud, cdd, or cuu quark content, the only states known before the start of the B-factories were the Λ_c^+ and $\Sigma_c(2455)^{0,+,++}$ ground states with $J^P = \frac{1}{2}^+$, the $\frac{3}{2}^+$ spin excitation $\Sigma_c(2520)$, as well as four Λ_c excitations observed by CLEO in the $\Lambda_c\pi\pi$ final state. Two states, the $\Lambda_c(2595)$ and the $\Lambda_c(2625)$, were identified as orbitally excited states, while the interpretation of $\Lambda_c(2765)$ and $\Lambda_c(2880)$ remained unknown. Except for the Λ_c, quantum numbers of charmed baryons were not measured but, instead, either assigned based on model predictions or

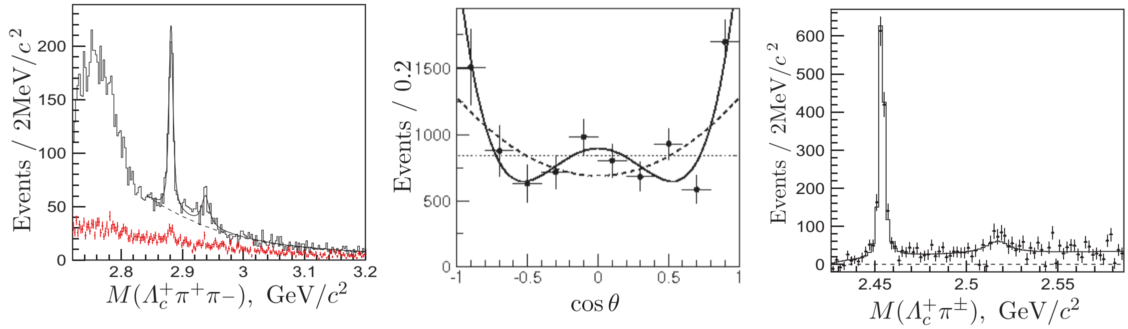

Fig. 77. Left: $M(\Lambda_c^+\pi^+\pi^-)$ distribution with $\Lambda_c^+\pi^\pm$ within $\Sigma_c(2455)^{0,++}$ signal (black) and sideband (red) regions. Middle: Helicity distribution of $\Lambda_c(2880) \to \Sigma_c(2455)\pi$ with fit results for the $J = \frac{1}{2}$ (dotted), $\frac{3}{2}$ (dashed), and $\frac{5}{2}$ (solid) hypotheses. Right: $\Lambda_c(2880)$ yield as a function of $M(\Lambda_c^+\pi^\pm)$.

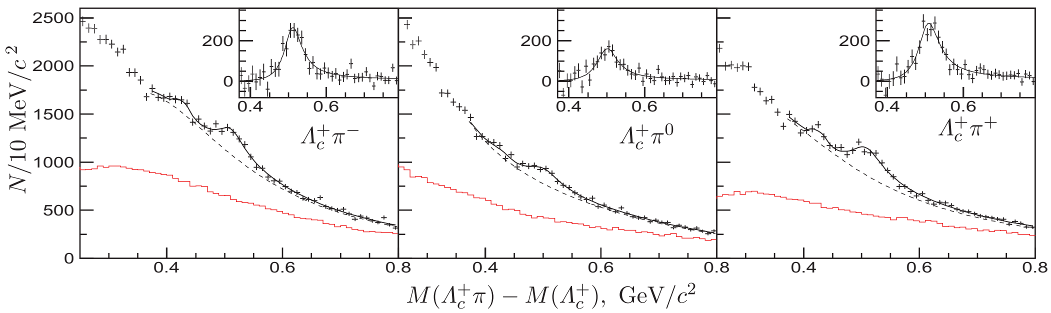

Fig. 78. $M(\Lambda_c\pi) - M(\Lambda_c)$ distributions for the Λ_c^+ signal window (points) and scaled sidebands (red histogram). Insets show background subtracted distributions for the $\Sigma_c(2800)$. The peaks at 0.43 GeV/c^2 are cross-feeds from $\Lambda_c(2880) \to \Sigma_c(2455)\pi$ where the pion from the $\Sigma_c(2455)$ decay is missing.

unknown. Since the predicted spectra are rich and dense, J^P assignment for a given state is difficult and requires experimental determination.

The first such measurement, performed for the $\Lambda_c(2880)$, is an excellent example of a comprehensive study of baryon properties [384]. Figure 77 shows the $\Lambda_c^+\pi^+\pi^-$ invariant mass, with the $\Lambda_c^+ \to pK^-\pi^+$ mode reconstructed. In addition to the $\Lambda_c(2880)$ signal, there are also peaks associated with the $\Lambda_c(2765)$, as well as the $\Lambda_c(2940)$ found by BaBar in the $D^0 p$ final state [385]. The parameters of the narrow baryons, obtained from a fit to the $M(\Lambda_c\pi^+\pi^-)$ distribution, are: $M_{\Lambda_c(2880)} = 2881.2 \pm 0.2 \pm 0.4\,\mathrm{MeV}/c^2$, $\Gamma_{\Lambda_c(2880)} = 5.8 \pm 0.7 \pm 1.1\,\mathrm{MeV}/c^2$, $M_{\Lambda_c(2940)} = 2938.0 \pm 1.3^{+2.0}_{-1.4}\,\mathrm{MeV}/c^2$, $\Gamma_{\Lambda_c(2940)} = 13^{+8}_{-5}{}^{+27}_{-7}\,\mathrm{MeV}/c^2$. The measured $\Lambda_c(2880)$ helicity distribution (see Fig. 77) is consistent with the spin $\frac{5}{2}$ hypothesis. The quark model predicts the lowest $\frac{5}{2}^-$ and $\frac{5}{2}^+$ Λ_c spin excitations at about 2900 MeV/c^2, in agreement with the $\Lambda_c(2880)$ mass. The distribution of the $\Lambda_c(2880)$ yield as a function of the $M(\Lambda_c^+\pi^\pm)$, shown in Fig. 77, indicates contributions from the $\Sigma_c(2455)$ and $\Sigma_c(2520)$. The measured $\Lambda_c(2880)$ partial width ratio, $\frac{\Gamma(\Sigma_c(2520)\pi)}{\Gamma(\Sigma_c(2455)\pi)} = 0.22 \pm 0.06 \pm 0.02$, is consistent with the prediction for the $\frac{5}{2}^+$ state [386].

Belle also studied excited charmed baryons decaying to $\Lambda_c\pi$ final states. Figure 78 shows distributions of the $\Delta M(\Lambda_c\pi) \equiv M(\Lambda_c\pi) - M(\Lambda_c)$ mass differences for the $\Lambda_c^+\pi^-$, $\Lambda_c^+\pi^0$, and $\Lambda_c^+\pi^+$ combinations [387]. Peaks near 0.51 GeV/c^2 were attributed to new baryons forming an isotriplet denoted as $\Sigma_c(2800)^{0,+,++}$. The measured $\Sigma_c(2800)$ mass splittings relative to the Λ_c and $\Sigma_c(2800)$ widths are summarized in Table 25. These new states could be members of the Σ_{c2} triplet with $J^P = \frac{3}{2}^-$ with total angular momentum of the light diquark equal to two, and are expected to have

Table 25. Parameters of charmed baryons discovered by Belle. The $\Sigma_c(2800)$ masses were measured with respect to the Λ_c mass of $2286.46 \pm 0.14\,\mathrm{MeV}/c^2$.

Name	Quark content	Decay mode	Mass (MeV/c^2)	Width (MeV/c^2)
$\Sigma_c(2800)^0$	cdd	$\Lambda_c^+\pi^-$	$515.4^{+3.2+2.1}_{-3.1-6.0} + M_{\Lambda_c}$	61^{+18+22}_{-13-13}
$\Sigma_c(2800)^+$	cud	$\Lambda_c^+\pi^0$	$505.4^{+5.8+12.4}_{-4.6-12.0} + M_{\Lambda_c}$	62^{+37+52}_{-23-38}
$\Sigma_c(2800)^{++}$	cuu	$\Lambda_c^+\pi^+$	$514.5^{+3.4+2.8}_{-3.1-4.9} + M_{\Lambda_c}$	75^{+18+12}_{-13-11}
$\Xi_c(2980)^+$	csu	$\Lambda_c^+K^-\pi^+$	$2978.5 \pm 2.1 \pm 2.0$	$43.5 \pm 7.5 \pm 7.0$
$\Xi_c(2980)^0$	csd	$\Lambda_c^+K_S^0\pi^+$	$2977.1 \pm 8.8 \pm 3.5$	43.5 (fixed)
$\Xi_c(3077)^+$	csu	$\Lambda_c^+K^-\pi^+$	$3076.7 \pm 0.9 \pm 0.5$	$6.2 \pm 1.2 \pm 0.8$
$\Xi_c(3077)^0$	csd	$\Lambda_c^+K_S^0\pi^+$	$3082.8 \pm 1.8 \pm 1.5$	$5.2 \pm 3.1 \pm 1.8$

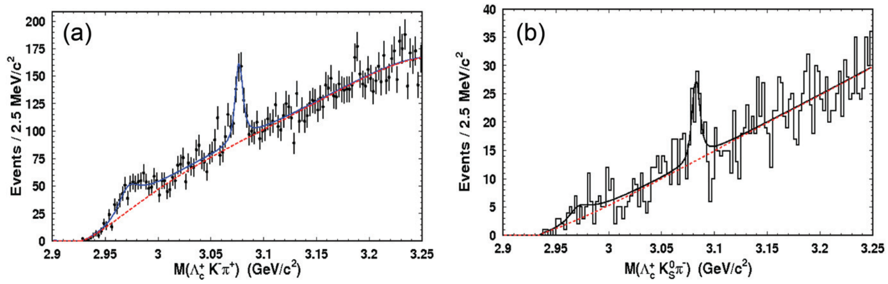

Fig. 79. Distributions of $M(\Lambda_c^+K^-\pi^+)$ (left) and $M(\Lambda_c^+K_s^0\pi^-)$ (right) with the fit curves overlaid.

$\Delta M(\Lambda_c\pi) \approx 0.5\,\mathrm{GeV}/c^2$ and a width of $15\,\mathrm{MeV}/c^2$. Mixing of the Σ_{c2} with other states predicted to lie nearby could be a reason for the wider observed state.

For charmed-strange baryons formed from csd or csu quarks, in addition to the ground states $\Xi_c^{(\prime)0,+}$ and the $\frac{3}{2}^+$ spin excitation $\Xi_c(2645)^{0,+}$, there were also two candidates for P-wave excitations, the $\Xi_c(2790)$ and $\Xi_c(2815)$, observed in the $\Xi_c'\pi$ and $\Xi_c(2645)\pi$ final states, respectively. Belle studied Ξ_c states decaying into $\Lambda_c K\pi$ [388], which requires the c and s quarks in the initial states to be carried away by different daughter particles. Two peaks in the $M(\Lambda_c^+K^-\pi^+)$ spectrum, shown in Fig. 79, were attributed to the new excited baryons denoted $\Xi_{cx}(2980)^+$ and $\Xi_{cx}(3077)^+$. Their neutral isospin partners were found in $\Lambda_c^+K_s^0\pi^-$. The $\Xi_{cx}(2980)$ and $\Xi_{cx}(3077)$ parameters, obtained from a fit to the $M(\Lambda_c K\pi)$ distribution, are summarized in Table 25. The spin parity assignments for these baryons remain unknown.

10. Two-photon physics

An e^+e^- collider is also a $\gamma\gamma$ collider. Through measurements of two-photon collision processes, we can study hadron spectroscopy. Two-photon physics at Belle includes searches for new resonances, tests of perturbative QCD, and measurements of photon–meson couplings and form factors. In this section, we report our investigations of scalar resonances and QCD tests in meson-pair production processes from two-photon collisions in the energy range between 1 GeV and 3 GeV. New resonances produced in two-photon processes are discussed in Sect. 9.

10.1. Hadron physics and QCD

The Feynman diagram for the two-photon process $\gamma\gamma \to X$ at an e^+e^- collider is shown in Fig. 80, where the reaction is regarded as a collision of two photons, each of which is emitted from one of the

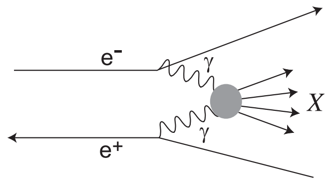

Fig. 80. A two-photon collision diagram for the process $e^+e^- \to e^+e^-X$.

initial e^+e^- beams, i.e. $e^+e^- \to e^+e^-\gamma\gamma \to e^+e^-X$. The CM energy of the two-photon collision system covers a wide range, and hence $\gamma\gamma$ reactions can be measured over a continuous and broad energy range. Usually, two-photon measurements are performed by exclusively reconstructing the final-state particle system X in order to determine the collision energy of the two photons ($W = M_X$) for each event.

Meson resonance formation processes are explored in measurements in the low energy region ($W \lesssim 3$ GeV). Since two or more overlapping resonances are often produced we extract each component from a partial-wave analysis, which takes into account interference. It is known that some light-quark scalar mesons, such as the $f_0(980)$ and $a_0(980)$, cannot easily be explained in a $q\bar{q}$ constituent model. The two-photon decay width $\Gamma_{\gamma\gamma}$ of these light quark mesons, which is measured by two-photon processes, is the most important parameter that provides information on the internal structure of such mesons.

In the higher energy region ($W \gtrsim 3$ GeV), we study the properties of charmonia and search for new hadronic states with even charge-conjugation C. Since the contributions from resonances are relatively small in this region, we can test QCD by measuring the differential cross section of meson-pair production processes, $\gamma\gamma \to MM'$, which is calculated theoretically in a model with quark-pair production $\gamma\gamma \to q\bar{q}$ followed by quark hadronization. The hadronization part is described by several different models based on perturbative and non-perturbative QCD. The Belle data sample has been used to perform such QCD tests with by far the highest statistics to date.

10.2. Principles of a two-photon process measurement at an e^+e^- collider

In a two-photon process at an e^+e^- collider, photons emitted from the beam particles are always virtual, and the four-momentum squared (q^2, which is the same as the invariant mass squared of the photon) is always negative. The virtuality of the photon $Q^2(= -q^2)$ is well approximated as $Q^2 = 4E_bE' \sin^2 \frac{\theta}{2}$, where E_b is the CM beam energy, and E' and θ are the recoil energy and the scattering angle of the beam particle, respectively, when θ is not very close to zero. However, the emission angle of the photon has a strong peak near $\theta \sim 0$ ($Q^2 \sim 0$). When the θ angles of both photons are small and the recoil e^- and e^+ are not detected, the reaction is regarded to a good approximation as a collision of two real photons (we call this case a “zero-tag event”).

In a zero-tag event, the transverse momentum component (p_t) of the final-state system X tends to be balanced, that is, close to zero. Requiring p_t balance and a much smaller detected energy compared with that for the e^+e^- beams, we can easily separate the two-photon signal process from background e^+e^- annihilation processes. However, if W is greater than about $0.5\sqrt{s}$ for the e^+e^- beams, measurement of two-photon processes becomes difficult due to the large background from annihilation processes and/or the small statistics of the signal. In the B-factory energy range, measurements up to $W \lesssim 4.5$ GeV are feasible.

The measured cross section $\sigma(e^+e^- \to e^+e^- X)$ can be translated into a two-photon collision cross section using the relation:

$$\sigma(e^+e^- \to e^+e^- X) = \int \sigma(\gamma\gamma \to X; W) \frac{dL_{\gamma\gamma}}{dW} dW,$$

where $dL_{\gamma\gamma}/dW$ is the two-photon luminosity function calculated in QED as a probability density distribution for the CM energy of the two-photon systems, which are emitted from the incident e^+e^-. The two-photon cross section depends very weakly (logarithmically) on the e^+e^- beam energy.

10.3. Single meson formation process

If only one meson is produced in a collision of two real photons, the quantum numbers of the meson, C, and spin-parity (J^{PC}) are restricted to be (even)$^{\pm+}$ or (odd, $J \neq 1)^{++}$. The production of $J = 1$ mesons is forbidden. Thus, two-photon production is complementary to e^+e^- annihilation processes where only 1^{--} mesons are produced directly.

In these processes, the production cross section of a meson is proportional to its two-photon decay width $\Gamma_{\gamma\gamma}$ via the relation:

$$\sigma(W) = 8\pi(2J+1) \frac{\Gamma_{\gamma\gamma}(R)\Gamma_R \mathcal{B}(R \to \text{final state})}{(W^2 - M_R^2)^2 + M_R^2\Gamma_R^2},$$

where M_R and Γ_R are the mass and total width of the meson, and $\mathcal{B}$ is the branching fraction.

In the zero-tag mode, we measure only the final-state particles from the decay of a produced meson. This significantly reduces backgrounds compared to the case of $\gamma\gamma$ inclusive meson production. The two-photon decay width of neutral mesons is a direct and sensitive probe of their internal structure, as mentioned above. In addition, detailed analyses of final states are useful to study the branching fractions and decay structures.

10.4. Production of light-quark mesons

Meson production through two-photon processes had been studied in the past at PEP, PETRA, TRISTAN, and LEP (see, e.g., the compilation in Ref. [389]). However, the more than three orders of magnitude larger statistics available at a B-factory compared to past experiments have qualitatively improved the analyses, allowing detailed studies of resonances that were impossible in the past.

Figure 81 shows an example of the large Belle two-photon data statistics; here we give the integrated cross section ($|\cos\theta^*| < 0.6$) for $\gamma\gamma \to \pi^+\pi^-$ as a function of W, where θ^* is the angle of the produced particle relative to one of the incident photons in the CM system of the two photons and W is the total CM energy [390,391]. This analysis used an early Belle data sample with an integrated luminosity of only 85 fb^{-1} ($\sim$ 9% of the full data). The Belle data have negligibly small error bars and a structure due to the $f_0(980)$ is clearly visible near $W \simeq 1$ GeV, as shown in the inset.

10.5. Measurements of pseudoscalar-meson-pair production at Belle

Belle has performed a study of $\gamma\gamma \to P_1P_2$, where P_1P_2 are $\pi^+\pi^-$ [390–392], K^+K^- and $K_S^0K_S^0$ [392–394], $\pi^0\pi^0$ [395,396], $\eta\pi^0$ [397], and $\eta\eta$ [398]. The angular coverage for charged-particle-pair production is restricted to the range $|\cos\theta^*| < 0.6$ due to the limitations of the charged track triggers. On the other hand, for $\pi^0\pi^0$, $\pi^0\eta$, and $\eta\eta$, we can extend the angular range to $|\cos\theta^*| < 0.8$ or even to $|\cos\theta^*| < 1.0$ (full angular coverage) owing to the wider coverage of the calorimeter trigger for multi-photon final-state events. It should be noted that a wider angular coverage plays an essential role in separating partial waves.

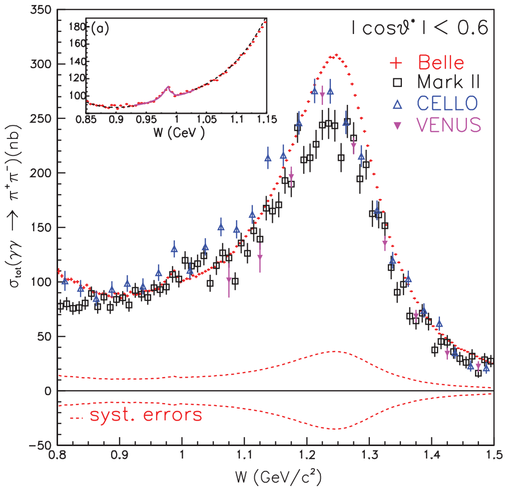

Fig. 81. Integrated cross section ($|\cos\theta^*| < 0.6$) of $\gamma\gamma \to \pi^+\pi^-$. The inset shows an enlarged view of the Belle data near the $f_0(980)$ peak. A fit with a resonance parameterization is superimposed.

A study of resonance production in two-photon collisions gives several resonance (R) parameters: its mass, its total width, and $\Gamma_{\gamma\gamma}\mathcal{B}(R \to P_1P_2)$. The latter is difficult to obtain otherwise.

10.6. Differential cross sections and partial wave amplitudes

Partial waves with even angular momenta contribute to the cross section of $\gamma\gamma \to P_1P_2$. Up to G waves may be considered at low energy ($W \lesssim 2\,\mathrm{GeV}$)[9]. The differential cross section can then be written as

$$\frac{d\sigma}{d\Omega}(\gamma\gamma \to P_1P_2) = \left|SY_0^0 + D_0Y_2^0 + G_0Y_4^0\right|^2 + \left|D_2Y_2^2 + G_2Y_4^2\right|^2, \tag{10.1}$$

where S is the $J = 0$ partial wave, D_0 and G_0 (D_2 and G_2) are the helicity-zero (-two) components of partial waves for $J = 2$ and 4, respectively, and Y_J^ms are spherical harmonics; partial waves determine the energy (W) dependence, while spherical harmonics govern the angular dependence. Because spherical harmonics are not independent of each other, the partial waves cannot be determined by only fitting the differential cross section.

If we write

$$\frac{d\sigma}{4\pi d|\cos\theta^*|}(\gamma\gamma \to P_1P_2) = \hat{S}^2|Y_0^0|^2 + \hat{D}_0^2|Y_2^0|^2 + \hat{D}_2^2|Y_2^2|^2 + \hat{G}_0^2|Y_4^0|^2 + \hat{G}_2^2|Y_4^2|^2, \tag{10.2}$$

we can determine the "hat amplitudes" $\hat{S}^2$, $\hat{D}_0^2$, $\hat{D}_2^2$, $\hat{G}_0^2$, and $\hat{G}_2^2$ by fitting differential cross sections in each W-bin, because the $|Y_J^m|^2$s are independent of each other. Spectra of hat amplitudes can give useful information on partial waves even though they contain terms arising from the interference of partial waves (S, D_0, D_2, G_0, and G_2) [395].

In order to obtain information on possible resonances, we have to parameterize the partial waves and then fit differential cross sections according to Eq. (10.1). Such analyses allow measurement of the two-photon widths of some mesons, including the $f_0(980)$ and $a_0(980)$.

The existence of the low-lying scalar nonet ($f_0(500)$ (or σ), $K^*(800)$ (or κ), $f_0(980)$, and $a_0(980)$) is a long-standing puzzle, yet these scalar mesons are thought to play the role of a "Higgs boson in QCD", by spontaneously breaking the chiral symmetry of the QCD vacuum [399–402].

[9] We denote individual partial waves by roman letters and parameterized waves by italic.

Table 26. Two-photon width ($\times\mathcal{B}$).

Meson	$\Gamma_{\gamma\gamma}(\times\mathcal{B})$ (eV)	Ref.
$f_0(980)$	$\Gamma_{\gamma\gamma} = 286 \pm 17^{+211}_{-70}$	[395]
$a_0(980)$	$\Gamma_{\gamma\gamma}\mathcal{B}(\eta\pi^0) = 128^{+3+502}_{-2-40}$	[397]
$f_2(1270)$	$\Gamma_{\gamma\gamma} = 3030 \pm 350$	[23]
$a_2(1320)$	$\Gamma_{\gamma\gamma} = 1000 \pm 60$	[23]

The measured two-photon widths of $f_0(980)$ and $a_0(980)$ are small (although the results have large systematic errors) compared to those of the $f_2(1270)$ and $a_2(1320)$, as listed in Table 26. This pattern of widths supports a picture in which the low-lying scalar mesons are made of color-triplet diquark pair [399–402].

A more satisfactory way to derive information on partial waves is to do partial wave analyses utilizing hadron data of the past and fully taking into account theoretical constraints [403]; we eagerly await such analyses using the high-statistics data from Belle.

10.7. QCD in the higher energy region

In the higher energy region ($W \gtrsim 3$ GeV) where resonance contributions are small, QCD can be studied by measuring exclusive two-body hadron production. It is believed that QCD gives reliable predictions at sufficiently high energy but the applicable energy is not known. Belle can measure two-photon processes up to W of 4.5 GeV. S.J. Brodsky and G.R. Farrar predicted

$$\frac{d\sigma}{dt} = s^{2-n_c} f(\theta^*) \tag{10.3}$$

for hadron-pair production in a two-photon process at sufficiently high energy, using the Mandelstam variables $s(= W^2)$ and t [404]. n_c is the total number of elementary particles involved in the initial and final states, eight for baryon-pair production ($\therefore \sigma \sim W^{-10}$) and six for meson-pair production ($\therefore \sigma \sim W^{-6}$). S.J. Brodsky and G.P. Lepage (BL) also calculated the differential cross section for meson-pair production [405]. Their calculation was based on perturbative QCD where the perturbatively calculable $\gamma\gamma \to q\bar{q}$ part is convoluted with the quark distribution amplitude. They obtained

$$\frac{d\sigma}{d|\cos\theta^*|} = 16\pi\alpha^2 \frac{|F_M(s)|^2}{s} \left\{ \frac{(e_1 - e_2)^4}{\sin^4\theta^*} + \frac{2(e_1e_2)(e_1 - e_2)^2}{\sin^2\theta^*} g(\theta^*) + 2(e_1e_2)^2 g^2(\theta^*) \right\}, \tag{10.4}$$

where $F_M(s)$ is the electromagnetic form factor for a meson M, e_i is the charge of a constituent quark, and g is a function that depends on the quark distribution function. For charged meson-pair processes this calculation predicts $d\sigma/d\cos\theta^* \sim \sin^{-4}\theta^*$, and $d\sigma(\pi^+\pi^-)/d\sigma(K^+K^-) = (f_K/f_\pi)^4$. The first term in Eq. (10.4), which is dominant for charged meson pair processes, does not depend on g because the dependence on the quark distribution function is absorbed into F_M. This prediction was improved by taking into account the effect of the s quark and modifying distribution functions [406,407]. Predictions for neutral meson-pair processes are not straightforward, since the terms that include g are dominant.

On the other hand, a non-perturbative calculation in the handbag model [408,409] (DKV) factorizes the non-perturbative hadronization part and gives the differential cross section

$$\frac{d\sigma}{d|\cos\theta^*|} = \frac{8\pi\alpha^2}{s} \frac{1}{\sin^4\theta^*} |R_{M\overline{M}}(s)|^2. \tag{10.5}$$

Table 27. Comparison between measured angular distribution and perturbative QCD prediction of $\sin^{-4}\theta^*$.

Mode	$\sin^{-4}\theta^*$	W (GeV)	$\lvert\cos\theta^*\rvert$	Ref.
$\pi^+\pi^-$	Well matched	3.0–4.1	<0.6	[392]
K^+K^-	Well matched	3.0–4.1	<0.6	[392]
$K^0_S K^0_S$	Matched	2.4–3.3	<0.6	[394]
$\pi^0\pi^0$	Better agreement with $\sin^{-4}\theta^* + b\cos\theta^*$	2.4–4.1	< 0.8	[395]
	Approaches $\sin^{-4}\theta^*$ above 3.1 GeV			
$\eta\pi^0$	Good agreement above 2.7 GeV	3.1–4.1	<0.8	[397]
$\eta\eta$	Poor agreement	2.4–3.3	<0.9	[398]
	Close to $\sin^{-6}\theta^*$ above 3.0 GeV			

Table 28. Energy dependence of the measured cross section. (n value in $\sigma_0 \propto W^{-n}$) and ratios of σ_0 between different processes. σ_0 is the cross section integrated over the sensitive angular region. An SU(3) octet (mixture of octet and singlet with mixing angle $-18°$) is assumed for the η meson. R_f is the ratio of decay constants squared, $f^2_\eta/f^2_{\pi^0}$.

Process	n or σ_0 ratio	W (GeV)	$\lvert\cos\theta^*\rvert$	BL [405]	BC [406,407]	DKV [408,409]
$\pi^+\pi^-$	$7.9 \pm 0.4 \pm 1.5$	3.0–4.1	<0.6	6	6	
K^+K^-	$7.3 \pm 0.3 \pm 1.5$	3.0–4.1	<0.6	6	6	
$K^0_S K^0_S$	$10.5 \pm 0.6 \pm 0.5$	2.4–4.0	<0.6	6	10	
$\pi^0\pi^0$	$8.0 \pm 0.5 \pm 0.4$	3.1–4.1	<0.8	6	10	
$\eta\pi^0$	$10.5 \pm 1.2 \pm 0.5$	3.1–4.1	<0.8	6	10	
$\eta\eta$	$7.8 \pm 0.6 \pm 0.4$	2.4–3.3	<0.8	6	10	
$p\bar{p}$	$12.4^{+2.4}_{-2.3}$	3.2–4.0	<0.6	10		
$K^+K^-/\pi^+\pi^-$	$0.89 \pm 0.04 \pm 0.15$	3.0–4.1	<0.6	2.3	1.06	
$K^0_S K^0_S/K^+K^-$	$\sim$0.13 to $\sim$0.01	2.4–4.0	<0.6		0.005	0.08
$\pi^0\pi^0/\pi^+\pi^-$	$0.32 \pm 0.03 \pm 0.06$	3.1–4.1	<0.6		0.04–0.07	0.5
$\eta\pi^0/\pi^0\pi^0$	$0.48 \pm 0.05 \pm 0.04$	3.1–4.0	<0.8	$0.24R_f (0.46R_f)$		
$\eta\eta/\pi^0\pi^0$	$0.37 \pm 0.02 \pm 0.03$	2.4–3.3	<0.8	$0.36R_f^2 (0.62R_f^2)$		

Although this model cannot predict absolute values for the cross sections, it gives a relation between annihilation form factors $R_{M\bar{M}}(s)$ in different processes.

The Belle experiment has measured cross sections for $\pi^+\pi^-$ [392], $\pi^0\pi^0$ [396], $\eta\pi^0$ [397], $\eta\eta$ [398], K^+K^- [392], $K^0_S K^0_S$ [394], and $p\bar{p}$ [410] production in two-photon production. Before the Belle experiment no data were available to test these models due to limited statistics and poor particle identification capabilities.

The angular distribution measurements are summarized in Table 27. The W^{-n} dependence of the cross section and ratios of cross sections are listed in Table 28. The measured angular dependences agree with $\sin^{-4}\theta^*$ except for the $\eta\eta$ process. We obtained larger n values than the BL prediction of six, and in the neutral meson-pair process the value is close to the BC prediction of ten, which may be due to a significant higher order contribution in this energy region [406,407].

The ratios of cross sections asymptotically approach a constant as energy increases, but no model can systematically reproduce all the measured values.

For baryon-pair processes, the measured n value is larger than the perturbative QCD prediction of ten, but decreases as W increases [410]. The angular distribution above 2.5 GeV agrees qualitatively with the perturbative QCD prediction but has a steeper rise.

10.8. Summary and outlook

Two-photon processes can be a background when studying CP violation, the main theme at a B-factory, as well as for other physics topics. However, a detailed study of two-photon data can contribute much to the understanding of hadron physics in its own right as described above. The topics that can be addressed are divided into four categories: the search for and study of new or exotic particles, the production and decay structure of charmonia, the nature of light-quark resonances, and tests of perturbative QCD. The overwhelming statistics available at a B-factory has opened a new era in two-photon physics.

Our study so far has mostly been limited to collisions of two real photons; a vast unstudied region remains open for future investigation, in which one or both of the photons are virtual, i.e. the study of single and double tagged two-photon physics.

11. Summary

The Belle experiment at KEKB is described in Sect. 2. Belle accomplished its main mission, which was the verification of Kobayashi and Maskawa's bold proposal that a single irreducible complex phase can explain all matter–antimatter asymmetries (CP-violating phenomena).

As discussed in detail in Sect. 3, Belle's observation of large time-dependent CP asymmetries in modes such as $B \to J/\psi K_S$ (together with similar results from BaBar) in 2001 demonstrated that the KM proposal was correct and laid the foundation for their 2008 Nobel Prize in Physics. In addition, the results provided a theoretically clean measurement of one of the interior angles of the unitarity triangle, ϕ_1 (or β). After the accumulation of the one ab^{-1} data set, the measurements of CP asymmetries involving ϕ_1 became precision results and important calibrations for new physics studies.

To check the consistency of the SM of particle physics, it is also necessary to measure the other two interior angles of the unitarity triangle, ϕ_2 (or α) and ϕ_3 (or γ). Although theoretical plans for the determination of these angles were proposed at the start of the B-factories, the final and most precise results were obtained by new methods that were not originally anticipated; e.g. for ϕ_3, the best sensitivity was obtained from Dalitz analysis of $B \to DK$, $D \to K_S\pi^+\pi^-$ decays.

The development of the methods for determination of the length of the sides of the unitarity triangle also followed a somewhat unexpected path that was determined by the convergence of high statistics B-factory data and theoretical insight. The results and methods used for $|V_{cb}|$ and $|V_{ub}|$ determination are described in Sect. 4.

The results for the sides and interior angles of the unitarity triangle are consistent. However, reasonably large new physics contributions, of order 10% the size of the SM amplitude, are still allowed. In parallel with the work on fixing the weak interaction parameters of the unitarity triangle, Belle also completed a decade of studies and publications on rare decays, as described in Sect. 5.

In rare decays for which the SM amplitude contribution is highly suppressed, the effects of NP could be clear and dramatic. Belle established the existence of a number of highly suppressed processes including $b \to d\gamma$ and $b \to s\ell^+\ell^-$. In addition, as the data sample has increased, there have been a number of intriguing hints of NP in various channels, e.g. exclusive hadronic $b \to s$ CP-violating modes, $B \to \tau\nu$, and $B \to K^*\ell^+\ell^-$, but so far there is no compelling evidence of NP at the current level of sensitivity in Belle. Exploration of NP will require the luminosity of SuperKEKB and Belle II.

A B-factory is also a high energy tau-charm factory and has the largest samples of τ leptons and reconstructed charm. The results on τ lepton physics are described in Sect. 6. Searches for lepton-flavor-violating (LFV) decays and CP violation in the τ sector have reached an interesting sensitivity at Belle but so far no NP signals have been found. The foundation for Belle II explorations of this sector has been established. The results on charm are discussed in Sect. 7. The highlights include two classes of unexpected and unanticipated results: the discovery of D–$\bar{D}$ mixing and the existence of a large number of new charmonium-like resonances (Sect. 9). The latter was completely unexpected by the theoretical community and was guided by Belle data.

Belle is also the world's leading two-photon facility. The results in this domain of physics are discussed in Sect. 10. Finally, KEKB's capabilities to operate in a range of center of mass energies allowed Belle to record a number of *unique* large data sets at the $\Upsilon(1S)$, $\Upsilon(2S)$, and $\Upsilon(5S)$ resonances. The $\Upsilon(5S)$ data were used, as expected, to study some properties and decays of B_s mesons (Sect. 8). However, theorists did not anticipate that these data could be used to discover a series of peculiar bottomonium-like resonances or find the missing bottomonia states such as the $\eta_b(2S)$, $h_b(1P)$, and $h_b(2P)$. These discoveries in hadron spectroscopy are described in Sect. 9.

In addition to establishing the KM model, measuring weak interaction parameters, and observing suppressed SM processes, the analysis of Belle data was marked by a series of unexpected discoveries driven by data. At the next stage in Belle II at SuperKEKB, the focus will shift to NP exploration. However, it is likely that the large increase in luminosity will also lead to unanticipated results and discoveries.

Acknowledgements

We thank the KEKB group for excellent operation of the accelerator; the KEK cryogenics group for efficient solenoid operations; and the KEK computer group, the NII, and PNNL/EMSL for valuable computing and SINET4 network support. We acknowledge support from MEXT, JSPS, and Nagoya's TLPRC (Japan); ARC and DIISR (Australia); NSFC (China); MSMT (Czechia); DST (India); INFN (Italy); MEST, NRF, GSDC of KISTI, and WCU (Korea); MNiSW (Poland); MES and RFAAE (Russia); ARRS (Slovenia); SNSF (Switzerland); NSC and MOE (Taiwan); and DOE and NSF (USA).

References

[1] S. Kurokawa and E. Kikutani, Nucl. Instrum. Methods Phys. Res., Sect. A **499**, 1 (2003).
[2] A. Abashian et al. (Belle Collaboration), Nucl. Instrum. Methods Phys. Res., Sect. A **479**, 117 (2002) and references therein.
[3] R. Abe et al., Nucl. Instrum. Methods Phys. Res., Sect. A **535**, 558 (2004).
[4] Z. Natkaniec et al., Nucl. Instrum. Methods Phys. Res., Sect. A **560**, 1 (2006).
[5] Y. Ushiroda et al., Nucl. Instrum. Methods Phys. Res., Sect. A **511**, 6 (2002).
[6] K. Miyabayashi et al., Nucl. Instrum. Methods Phys. Res., Sect. A **494**, 298 (2002).
[7] I. Nakamura et al., J. Phys.: Conf. Ser. **160**, 012003 (2009).
[8] B. Shwartz et al., Nucl. Instrum. Methods Phys. Res., Sect. A **598**, 220 (2009).
[9] J. G. Wang et al., Nucl. Instrum. Methods Phys. Res., Sect. A **508**, 133 (2003).
[10] Y. Hoshi et al., Nucl. Phys. Proc. Suppl. **158**, 190 (2006).
[11] S. Y. Suzuki et al., Nucl. Instrum. Methods Phys. Res., Sect. A **494**, 535 (2002).
[12] M. Nakao et al., IEEE Trans. Nucl. Sci. **48**, 2385 (2001).
[13] E. Won et al., IEEE Trans. Nucl. Sci. **55**, 122 (2008).
[14] B. G. Cheon et al., Nucl. Instrum. Methods Phys. Res., Sect. A **494**, 548 (2002).
[15] T. Higuchi et al., IEEE Trans. Nucl. Sci. **52**, 1912 (2005).
[16] E. Nakano et al., Nucl. Instrum. Methods Phys. Res., Sect. A **494**, 402 (2002).
[17] K. Hanagaki et al., Nucl. Instrum. Methods Phys. Res., Sect. A **485**, 490 (2002).
[18] Y. Yusa et al., Nucl. Instrum. Methods Phys. Res., Sect. A **598**, 183 (2009).

[19] A. Abashian et al., Nucl. Instrum. Methods Phys. Res., Sect. A **491**, 69 (2002).
[20] J. H. Christenson et al., Phys. Rev. Lett. **13**, 138 (1964).
[21] M. Kobayashi and T. Maskawa, Prog. Theor. Phys. **49**, 652 (1973).
[22] L. Wolfenstein, Phys. Rev. Lett. **51**, 1945 (1983).
[23] J. Beringer et al. (Particle Data Group), Phys. Rev. D **86**, 010001 (2012).
[24] A. B. Carter and A. I. Sanda, Phys. Rev. Lett. **45**, 952 (1980).
[25] A. B. Carter and A. I. Sanda, Phys. Rev. D **23**, 1567 (1981).
[26] I. I. Bigi and A. I. Sanda, Nucl. Phys. B **193**, 85 (1981).
[27] H. Kakuno et al., Nucl. Instrum. Methods Phys. Res., Sect. A **533**, 516 (2004).
[28] H. Tajima et al., Nucl. Instrum. Methods Phys. Res., Sect. A **533**, 370 (2004).
[29] I. Adachi et al. (Belle Collaboration), Phys. Rev. Lett. **108**, 171802 (2012).
[30] K. Abe et al. (Belle Collaboration), Phys. Rev. Lett. **91**, 261602 (2003).
[31] K.-F. Chen et al. (Belle Collaboration), Phys. Rev. Lett. **98**, 031802 (2007).
[32] Y. Nakahama et al. (Belle Collaboration), Phys. Rev. D **82**, 073011 (2010).
[33] K. Abe et al. (Belle Collaboration), Phys. Rev. Lett. **89**, 071801 (2002).
[34] R. A. Fisher, Ann. Eugenics **7**, 179 (1936).
[35] C. C. Fox and S. Wolfram, Phys. Rev. Lett. **41**, 1581 (1978).
[36] H. Ishino et al. (Belle Collaboration), Phys. Rev. Lett. **95**, 101801 (2005).
[37] K. Abe et al. (Belle Collaboration), Phys. Rev. Lett. **93**, 021601 (2004).
[38] Y. Amhis et al. (Heavy Flavor Averaging Group), arXiv:1207.1158 and online update at http://www.slac.stanford.edu/xorg/hfag.
[39] M. Gronau and D. London, Phys. Rev. Lett. **65**, 3381 (1990).
[40] J. Charles et al. (CKMfitter Group), Eur. Phys. J. C **41**, 1 (2005).
[41] H. R. Quinn and A.E. Snyder, Phys. Rev. D **48**, 2139 (1993).
[42] A. Kusaka et al. (Belle Collaboration), Phys. Rev. Lett. **98**, 221602 (2007).
[43] A. Kusaka et al. (Belle Collaboration), Phys. Rev. D **77**, 072001 (2008).
[44] J. Zhang et al. (Belle Collaboration), Phys. Rev. Lett. **91**, 221801 (2003).
[45] A. Somov et al. (Belle Collaboration), Phys. Rev. Lett. **96**, 171801 (2006).
[46] B. Aubert et al. (BaBar Collaboration), Phys. Rev. Lett. **97**, 261801 (2006).
[47] B. Aubert et al. (BaBar Collaboration), Phys. Rev. D **76**, 052007 (2007).
[48] A. Somov et al. (Belle Collaboration), Phys. Rev. D **76**, 011104 (2007).
[49] M. Gronau, D. London, and D. Wyler, Phys. Lett. B **253**, 483 (1991).
[50] M. Gronau, D. London, and D. Wyler, Phys. Lett. B **265**, 172 (1991).
[51] D. Atwood, I. Dunietz, and A. Soni, Phys. Rev. Lett. **78**, 3357 (1997).
[52] Y. Horii et al. (Belle Collaboration), Phys. Rev. Lett. **106**, 231803 (2011).
[53] A. Giri, Yu. Grossman, A. Soffer, and J. Zupan, Phys. Rev. D **68**, 054018 (2003).
[54] A. Poluektov et al. (Belle Collaboration), Phys. Rev. D **81**, 112002 (2010).
[55] A. Bondar, A. Poluektov, Eur. Phys. J. C **47**, 347 (2006).
[56] A. Bondar, A. Poluektov, Eur. Phys. J. C **55**, 51 (2008).
[57] R. A. Briere et al. (CLEO Collaboration), Phys. Rev. D **80**, 032002 (2009).
[58] H. Aihara et al. (Belle Collaboration), Phys. Rev. D **85**, 112014 (2012).
[59] M. Neubert, Phys. Rep. **245**, 259 (1994).
[60] I. Caprini, L. Lellouch, and M. Neubert, Nucl. Phys. B **530**, 153 (1998).
[61] N. Isgur and M. B. Wise, Phys. Lett. B **237**, 527 (1990).
[62] J. A. Bailey et al. (Fermilab Lattice and MILC Collaborations), PoS **LATTICE2010**, 311 (2010).
[63] M. Okamoto et al., Nucl. Phys. Proc. Suppl. **140**, 461 (2005).
[64] W. Dungel et al. (Belle Collaboration), Phys. Rev. D **82**, 112007 (2010).
[65] K. Abe et al. (Belle Collaboration), Phys. Lett. B **526**, 258 (2002).
[66] D. Benson, I. I. Bigi, T. Mannel, and N. Uraltsev, Nucl. Phys. B **665**, 367 (2003).
[67] C. W. Bauer, Z. Ligeti, M. Luke, A. V. Manohar, and M. Trott, Phys. Rev. D **70**, 094017 (2004).
[68] P. Gambino and N. Uraltsev, Eur. Phys. J. C **34**, 181 (2004).
[69] P. Urquijo et al. (Belle Collaboration), Phys. Rev. D **75**, 032001 (2007).
[70] C. Schwanda et al. (Belle Collaboration), Phys. Rev. D **75**, 032005 (2007).
[71] A. Höcker and V. Kartvelishvili, Nucl. Instrum. Methods Phys. Res., Sect. A **372**, 469 (1996).
[72] C. Schwanda et al. (Belle Collaboration), Phys. Rev. D **78**, 032016 (2008).
[73] D. Benson, I. I. Bigi, and N. Uraltsev, Nucl. Phys. B **710**, 371 (2005).

[74] C. Schwanda et al. (Belle Collaboration), Phys. Rev. Lett. **93**, 131803 (2004).
[75] T. Hokuue et al. (Belle Collaboration), Phys. Lett. B **648**, 139 (2007).
[76] H. Ha et al. (Belle Collaboration), Phys. Rev. D **83**, 032007 (2011).
[77] J. A. Bailey et al. (Fermilab Lattice and MILC Collaboration), Phys. Rev. D **79**, 054507 (2009).
[78] P. Ball and R. Zwicky, Phys. Rev. D **71**, 014015 (2005).
[79] E. Gulez et al. (HPQCD Collaboration), Phys. Rev. D **73**, 074502 (2006).
[80] A. Limosani et al. (Belle Collaboration), Phys. Lett. B **621**, 28 (2005).
[81] H. Kakuno et al. (Belle Collaboration), Phys. Rev. Lett. **92**, 101801 (2004).
[82] P. Urquijo et al. (Belle Collaboration), Phys. Rev. Lett. **104**, 021801 (2010).
[83] B. O. Lange, M. Neubert, and G. Paz, Phys. Rev. D **72**, 073006 (2005).
[84] J. R. Andersen and E. Gardi, J. High Energy Phys. **0601**, 097 (2006).
[85] P. Gambino, P. Giordano, G. Ossola, and N. Uraltsev, J. High Energy Phys. **0710**, 058 (2007).
[86] U. Aglietti, F. Di Lodovico, G. Ferrera, and G. Ricciardi, Eur. Phys. J. C **59**, 831 (2009).
[87] K. Ikado et al. (Belle Collaboration), Phys. Rev. Lett. **97**, 251802 (2006).
[88] K. Hara et al. (Belle Collaboration), Phys. Rev. D **82**, 071101 (2010).
[89] P. del Amo Sanchez et al. (BaBar Collaboration), arXiv:1008.0104 [hep-ex].
[90] B. Aubert et al. (BaBar Collaboration), Phys. Rev. D **81**, 051101 (2010).
[91] I. Adachi et al. (Belle Collaboration), arXiv:1208.4678 [hep-ex].
[92] M. Feindt et al., Nucl. Instrum. Methods Phys. Res., Sect. A **654**, 432 (2011).
[93] N. Satoyama et al. (Belle Collaboration), Phys. Lett. B **647**, 67 (2007).
[94] J. Conrad et al., Phys. Rev. D **67**, 012002 (2003).
[95] Presentation by Y. M. Yook on behalf of Belle Collaboration, at 36th Int. Conf. on High Energy Phys., Melbourne, Australia (2012).
[96] C.-H. Chen and C.-Q. Geng, J. High Energy Phys. **10**, 053 (2006).
[97] A. Matyja et al. (Belle Collaboration), Phys. Rev. Lett. **99**, 191807 (2007).
[98] A. Bozek et al. (Belle Collaboration), Phys. Rev. D **82**, 072005 (2010).
[99] I. Adachi et al. (Belle Collaboration), arXiv:0910.4301 [hep-ex].
[100] J. P. Lees et al. (BaBar Collaboration), Phys. Rev. Lett. **109**, 101802 (2012).
[101] M. Beneke, G. Buchalla, M. Neubert, and C. T. Sachrajda, Phys. Rev. Lett. **83**, 1914 (1999).
[102] M. Beneke, G. Buchalla, M. Neubert, and C. T. Sachrajda, Nucl. Phys. B **591**, 313 (2000).
[103] M. Beneke, G. Buchalla, M. Neubert, and C. T. Sachrajda, Nucl. Phys. B **606**, 245 (2001).
[104] C. W. Chiang, M. Gronau, Z. Luo, J. L. Rosner, and D. A. Suprun, Phys. Rev. D **69**, 034001 (2004).
[105] C. W. Chiang, M. Gronau, J. L. Rosner, and D. A. Suprun, Phys. Rev. D **70**, 034020 (2004).
[106] C. W. Chiang and Y. F. Zhou, J. High Energy Phys. **12**, 027 (2006).
[107] A. Soni and D. A. Suprun, Phys. Rev. D **75**, 054006 (2007).
[108] C. W. Chiang and Y. F. Zhou, J. High Energy Phys. **03**, 055 (2009).
[109] H. N. Li and H. L. Yu, Phys. Rev. D **53**, 2480 (1996).
[110] H. N. Li and H. L. Yu, Phys. Lett. B **353**, 301 (1995).
[111] Y. Y. Keum, H. N. Li, and A. I. Sanda, Phys. Rev. D **63**, 054008 (2001).
[112] Y. T. Duh et al. (Belle Collaboration), arXiv:1210.1348 [hep-ex].
[113] Y. Y. Charng and H. N. Li, Phys. Rev. D **71**, 014036 (2005).
[114] A. J. Buras, R. Fleischer, S. Recksiegel, and F. Schwab, Nucl. Phys. B **697**, 133 (2004).
[115] S. Baek and D. London, Phys. Lett. B **653**, 249 (2007).
[116] W. S. Hou, H. N. Li, S. Mishima, and M. Nagashima, Phys. Rev. Lett. **98**, 131801 (2007).
[117] M. Imbeault, S. Baek, and D. London, Phys. Lett. B **663**, 410 (2008).
[118] S. Khalil, A. Masiero, and H. Murayama, Phys. Lett. B **682**, 74 (2009).
[119] M. Gronau, Phys. Lett. B **627**, 82 (2005).
[120] Y. Chao et al. (Belle Collaboration), Phys. Rev. Lett. **94**, 181803 (2005).
[121] Y. T. Tsai et al. (Belle Collaboration), Phys. Rev. D **75**, 111101 (2007).
[122] G. Kramer and W. F. Palmer, Phys. Rev. D **45**, 193 (1992).
[123] C. T. Hoi et al. (Belle Collaboration), Phys. Rev. Lett. **108**, 031801 (2012).
[124] P. Chang et al. (Belle Collaboration), Phys. Rev. D **71**, 091106 (2005).
[125] J. Schumann et al. (Belle Collaboration), Phys. Rev. Lett. **97**, 061802 (2006).
[126] J. Schumann et al. (Belle Collaboration), Phys. Rev. D **75**, 092002 (2007).
[127] C. H. Wang et al. (Belle Collaboration), Phys. Rev. D **75**, 092005 (2007).
[128] A. Garmash et al. (Belle Collaboration), Phys. Rev. D **75**, 012006 (2007).

[129] A. Garmash et al. (Belle Collaboration), Phys. Rev. Lett. **96**, 251803 (2006).
[130] P. Chang et al. (Belle Collaboration), Phys. Lett. B **599**, 148 (2004).
[131] C. M. Jen et al. (Belle Collaboration), Phys. Rev. D **74**, 111101 (2006).
[132] A. Garmash et al. (Belle Collaboration), Phys. Rev. D **71**, 092003 (2005).
[133] K. F. Chen et al. (Belle Collaboration), Phys. Rev. Lett. **91**, 201801 (2003).
[134] J. H. Kim et al. (Belle Collaboration), Phys. Rev. D **86**, 031101 (2012).
[135] J. Zhang et al. (Belle Collaboration), Phys. Rev. Lett. **94**, 031801 (2005).
[136] A. Gordon et al. (Belle Collaboration), Phys. Lett. B **542**, 183 (2002).
[137] G. Barr et al. (NA31 Collaboration), Phys. Lett. B **317**, 233 (1993).
[138] J. R. Batley et al. (NA48 Collaboration), Phys. Lett. B **544**, 97 (2002).
[139] A. Alavi-Harati et al. (KTeV Collaboration), Phys. Rev. D **67**, 012005 (2003).
[140] J. P. Lees et al. (BaBar Collaboration), arXiv:1206.3525 [hep-ex].
[141] R. Aaij et al. (LHCb Collaboration), Phys. Rev. Lett. **108**, 111602 (2012).
[142] T. Aaltonen et al. (CDF Collaboration), Phys. Rev. Lett. **109**, 111801 (2012).
[143] C. C. Chiang et al. (Belle Collaboration), Phys. Rev. D **81**, 071101 (2010).
[144] J. Zhang et al. (Belle Collaboration), Phys. Rev. Lett. **95**, 141801 (2005).
[145] S. H. Kyeong et al. (Belle Collaboration), Phys. Rev. D **80**, 051103 (2009).
[146] P. Goldenzweig et al. (Belle Collaboration), Phys. Rev. Lett. **101**, 231801 (2008).
[147] K. F. Chen et al. (Belle Collaboration), Phys. Rev. Lett. **94**, 221804 (2005).
[148] C. C. Chiang et al. (Belle Collaboration), Phys. Rev. D **78**, 111102 (2008).
[149] A. Ali, J. G. Korner, and G. Kramer, Z. Phys. C **1**, 269 (1979).
[150] M. Suzuki, Phys. Rev. D **66**, 054018 (2002).
[151] A. Kagan, Phys. Lett. B **601**, 151 (2004).
[152] C. Bauer, D. Pirjol, I. Z. Rothstein, and I. W. Stewart, Phys. Rev. D **70**, 054015 (2004).
[153] P. Colangelo, F. D. Fazio, and T. N. Pham, Phys. Lett. B **597**, 291 (2004).
[154] M. Ladisa, V. Laporta, G. Nardulli, and P. Santorelli, Phys. Rev. D **70**, 114025 (2004).
[155] H. N. Li and S. Mishima, Phys. Rev. D **71**, 054025 (2005).
[156] M. Beneke, J. Rohrer, and D. Yang, Phys. Rev. Lett. **96**, 141801 (2006).
[157] A. Garmash et al. (Belle Collaboration), Phys. Rev. D **69**, 012001 (2004).
[158] Y. T. Shen et al. (Belle Collaboration), arXiv:0802.1547 [hep-ex].
[159] J. T. Wei et al. (Belle Collaboration), Phys. Lett. B **659**, 80 (2008).
[160] J. H. Chen et al. (Belle Collaboration), Phys. Rev. Lett. **100**, 251801 (2008).
[161] M. Z. Wang et al. (Belle Collaboration), Phys. Rev. D **76**, 052004 (2007).
[162] M. Z. Wang et al. (Belle Collaboration), Phys. Rev. Lett. **90**, 201802 (2003).
[163] Y. J. Lee et al. (Belle Collaboration), Phys. Rev. Lett. **93**, 211801 (2004).
[164] C. K. Chua, W. S. Hou, and S. Y. Tsai, Phys. Lett. B **544**, 139 (2002).
[165] J. L. Rosner, Phys. Rev. D **68**, 014004 (2003).
[166] B. Kerbikov, A. Stavinsky, and V. Fedotov, Phys. Rev. C **69**, 055205 (2004).
[167] J. Haidenbauer, U.-G. Meissner, and A. Sibirtsev, Phys. Rev. D **74**, 017501 (2006).
[168] D. R. Entem and F. Fernandez, Phys. Rev. D **75**, 014004 (2007).
[169] M. Misiak et al., Phys. Rev. Lett. **98**, 022002 (2007).
[170] A. L. Kagan and M. Neubert Eur. Phys. J. C **7**, 5 (1999).
[171] O. Büchmuller and H. Flächer, Phys. Rev. D **73**, 073008 (2006).
[172] A. Limosani et al. (Belle Collaboration), Phys. Rev. Lett. **103**, 241801 (2009).
[173] M. Nakao et al. (Belle Collaboration), Phys. Rev. D **69**, 112001 (2004).
[174] Y. Y. Keum, M. Matsumori, and A. I. Sanda, Phys. Rev. D **72**, 014013 (2005).
[175] S. W. Bosch and G. Buchalla, Nucl. Phys. B **621**, 459 (2001).
[176] A. Ali and A. Y. Parkhomenko, Eur. Phys. J. C **23**, 89 (2002).
[177] S. Nishida et al. (Belle Collaboration), Phys. Rev. Lett. **89**, 231801 (2002).
[178] H. Yang et al. (Belle Collaboration), Phys. Rev. Lett. **94**, 111802 (2005).
[179] J. Li et al. (Belle Collaboration), Phys. Rev. Lett. **101**, 251601 (2008).
[180] S. Nishida et al. (Belle Collaboration), Phys. Lett. B **610**, 23 (2005).
[181] R. Wedd et al. (Belle Collaboration), Phys. Rev. D **81**, 111104 (2010).
[182] H. Sahoo et al. (Belle Collaboration), Phys. Rev. D **84**, 071101 (2011).
[183] Y.-J. Lee et al. (Belle Collaboration), Phys. Rev. Lett. **95**, 061802 (2005).
[184] D. Atwood, M. Gronau, and A. Soni, Phys. Rev. Lett. **79**, 185 (1997).

[185] Y. Ushiroda et al. (Belle Collaboration), Phys. Rev. D **74**, 111104 (2006).
[186] D. Atwood et al., Phys. Rev. D **71**, 076003 (2005).
[187] A. Abulencia et al. (CDF Collaboration), Phys. Rev. Lett. **97**, 242003 (2006).
[188] Y. Ushiroda et al. (Belle Collaboration), Phys. Rev. Lett. **100**, 021602 (2008).
[189] D. Mohapatra et al. (Belle Collaboration), Phys. Rev. Lett. **96**, 221601 (2006).
[190] N. Taniguchi et al. (Belle Collaboration), Phys. Rev. Lett. **101**, 111801 (2008).
[191] G. Burdman, Phys. Rev. D **52**, 6400 (1995).
[192] L. Hewett and J. D. Wells, Phys. Rev. D **55**, 5549 (1997).
[193] G. Buchalla, G. Hiller, and G. Isidori, Phys. Rev. D **63**, 014015 (2000).
[194] F. Kruger, L. M. Sehgal, N. Sinha, and R. Sinha, Phys. Rev. D **61**, 114028 (2000); **63**, 019901 (2001) [erratum].
[195] A. Ali, E. Lunghi, C. Greub, and G. Hiller, Phys. Rev. D **66**, 034002 (2002).
[196] T. M. Aliev, A. Ozpineci, and M. Savci, Eur. Phys. J. C **29**, 265 (2003) and references therein.
[197] W. S. Hou, A. Hovhannisyan, and N. Mahajan, Phys. Rev. D **77**, 014016 (2008).
[198] J. Charles et al. (CKMfitter Group), Phys. Rev. D **85**, 033005 (2011).
[199] G. Buchalla and A. J. Buras, Nucl. Phys. B **400**, 225 (1993).
[200] J. C. Pati and A. Salam, Phys. Rev. D **10**, 275 (1974).
[201] A. Masiero and S. K. Vempati, Nucl. Phys. B **649**, 189 (2003).
[202] S. Baek, T. Goto, Y. Okada, and K. I. Okumura, Phys. Rev. D **64**, 095001 (2001).
[203] M. E. Gomez and H. Goldberg, Phys. Rev. D **53**, 5244 (1996).
[204] A. Ishikawa et al. (Belle Collaboration), Phys. Rev. Lett. **88**, 021801 (2002).
[205] A. Ishikawa et al. (Belle Collaboration), Phys. Rev. Lett. **91**, 261601 (2003).
[206] A. Ishikawa et al. (Belle Collaboration), Phys. Rev. Lett. **96**, 251801 (2006).
[207] J.-T. Wei et al. (Belle Collaboration), Phys. Rev. Lett. **103**, 171801 (2009).
[208] LHCb-CONF-2012-008.
[209] Y. Wang and D. Atwood, Phys. Rev. D **68**, 094016 (2003).
[210] J.-T. Wei et al. (Belle Collaboration), Phys. Rev. D **78**, 011101 (2008).
[211] J. Kaneko et al. (Belle Collaboration), Phys. Rev. Lett. **90**, 021801 (2003).
[212] Belle Collaboration, talk by T. Iijima presented at Lepton Photon (2009).
[213] A. Ali, P. Ball, L.T. Handoko, and G. Hiller, Phys. Rev. D **61**, 074024 (2000).
[214] F. Křuger and L.M. Sehgal, Phys. Lett. B **380**, 199 (1996).
[215] A. Ali and E. Pietarinen, Nucl. Phys. B **154**, 519 (1979).
[216] G. Altarelli, N. Cabibbo, G. Corbo, L. Maiani, and G. Martinelli, Nucl. Phys. B **208**, 365 (1982).
[217] T. Sjöstrand, Comput. Phys. Commun. **82**, 74 (1994).
[218] C.-L. Hsu et al. (Belle Collaboration), Phys. Rev. D **86**, 032002 (2012).
[219] M.-C. Chang et al. (Belle Collaboration), Phys. Rev. D **68**, 111101 (2003).
[220] W. J. Marciano and A. I. Sanda, Phys. Lett. B **67**, 303 (1977).
[221] B. W. Lee and R. E. Shrock, Phys. Rev. D **16**, 1444 (1977).
[222] T. P. Cheng and L. F. Li, Phys. Rev. D **16**, 1425 (1977).
[223] K. Hayasaka et al. (Belle Collaboration), Phys. Lett. B **666**, 16 (2008).
[224] K. Hayasaka et al. (Belle Collaboration), Phys. Lett. B **687**, 139 (2010).
[225] J. Lees et al. (BaBar Collaboration), Phys. Rev. D **81**, 111101 (2010).
[226] Y. Miyazaki et al. (Belle Collaboration), Phys. Lett. B **660**, 154 (1008).
[227] Y. Miyazaki et al. (Belle Collaboration), Phys. Lett. B **648**, 341 (2007).
[228] E. Christova, H. Eberl, W. Majerotto, and S. Kraml, J. High Energy Phys. **12**, 021 (2002).
[229] T. Ibrahim and P. Nath, Rev. Mod. Phys. **80**, 577 (2008).
[230] Y. Grossman, Nucl. Phys. B **426**, 355 (1994).
[231] J. H. Kühn and E. Mirkes, Phys. Lett. B **398**, 407 (1997).
[232] M. Bischofberger et al. (Belle Collaboration), Phys. Rev. Lett. **107**, 131801 (2011).
[233] G. Bonvicini et al. (CLEO Collaboration), Phys. Rev. Lett. **88**, 111803 (2002).
[234] D. Atwood and A. Soni, Phys. Rev. D **45**, 2405 (1992).
[235] K. Inami et al. (Belle Collaboration), Phys. Lett. B **551**, 16 (2003).
[236] K. Belous et al. (Belle Collaboration), Phys. Rev. Lett. **99**, 011801 (2007).
[237] B. Aubert et al. (BaBar Collaboration), Phys. Rev. D **80**, 092005 (2009).
[238] V. V. Anashin et al. (KEDR Collaboration), JETP Lett. **85**, 347 (2007).
[239] M. Fujikawa et al. (Belle Collaboration), Phys. Rev. D **78**, 072006 (2008).

[240] M. Davier, A. Hoecker, B. Malaescu, and Z. Zhang, Eur. Phys. J. C **71**, 1515 (2011); **72**, 1874 (2012) [erratum].
[241] J. P. Lees et al. (BaBar Collaboration), Phys. Rev. D **86**, 032013 (2012).
[242] F. Jegerlehner and R. Szafron, Eur. Phys. J. C **71**, 1632 (2011).
[243] M. Benayoun, P. David, L. DelBuono, and F. Jegerlehner, Eur. Phys. J. C **72**, 1848 (2012).
[244] C. Aubin and T. Blum, Phys. Rev. D **75**, 114502 (2007).
[245] P. Boyle, L. Debbio, E. Kerrane, and J. Zanotti, Phys. Rev. D **85**, 074504 (2012).
[246] K. Inami et al. (Belle Collaboration), Phys. Lett. B **643**, 5 (2006).
[247] B. Aubert et al. (BaBar Collaboration), Phys. Rev. Lett. **100**, 011801 (2008).
[248] D. Epifanov et al. (Belle Collaboration), Phys. Lett. B **654**, 65 (2007).
[249] K. Inami et al. (Belle Collaboration), Phys. Lett. B **672**, 209 (2009).
[250] M. Artuso et al. (CLEO Collaboration), Phys. Rev. Lett. **69**, 3278 (1992).
[251] J. Bartelt et al. (CLEO Collaboration), Phys. Rev. Lett. **76**, 4119 (1996).
[252] M. Bishai et al. (CLEO Collaboration), Phys. Rev. Lett. **82**, 281 (1999).
[253] D. Busculic et al. (ALEPH Collaboration), Z. Phys. C **74**, 263 (1997).
[254] S. Eidelman and V. Ivanchenko, Phys. Lett. B **257**, 437 (1991).
[255] M. Lee et al. (Belle Collaboration), Phys. Rev. D **81**, 113007 (2010).
[256] H. N. Nelson, Proc. 19th Int. Symp. on Photon and Lepton Interactions at High Energy LP99, arXiv:hep-ex/9908021.
[257] A. F. Falk, Y. Grossman, Z. Ligeti, and A. A. Petrov, Phys. Rev. D **65**, 054034 (2002).
[258] J. Brod, A.L. Kagan, and J. Zupan, arXiv:1111.5000.
[259] M. Staric et al. (Belle Collaboration), Phys. Rev. Lett. **98**, 211803 (2007).
[260] L. M. Zhang et al. (Belle Collaboration), Phys. Rev. Lett. **96**, 151801 (2006).
[261] D. M. Asner et al. (CLEO Collaboration), Phys. Rev. D **72**, 012001 (2005).
[262] L. M. Zhang et al. (Belle Collaboration), Phys. Rev. Lett. **99**, 131803 (2007).
[263] A. Zupanc et al. (Belle Collaboration), Phys. Rev. D **80**, 052006 (2009).
[264] B. Aubert et al. (BaBar Collaboration), Phys. Rev. D **78**, 034023 (2008).
[265] U. Bitenc et al. (Belle Collaboration), Phys. Rev. D **77**, 112003 (2008).
[266] E. Golowich, J. Hewett, S. Pakvasa, and A. A. Petrov, Phys. Rev. D **76**, 095009 (2007).
[267] B. R. Ko et al. (Belle Collaboration), Phys. Rev. Lett. **109**, 021601 (2012).
[268] B. R. Ko et al. (Belle Collaboration), Phys. Rev. D **84**, 111501 (2011).
[269] B. R. Ko et al. (Belle Collaboration), Phys. Rev. Lett. **106**, 211801 (2011).
[270] M. Staric et al. (Belle Collaboration), Phys. Lett. B **670**, 190 (2008).
[271] K. Arinstein et al. (Belle Collaboration), Phys. Lett. B **662**, 102 (2008).
[272] X. C. Tian et al. (Belle Collaboration), Phys. Rev. Lett. **95**, 231801 (2005).
[273] M. Stari et al. (Belle Collaboration), Phys. Rev. Lett. **108**, 071801 (2012).
[274] E. Won et al. (Belle Collaboration), Phys. Rev. Lett. **107**, 221801 (2011).
[275] B. R. Ko et al. (Belle Collaboration), Phys. Rev. Lett. **104**, 181602 (2010).
[276] R. Louvot et al. (Belle Collaboration), Phys. Rev. Lett. **102**, 021801 (2009).
[277] A. Drutskoy et al. (Belle Collaboration), Phys. Rev. Lett. **98**, 052001 (2007).
[278] G. S. Huang et al. (CLEO Collaboration), Phys. Rev. D **75**, 012002 (2007).
[279] M. Artuso et al. (CLEO Collaboration), Phys. Rev. Lett. **95**, 261801 (2005).
[280] A. Drutskoy et al. (Belle Collaboration), Phys. Rev. D **81**, 112003 (2010).
[281] R. Louvot et al. (Belle Collaboration), Phys. Rev. Lett. **104**, 231801 (2010).
[282] A. G. Grozin and M. Neubert, Phys. Rev. D **55**, 272 (1997).
[283] J. L. Rosner, Phys. Rev. D **42**, 3732 (1990).
[284] R. Aleksan et al., Phys. Lett. B **316**, 567 (1993).
[285] I. Dunietz, R. Fleischer, and U. Nierste, Phys. Rev. D **63**, 114015 (2001).
[286] I. Dunietz, Phys. Rev. D **52**, 3048 (1995).
[287] A. Lenz and U. Nierste, arXiv:1102.4274; J. High Energy Phys. **0706**, 072 (2007).
[288] A. J. Buras et al., J. High Energy Phys. **1010**, 009 (2010).
[289] Z. Ligeti et al., Phys. Rev. Lett. **105**, 131601 (2010).
[290] S. Esen et al. (Belle Collaboration), KEK Preprint 2012-20, arXiv:1208.0323.
[291] R. Aaij et al. (LHCb Collaboration), Phys. Rev. Lett. **108**, 101803 (2012).
[292] T. Aaltonen et al. (CDF Collaboration), Phys. Rev. Lett. **108**, 201801 (2012).
[293] J. Rosner, Phys. Rev. D **42**, 3732 (1990).

[294] C.-K. Chua, W.-S. Hou, and C.-H. Shen, Phys. Rev. D **84**, 074037 (2011).
[295] C. C. Peng et al. (Belle Collaboration), Phys. Rev. D **82**, 072007 (2010).
[296] P. Ball, G. W. Jones, and R. Zwicky, Phys. Rev. D **75**, 054004 (2007).
[297] A. Ali, B. D. Pecjak, and C. Greub, Eur. Phys. J. C **55**, 577 (2008).
[298] J. Wicht et al. (Belle Collaboration), Phys. Rev. Lett. **100**, 121801 (2008).
[299] C.-H.V. Chang, G.-L. Lin, and Y.-P. Yao, Phys. Lett. B **415**, 395 (1997).
[300] L. Reina, G. Ricciardi, and A. Soni, Phys. Rev. D **56**, 5805 (1997).
[301] S. W. Bosch and G. Buchalla, J. High Energy Phys. **0208**, 054 (2002).
[302] K. Abe et al., KEK Report 04-4 (2004).
[303] M. Bona et al., arXiv:0709.0451.
[304] Y. Sato et al. (Belle Collaboration), Phys. Rev. Lett. **108**, 171801 (2012).
[305] C. Edwards et al. (Crystal Ball Collaboration), Phys. Rev. Lett. **48**, 70 (1982).
[306] A. M. Badalian and B.L.G. Bakker, Phys. Rev. D **67**, 071901 (2003).
[307] S.-K. Choi et al. (Belle Collaboration), Phys. Rev. Lett. **89**, 102001 (2002).
[308] K. Abe et al. (Belle Collaboration), Phys. Rev. D **70**, 071102 (2004).
[309] A. Vinokurova et al. (Belle Collaboration), Phys. Lett. B **706**, 139 (2011).
[310] S.-K. Choi et al. (Belle Collaboration), Phys. Rev. Lett. **91**, 262001 (2003).
[311] D. Acosta et al. (CDF Collaboration), Phys. Rev. Lett. **93**, 072001 (2004).
[312] V. M. Abazov et al. (D0 Collaboration), Phys. Rev. Lett. **93**, 162001 (2004).
[313] B. Aubert et al. (BaBar Collaboration), Phys. Rev. D **71**, 071103 (2005).
[314] V. Bhardwaj et al. (Belle Collaboration), Phys. Rev. Lett. **107**, 091803 (2011).
[315] B. Aubert et al. (BaBar Collaboration), Phys. Rev. Lett. **102**, 132001 (2009).
[316] K. Abe et al. (Belle Collaboration), arXiv:hep-ex/0505038.
[317] P. del Amo Sanchez et al. (BaBar Collaboration), Phys. Rev. D **82**, 011001 (2010).
[318] T. Aushev et al. (Belle Collaboration), Phys. Rev. D **81**, 031103 (2010).
[319] B. Aubert et al. (BaBar Collaboration), Phys. Rev. D **77**, 011102 (2008).
[320] G. Gokhroo et al. (Belle Collaboration), Phys. Rev. Lett. **97**, 162002 (2006).
[321] A. Abulencia et al. (CDF Collaboration), Phys. Rev. Lett. **98**, 132002 (2007).
[322] S.-K. Choi et al. (Belle Collaboration), Phys. Rev. D **84**, 052004 (2011).
[323] E. Oset et al., arXiv:1101.2071, and references therein.
[324] B.-Q. Li and K.-T. Chao, Phys. Rev. D **79**, 094004 (2009).
[325] N. V. Drenska, A.R. Faccini, and A.D. Polosa, Phys. Rev. D **79**, 077502 (2009).
[326] S.-K. Choi et al. (Belle Collaboration), Phys. Rev. Lett. **94**, 182002 (2005).
[327] B. Aubert et al. (BaBar Collaboration), Phys. Rev. Lett. **101**, 082001 (2008).
[328] S. Uehara et al. (Belle Collaboration), Phys. Rev. Lett. **104**, 092001 (2010).
[329] J. Brodzicka et al. (Belle Collaboration), Phys. Rev. Lett. **100**, 092001 (2007).
[330] B. Aubert et al. (BaBar Collaboration), Phys. Rev. D **77**, 011002 (2008).
[331] J. P. Lees et al. (BaBar Collaboration), Phys. Rev. D **86**, 072002 (2012).
[332] T. Barnes, S. Godfrey, and E.S. Swanson, Phys. Rev. D **72**, 054026 (2005).
[333] S. Uehara et al. (Belle Collaboration), Phys. Rev. Lett. **96**, 082003 (2006).
[334] K. Abe et al. (Belle Collaboration), Phys. Rev. Lett. **98**, 082001 (2007).
[335] B. Aubert et al. (BaBar Collaboration), Phys. Rev. Lett. **95**, 142001 (2005).
[336] Q. He et al. (CLEO Collaboration), Phys. Rev. D **74**, 091104 (2006).
[337] C. Z. Yuan et al. (Belle Collaboration), Phys. Rev. Lett. **99**, 182004 (2007).
[338] J. Z. Bai et al. (BESII Collaboration), Phys. Rev. Lett. **88**, 101802 (2002).
[339] X. H. Mo et al., Phys. Lett. B **640**, 182 (2006).
[340] B. Aubert et al. (BaBar Collaboration), Phys. Rev. Lett. **98**, 202001 (2007).
[341] X. L. Wang et al. (Belle Collaboration), Phys. Rev. Lett. **99**, 142002 (2007).
[342] S.-K. Choi et al. (Belle Collaboration), Phys. Rev. Lett. **100**, 142001 (2008).
[343] R. Mizuk et al. (Belle Collaboration), Phys. Rev. D **80**, 031104 (2009).
[344] R. Mizuk et al. (Belle Collaboration), Phys. Rev. D **78**, 072004 (2008).
[345] B. Aubert et al. (BaBar Collaboration), Phys. Rev. D **79**, 112001 (2009).
[346] J. P. Lees et al. (BaBar Collaboration), Phys. Rev. D **85**, 052003 (2012).
[347] M. Ablikim et al. (BESII Collaboration), Phys. Lett. B **660**, 315 (2008).
[348] G. Pakhlova et al. (Belle Collaboration), Phys. Rev. D **77**, 011103 (2008).
[349] G. Pakhlova et al. (Belle Collaboration), Phys. Rev. Lett. **98**, 092001 (2007).

[350] G. Pakhlova et al. (Belle Collaboration), Phys. Rev. Lett. **100**, 062001 (2008).
[351] G. Pakhlova et al. (Belle Collaboration), Phys. Rev. D **80**, 091101 (2009).
[352] G. Pakhlova et al. (Belle Collaboration), Phys. Rev. Lett. **101**, 172001 (2008).
[353] A. M. Badalian, B. L. G. Bakker, and I.V. Danilkin, Phys. Atom. Nucl. **72**, 638 (2009).
[354] P. Pakhlov et al. (Belle Collaboration), Phys. Rev. Lett. **100**, 202001 (2008).
[355] T. Aaltonen et al. (CDF Collaboration), Phys. Rev. Lett. **102**, 242002 (2009).
[356] C. P. Shen et al. (Belle Collaboration), Phys. Rev. Lett. **104**, 112004 (2010).
[357] P. Pakhlov et al. (Belle Collaboration), Phys. Rev. D **79**, 071101 (2009).
[358] P. Cho and A. K. Leibovich, Phys. Rev. D **53**, 150 (1996).
[359] S. Baek et al., J. Korean Phys. Soc. **33**, 97 (1998).
[360] E. Braaten and J. Lee, Phys. Rev. Lett. **89**, 142001 (2003).
[361] N. Brambilla et al. (Quarkonium Working Group), Eur. Phys. J. C **71**, 1534 (2011).
[362] S. Godfrey and S. L. Olsen, Annu. Rev. Nucl. Part. Sci. **58**, 51 (2008).
[363] K.-F. Chen et al. (Belle Collaboration), Phys. Rev. Lett. **100**, 112001 (2008).
[364] I. Adachi et al. (Belle Collaboration), Phys. Rev. Lett. **108**, 032001 (2012).
[365] A. Bondar et al. (Belle Collaboration), Phys. Rev. Lett. **108**, 122001 (2012).
[366] I. Adachi et al. (Belle Collaboration), arXiv:1207.4345.
[367] R. Mizuk et al. (Belle Collaboration), arXiv:1205.6351.
[368] S. Godfrey and N. Isgur, Phys. Rev. D **32**, 189 (1985).
[369] F. E. Close et al., Phys. Lett. B **647**, 159 (2007).
[370] B. Aubert et al. (BaBar Collaboration), Phys. Rev. Lett. **90**, 242001 (2003).
[371] D. Besson et al. [CLEO Collaboration], Phys. Rev. D **68**, 032002 (2003).
[372] Y. Mikami et al. (Belle Collaboration), Phys. Rev. Lett. **92**, 012002 (2004).
[373] T. Barnes et al., Phys. Rev. D **68**, 054006 (2003).
[374] T. E. Browder et al., Phys. Lett. B **578**, 365 (2004).
[375] W. A. Bardeen and C. T. Hill, Phys. Rev. D **49**, 409 (1994).
[376] P. Krokovny et al. (Belle Collaboration), Phys. Rev. Lett. **91**, 262002 (2003).
[377] T. Matsuki et al., Prog. Theor. Phys. **117**, 1077 (2007).
[378] K. Abe et al. (Belle Collaboration), Phys. Rev. D **69**, 112002 (2004).
[379] A. Kuzmin et al. (Belle Collaboration), Phys. Rev. D **76**, 012006 (2007).
[380] V. Balagura et al. (Belle Collaboration), Phys. Rev. D **77**, 032001 (2008).
[381] P. Colangelo et al., Phys. Rev. D **77**, 014012 (2008).
[382] S. Capstick and N. Isgur, Phys. Rev. D **34**, 2809 (1986).
[383] N. Isgur and M. B. Wise, Phys. Rev. Lett. **66**, 1130 (1991).
[384] R. Mizuk et al. (Belle Collaboration), Phys. Rev. Lett. **98**, 262001 (2007).
[385] B. Aubert et al. (BaBar Collaboration), Phys. Rev. Lett. **98**, 012001 (2007).
[386] H. Y. Cheng and C. K. Chua, Phys. Rev. D **75**, 014006 (2007).
[387] R. Mizuk et al. (Belle Collaboration), Phys. Rev. Lett. **94**, 122002 (2005).
[388] R. Chistov et al. (Belle Collaboration), Phys. Rev. Lett. **97**, 162001 (2006).
[389] http://durpdg.dur.ac.uk/spires/hepdata/online/2gamma/2gammahome.html.
[390] T. Mori et al. (Belle Collaboration), Phys. Rev. D **75**, 051101 (2007).
[391] T. Mori et al. (Belle Collaboration), J. Phys. Soc. Jpn. **76**, 074102 (2007).
[392] H. Nakazawa et al. (Belle Collaboration), Phys. Lett. B **615**, 39 (2005).
[393] K. Abe et al. (Belle Collaboration), Eur. Phys. J. C **32**, 323 (2004).
[394] W. T. Chen et al. (Belle Collaboration), Phys. Lett. B **651**, 15 (2007).
[395] S. Uehara et al. (Belle Collaboration), Phys. Rev. D **78**, 052004 (2008).
[396] S. Uehara et al. (Belle Collaboration), Phys. Rev. D **79**, 052009 (2009).
[397] S. Uehara et al. (Belle Collaboration), Phys. Rev. D **80**, 032001 (2009).
[398] S. Uehara et al. (Belle Collaboration), Phys. Rev. D **82**, 114031 (2010).
[399] C. Amsler and N.A. Törnqvist, Phys. Rep. **389**, 61 (2004).
[400] D. V. Bugg, Phys. Rep. **397**, 257 (2004).
[401] F. E. Close and N. A. Törnqvist, J. Phys. G **28**, R249 (2002).
[402] E. Klempt and A. Zaitsev, Phys. Rep. **454**, 1 (2007).
[403] M. R. Pennington, T. Mori, S. Uehara, and Y. Watanabe, Eur. Phys. J. C **56**, 1 (2008).
[404] S. J. Brodsky and G. R. Farrar, Phys. Rev. Lett. **31**, 1153 (1973).
[405] S. J. Brodsky and G. P. Lepage, Phys. Rev. D **24**, 1808 (1981).

[406] M. Benayoun and V. L. Chernyak, Nucl. Phys. B **329**, 285 (1990).
[407] V. L. Chernyak, Phys. Lett. B **640**, 246 (2006).
[408] M. Diehl, P. Kroll, and C. Vogt, Phys. Lett. B **532**, 99 (2002).
[409] M. Diehl and P. Kroll, Phys. Lett. B **683**, 165 (2010).
[410] C. C. Kuo et al. (Belle Collaboration), Phys. Lett. B **621**, 41 (2005).